Regional simulation of coupled hydromechanical processes in fractured and granular porous aquifer using effective stress-dependent parameters

PhD Thesis

Giona Preisig*

Thesis Director:	Prof. Pierre Perrochet, University of Neuchâtel, Switzerland
Jury Member:	Prof. Philip Brunner, University of Neuchâtel, Switzerland
Jury Member:	Prof. Lyesse Laloui, Swiss Federal Institute of Technology Lausanne, Switzerland
Jury Member:	Prof. Andrea Moscariello, University of Geneva, Switzerland
Jury Member:	Dr. Antonio Dematteis, SEA Consulting s.r.l., Italy

PhD Thesis Defence Date: 17.01.2013
Public Presentation Date: 15.03.2013

*University of Neuchâtel, Center for Hydrogeology and Geothermics (CHYN), Emile-Argand 11, 2000 Neuchâtel, Switzerland, giona.preisig@unine.ch

UNIVERSITÉ DE
NEUCHÂTEL

Faculté des sciences
Secrétariat-décanat de Faculté
Rue Emile-Argand 11
2000 Neuchâtel - Suisse
Tél: + 41 (0)32 718 2100
E-mail: secretariat.sciences@unine.ch

IMPRIMATUR POUR THESE DE DOCTORAT

La Faculté des sciences de l'Université de Neuchâtel autorise l'impression de la présente thèse soutenue par

Monsieur Giona PREISIG

Titre: Regional simulation of coupled hydromechanical processes in fractured and granular porous aquifer using effective stress-dependent parameters

sur le rapport des membres du jury:

- Prof. Pierre Perrochet, Université de Neuchâtel, directeur de thèse
- Prof. Philip Brunner, Université de Neuchâtel
- Prof. Andrea Moscariello, Université de Genève
- Prof. Lyesse Laloui, EPF Lausanne
- Dr Antonio Dematteis, SEA consulting, Turin, Italie

Neuchâtel, le 31 janvier 2013

Le Doyen, Prof. P. Kropf

Acknowledgments

Il est évident qu'un travail de Doctorat résulte de l'interaction entre plusieurs personnes. Pendant cette thèse, j'ai passé suffisamment de temps avec certaines personnes pour qu'ils deviennent importants pour moi. Avec ces quelques lignes, j'aimerais leur exprimer ma gratitude.

Merci au Professeur Pierre Perrochet de m'avoir donné la possibilité de réaliser ce travail. Sa porte est toujours ouverte et après réflexion Pierre trouve toujours la bonne réponse ou les bons mots à dire. Je te remercie Pierre, je ne pensais pas pouvoir apprendre autant de choses en si peu de temps.

Je remercie également le Professeur Fabien Cornaton, qui m'a aussi appris énormément de choses. Malgré les grandes distances, Fabien a énormément contribué à la réalisation de ce travail. Il m'a toujours donné de son temps sans compter.

Un ringraziamento particolare va al Dottor Antonio Dematteis di SEA Consulting per l'interesse e la sua disponibilità. Solo tramite ad Antonio é potuta nascere la collaborazione con Lione-Torino Ferroviaria.

Je remercie également le Professeur Philip Brunner, le Professeur Lyesse Laloui et le Professeur Andrea Moscariello pour l'intérêt qu'ils ont porté à ce travail et pour avoir accepté d'être membres du jury de thèse.

Un remarquable merci va aux Docteurs Ellen Milnes, Jaouher Kerrou, François Negro, Michel Pronk, Julien Straubhaar, Daniel Kaeser, Grégoire Mariethoz et Daniel Bouchard pour le soutien, les révisions et l'amitié.

J'aimerais également remercier Nathalie Monin responsable secteur études géologiques de Lyon-Turin Ferroviaire, Riccardo Torri de SEA Consulting, le Docteur Jaime Carrera Hernández de l'UNAM et le Professeur Alessandro Gargini de l'Université de Bologna.

Un remerciement spécial va aux membres du CHYN. En particulier, les Professeurs François Zwahlen et Philippe Renard pour lesquels j'ai beaucoup d'admiration. Le personnel technique et administratif, notamment Carine Erard Brayek avec laquelle j'ai beaucoup travaillé dans le

cadre de la coordination du Master. Sans oublier tous les doctorants, spécialement Damian et Pierik ; et les étudiants, particulièrement Yannick et Jeanne.

Enfin, je tiens à exprimer toute ma gratitude envers ma famille, mon épouse Pascale et mon fils Sacha.

Abstract

Field observations and laboratory experiments have clearly demonstrated that heavily perturbed / exploited aquifers are subject to 3D deformations, which may cause significant socio-economic impacts at regional scale. Most common examples include: (1) excessive pumping of groundwater from deep aquifers leading to land subsidence; (2) deep excavation of tunnels in permeable geological units resulting in dangerous differential consolidation, especially for dams; and (3) fluid injection into deep reservoirs causing ground uplift and microsismicity. These manifestations are due to a substantial modification of water pressures within the aquifer, leading to effective stress variations, and deformations. Moreover, such deformations modify hydrodynamic parameters, i.e., hydraulic conductivity, porosity and storage coefficient. In confined or deep aquifer systems, hydrodynamic parameters have to be considered as effective stress-dependent variables. In such environments the assumption of constant parameters can lead to significant quantitative errors. The afore-mentioned fluid-to-solid hydromechanical processes seem to be essentially governed by hydrogeological, geomechanical and structural properties of the aquifer system. In order to take into account the major processes, as well as their principal properties, regional coupled hydromechanical simulation necessarily requires simplification of the governing equations to be operational in real, large scale, hydrogeological systems.

In the present thesis, model functions relating effective stress to hydrodynamic parameters are developed from fundamental hydrogeological and physical concepts, and implemented in the groundwater flow equation. Proposed stress-dependent equations are verified by a comparison with laboratory and field data. This is carried out for (1) fractured aquifers, i.e., consolidated rocks whose porosity results principally from the presence of fractures, cracks, joints and faults, and (2) granular porous aquifers, i.e., unconsolidated rocks whose porosity results from voids between solid grains. The relation between porosity and stress is also used to elaborate a deformation model for solving aquifer vertical volume change, i.e., ground settlement / uplift. A modelling approach is proposed in order to solve fluid-to-solid hydromechanical processes at regional scale, considering detailed geological structures. In this numerical method, hydrodynamic parameters are considered as stress-dependent variables.

Exact analytical solutions solving flow in a media under stress are developed in order to verify the numerical method. The proposed approach is then applied to the analysis of real case studies. In particular, to (1) the abnormal deformation of the Zeuzier arch dam (Wallis, Switzerland) due to the drainage of an unexpected confined aquifer by the Rawyl exploratory adit; (2) the problematic of water inflow into tunnels based on the geological investigations

undertaken by the Lyon-Turin railway project for the 57 km basis tunnel; as well as (3) the anthropogenic land subsidence affecting the Mexico City basin.

Quantitative studies of deep aquifer systems considering constant hydrodynamic parameters result in non-accurate volumetric discharge rates and pressure head fields. On one hand, increasing effective stress leads to decreasing hydrodynamic parameters. This results in a diminution of volumetric flow rates through a deep reservoir or in a deep excavation. Moreover, the decrease of water pressure is slowed down due to the decrease of hydraulic conductivity. This has repercussion on consolidation time. On the other hand, if - and only if - the rock is elastic, decreasing effective stress can lead to increasing hydrodynamic parameters and volumetric discharge rates.

For analytical solutions of volumetric discharge rate in deep wells or into a tunnel, the dependency of hydrodynamic parameters on effective stress can be taken into account by using a factor allowing stress consideration; whereas, in numerical analysis, such a process can be considered by implementing stress-dependent parameters in the groundwater flow and aquifer deformation models.

The proposed numerical approach for fluid-to-solid coupled hydromechanical processes, is computationally simple, based on few unknowns, and efficiently reproduces regional consolidations in geologically oriented 3D meshes.

This method is critical for hydrogeological and geomechanical quantitative studies investigating the sensitivity of deep aquifers on decreasing / increasing effective stresses. In particular for regional scale projects where water pressure may be subject to substantial modifications, such as dam construction or tunnel excavation, geologic radioactive waste repositories, deep reservoir exploitation for CO_2 sequestration, geothermal energy production, as well as extraction of groundwater and / or hydrocarbons.

Key words hydromechanical coupling · fractured aquifers · granular porous aquifers · hydraulic conductivity · storage coefficient · porosity · effective stress · modelling · regional scale

Glossary

Consolidation	reduction in the volume of the porous mass due to an increase in effective stress *syn.*: compaction ; *ant.*: expansion
Effective Stress	difference between stress and water pressure acting in intergranular/fracture porosity
Fluid-to-Solid coupled process	change in fluid pressure resulting in a change in the volume of the porous mass
Ground Fracturing	brittle deformation of the ground due to high strains *syn.*: ground cracking
Hydraulic Conductivity	conductive parameter expressing the ability of a medium to let groundwater flow through its pores / fractures
Hydromechanical Coupling	interaction between subsurface fluid flow and host-rock deformation
Land Subsidence	sinking of the ground surface *syn.*: ground settlement ; *ant.*: ground uplift
Overburden Stress	weight of geological materials above an unitary surface *syn.*: lithostatic stress
Porosity	fraction of a media that is void of material *syn.*: void ratio
Solid-to-Fluid coupled process	change in applied stress resulting in a change of fluid pressure
Storage Coefficient	capacitive parameter expressing the ability of a porous media to store or release fluid in case of pore pressure variation
Strain	deformation within a rock in which two particles originally adjacent have changed positions relative to each other

List of symbols

Symbol	Unit	Designation
a	m	Chap. 2: fracture aperture (asperity length under compression)
	m	Chap. 5: lateral spacing of the aquifer
a_0	m	fracture aperture at no stress (original length of the longest asperities)
A	m^2	area
A_s	m^{-1}	specific contact area
b	-	Chap. 3: coefficient of shape and spatial arrangement of grains
	m^{-1}	Chap. 5: coefficient characterising the elastic resistance of fractures to compression
c_v	$m^2\ s^{-1}$	consolidation coefficient
C_v	m^{-1}	aquifer compressibility
C	m^{-1}	coefficient describing the inverse of the harmonic mean radius of grains in a soil sample
D	m	distance
e	m	aquifer thickness
E	Pa	formation elasticity coefficient under fully saturated conditions
E_s	Pa	skeletal elasticity: reciprocal of skeletal compressibility $\alpha_s = E_s^{-1}$
E_w	Pa	water elasticity: reciprocal of water compressibility $\beta_w = E_w^{-1}$
E_Y	Pa	Young's modulus of the porous medium
d	m	distance
$D(z)$	-	statistical distribution of the asperity length
f	m^{-1}	frequency of the fracture family
F	N	force
g	$m\ s^{-2}$	gravitational acceleration
h	m	pressure head
h_0	m	initial pressure head in tunnel
H	m	hydraulic head
H_0	m	initial hydraulic head in tunnel
k	m^2	intrinsic permeability
k_0	m^2	intrinsic permeability at no stress
K	$m\ s^{-1}$	hydraulic conductivity
K_0	$m\ s^{-1}$	hydraulic conductivity at no stress

Symbol	Unit	Designation
$\mathbf{K}$	$\mathrm{m\,s^{-1}}$	hydraulic conductivity tensor
l_0	m	original aquifer thickness
L	m	Chap. 4: fracture length
	m	Chap. 5: length of a tunnel sector
m	-	number of fracture families
m_{zz}	$\mathrm{Pa^{-1}}$	vertical compressibility
n	-	coefficient of asperity length statistical distribution
n_x, n_y, n_z	-	components of the unit normal vector
$\mathbf{n}$	-	unit normal vector
N	-	number of fracture over a distance
N_c	-	number of compressed asperities
N_f	-	number of fractures
N_t	-	total number of asperities
$\mathbf{N}$	-	singular 3D tensor with vertical anisotropy
p	Pa	water pressure
$P(r)$	-	frequency distribution of grains radius
q	$\mathrm{m\,s^{-1}}$	specific discharge rate
Q	$\mathrm{m^3\,s^{-1}}$	volumetric flow rate
Q_0	$\mathrm{m^3\,s^{-1}}$	volumetric flow rate considering constant parameters
Q_{red}	$\mathrm{m^3\,s^{-1}}$	volumetric flow rate considering stress-dependent parameters
r	m	Chap. 3: grain radius
	m	Chap. 5: radial distance
r_0	m	tunnel radius
s	$\mathrm{m^2}$	Chap. 2: average asperity section
	m	Chap. 4: local position along a flow path
	m	Chap. 5: water table drawdown
s_0	m	drawdown at the tunnel
S_s	$\mathrm{m^{-1}}$	specific storage coefficient
S_{sf}	$\mathrm{m^{-1}}$	fracture specific storage coefficient
S_{sm}	$\mathrm{m^{-1}}$	rock matrix specific storage coefficient
S_{s_s}	$\mathrm{m^{-1}}$	solid skeleton specific storage coefficient
S_{s_w}	$\mathrm{m^{-1}}$	water specific storage coefficient
S_{s_0}	$\mathrm{m^{-1}}$	specific storage coefficient at no stress
S_{sf_0}	$\mathrm{m^{-1}}$	fracture specific storage coefficient at no stress
t	s	time
T	m	ground settlement or expansion
	$\mathrm{m^2\,s^{-1}}$	Chap. 5: transmissivity
$\mathbf{u}$	m	displacement vector of the porous media
v	$\mathrm{m\,s^{-1}}$	excavation speed
V	$\mathrm{m^3}$	bulk volume
x,y	m	spatial coordinates
z	m	1: asperity's original length, 2: elevation head, spatial coordinate
Z	m	depth

Symbol	**Unit**	**Designation**
α	-	reduction factor
α_b	-	Biot-Willis coefficient
Γ	-	boundary of a simulation domain
ϵ	-	volumetric strain
ϵ_v	-	vertical deformation
η	m^{-2}	asperity areal density
θ	-	volumetric moisture content
λ	-	ratio of horizontal to vertical stress
μ_w	$\mathrm{kg\,m^{-1}\,s^{-1}}$	water viscosity
ν	-	Poisson's ratio
ρ_r	$\mathrm{kg\,m^{-3}}$	rock mass density
ρ_s	$\mathrm{kg\,m^{-3}}$	density of the solid granular matter
ρ_w	$\mathrm{kg\,m^{-3}}$	water density
$\boldsymbol{\sigma}$	Pa	stress tensor
σ	Pa	normal stress
σ_0	Pa	fracture closure stress
σ_h	Pa	horizontal stress
σ_v	Pa	vertical stress
$\boldsymbol{\sigma'}$	Pa	effective stress tensor
σ'	Pa	normal effective stress
σ'_0	Pa	fracture closure effective stress
ϕ	-	porosity
ϕ_0	-	porosity at no stress
Δl	m	change in aquifer thickness
$\Delta\phi$	-	porosity variation
ΔV_ϕ	-	pore volume change
ΔV_B	-	total bulk volume change
ΔV_z	m	ground settlement
Ω	-	simulation domain

Contents

List of Figures

List of Tables

Chapter 1

Introduction and state of the art

1.1 Background

Aquifers have long been considered as static systems by the hydrogeologists because of the difficulty in measuring and observing the subtle dynamics. However, several studies have shown that aquifers undergo deformations in response to changes in effective stresses, especially in case of deep confined aquifers. Significant groundwater withdrawal leads to decreasing water pressures and consequently, increases effective stresses. This reduces the porosity, and decreases the hydraulic conductivity and the storage capacity. Moreover, the loss of porosity causes land subsidence. In contrast, significant increasing water pressures result in decreasing effective stresses, which increase aquifer porosity, permeability and storage. In such a case, ground uplifts can be detected [59, 6, 60, 41, 28, 63, 44, 45, 53, 23].

Karl Terzaghi [59] was the first to link aquifer deformation to groundwater flow. In 1923, Terzaghi introduced the *Principle of Effective Stress* and the *Theory of Consolidation* to explain the consolidation of a saturated clay layer under top and bottom vertical drainage (change in water pressure). Both theories have found wide application in geotechnical works, in particular to evaluate clays deformation due to pressure head variations induced by civil engineering constructions. At a regional scale, this hydromechanical coupled process was observed in petroleum engineering and in hydrogeology because of the land subsidence induced by oil, gas or groundwater pumping. At that time, a decrease in well productivity associated to the decrease in reservoir permeability was also highlighted [44]. A few years after the *Principle of Effective Stress* [59], Jacob [32, 33] defined the specific storage coefficient based on the elastic response of aquifers to changes in water table levels, and Biot [6] developed the linear poroelasticity theory. Both approaches describe the coupled process between groundwater flow and aquifer deformation. However, Jacob's formulation is limited to vertical deformation, i.e., the change in aquifer thickness, and neglects horizontal strains, while Biot's theory allows 3D aquifer deformation [23]. At this time, aquifers consolidation due to water pressures variations was considered a problem restricted to unconsolidated geological materials. Fractured rocks consolidation was only addressed in petroleum engineering. However, at the end of 1978, the Zeuzier arch dam in Switzerland showed an unexpected deformation due to the regional consolidation of an un-

derlying confined and fractured aquifer [55]. Close to the dam lake, the drilling of the Rawyl exploratory adit drained the aquifer. The release of water pressures in the fractures leaded to increasing effective stresses in the rock mass, and consequently in the closure of fracture porosity and in the consolidation of the confined aquifer. The regional settlement caused by the aquifer consolidation resulted in an arch dam abnormal behaviour. This unexpected event has demonstrated that (1) even stiff rock masses deform due to changes in water pressure, and that (2) the drilling of deep draining tunnels can cause non negligible aquifer consolidations and ground subsidence [37, 67].

Nowadays, through increasingly sophisticated measurement techniques, the subtle aquifers dynamic can be observed in details. Both, granular porous aquifers (unconsolidated sediments) and fractured aquifers (rock masses) are subject to cyclic deformations following the natural or anthropogenic recharge and discharge groundwater cycle [4, 36]. The decrease/increase of water pressures leads principally to vertical deformations, but also to horizontal strains [66, 10]. The combination of differential vertical settlements and horizontal deformations can cause brittle deformations in the aquifer [31, 1]. Injection sites for CO_2 sequestration or hydraulic stimulation for geothermics are affected by ground uplift and/or fault reactivation [22, 54]. However, the Darcy's law used to simulate regional groundwater flow, and the fully coupled Biot equations able to solve for flow and 3D deformations generally consider the hydraulic conductivity and the storage coefficient as stress-independent constants [43, 18]. This is also the case in traditional analytical equations used to estimate groundwater flow rates in underground excavation, such as tunnels. This assumption is certainly acceptable for shallow aquifers and in the presence of incompressible rocks. In contrast, it can however, lead to significant differences in deep and confined units, where hydrodynamic parameters, i.e. hydraulic conductivity, porosity and specific storage coefficient, must be considered as a function of effective stresses.

1.2 Effective stress in hydrogeology

In 1923 Karl Terzaghi [59] introduced the principle of effective stress σ', describing the stress state of a porous medium filled with a fluid:

$$\begin{aligned} \boldsymbol{\sigma'} &= \boldsymbol{\sigma} - \boldsymbol{\alpha_b}\, p \\ \begin{bmatrix} \sigma'_{xx} & \sigma'_{xy} & \sigma'_{xz} \\ \sigma'_{yx} & \sigma'_{yy} & \sigma'_{yz} \\ \sigma'_{zx} & \sigma'_{zy} & \sigma'_{zz} \end{bmatrix} &= \begin{bmatrix} \sigma_{xx} & \sigma_{xy} & \sigma_{xz} \\ \sigma_{yx} & \sigma_{yy} & \sigma_{yz} \\ \sigma_{zx} & \sigma_{zy} & \sigma_{zz} \end{bmatrix} - \begin{bmatrix} \alpha_b & 0 & 0 \\ 0 & \alpha_b & 0 \\ 0 & 0 & \alpha_b \end{bmatrix} p \end{aligned} \tag{1.1}$$

where $\boldsymbol{\sigma}$ and $\boldsymbol{\alpha_b}$ are the total stress and the Biot-Willis coefficient tensors, and p is the fluid pressure. If the fluid is water, then $p = \rho_w g h$, where ρ_w is water density, g is the gravitational acceleration and h is the pressure head. A Newtonian fluid can not support shear stresses, indeed the effective shear stresses correspond to those of the total stress tensor. The Biot-Willis coefficient α_b expresses the ratio of pore volume change ΔV_ϕ to total bulk volume change ΔV_B, i.e. solid skeleton (aquifer) and voids (porosity), under drained conditions, i.e., the fluid

can escape the pores [9]:

$$\alpha_b = \frac{\Delta V_\phi}{\Delta V_B} \tag{1.2}$$

If there are no voids, then the Biot-Willis coefficient is zero. If the bulk volume change is governed only by the pore volume change (no rock matrix deformation), then the Biot-Willis coefficient is unity.

From Eq. (1.1) it follows that a change in effective stress can result from (1) a variation of total stress and/or (2) a change in fluid pressure (Figure 1.1). On one hand, a variation of total stress leads to a solid-to-fluid hydromechanical coupled process, i.e., a change in applied stress results in a change of fluid pressure. On the other hand, a variation in fluid pressure results in a fluid-to-solid hydromechanical coupled process, i.e., a change in fluid pressure results in a change in the volume of the porous mass [65, 53, 9].

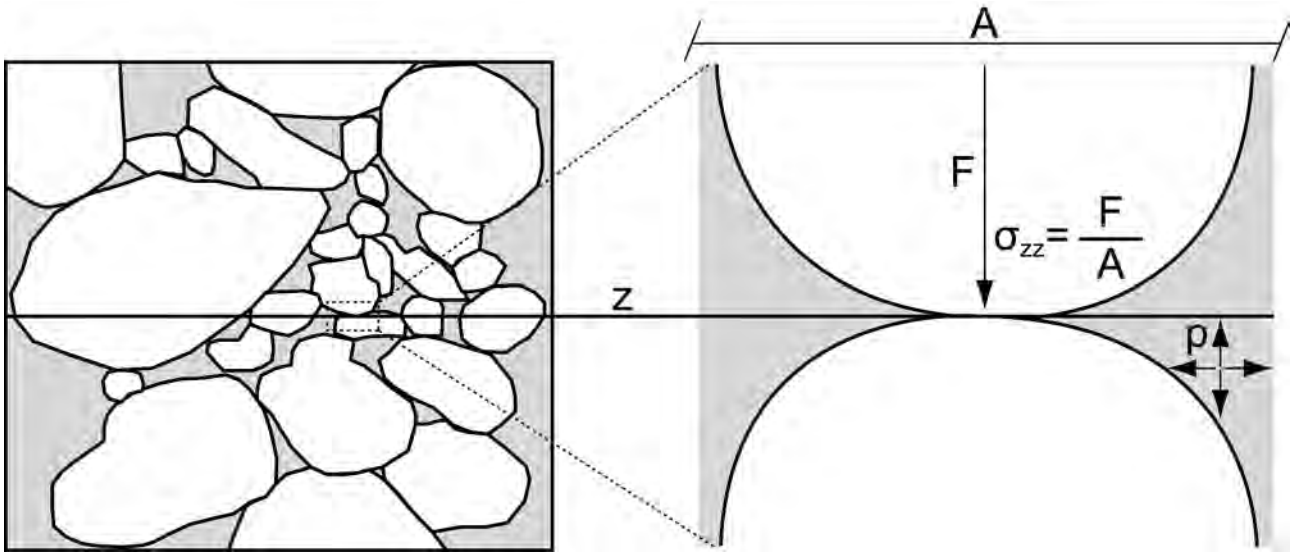

Figure 1.1: Effective stress state in an aquifer results from total stress σ lowered by pore pressure p. Only the vertical component of the stress tensor is shown in this schematic illustration. At the elevation z the vertical stress is the weight of overlying geological materials F per unit area A.

The diagonal terms of the total stress tensor are principal stresses, the non-diagonal terms shear stresses. Under lithostatic stress conditions, the principal stress is vertical and depends on the weight of the overlying geological materials above elevation z (the overburden):

$$\sigma_v = g \int_z^{z_t} \rho_r(u)\, du \tag{1.3}$$

where $\sigma_v = \sigma_{zz}$ is the vertical stress, z_t is the surface elevation and ρ_r is the saturated aquifer bulk density. Under such overburden conditions, horizontal stresses result from the deformation of the rock mass under vertical stress. In case of elasticity, homogeneity and isotropy of the aquifer, the amount of horizontal stress $\sigma_h = \sigma_{xx} = \sigma_{yy}$ depends only on the Poisson's ratio effect [17, 51]:

$$\sigma_h = \lambda\, \sigma_v \;\; ; \quad \lambda = \frac{\nu}{1-\nu} \tag{1.4}$$

where ν is the Poisson's ratio, and λ is the ratio of horizontal to vertical stress. Note that, in such a case, principal horizontal stresses are equivalent. In elastic rocks, the Poisson's ratio ranges between $0 < \nu < 0.5$, which implies a λ-range of $0 < \lambda < 1.0$. Typical values for granites are: $\nu \approx 0.25$ and $\lambda \approx 0.33$. At great depths (> 2500 m), in plastic rocks (clays) and for Newtonian fluids $\nu = 0.5$, and horizontal stresses match the vertical stress with: $\lambda = 1.0$ [17, 47, 51].

Horizontal stresses can be greater than vertical stress ($\lambda > 1.0$), due to tectonics, erosion and glacial history. In compressive tectonic systems, such as orogenic belts (mountains), horizontal stresses can be anisotropic and exceed up to ten times the local vertical stress [51, 42]. In the case of erosion or ice load retreat, due to the time delay of mechanical deformation, horizontal stresses still reflect the past overlay and must be calculated considering the eroded or retreated cover Δz [17]:

$$\sigma_h = \frac{\nu}{1-\nu}\, g \int_z^{z_t+\Delta z} \rho_r(u)\, du\,; \quad \text{if erosion} \tag{1.5}$$

$$\sigma_h = \frac{\nu}{1-\nu}\, g \int_z^{z_t} \rho_r(u)\, du + g \int_{z_t}^{z_t+\Delta z} \rho_{ice}(u)\, du\,; \quad \text{if ice retreat} \tag{1.6}$$

where ρ_{ice} is the ice density. In this latter case, the water bearing formations are defined as preconsolidated [24]. Such media could be expanded after the erosion / removal of overlying lithologies. This complicates the in situ stress characterization.

In **fractured aquifers** under overburden conditions, the effective stress acting perpendicularly at a depth Z on a given fracture plane is:

$$\begin{aligned} \sigma' &= \boldsymbol{\sigma}\mathbf{n}\cdot\mathbf{n} - \boldsymbol{\alpha_b} p\,, \qquad \boldsymbol{\sigma} = \begin{bmatrix} \sigma_v\lambda & 0 & 0 \\ 0 & \sigma_v\lambda & 0 \\ 0 & 0 & \sigma_v \end{bmatrix} \\ &= \rho_r g Z(\lambda n_x^2 + \lambda n_y^2 + n_z^2) - \alpha_b \rho_w g h \end{aligned} \tag{1.7}$$

where n_x, n_y, n_z are the components of the unit vector $\mathbf{n}$ normal to the fracture plane. Shear stresses are neglected as they do not affect significantly the hydraulic aperture of the fracture. Note that in Eq. (1.7), the aquifer bulk density ρ_r expresses the density of a saturated fractured medium composed of two phases (rock matrix and water in fracture porosity): $\rho_r = (1-\phi)\rho_s + \phi\rho_w$, where ρ_s is the density of the fractured solid rock mass and ϕ is the aquifer porosity. For fractured rock masses where $\phi < 0.02$, the contribution of water on aquifer density can be neglected ($\rho_r = \rho_s$).

In **granular porous aquifer**, the porosity is significantly higher and the detailed vertical effective stress is the sum of the weight of the granular material, the weight of the soil moisture

in the unsaturated zone, the weight of water in the saturated zone, subtracted by water pressure:

$$\begin{aligned} \sigma'_v &= \sigma_v - \alpha_b\, p \ ; \\ \sigma_v &= (1-\phi)\rho_s g Z + \theta \rho_w g (Z-h) + \phi \rho_w g h \ ; \\ p &= \rho_w g h \end{aligned} \tag{1.8}$$

where ρ_s is the density of the solid granular matter and θ is the soil humidity. In large scale analysis, the detailed vertical stress in Eq. (1.8) is simplified by using a wet density ρ_{r_w}, and neglecting the unsaturated zone. This leads to the overburden stress definition in Eq. (1.3).

1.3 Measurement techniques and detection

The dynamic of aquifers can be observed by detailed geodetic monitoring, such as repeated ground leveling, GPS surveys or satellite/airborne investigations (InSAR, LiDAR) [23]. Extensometers and borehole geophysical methods, such as radioactive markers, can also be used to measure *in situ* the system deformation [24]. However, such deformations are related to the groundwater pressure state, and the monitoring of water table levels can be an indirect measure of the deformation state (Figure 1.2).

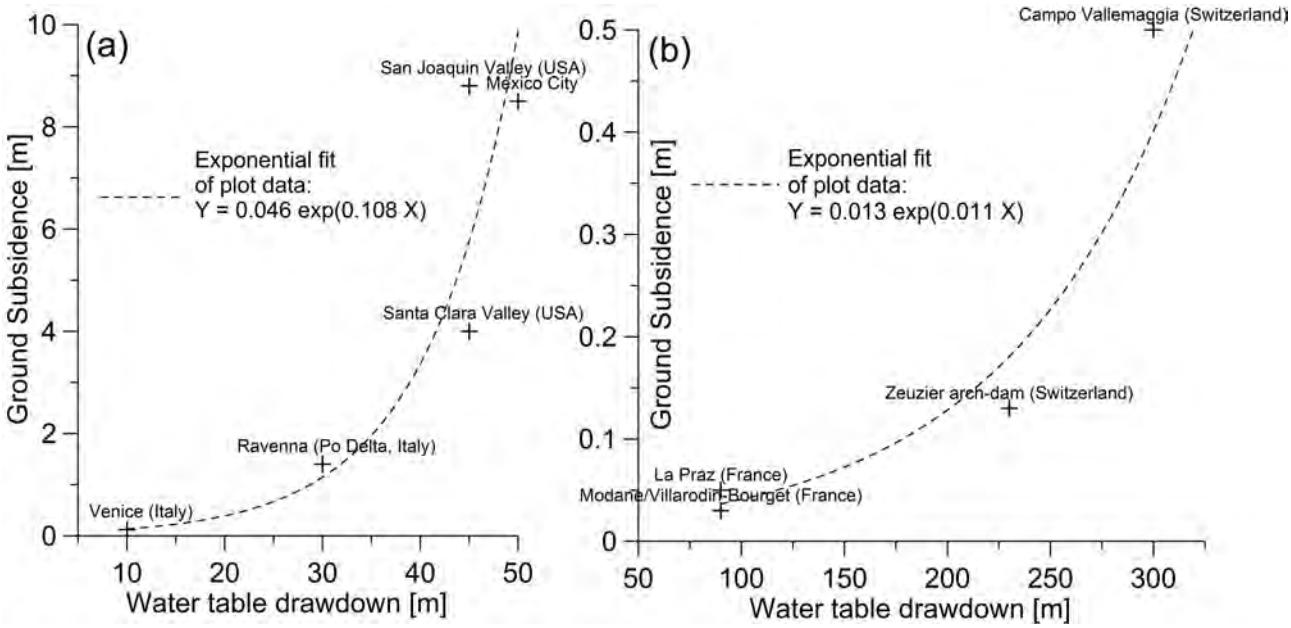

Figure 1.2: Relation between water table drawdown and ground subsidence in (a) granular porous aquifers and (b) fractured aquifers, with exponential fits of observed data. Data source: [64, 58, 37, 8, 20, 35].

The response of aquifers to water pressures/effective stresses variations can also be measured within the context of hydraulic tests. By closing and opening the discharge zone of a fractured shallow system, Cappa [15] studied the dependency of the fracture hydraulic aperture to increasing and decreasing water pressure (Figure 1.3). Schweisinger et al. [56] introduced a field

method to perform hydromechanical well tests: a fracture is isolated by packers and small displacements are measured using extensometers during transient pressure injections. Burbey et al. [14, 11, 12] carried out a long constant-rate pumping test in a 400 m thick basin-fill aquifer, and recorded the surface vertical ground settlements and horizontal strains using high-precision GPS.

In the context of laboratory tests, Louis [41] used an experimental setup to measure the opening of fracture aperture within water pressure changes. The fracture is subjected to a steady discharge rate, and then a fluid injection causes a rapid hydraulic load followed by a slow decay phase (pulse-test). Durham [19] carried out some laboratory tests to study the decrease of the permeability of a natural fracture, taken at approximately 3.8 km deep, with increasing confining stress.

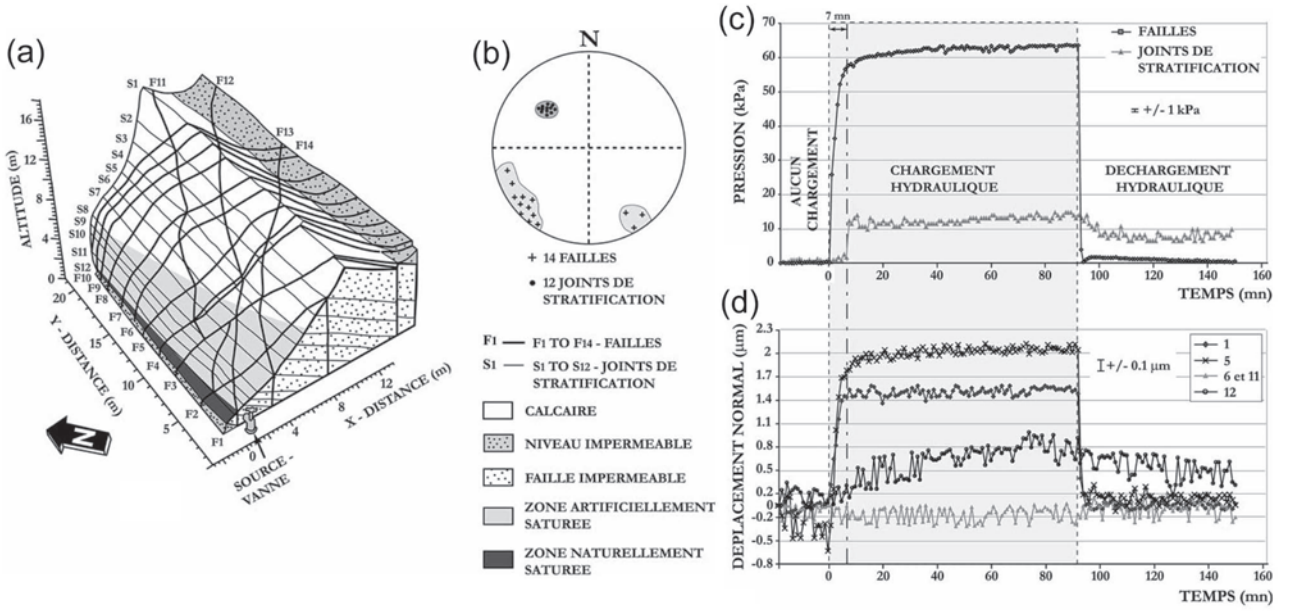

Figure 1.3: Field hydromechanical tests carried out by Cappa [15]: (a) field study area with the fracture network, (b) stereographic plot showing the principal fracture families, (c) fluid pressure and (d) normal displacement recorded during a cycle of hydraulic load-unload (modified from [15]).

1.4 Model functions relating effective stress to hydrodynamic parameters

Given the previous observations, mathematical functions relating effective stress to hydrodynamic parameters can be formulated from empirical data (field/laboratory tests) or by theoretical developments.

Fractured aquifers

There is a considerable amount of literature on the dependency of fracture aperture to effective stress.

The laboratory tests of Louis [41] allowed Perrochet [49] to elaborate an exponential relationship between the fracture hydraulic conductivity and water pressure:

$$K(h) = K_0 \, e^{-3 \, b \, (h_0 - h)} \tag{1.9}$$

where $K(h)$ is the hydraulic conductivity at pressure head h, K_0 is the hydraulic conductivity prior to a change in pressure head, h_0 is the initial pressure head state, and b is a parameter characterizing the elastic resistance of fractures to compression: $b = \rho_w g / \phi / E_s$, where ϕ is rock porosity and E_s is rock elasticity. This formula is generally used to analyze the decrease of fracture hydraulic conductivity, in case of decreasing water pressures.

Walsh [63] developed an effective stress-dependent hydraulic conductivity $K(\sigma')$ based on two coupled considerations. First, the fracture aperture decreases under increasing compression, and second, the resistance to flow increases with smaller aperture:

$$K(\sigma') = K_0 \left[1 - \left(\sqrt{2} \frac{h}{a_0} \right) \ln \left(\frac{\sigma'}{\sigma'_0} \right) \right]^3 \tag{1.10}$$

where the symbols K_0 and a_0 stand for hydraulic conductivity and half-aperture at some reference effective stress σ'_0, respectively. h is the root mean square value of the fracture height statistical distribution.

In his investigation on the Zeuzier arch dam case, Lombardi [38, 39] elaborated the FES (Fissured Elastic Saturated) rock mass model. In this work, he obtained by analytical fittings an effective stress-dependent hydraulic conductivity and porosity, specific for the Dogger formation of the Zeuzier area (Wallis, Switzerland):

$$K = K_0 \left(1 - \frac{\sigma'}{\sigma'_0} \right)^{m_1} \tag{1.11}$$

$$\phi = \phi_0 \, e^{(-m_2 \, \frac{\sigma'}{\sigma'_0})} \tag{1.12}$$

where σ'_0 is the effective stress at joint closure, ϕ_0 is the rock mass porosity at no effective stress, and m_1, m_2 are fitting coefficients.

Gangi [25] was one of the first to consider the role played by fracture asperities. He developed analytically a confining pressure-dependent hydraulic conductivity, where rod-shaped asperities resist to fracture compression:

$$K(P) = K_0 \left[1 - \left(\frac{P}{P_1} \right)^m \right]^3 \tag{1.13}$$

where P is the confining pressure (effective stress), P_1 is the effective elastic modulus of asperities, and m is a constant ($0 < m < 1$) characterizing the distribution function of the asperity lengths.

Granular porous aquifers

Two main theoretical approaches enable the development of effective stress-dependent equations for granular porous aquifers: (1) functions based on the size change of solid grains, and (2) functions based on the volumetric deformation of the bulk volume of the granular porous media, i.e. grains and voids.

In his 1978 paper, Gangi [25] also proposed a pressure-dependent hydraulic conductivity for granular porous aquifers on the basis of the Hertzian theory of spheres deformation:

$$K(P) = K_0 \left\{1 - C_0 \left[(P + P_i)/P_0\right]^{2/3}\right\}^4 \tag{1.14}$$

where the symbols stand for C_0 (≈ 2) a constant depending upon the packing, P confining pressure, P_i pressure due to the cementation and permanent deformation of grains, and P_0 effective elastic modulus of grains.

Kim and Parizek [34] investigated porosity and hydraulic conductivity changes due to the deformation of the bulk volume in case of variations in effective stress:

$$K = K_0 \left[\left(\frac{1}{\phi_0}\right)(1+\epsilon)^{2/3} - \left(\frac{1-\phi_0}{\phi_0}\right)(1+\epsilon)^{-1/3}\right]^3 \tag{1.15}$$

$$\phi = 1 - \frac{1-\phi_0}{1+\epsilon} \tag{1.16}$$

where ϵ is the volumetric strain.

Generalities and limitations

To summarize, the relation between hydrodynamic parameters and effective stress can be correctly approximated by a mathematical function of the exponential type for both fractured and granular aquifers. In the literature, there are many model functions relating effective stress to permeability, but few models for porosity and none for storage. In a stress-strain diagram these models apply for porosity closure (Figure 1.4). If the aquifer is elastic, e.g. fractured rock masses [27] or coarse-grained sediments (blocks and gravels), the porosity closure is reversible and only a model function is necessary to reproduce compression and swelling under loading and unloading, respectively. Contrary, for fine-grained materials, i.e. sands, silts and clays, the porosity closure is not reversible [29, 30, 23]. In such cases, different model functions have to be used to simulate loading/unloading cycles.

As proposed by Murdoch and Germanovich [43], a sound effective stress-dependent equation for fractures must consider the principal stresses on the contacting asperities and the fluid (water) pressure in the fracture porosity. In granular porous media, solid grains are relatively incompressible compared to the total deformation of the bulk volume. Model functions based on this latter conceptualization appear to be better adapted to analyze the effect of effective stresses on hydrodynamic parameters, especially at regional scales.

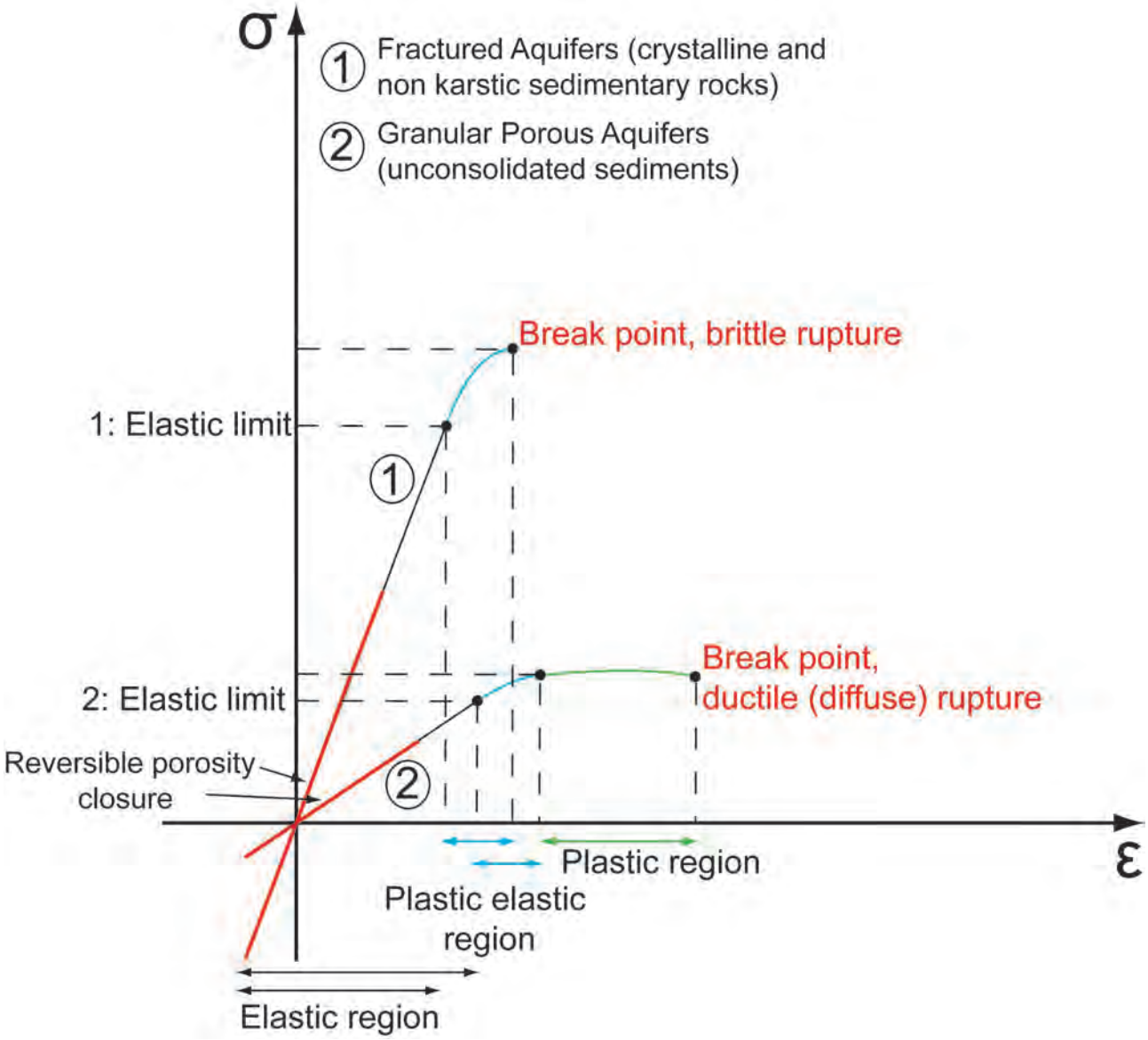

Figure 1.4: Theoretical stress (σ) - strain (ϵ) diagram for fractured and granular porous aquifers. Model functions relating effective stress to hydrodynamic parameters locate generally in the reversible porosity closure region.

1.5 Simulation and analysis

Two main methods are used to study the mechanical response of aquifers/reservoirs to water/fluid pressure variations: (1) the non-simultaneous analysis of water pressure changes and aquifer deformations, and (2) the Biot's poroelasticity theory. The latter solves simultaneously for the flow and the deformation [3]. **The main assumptions of both approaches are that the flow through the porous medium is laminar and obeys Darcy's law, and that the porous medium deforms elastically and obeys Hooke's law, having only small, reversible strains** [18, 3, 9]. It is fundamental to note that **both methods neglect the dependency of hydrodynamic parameters on effective stresses** [18, 34]. In the analysis of hydromechanical processes, the porous media is assumed as fully saturated of water,

i.e., fracture/intergranular porosity is completely filled by water exerting the pressure p. The non-saturated zone is in general neglected.

1.5.1 The non simultaneous analysis of groundwater flow and deformation

This method allows to analyze the vertical deformation of aquifers, i.e. thickness change, due to a variation in water pressure, as described by Jacob [32, 33]. In addition to the prior hypothesis, this method assumes no lateral deformations, incompressible solid grains and considers principal stresses constant during water pressure changes [32, 23]. The neglect of principal stresses implies that the change in effective stress results only from the change in water pressure: $\Delta\sigma' = -\Delta p$.

First, the classical groundwater flow equation is used to investigate changes in water pressures:

$$S_s \frac{\partial H}{\partial t} = \nabla \cdot (\mathbf{K} \nabla H) \quad ; \quad H = h + z \tag{1.17}$$

where H denotes hydraulic head, t is time, and S_s is the specific storage defined by Jacob [32]:

$$S_s = S_{s_s} + S_{s_w} \tag{1.18}$$

$$S_s = \rho_w g \left(\frac{1}{E_s} + \frac{\phi}{E_w} \right) \tag{1.19}$$

where S_{s_s} identifies the solid skeleton specific storage, S_{s_w} the water specific storage, E_s is the skeletal elasticity, and E_w is water elasticity. Specific storage defines the water volume released / accumulated in case of an unitary change in hydraulic head.

Second, assuming that water is incompressible, the vertical aquifer deformation is determined by [32]:

$$\Delta l = l_0 \frac{1}{E_s} \Delta p = l_0 S_{s_s} \Delta H \tag{1.20}$$

where Δl is the change in aquifer thickness: $\Delta l > 0$ in consolidation (ground subsidence), $\Delta l < 0$ in expansion (ground uplift), and l_0 is aquifer thickness prior to the change in water pressure Δp. In Jacob's approach [32, 33] the groundwater flow and the vertical deformation Eqs. (1.17), (1.20) are partially coupled via the specific storage coefficient.

The above approach has been developed for granular porous aquifers, and extended to fractured aquifers. Because of governing elastic equations, the aquifer deformation follows immediately the change in water pressures. In such a case, the hydraulic conductivity and the storage coefficient control the consolidation / expansion time. This seems to be realistic for fractured and coarse-grained aquifers, but not for silty and clayey systems. In these latter cases, deformation is not purely elastic and a time lag happens between the change in fluid pressures and the deformation [59, 60, 3]. In this context, Terzaghi [59, 60] divided the consolidation of clays in two phases: (1) a primary consolidation due to the expulsion of water, and (2) a secondary consolidation due to the rearrangement of grains.

1.5.2 The simultaneous analysis: Biot's poroelastic theory

Biot [6] successfully coupled the governing equations describing the groundwater flow in a 3D deformable porous medium via the volumetric strain. Earlier, this was partially done by Karl Terzaghi [59, 60] in his theory of consolidation of clays, which was extended to the study of land subsidence caused by the drainage of compressible aquitards (aquitard drainage model) [52, 29, 30, 23].

Terzaghi's consolidation theory

Terzaghi's consolidation theory is a particular case of Biot's poroelastic theory. It describes the vertical deformation of a compressible layer under vertical drainage. Terzaghi elaborated this theory to analyze the settlement of heavy buildings lying on a compressible clay layer. The increase of vertical stress due to the structure weight results in water overpressure leading to layer drainage and consolidation (Figure 1.5). Assuming incompressibility of both the solid grains and the fluid in the pores, as well as vertical flow, the groundwater flow equation becomes [60, 61]:

$$m_{zz}\gamma_w \frac{\partial H}{\partial t} = K_{zz}\frac{\partial^2 H}{\partial z^2} \tag{1.21}$$

where m_{zz} is the vertical compressibility of the layer: $m_{zz} = 1/E_s$, and γ_w is the specific weight of water: $\gamma_w = \rho_w g$. Eq. (1.21) may be formulated as:

$$\frac{\partial H}{\partial t} = c_v \frac{\partial^2 H}{\partial z^2} \tag{1.22}$$

where c_v is the consolidation coefficient: $c_v = \frac{K_{zz}}{m_{zz}\gamma_w}$ in m^2/s.

Eq. (1.22) can be solved, for example, to study the consolidation of a clay stratum subjects to an increase of applied stress, e.g., the deposition of a permeable and incompressible layer or the construction of a heavy building. This example is taken from Verruijt [61].

At the initial consolidation time $t = 0$, the applied load causes a pressure head increase in the compressible clay stratum:

$$t = 0 \ : \ \Delta h = \frac{q_l}{\gamma_w} \tag{1.23}$$

where q_l denotes the constant applied load. The system bottom is impervious implying a boundary condition of no flow at $z = 0$: $\partial h/\partial z = 0$. On the opposite, at the top of the clay layer, the pressure head is zero $z = z_{top}$: $h = 0$.

For this example, Eq. (1.22) is then solved leading to [59, 60, 61]:

$$h = \frac{q_l 4}{\gamma_w \pi}\sum_{j=1}^{\infty}\frac{(-1)^{j-1}}{2j-1}\cos\left[(2j-1)\frac{\pi z}{2z_{top}}\right]\exp\left[-(2j-1)^2\frac{\pi^2 c_v t}{4z_{top}^2}\right] \tag{1.24}$$

From Eq. (1.24) it follows that the consolidation is quasi finished when $c_v t/z_{top}^2 = 2$. This also indicates that if a sample of clay of thickness 2 cm takes 1 h to consolidate in the laboratory, in the field the consolidation of a 4 m stratum of the same clay with drainage on both sides

will take 417 days [61].

The variation in pressure head with consolidation time is then coupled with the vertical change in stratum thickness by using Eq. (1.20).

The extension of Terzaghi's consolidation theory to the aquitard drainage model for studying the compaction of an aquifer system allows to take into account the time lag between the decrease of hydraulic head in main aquifers and the subsequent aquitards drainage and consolidation [52, 29, 30, 23].

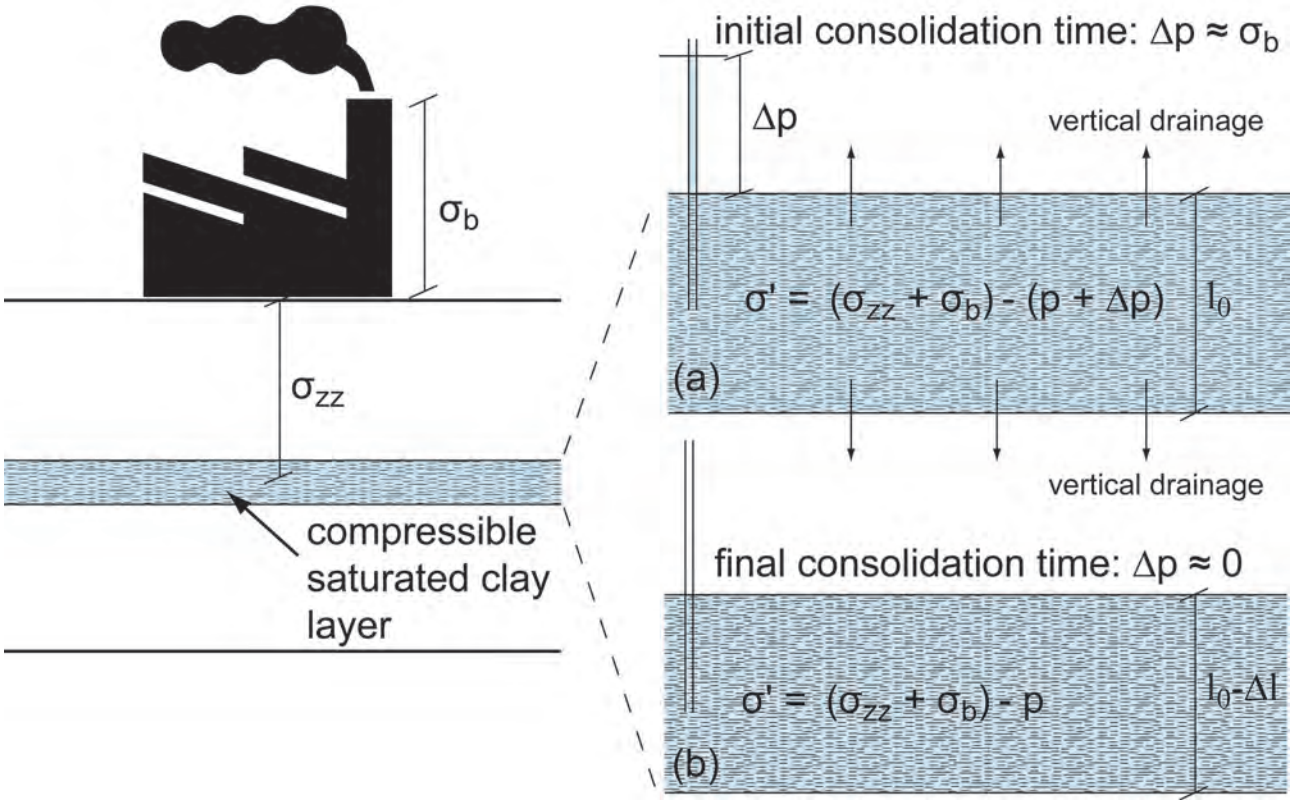

Figure 1.5: Consolidation of a clayey saturated layer under the increase of vertical stress due to the construction of a heavy structure. (a) Immediately after the building construction, the overload σ_b is supported by water overpressure Δp in the compressible layer. (b) Water escapes because of the overpressure, and the overload is not longer supported, causing the consolidation Δl of the layer.

Biot's poroelastic theory

At this point, the following two fundamental hydromechanical processes have been identified but not coupled [65, 53, 9]:

- a change in fluid pressure (decrease/increase) leads to a change in the volume of the porous reservoir (compression/expansion). This is a fluid-to-solid interaction.
- a change in applied stress induces a change in fluid pressure, leading to flow if the fluid can escape the host rock. This is a solid-to-fluid interaction.

The main contribution of Biot's poroelastic theory is to have coupled the above fundamental phenomena in a set of governing equations, synthesized here as [34, 61, 23]:

$$\frac{\phi\gamma_w}{E_w}\frac{\partial H}{\partial t} = \nabla\cdot(\mathbf{K}\nabla H) - \frac{\partial}{\partial t}\nabla\cdot\mathbf{u} \tag{1.25}$$

$$0 = (\lambda_L + G)\nabla(\nabla\cdot\mathbf{u}) + G\nabla^2\mathbf{u} - \gamma_w\nabla H \tag{1.26}$$

where $\nabla\cdot\mathbf{u} = \left(\frac{\partial u_x}{\partial x} + \frac{\partial u_y}{\partial y} + \frac{\partial u_z}{\partial z}\right) = \epsilon$ is the volumetric strain (bulk volume deformation) of the porous saturated solid. Note that here the positive sign designates tension. u_x, u_y, u_z are the components of the displacement vector $\mathbf{u}$, λ_L is the Lamé modulus expressing the porous rock resistance to tension/compression: $\lambda_L = \frac{E\nu}{(1+\nu)(1-2\nu)}$, and G is the shear modulus defining the rock resistance to shear: $G = \frac{1}{2}\frac{\sigma_{xy}}{\epsilon_{xy}}$. Eq. (1.25) describes the transient groundwater flow taking into account storage from volume deformation, and Eq. (1.26) describes the 3D deformation of the porous solid considering the displacement and the hydraulic head fields [34, 9, 23]. For the detailed development of Biot's poroelastic equations refer to [6, 18, 9].

In poroelasticity, the stress state of a porous saturated solid (aquifer) is defined by a symmetric tensor $\boldsymbol{\sigma_T}$ of sixteen components σ_{ij} considering stresses from the solid phase $\boldsymbol{\sigma_B}$ and stresses from the fluid phase $\boldsymbol{\sigma_f}$ [9]:

$$\boldsymbol{\sigma_T} = \boldsymbol{\sigma_B} + \boldsymbol{\sigma_f} \tag{1.27}$$

$$\begin{bmatrix} \sigma_{xx} & \sigma_{xy} & \sigma_{xz} & 0 \\ \sigma_{xy} & \sigma_{yy} & \sigma_{yz} & 0 \\ \sigma_{xz} & \sigma_{yz} & \sigma_{zz} & 0 \\ 0 & 0 & 0 & \sigma_f \end{bmatrix} = \epsilon_v \begin{bmatrix} \lambda_U & 0 & 0 & 0 \\ 0 & \lambda_U & 0 & 0 \\ 0 & 0 & \lambda_U & 0 \\ 0 & 0 & 0 & -C \end{bmatrix} + 2G \begin{bmatrix} \epsilon_{xx} & \epsilon_{xy} & \epsilon_{xz} & 0 \\ \epsilon_{xy} & \epsilon_{yy} & \epsilon_{yz} & 0 \\ \epsilon_{xz} & \epsilon_{yz} & \epsilon_{zz} & 0 \\ 0 & 0 & 0 & 0 \end{bmatrix} - \zeta \begin{bmatrix} C & 0 & 0 & 0 \\ 0 & C & 0 & 0 \\ 0 & 0 & C & 0 \\ 0 & 0 & 0 & -M \end{bmatrix} \tag{1.28}$$

(1.29)

where λ_U is the Lamé modulus measured at undrained conditions, i.e., the fluid can not escape the system volume despite a change in applied stress, and defined by Biot as $\lambda_U = \lambda + C\alpha_B$. C is a coefficient expressing the coupling of deformations between the solid grains and the fluid, and M denotes the change in fluid pressure when the variation of fluid content ζ changes.

Biot's poroelasticity is a physical-mathematical theory describing the 3-D deformation of porous solids saturated with a fluid. However, hydrogeologists prefer to use the Jacob's approach or the "aquitard drainage model" in the analysis of aquifer dynamic as (1) the mathematics are simpler, (2) the large number of variables in Biot's poroelasticity limits its tractability at hydrogeological scales, and (3) horizontal strains can be neglected at regional scales.

1.6 Example of hydromechanical coupled processes

This section presents the fundamental hydromechanical phenomena. It begins by examining fluid-to-solid processes, followed by a brief overview of solid-to-fluid interactions. Note that the origin of such phenomena is mainly anthropogenic, but may also be purely natural.

1.6.1 Processes related to fluid-to-solid coupling

These processes are mostly large-scale mechanisms and mainly concern the hydrogeologists and the geologists. Applied principal stresses can be assumed to remain constant during water depletion/increment.

Land subsidence due to fluid (groundwater) pumping

The reduction in porosity, in all geological formations (aquifers and aquitards) affected by a decrease in pore pressure due to pumping activities, results in the subsidence of ground surface [32, 28, 29, 30, 31, 23]. This anthropogenic event particularly occurs in large sedimentary basins (deltas, valleys, endorheic systems) filled by quaternary unconsolidated sediments, where the excess of outflow over inflow due to pumping leads to important drop of the piezometric surface. The largest reported sinking rate was measured by differential interferometry in the Mexico City basin and reaches 300 mm/y [46].

Helm [29, 30] demonstrated that seasonal variations of water table levels in aquitards are sufficient to cause non recoverable deformations. In his paper, the author reported the compaction of an aquifer system near Pixley (San Joaquin Valley, California, U.S.A.) despite only seasonal variations of groundwater levels (Figure 1.7a-b). This because in dry seasons applied effective stresses exceed the elastic limit of aquitards causing non recoverable consolidations. This loss of pore volume is not recoverable during wet seasons due to the geomechanical behaviour of silts and clays (Figure 1.7c). As stated in section 1.4, such a situation needs at least two different model functions relating effective stress to hydrodynamic parameters to reproduce stress loading during dry seasons and unloading during wet seasons.

Differential consolidations due to the presence of an abrupt slope of the basement topography or in case of aquifer heterogeneity can lead to ground failures (Figure 1.8) [13, 1, 2]. In heavily pumped systems, such as in Mexico City, the propagation of earth fissures can result in a long and slow "collapse" of the basin affecting surface and subsurface civil engineering structures (buildings, tunnels, metros, airports) and in deterioration of the groundwater quality, because fractures become preferential infiltration flow paths for surface waters [7].

In sedimentary rocks exploited for gas and petroleum production non-differential consolidation caused by pore space reduction following fluid drainage can lead to reservoir failure as a result of decreased host rock bearing capacity. The rock breaking point is reached as the effective stress overcomes the rock strength, resulting in brittle ruptures. Despite the dangerous effects for surface structure, such as drilling platforms, this latter phenomenon may increase

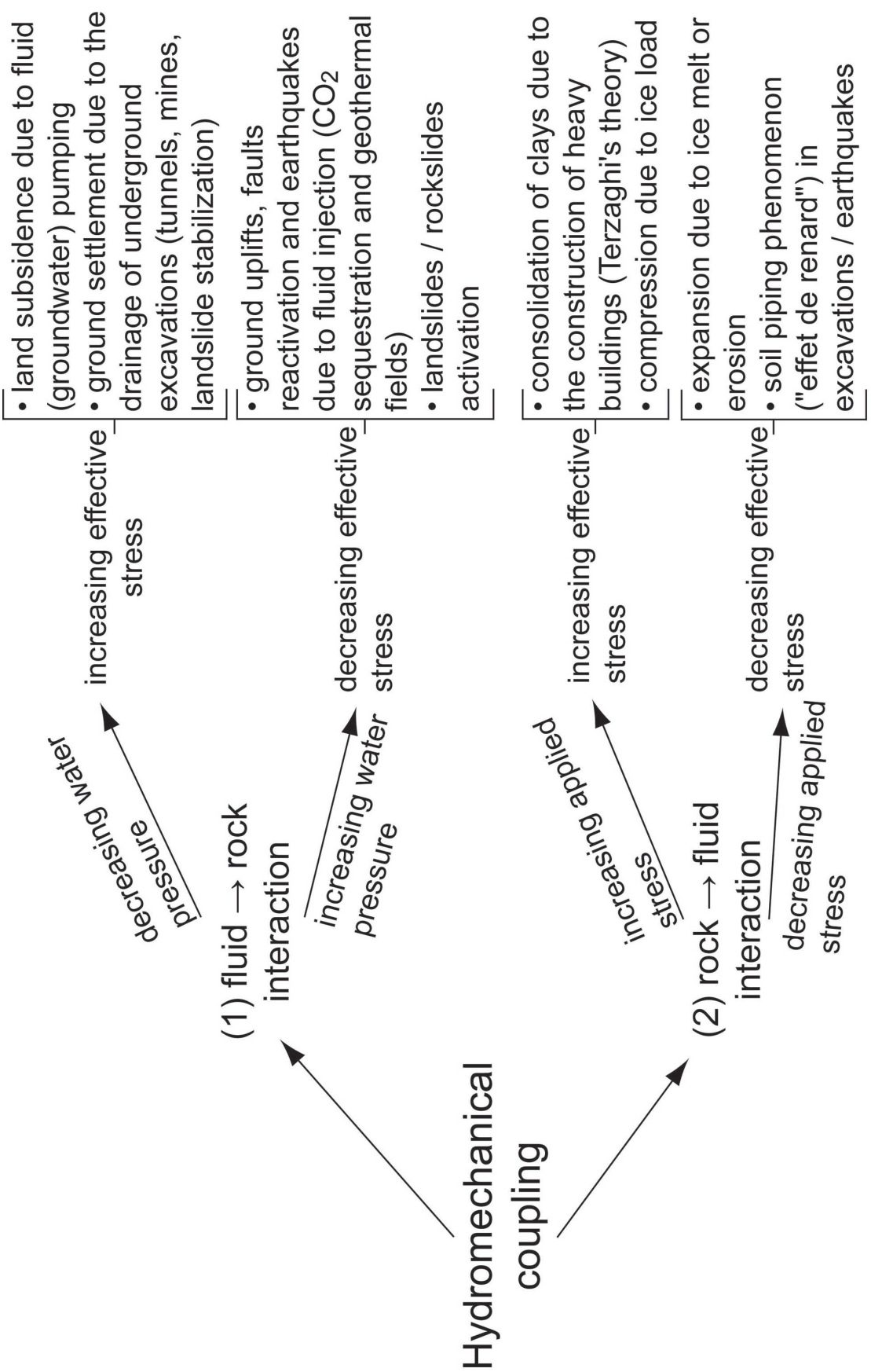

Figure 1.6: Diagram illustrating the main socio-economic implications of hydromechanical processes.

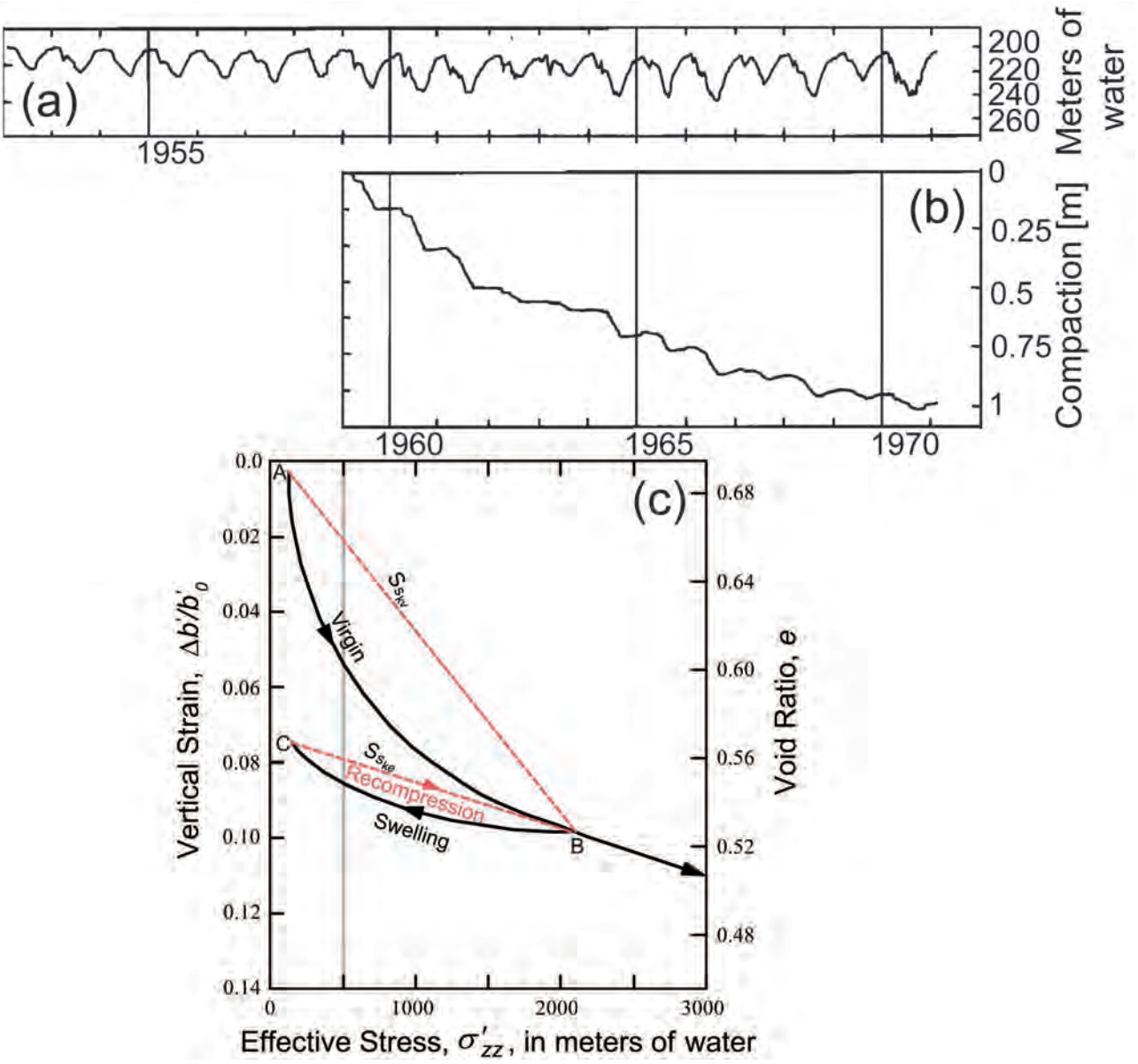

Figure 1.7: (a) Seasonal changes in groundwater levels without a long term decline, but leading to (b) an aquifer system compaction near Pixley, San Joaquin Valley, California (modified from Helm [29]). (c) Geomechanical behaviour of aquitards under virgin compression due to increasing effective stress, and swelling due to decreasing effective stress (Galloway and Burbey [23] modified from Helm [29]).

the hydrocarbon productivity as the reservoir permeability and connectivity increases with fracturing [51].

González et al. [26] associated the M_w 5.1 Lorca earthquake (southeast Spain, 11 May 2011) to groundwater extraction in a nearby basin-fill aquifer system. The authors [26] suggested that this earthquake could be triggered by crustal unloading due to groundwater withdrawal.

Discharge rates and ground settlement induced by tunnel excavation

The drilling of tunnels modifies the natural hydrodynamic behaviour of groundwater systems. The presence of a tunnel behaves as a draining structure and causes important drawdowns, especially in the case of deep tunnels. In terms of problem related to tunnel drainage, the

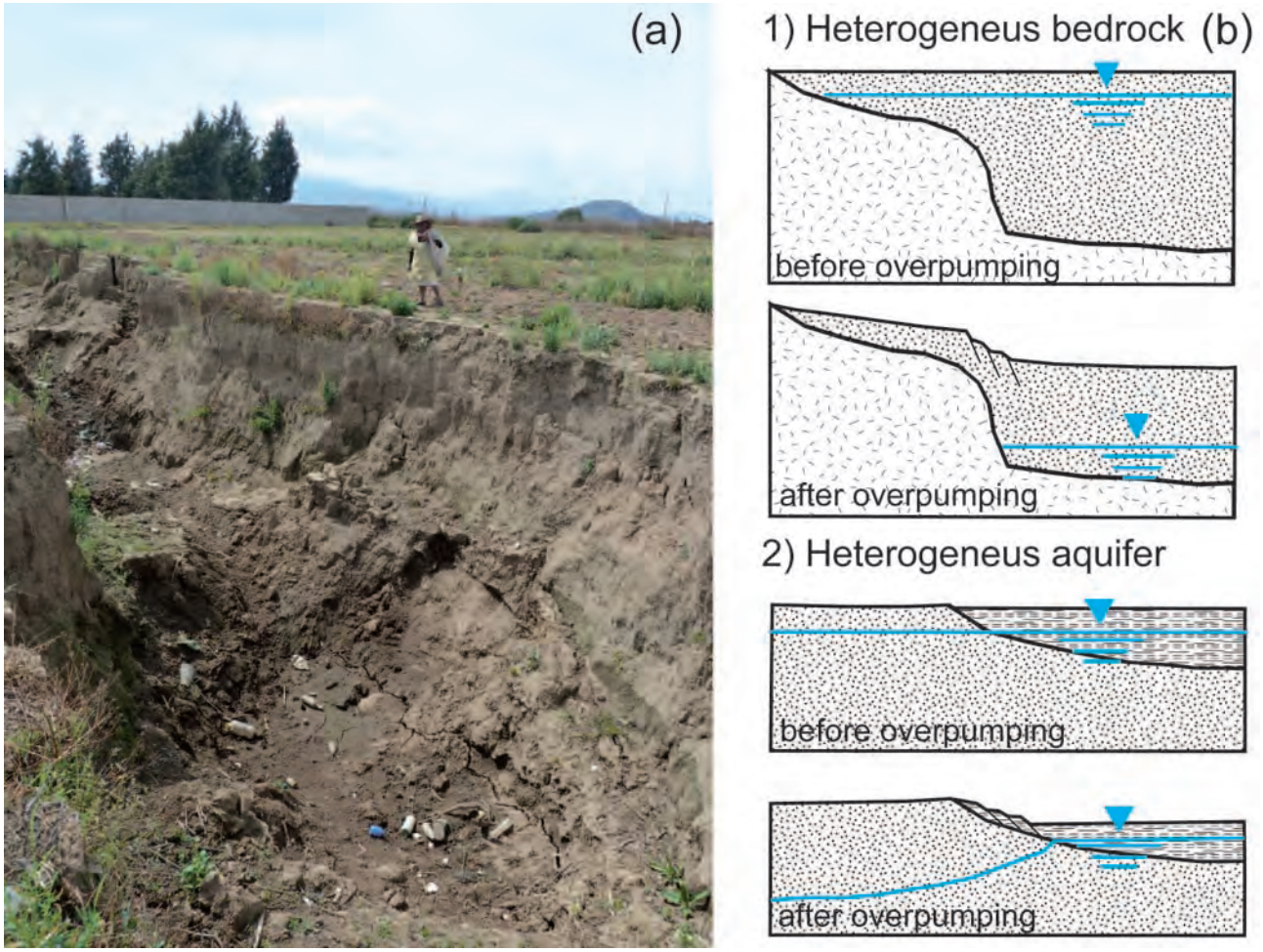

Figure 1.8: (a) Earth fissure in Mexico City (photo by J. Mercier, November 2011), and (b) main mechanisms leading to earth fracturing: (1) heterogeneity of the bedrock and (2) heterogeneity of the aquifer system.

decrease of hydraulic conductivity due to the increase of effective stress goes in the line of safety for the underground structure [50]. In contrast, ground settlement caused by the reduction of aquifer porosity can be very dangerous for structures located at the ground surface, and particularly for dams [55, 37, 38, 39, 67]. These problems concern primarily the drilling of deep tunnels through the fractured rock masses of alpine systems (Table 1.1). Theoretically, in a homogeneous and isotropic rock mass the shape of the ground settlement must reflect the shape of the water table drawdown caused by the tunnel drainage.

The differential settlement that occurred at the Zeuzier arch dam, Canton Wallis (Switzerland), due to the drilling of the Rawyl exploratory tunnel, is a well known case study. Through a series of vertical fractures the tunnel drained an unexpected underlying confined aquifer in the Dogger meta-sedimentary fractured rocks (Figure 1.9). The aquifer consolidation resulted in a regional subsidence dangerously affecting the dam foundations [55, 37]. Nowadays, several ground settlements of the same magnitude have been related to the excavation of deep tunnels in fractured crystalline and sedimentary rocks (Table 1.1).

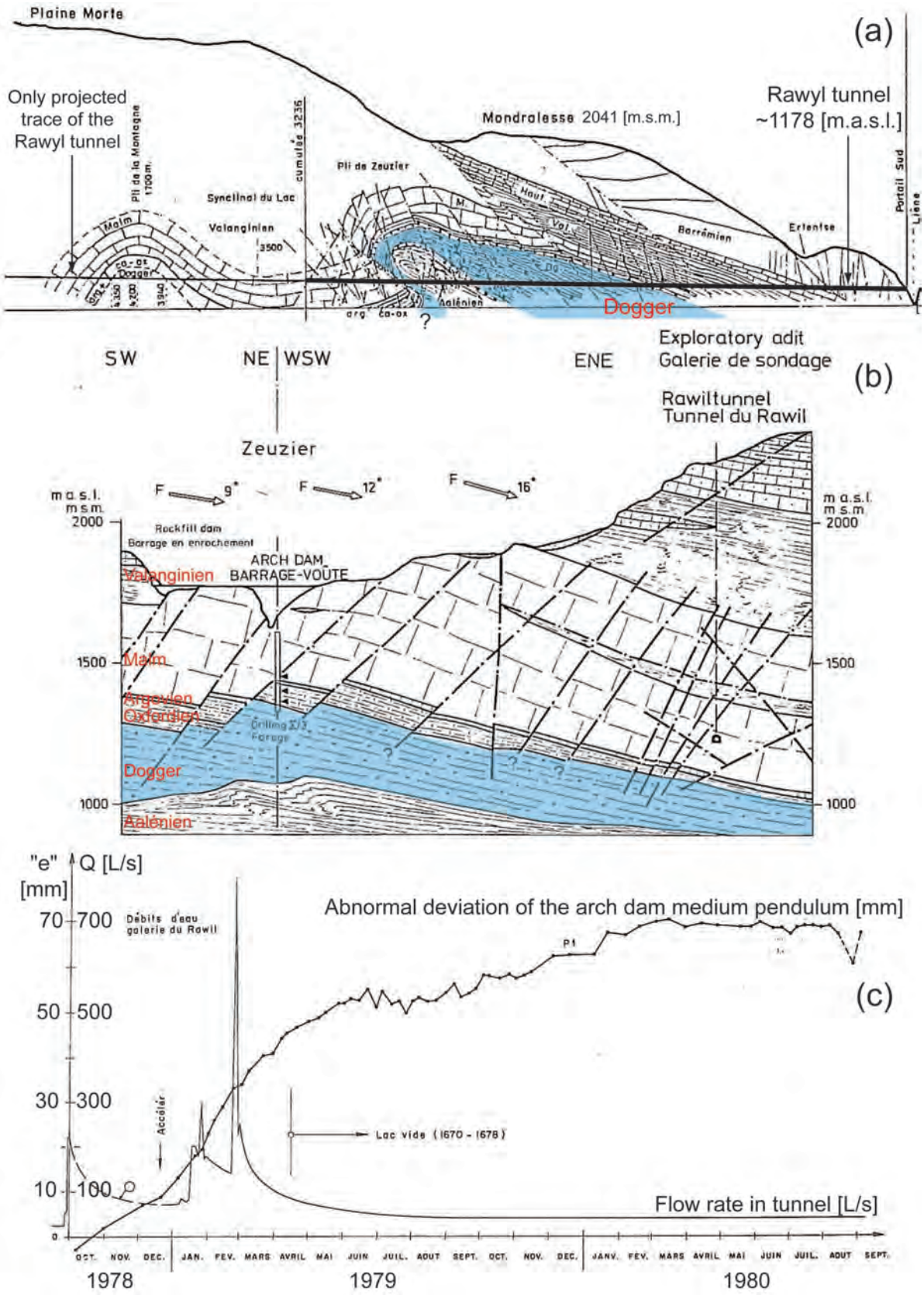

Figure 1.9: (a) Cross section along the Rawyl exploratory tunnel and (b) cross section between the Zeuzier arch dam and the Rawyl adit showing the geometry of the unexpected confined aquifer in the Dogger formations and the numerous fractures connecting the aquifer to the tunnel (modified from Schneider [55]). (c) Flow rate in tunnel and deviation of the dam medium pendulum in function of time. The increase of flow rate in the tunnel inversely evolves with the abnormal deviation of the pendulum due to the regional land subsidence (modified from Lombardi [37]).

Table 1.1: Maximum inflow, drawdown and ground settlement for different alpine tunnels

Tunnel	**Flow Rate** L/s	**Drawdown** m	**Settlement** cm	**Geology**	**References**
Gotthard Road Tunnel Switzerland	300	no data	12	fractured crystalline rocks	Zangerl et al., 2003 [67]
Rawyl Exploratory Adit Switzerland	> 1000	230	12	fractured meta-sedimentary calcareous schist	Schneider, 1982 [55] Lombardi, 1988 [37]
La Praz Exploratory Adit France	40	90	5	fractured meta-sedimentary sandy schist	Dzikowski and Villemin, 2009 [20]
Modane/Villarodin-Bourget Exploratory Adit France	180	90	> 3	cargnieules, mylonitic marbles and faults	SOGREAH Consultants, 2007 [57] Lassiaz and Previtali, 2007 [35]
Loetschberg Railway Tunnel Switzerland	no data	60	19	limestones and unconsolidated sediments	Vulliet et al., 2003 [62]
Campo Valle Maggia Landslide drain Switzerland	no data	300	50	fractured crystalline rocks and unconsolidated sediments	Bonzanigo, 1999 [8]

Ground uplift due to fluid injection

High-pressure injections of water in porous rock results in decreasing effective stresses. This can lead to the expansion of the porous rock, resulting in surface uplifts. In the framework of the In Salah CO_2 sequestration project, a ground uplift up to 5 mm/y was observed by InSAR techniques during injection activities [54].

Hydraulic fracturing injections to increase the permeability of a reservoir for geothermal energy production or for hydrocarbons extraction can lead to the opening and reactivation of pre-existing faults resulting in shear deformations and man-induced microseismicity. In 2006 and 2007, several earthquakes occurred in Basel (Switzerland), that exceeded the safety threshold (one event of magnitude $M_L = 3.4$), due to injection activities in order to stimulate a potential geothermal reservoir located in the 5 km deep crystalline basement [16].

Landslides/rockslides activation

Similar to the previous mechanism, increasing water pressures in rock fractures or in soil of a slope leads to uplift forces U and forward thrusts V reducing the resistance to slope movements. Moreover, forward thrusts increase forces promoting the slope motion (Figure 1.10). In case of important rainfalls events or during filling of dam lakes, the security factor of a slope F_s may

become < 1 resulting in a possible landslide/rockslide activation [51, 48]:

$$\begin{aligned} F_s &= \frac{\text{Forces resisting movement}}{\text{Forces promoting movement}} \\ F_s &= \frac{c'\,A + (W\,\cos\alpha - U - V\sin\alpha)\,\tan\varphi'}{W\,\sin\alpha + V\,\cos\alpha} \end{aligned} \tag{1.30}$$

where the symbols stand for cohesion c', contact area at the base $A = L_b\,L_y$, base length L_b, system length in the y-direction L_y, system weight W, angle of slope α, and angle of shearing resistance φ'. Eq. (1.30) applies to theoretical simplified geometry, as shown in Figure 1.10. In this system, the slope is the most stable at dry conditions. Under hydrodynamic conditions (Figure 1.10a): $V = 1/2\,\gamma_w\,h_1^2$ and $U = 1/2\,\gamma_w\,h_1\,L_b$, the slope becomes unstable. At hydrostatic conditions (Figure 1.10b): $V = 1/2\,\gamma_w\,h_1^2$ and $U = \gamma_w\,(h_1 + h_2/2)\,L_b$, the slope is strongly unstable and the landslide/rockslide can activate [51, 48]. Note that, in this simple example the rock mass creep within the landslide/rockslide matrix is not taken into account.

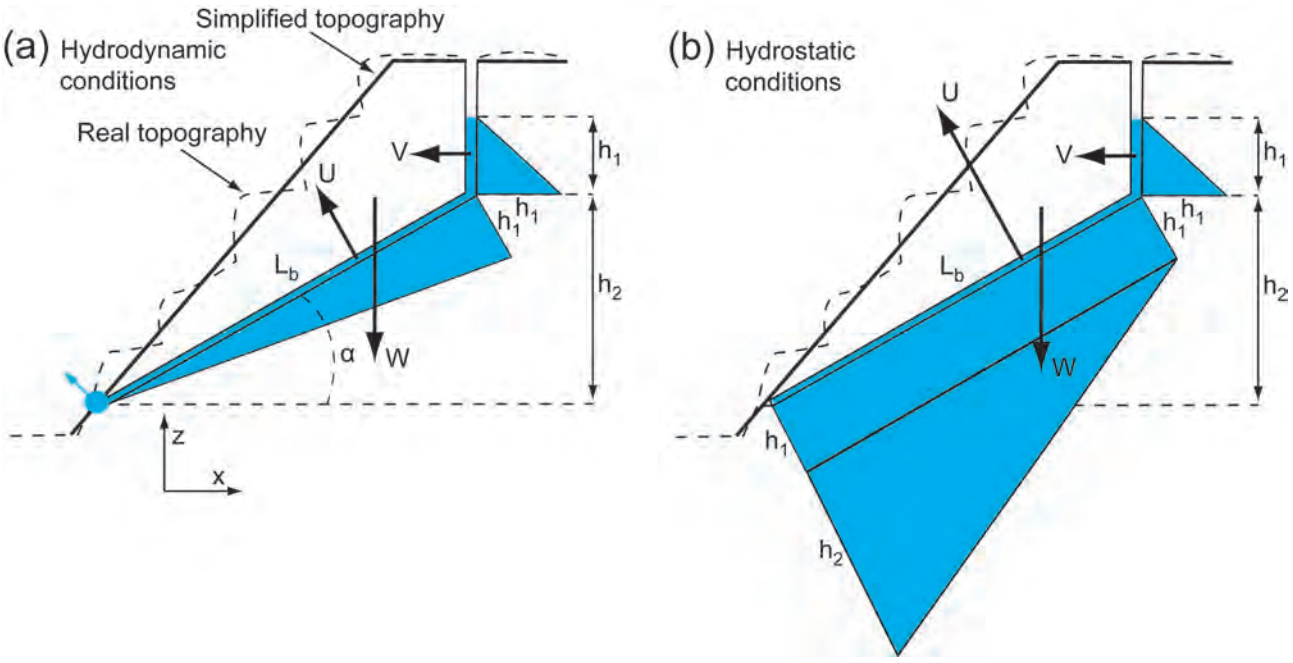

Figure 1.10: Landslide/rockslide activation due to the presence of groundwater. (a) At hydrodynamic condition water pressures in the fracture/sliding plane reduce the stability, (b) which becomes highly unstable if groundwater can not escape the system (modified from [51, 48]).

In the Alps, there are many examples of landslides and rockslides whose displacement rates correlate well with increasing groundwater pressures due to important rainfall or snow melt events [48]. To stabilize the mass movement, one approach consists in decreasing water pressures by pumping or draining activities. The deep-seated rockslide located at Campo Valle Maggia (Canton Ticino, Switzerland) was successfully stabilized by drainage through an underlying tunnel. A ground settlement of 50 cm was associated to the mass stabilization, due to the decrease of hydraulic heads [8, 21].

Some catastrophic landslides activation are related to the increasing of water pressures due to the filling of dam lakes. The well known example occurred at Vajont (Italy), where a landslide was activated on the left slope of the dam lake. The mass slid into the lake creating a huge wave that destroyed the downstream village of Longarone. 1900 people lost their lives in the disaster [47]. Londe [40] explained the failure of the Malpassat Dam (France) by two related events: (1) the weight of the dam decreased the hydraulic conductivity of an open fault underlying the structure, and (2) the subsequent increase of water pressures due to the dam impoundment resulted in the fault activation leading to a deep rockslide affecting the dam foundations. This latter accident is well illustrated by the theoretical case of Figure 1.10b. In Switzerland, the filling of the Salanfe Dam lake (Canton Wallis) was followed by a seismic event and by the emergence of some springs in the Val d'Illiez, located on the other side of the mountain overlooking the dam lake [5]. The seismic event and the springs can be explained by the opening and the deformation of a faulted and fractured deep aquifer system connecting the Salanfe Lake to the Val d'Illiez.

1.6.2 Processes related to solid-to-fluid coupling

As stated before, the definition "Solid-to-Fluid Coupling" refers to a change in applied stress inducing a change in fluid pressure [9]. In open systems, this overpressure results in fluid flow.

Increasing effective stress

The well known example of increasing effective stress due to an increase in applied stress is the Terzaghi's consolidation theory presented in section 1.5.2 [59, 60]. The compression of a clayey stratum under the applied load of a heavy building causes an increase in the water pressure leading to the stratum drainage and consolidation (Figure 1.5). At a different time scale and in case of a glaciation, the same process can occur in compressible units under ice load.

Decreasing effective stress

Theoretically, a decrease in effective stress due to the decrease of applied stress will lead to an expansion under the uplift force of the fluid. This mechanism can happen in the case of important erosions / ice melts, or in large and deep excavations.

A well known case is the soil piping phenomenon ("boiling" of the foundation floor), which can be very dangerous for deep foundations below the water table [51]. Prior the excavation works, a saturated soil is stable because the applied overburden load on contacting grains is greater than the pressure of water in voids. The digging activities reduce the overburden load and induce a groundwater flow towards the excavation. If the water table is not lowered by pumping, sheet piling or grouting, the water pressure can become greater than the applied overburden load leading to the "boiling" of the foundation floor (solid grains are no more in contact with each other, but suspended in the fluid).

A catastrophic soil piping phenomenon can occur during important earthquakes. In saturated soils, shear stresses induced by the transit of P-Waves decrease the pore volume, leading to an instantaneous rise of water pressures. This results in negative effective stresses synonymous of ground collapse, and subsequent groundwater flow to the surface.

1.6.3 Manifestations in Switzerland

In Switzerland, observed hydromechanical phenomena are related to the drilling of tunnels through aquifers [55, 37, 62, 67], the drainage of landslides [8], the filling of dam lakes [5] and fluid injection for geothermics [16] (Table 1.2). To date, land subsidence due to groundwater pumping in unconsolidated quaternary aquifers has not been observed. This can be explained by the absence of significant water table drawdown (higher than ten meters) in basin-fill aquifer systems. The Po Delta subsidence partly due to heavy groundwater and hydrocarbons pumping affecting cities such as Venice and Ravenna, is the closest case study [64, 58, 24].

Table 1.2: Hydromechanical phenomena in Switzerland

(1) Ground settlement induced by tunnel excavation:		
1978/1979 2002 1970-1993/1998	Zeuzier, Wallis St-German, Wallis Gotthard Pass, Uri/Ticino	Schneider (1982) [55], Lombardi (1988) [37] Vulliet et al. (2003) [62] Zangerl et al. (2003) [67]
(2) Ground settlement induced by the drainage of landslides:		
1993-1996	Campo Valle Maggia, Ticino	Bonzanigo (1999) [8]
(3) Earthquakes due to fluid injection / reservoir filling:		
1952 2006-2007	Salanfe, Wallis Basel	Bianchetti (1992) [5] Deichmann (2009) [16]

Within the framework of the Gotthard Alptransit Base Tunnel, Hansmann et al. [27] detected a cyclical extension/shortening of the distance between slopes of the Val Termine, located in the North of Canton Ticino (Figure 1.11a). This was interpreted as a consequence of water pressures in the fractured granitic rocks of the Gotthard massif. A slow lowering of the water table in the fractured rocks occurs outside of snow melt periods, leading to increasing effective stresses and in the compression of the massif. This results in an extension of the distance orthogonal to the valley. On the opposite, a rapid recovery of the water table follows snow melt events, leading to decreasing effective stresses and in the expansion of the fractured granitic rocks. This results in a shortening of the distance orthogonal to the valley (Figure 1.11b). These measurements also indicate that, in the short term, fractured granitic rocks are subject to small reversible elastic strains with seasonal variations in water table levels.

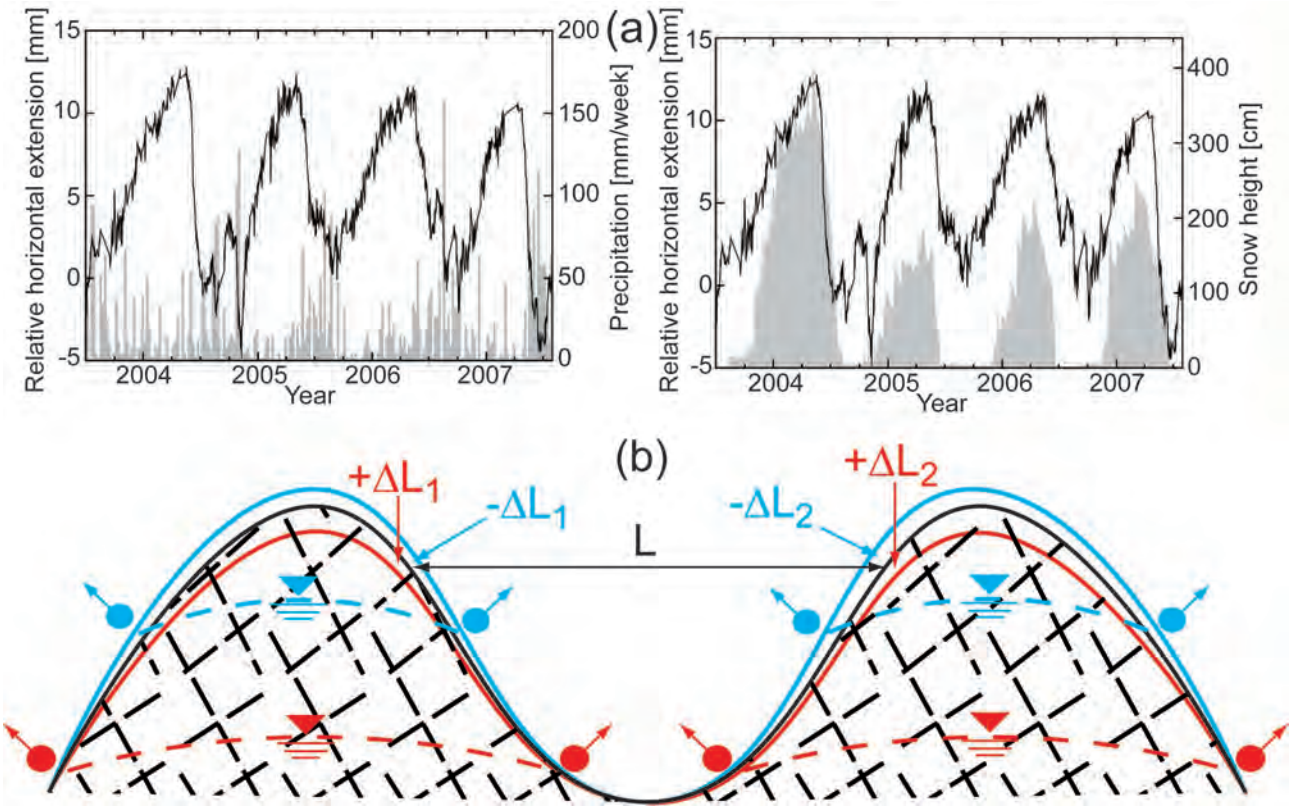

Figure 1.11: (a) Relative horizontal extension between two reflectors located on slopes of the Val Termine (solid black line), precipitation and snow height (in gray) as a function of time [27]. (b) Conceptual model illustrating the fractured rock mass expansion (blue line) / compression (red line) under seasonal variations in water table levels, leading to a shortening/extension of the distance L orthogonal to the valley (modified from [27]).

1.7 Scope and structure of this Work

As mentioned in the section 1.5, the modelling of coupled hydromechanical processes at hydrogeological scales and considering detailed geology can not be addressed by poroelastic equations due to the large number of parametric information and the complexity of solution algorithms, leading to computational complications. In contrast, Jacob's approach and "the aquitard drainage model" are limited by the consideration of constant hydrodynamic parameters and by the neglect of the role of principal stresses, as well as the fact that in general only aquitards are considered as compressible in an aquifer system.

Within this context, the aim of this thesis is to present a simulation approach able to investigate coupled fluid-to-solid hydromechanical processes at regional scales, with geologically oriented 3D meshes, and considering the dependency of hydrodynamic parameters on effective stress. The proposed stress-dependent functionals are developed from sound physical and hydrogeological concepts by analytical analysis, and compared with real laboratory and/or field data. The verification of the modelling approach is based on the comparison with the results obtained via exact analytical solutions specific to the hydrodynamic of groundwater flow in systems under stress. The thesis also presents the application of the proposed method on real case studies, and proposes some improvements of analytical equations solving for the groundwater

flow rates in underground excavations (tunnels).

The manuscript is organized as follows. In Chapter 2 and Chapter 3, constitutive model functions relating effective stress to hydrodynamic parameters are first developed for fractured and granular porous media, respectively. Second, the stress-dependent equations are verified on real laboratory and field measurements. In Chapter 4, the numerical simulation approach for regional fluid-to-solid processes is presented, verified by a comparison with results obtained via exact analytical solutions, and applied to the settlement of the Zeuzier arch dam. In Chapter 5 the modelling approach is used to study the response of aquifers intersected by deep excavations (tunnels) and is compared with the existing analytical solutions specific for this problematic. Chapter 6 deals with the modelling of the anthropogenic land subsidence affecting Mexico City.

Bibliography

[1] Auvinet, G.: Soil fracturing induced by land subsidence. In: Land Subsidence, Associated Hazards and the Role of Natural Resources Development, pp. 20–26 (2010)

[2] Auvinet, G., Méndez, E., Lermo, J.: Advances in geotechnical characterization of soil fracturing in Mexico City basin. In: Land Subsidence, Associated Hazards and the Role of Natural Resources Development, pp. 3–8 (2010)

[3] Bear, J., Cheng, A.H.D.: Modeling Groundwater Flow and Contaminant Transport. Springer Science (2010)

[4] Bell, J., Amelung, F., Ferretti, A., Bianchi, M., Novali, F.: Permanent scatterer InSAR reveals seasonal and long-term aquifer system response to groundwater pumping and artificial recharge. Water Resources Research **44**, 18pp (2008)

[5] Bianchetti, G., Roth, P., Vuataz, F.D., Vergain, J.: Deep Groundwater Circulation in the Alps: Relations between Water Infiltration, Induced Seismicity and Thermal Springs. The Case of Val d'Illiez, Wallis, Switzerland. Eclogae Geol. Helv. **85**(2), 291–305 (1992)

[6] Biot, M.: General theory of three-dimensional consolidation. J App Phys **12**(2), 155–164 (1941)

[7] Blunier, P.: Méthodologie de gestion durable des ressources du sous-sol urbain. Ph.D. thesis, Ecole Polytechnique Fédérale de Lausanne (2009)

[8] Bonzanigo, L.: Lo slittamento di Campo Vallemaggia. Ph.D. thesis, Swiss Federal Institute of Technology Zürich (1999)

[9] Bundschuh, J., Arriaga, M.: Introduction to the Numerical Modeling of Groundwater and Geothermal Systems, chap. Rock and fluid, pp. 13–100. Taylor & Francis Group, CRC Press (2010)

[10] Burbey, T.: Stress-strain analyses for aquifer-system characterization. Ground Water **39**(1), 128–136 (2001)

[11] Burbey, T.: Three-dimensional deformation and strain induced by municipal pumping, Part 2: Numerical analysis. Journal of Hydrology **330**(3–4), 422–434 (2006)

[12] Burbey, T.: The Influence of Geologic Structures on Deformation due to Ground Water Withdrawal. Ground Water **46**(2), 202–211 (2008)

[13] Burbey, T.: Mechanisms for earth fissure formation in heavily pumped basins. In: Land Subsidence, Associated Hazards and the Role of Natural Resources Development, pp. 3–8 (2010)

[14] Burbey, T., Warner, S., Blewitt, G., Bell, J., Hill, E.: Three-dimensional deformation and strain induced by municipal pumping, Part 1: Analysis of field data. Journal of Hydrology **319**(1–4), 123–142 (2006)

[15] Cappa, F.: Role of fluids in the hydromechanical behavior of heterogeneous fractured rocks: in situ characterization and numerical modelling. Bull. Eng. Geol. Env. **65**, 321–337 (2006)

[16] Deichmann, N., Ernst, J.: Earthquake focal mechanisms of the induced seismicity in 2006 and 2007 below Basel (Switzerland). Swiss J. Geosci. **102**, 457–466 (2009)

[17] Descoeudres, F.: Mécaniques des roches. Presses Polytechniques et Universitaires Romandes (1984)

[18] Detournay, E., Cheng, A.D.: Comprehensive Rock Engineering: Principles, Practice and Projects, Vol. II, chap. Fundamentals of poroelasticity, pp. 113–171. C. Fairhurst, Pergamon Press (1993)

[19] Durham, W.B.: Laboratory observations of the hydraulic behavior of a permeable fracture from 3800 m depth in the KTB pilot hole. J. Geophys. Res. **102**, 18,405–18,416 (1997)

[20] Dzikowski, M., Villemin, T.: Rapport d'expertise: hydrogéologie et géodésie de la descenderie de La Praz. Tech. rep., Belonging to Lyon Turin Ferroviaire (LTF), Chambery, France (2009)

[21] Eberhardt, E., Bonzanigo, L., Loew, S.: Long-term investigation of a deep-seated creeping landslide in crystalline rock. Part II. Mitigation measures and numerical modelling of deep drainage at Campo Vallemaggia. Canadian Geotechnical Journal **44**, 1181–1199 (2007)

[22] Ferronato, M., Gambolati, G., Janna, C., Teatini, P.: Geomechanical issues of anthropogenic CO2 sequestration in exploited gas fields. Energy Conversion and Management **51**(10), 1918–1928 (2010)

[23] Galloway, D., Burbey, T.: Review: Regional land subsidence accompanying groundwater extraction. Hydrogeology Journal **19**, 1459–1486 (2011)

[24] Gambolati, G., Teatini, P., Ferronato, M.: Encyclopedia of Hydrological Sciences, chap. Anthropogenic Land Subsidence, p. 17pp. Anderson M.G., John Wiley & Sons (2005)

[25] Gangi, A.F.: Variation of whole and fractured porous rock permeability with confining pressure. Int. J. Rock Mech. Min. Sci. Geomech. Abstr. **15**(5), 249–257 (1978)

[26] González, P., Tiampo, K., Palano, M., Cannavó, F., Fernández, J.: The 2011 lorca earthquake slip distribution controlled by groundwater crustal unloading. Nature Geoscience (DOI: 10.1038/NGEO1610) (2012)

[27] Hansmann, J., Loew, S., Evans, K.: Reversible rock-slope deformations caused by cyclic water-table fluctuations in mountain slopes of the Central Alps, Switzerland. Hydrogeology Journal **20**(1), 73–91 (2012)

[28] Helm, D.: Simulation of aquitard compaction due to changes in stress. Trans Am Geophys Union **53**(11), 979 (1972)

[29] Helm, D.: One-Dimensional Simulation of Aquifer System Compaction Near Pixley, California. 1. Constant Parameters. Water Resources Research **11**(3), 465–478 (1975)

[30] Helm, D.: One-Dimensional Simulation of Aquifer System Compaction Near Pixley, California. 2. Stress-Dependent Parameters. Water Resources Research **12**(3), 375–391 (1976)

[31] Holzer, T.: Man induced land subsidence. Geol. Soc. of America, Washington, DC (1984)

[32] Jacob, C.: On the flow of water in an elastic artesian aquifer. American Geophysical Union **21** (1940)

[33] Jacob, C.: Engineering hydraulics: Proceedings of the Fourth Hydraulics Conference, Iowa Institute of Hydraulic Research, Iowa City, IW, chap. Flow of ground water. Rouse H (ed) (1950)

[34] Kim, J.M., Parizek, R.: A Mathematical Model for the Hydraulic Properties of Deforming Porous Media. Ground Water **37**(4), 546–554 (1999)

[35] Lassiaz, P., Previtali, I.: Descenderie et Galerie de reconnaissance de Modane / Villarodin-Bourget: Suivi et Auscultation Géodésique. Tech. rep., Lyon Turin Ferroviaire, Chambéry Cedex, France (2007)

[36] Loew, S., Hansmann, J.: Annual opening and closure of alpine valleys. In: Conference. Centre for Hydrogeology and Geothermics, Neuchâtel (2010)

[37] Lombardi, G.: Les tassements exceptionnels au barrage de Zeuzier. Publ. Swiss Soc. Soil Rock Mech. **118**, 39–47 (1988)

[38] Lombardi, G.: The FES rock mass model - Part one. Dam Engineering **3**, 201–221 (1992)

[39] Lombardi, G.: The FES rock mass model - Part two: Some examples. Dam Engineering **3**(3), 201–221 (1992)

[40] Londe, P.: The Malpasset dam failure. Eng. Geol. **24**(1–4), 295–329 (1987)

[41] Louis, C.: A study of groundwater flow in jointed rock and its influence on the stability of rock masses. Tech. Rep. 9, Rock Mechanics, Imperial College, London, UK (1969)

[42] Mayeur, B., Fabre, D.: Measurement and modeling of natural stresses. Application to the Maurienne-Ambin tunnel project. Bulletin of Engineering Geology and the Environment **58**(1), 45–59 (1999)

[43] Murdoch, L., Germanovich, L.: Analysis of a deformable fracture in permeable material. International Journal for Numerical and Analytical Methods in Geomechanics **30**(6), 529–561 (2006)

[44] National Research Council: Rock Fractures and fluid flow. National Academy Press, Washington, DC (1996)

[45] Neuzil, C.: Hydromechanical coupling in geologic processes. Hydrogeology Journal **11**, 41–83 (2003)

[46] Osmanoglu, B., Dixon, T., Wdowinski, S., Cabral-Cano, E., Jiang, Y.: Mexico City subsidence observed with persistent scatterer InSAR. Int Journal Applied Earth Observation **13**(1), 1–12 (2011)

[47] Parriaux, A.: Géologie: Bases pour l'Ingénieur. Presses Polytechniques et Universitaires Romandes (2006)

[48] Parriaux, A., Bonnard, C., Tacher, L.: Glissements de terrain: hydrogéologie et techniques d'assainissement par drainage. Guide Pratique. Tech. rep., Office Fédéral de l'Environnement OFEV, Berne, Switzerland (2010)

[49] Perrochet, P.: Facteur de réduction des débits en tunnels profonds. Tech. rep., Centre d'Hydrogéologie Neuchâtel, Neuchâtel, Suisse

[50] Preisig, G., Cornaton, F., Perrochet, P.: Regional Flow Simulation in Fractured Aquifers Using Stress-Dependent Parameters. Ground Water **50**(3), 376–385 (2012)

[51] Price, D., de Freitas, M.: Engineering Geology. Springer-Verlag Berlin Heidelberg (2009)

[52] Riley, F.: Analysis of borehole extensometer data from central California. In: Land Subsidence, IAHS RedBooks Pub. 88, pp. 423–431 (1969)

[53] Rutqvist, J., Stephansson, O.: The role of hydromechanical coupling in fractured rock engineering. Hydrogeology Journal **11**(1), 7–40 (2003)

[54] Rutqvist, J., Vasco, D., Myer, L.: Coupled reservoir-geomechanical analysis of CO2 injection and ground deformations at In Salah, Algeria. International Journal of Greenhouse Gas Control **4**(2), 225–230 (2010)

[55] Schneider, T.: Geological Aspects of the Extraordinary Behaviour of Zeuzier Arch Dam. Wasser, energie, luft - eau, énergie, air **74**(3), 81–94 (1982)

[56] Schweisinger, T., Svenson, E., Murdoch, L.: Introduction to hydromechanical well tests in fractured rock aquifers. Ground Water **47**(1), 69–79 (2009)

[57] SOGREAH Consultants: Descenderie de Modane/Villarodin-Bourget: étude de faisabilité de reutilisation des eaux d'exhaure de la partie montante. Tech. rep., Lyon Turin Ferroviaire (LTF), Chambery, France (2007)

[58] Teatini, P., Ferronato, M., Gambolati, G., Bertoni, W., Gonella, M.: A century of land subsidence in Ravenna, Italy. Environ Geol **47**(6), 831–846 (2005)

[59] Terzaghi, K.: Die berechnung der durchlässigkeitziffer des tones aus dem verlauf der hydrodynamischen spannungserscheinungen. Akad Wissensch Wien Sitzungsber Mathnaturwissensch Klasse IIa **142**(3–4), 125–138 (1923)

[60] Terzaghi, K., Peck, R.: Soil Mechanics in Engineering Practice. John Wiley and Sons, Inc. (1967)

[61] Verruijt, A.: Encyclopedia of Hydrological Sciences, chap. Consolidation of Soils, p. 15pp. Anderson M.G., John Wiley & Sons (2008)

[62] Vulliet, L., Koelbl, O., Parriaux, A., Védy, J.C.: Gutachtenbericht über die Setzungen von St. German, in Auftrag der BLS Alptransit AG. Tech. rep. (2003)

[63] Walsh, J.B.: Effect of pore pressure and confining pressure on fracture permeability. Int. J. Rock Mech. Min. Sci. Geomech. Abstr. **18**, 429–435 (1981)

[64] Waltham, T.: Sinking cities. Geology Today **18**(3), 95–100 (2002)

[65] Wang, H.F.: Theory of linear poroelasticity. Princeton University Press (2000)

[66] Wolff, R.: Relationship between horizontal strain near a well and reverse water-level fluctuations. Water Resources Research **6**, 1721–1728 (1970)

[67] Zangerl, C., Eberhardt, E., Loew, S.: Ground settlements above tunnels in fractured crystalline rock: numerical analysis of coupled hydromechanical mechanisms. Hydrogeology Journal **11**, 162–173 (2003)

Chapter 2

Constitutive model functions relating effective stress to hydrodynamic parameters in fractured aquifers *

Abstract

A model function relating effective stress to fracture permeability is developed from Hooke's law, implemented in the tensorial form of Darcy's law, and used to evaluate discharge rates and pressure distributions at regional scales. The model takes into account elastic and statistical fracture parameters, and is able to simulate real stress-dependent permeabilities from laboratory to field studies. This modeling approach gains in phenomenology in comparison to the classical ones because the permeability tensors may vary in both strength and principal directions according to effective stresses. Moreover this method allows evaluation of the fracture porosity changes, which are then translated into consolidation of the medium.

2.1 Introduction

Crystalline and non karstic sedimentary rocks are anisotropic geological media with low hydraulic conductivity [32]. In such media, if the primary porosity by intergranular is neglected, groundwater flow occurs primarily and sometimes exclusively through non-filled fractures. Their spatial arrangement (i.e. fracture network) leads to groundwater flow at a regional scale. At this scale, the most simple and useful way to conceptualize these aquifers is the equivalent porous media; the principal permeabilities of each fracture family are combined in space and result in a tensor describing the equivalent hydraulic conductivity of the rock mass [21, 2].

The sensitivity of aquifers dynamics to effective stress was first described for granular porous media [41]; the process was then also observed in fractured aquifers [28]. Nowadays, the depen-

*This Chapter is based on the paper:
Preisig, G., Cornaton, F.J., Perrochet, P.: Regional Flow Simulation in Fractured Aquifers Using Stress-Dependent Parameters. Ground Water **50**(3), 376–385 (2012).

dency of fracture permeability on effective stress is a well known research topic and has been intensively studied during the last decades, especially to evaluate the stability of rock masses in presence of dams, tunnels, geologic radioactive waste repositories or CO_2 sequestration fields [27, 25, 38, 45, 15]. In regional and deep groundwater flow systems, the reduction of water pressures leads to increasing effective stresses and decreasing permeabilities, with a possible consolidation of the aquifer. On the contrary, increasing groundwater pressures result in decreasing effective stresses and in increased permeabilities. Based on field and laboratory test results, Louis [28] and later Walsh [43] derived respectively an exponential and a logarithmic model to explain permeability decreases with increasing effective stresses. The relationship between effective stress and permeability has been clearly identified both at local and regional scales via laboratory tests (see [42, 14, 19]), field tests (see [7, 39]), and observations of aquifer consolidation by measurements and modeling of ground subsidence (see [25, 37, 45]).

However, the equivalent porous medium approach and consequently the classical Darcy solution implemented in regional groundwater numerical models generally ignores this relationship [30], hence the interest in modifying the flow equation to a more realistic one, explicitly accounting for stress-dependent permeabilities. The present approach consists in inserting constitutive laws relating effective stress to permeability in the tensor form of Darcy's law, so that the permeabilities vary with stress (depth and geology) and water pressure. The constitutive model must: (1) respect most of the physical process at the microscopic scale but should also lend itself to practical application at large scales, and (2) be simple from a numerical point of view. Note that a number of rock mechanics codes exist (see for example [11, 20, 1, 8, 44]) that solve coupled hydromechanical problems. However, these generally apply to relatively small scale problems, because they involve full and detailed deformation processes, and, therefore, become computationally prohibitive at hydrogeological scales. On the contrary, the present work focuses on a macroscopic approach allowing efficient large scale computations, while preserving the essence of the hydromechanical processes.

This Chapter begins by examining the hydrogeology of fractured rocks. Then, a constitutive model is presented where fracture permeability is a function of the effective stress, as well as of the statistical distribution of the length of the asperities and their elasticity. Expressed in its tensor form, this law describes the process at the rock mass scale. Next, simulated stress-dependent permeabilities are compared with laboratory and field measurements from Durham [14] and Cappa [7]. Toward the Chapter end, some theoretical problems are performed in order to illustrate this modeling approach. The constitutive model is also used to evaluate the changes in porosity between an initial and a modified hydrogeological state, and to compute the resulting subsidence.

2.2 Fractured rock hydrogeology

As stated in the Introduction 2.1, fractured aquifers consist of crystalline and non karstic sedimentary rocks. In such media, the porosity is generally low ($\leq$ 2 %) and results from

the presence of cracks, joints, fractures and faults associated with the porosity within the rock matrix (Figure 2.1). Cracks, joints, fractures and faults have mainly a conductive role, while the rock matrix porosity (if existing) is mostly involved in capacitive and retardation mechanisms [2, 32]. In this thesis, the following classification is used to characterize the hydraulic properties of fractured aquifers [40, 6]:

- micropermeability occurs within the rock matrix porosity.
- permeability results from the spatial arrangement (i.e., fracture network) of cracks, joints and fractures. Note that, in this work the term fracture will be used to refer to these structures.
- macropermeability is related to open faults.

These different permeabilities can be connected or not with each other. In this context, at a regional scale, a practical way to simulate groundwater flow through fractured rocks is to (1) consider only the capacitive role of the rock matrix porosity, (2) treat the permeability within the fracture network as a tensor, (3) insert open faults as discrete elements, and (4) use Darcy's law to describe groundwater flow [21, 2, 32, 33]. Note that groundwater flow through fractured rocks can also be analyzed by stochastic approaches [10, 11].

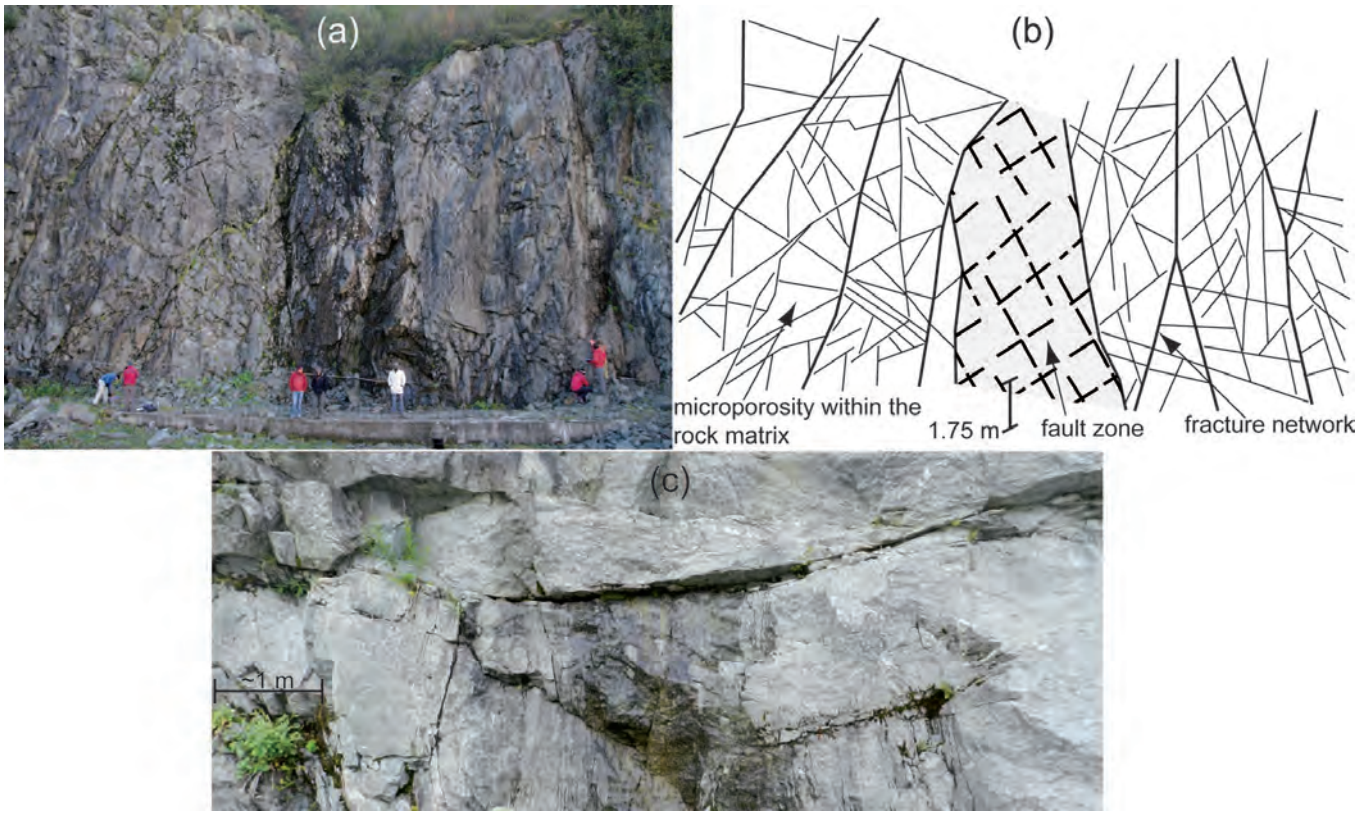

Figure 2.1: (a) Fractured granite of the Emosson area, Wallis, Switzerland (photo by Dr. F. Negro, September 2010); and (b) illustrative conceptualization of the rock mass showing the different structures allowing the presence and the flow of groundwater. (c) Groundwater resurgence from a conductive fracture of the Emosson granite (photo by G. Preisig, August 2012).

Fractures and faults can become impervious due to the presence of filling materials (clays) or mineralization, and under stress load. Within this context, stress acts on contacting asperities and closes voids. On the contrary, if present, groundwater pressure in voids alleviates the load on asperities and opens the porosity. In general, alpine fractured rock masses are characterized by (1) a shallow post-glacial fractured decompression zone of variable thickness: 100-300 m, and (2) a deeper unaltered zone [3]. The post-glacial decompression zone is permeable due to the presence of shallow fracture networks and open faults. On the contrary, the deeper zone becomes impervious because of the closure of fractures and faults under the stress load and because of the decrease of fracture occurrence [4]. Measurements of Hansmann et al. [18] (see section 1.6.3) indicate that in the short term, fractured rock masses can be treated as Hookean materials having an elastic reversible behaviour.

In the field, hydrodynamic parameters of fractured systems can be quantified by hydraulic tests, such as packer tests [31], or by detailed analysis of the aperture and the spatial orientation of fractures and faults, such as scanline survey [36, 34, 35]. In their MSc Thesis, Devenoges [12] and Dupont [13] performed scanline surveys in order to characterize the anisotropy and heterogeneity of permeability in the fractured rock masses between the Salanfe Dam Lake and the Val d'Illiez (Wallis, Switzerland) (Figure 2.2).

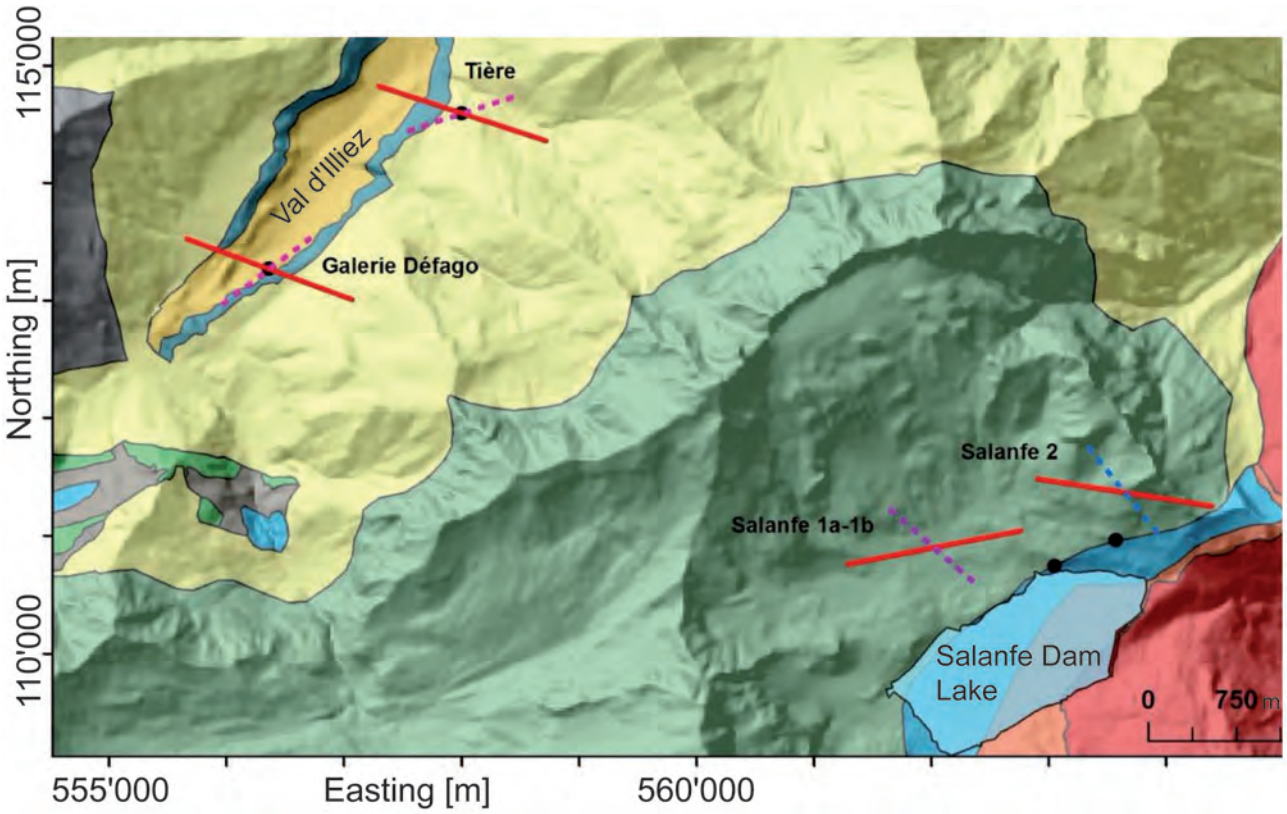

Figure 2.2: Map projection of 3D permeability tensors carried out by scanline surveys. The red solid lines indicate the direction of the maximum permeability, the dotted lines the direction of the minimum permeability. This anisotropy correlates well with the regional groundwater flow from the Salanfe area to the Val d'Illiez (modified from [12]).

2.3 Constitutive aperture-stress model

The model considers a single fracture as a pair of surfaces, characterized by a set of asperities, the length of which follows a statistical distribution. This asperity population can be characterized by fracture morphology analysis (see [5, 17]). Assuming that each asperity i obeys Hooke's law, the resulting normal stress, σ_i, proportional to its deformation is:

$$\sigma_i = E_i \frac{\Delta z_i}{z_i} = E_i \frac{z_i - a}{z_i} = \frac{F_i}{s_i} \tag{2.1}$$

where the symbols stand for asperity original length z_i, compression $\Delta z_i = z_i - a$, elastic modulus E_i, average asperity section s_i, exerting force F_i and fracture aperture a. Eq. (2.1) implies the following conditions:

First, if $a \geq z_i$, $\sigma_i = 0$ (the asperity is at its original length).

Second, if $a = 0$, $\sigma_i = E_i$ (the asperity is subjected to a total compression).

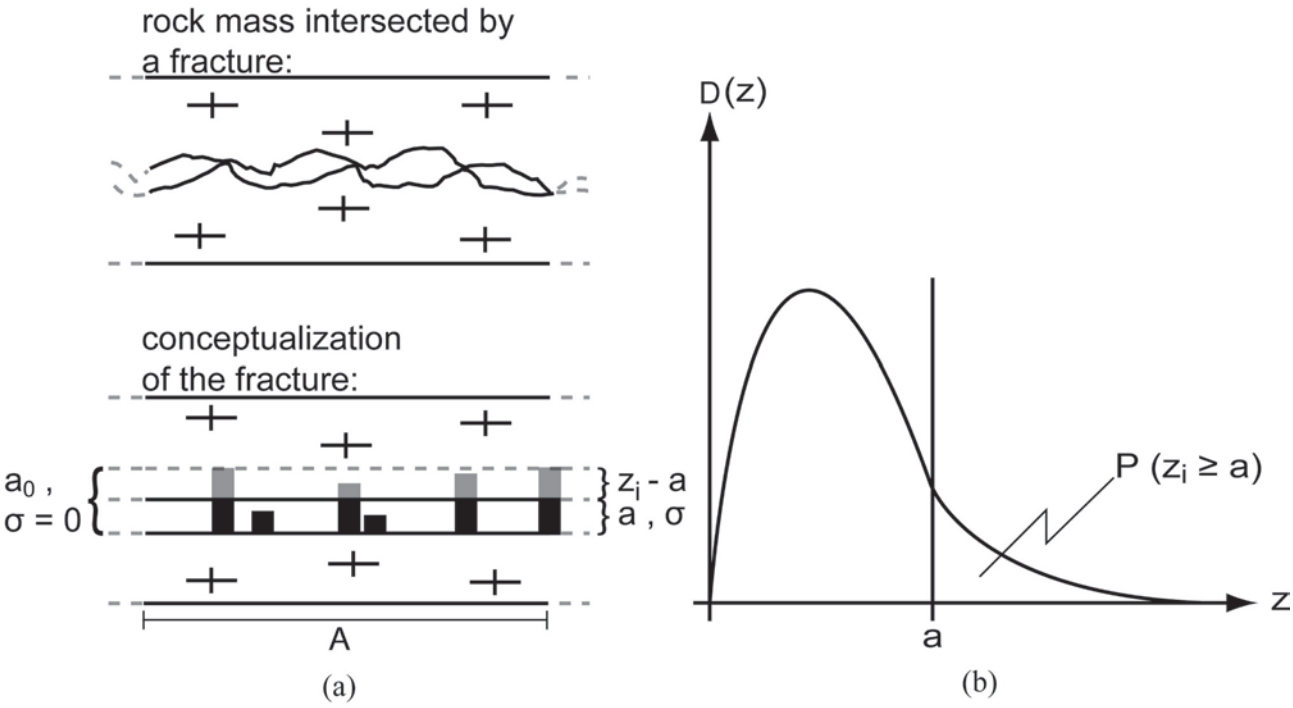

Figure 2.3: (a) Schematic illustration of a rock mass intersected by a fracture and its conceptualization with a set of asperities. The fracture under the normal stress σ has the aperture a, the maximum fracture aperture a_0 is reached when there is no stress. (b) Continuous statistical distribution, $D(z)$, of the asperity length, z, and probability of contact.

Under a given normal stress, the asperities return an equilibrium equivalent stress σ defining a specific aperture a (Figure 2.3a). This normal stress results from the integration of all stresses exerted by individual asperities compressed to various degrees. For a given aperture, the probability that an asperity is in contact with both fracture faces $P(z_i \geq a)$ corresponds to

the ratio between the number of compressed asperities and the total number of asperities:

$$P(z_i \geq a) = \int_a^{\infty} D(z)dz = \frac{N_c}{N_t} \tag{2.2}$$

where $D(z)$ is the statistical distribution of the asperity lengths (Figure 2.3b), N_c is the number of compressed asperities and N_t is the total number of asperities. In Eq. (2.2) the infinite upper bound of the integral can be replaced by the maximum fracture aperture a_0, which also represents the original length of the longest asperities. Note that the integral of $D(z)$ must be equal to unity. Glover et al. [17] note that $D(z)$ is frequently assumed of Gaussian type. In this work, a number of simple typical distributions are considered, as well as the more realistic Weibull distribution.

Assuming average values for asperity elastic modulus and section, and associating Eqs. (2.2) and (2.1), the equilibrium normal stress for a fracture with an aperture a is obtained by weighting each asperity contribution by its probability density. Integrating over all active asperities yields:

$$\sigma = \frac{F}{A} = \frac{N_t}{A} Es \int_a^{a_0} \frac{(z-a)}{z} D(z)dz \tag{2.3}$$

where F is the force exerted by the compressed asperities, A is the fracture surface area, E is the elastic modulus of the fractured rock and s is an average asperity section. $N_t/A = \eta$ is the asperity areal density. Eq. (2.3) respects the same conditions as Eq. (2.1). Firstly, the maximum fracture aperture a_0 is reached at $\sigma = 0$ ($a = a_0$, no compression). Secondly, total fracture compression ($a = 0$) occurs when $\sigma = \eta Es = \sigma_0$, where σ_0 is the fracture closure normal stress.

2.4 Model adjustment for different statistical distributions

Different $\sigma(a)$ models are obtained depending on the statistical distribution $D(z)$. For example, for the uniform distribution (Figure 2.4a) $D(z) = 1/a_0$, Eq. (2.3) becomes:

$$\begin{aligned} \sigma &= \sigma_0 \int_a^{a_0} \frac{(z-a)}{z} \frac{1}{a_0} dz \\ &= \sigma_0 \left[1 - \frac{a}{a_0} + \frac{a}{a_0} \ln\left(\frac{a}{a_0}\right) \right] \end{aligned} \tag{2.4}$$

Several constitutive models are found proceeding in the same way for different types of distribution $D(z)$ (Table 2.1). After integration the fracture aperture a is directly related to normal stress σ. As mentioned in the introduction, the model must be simple from a numerical point of view, hence the need to reformulate the specific models presented in Table 2.1 in a generic equation of the form:

$$\sigma = \sigma_0 \left(1 - \frac{a}{a_0}\right)^n , n \geq 1 \tag{2.5}$$

Depending on the value of coefficient n, Eq. (2.5) provides exact stress-dependent apertures for

Table 2.1: Example of aperture-stress models for different statistical distributions of asperity length.

	statistical distribution	model
singular	$D(z) = \delta(z - a_0)$	$\sigma = \sigma_0 \left(1 - \frac{a}{a_0}\right)$
uniform	$D(z) = \frac{1}{a_0}$	$\sigma = \sigma_0 \left[1 - \frac{a}{a_0} + \frac{a}{a_0} \ln\left(\frac{a}{a_0}\right)\right]$
linear increasing	$D(z) = \frac{2z}{a_0^2}$	$\sigma = \sigma_0 \left(1 - \frac{a}{a_0}\right)^2$
linear decreasing	$D(z) = \frac{2}{a_0}\left(1 - \frac{z}{a_0}\right)$	$\sigma = \sigma_0 \left[1 - \left(\frac{a}{a_0}\right)^2 + 2\frac{a}{a_0} \ln\left(\frac{a}{a_0}\right)\right]$
parabolic	$D(z) = \frac{6}{a_0^2} z \left(1 - \frac{z}{a_0}\right)$	$\sigma = \sigma_0 \left(1 - \frac{a}{a_0}\right)^3$
Weibull distribution	$D(z) = \frac{\epsilon}{\beta a_0} \left(\frac{z}{\beta a_0}\right)^{(\alpha-1)} \times e^{\left[-\left(\frac{z}{\beta a_0}\right)^{\epsilon}\right]} \frac{1}{C}$ C: normalization constant so that $\int_0^\infty D(z)dz = 1$	$\sigma = \frac{\sigma_0}{C}\left[e^{(-10\frac{a}{a_0})} + C - 1 + \frac{a}{a_0} e^{(-10)}\right]$ for $\epsilon = 1$, $\alpha = 2$ and $\beta = 0.1$ ($C = 0.9995$)

the non-logarithmic functions of Table 2.1 and good approximations for the logarithmic ones (Figure 2b). The symbol n stands for the coefficient of asperities length statistical distribution. Statistical distributions characterized by many large asperities, such as singular and linear increasing, get low coefficients n, 1 and 2, respectively. On the contrary, distributions with many small asperities (linear decreasing and Weibull) are correctly approximated with relatively high coefficients n (4.7 and 9). Inversely, the distribution $D(z)$ can be found for a given stress/aperture function $\sigma(a)$. Differentiating Eq. (2.3) twice with respect to a yields:

$$\frac{\partial^2 \sigma(a)}{\partial a^2} = \frac{\sigma_0}{a} D(a) \tag{2.6}$$

For the general model assumed in Eq. (2.5), this yields:

$$\frac{\partial^2 \sigma(a)}{\partial a^2} = \sigma_0 \frac{n(n-1)}{a_0^2} \left(1 - \frac{a}{a_0}\right)^{n-2} \tag{2.7}$$

and the distribution $D(z)$ is obtained by equating Eqs. (2.6) and (2.7) and substituting a by z, so that:

$$D(z) = n(n-1) \frac{z}{a_0^2} \left(1 - \frac{z}{a_0}\right)^{n-2}, n \geq 1 \tag{2.8}$$

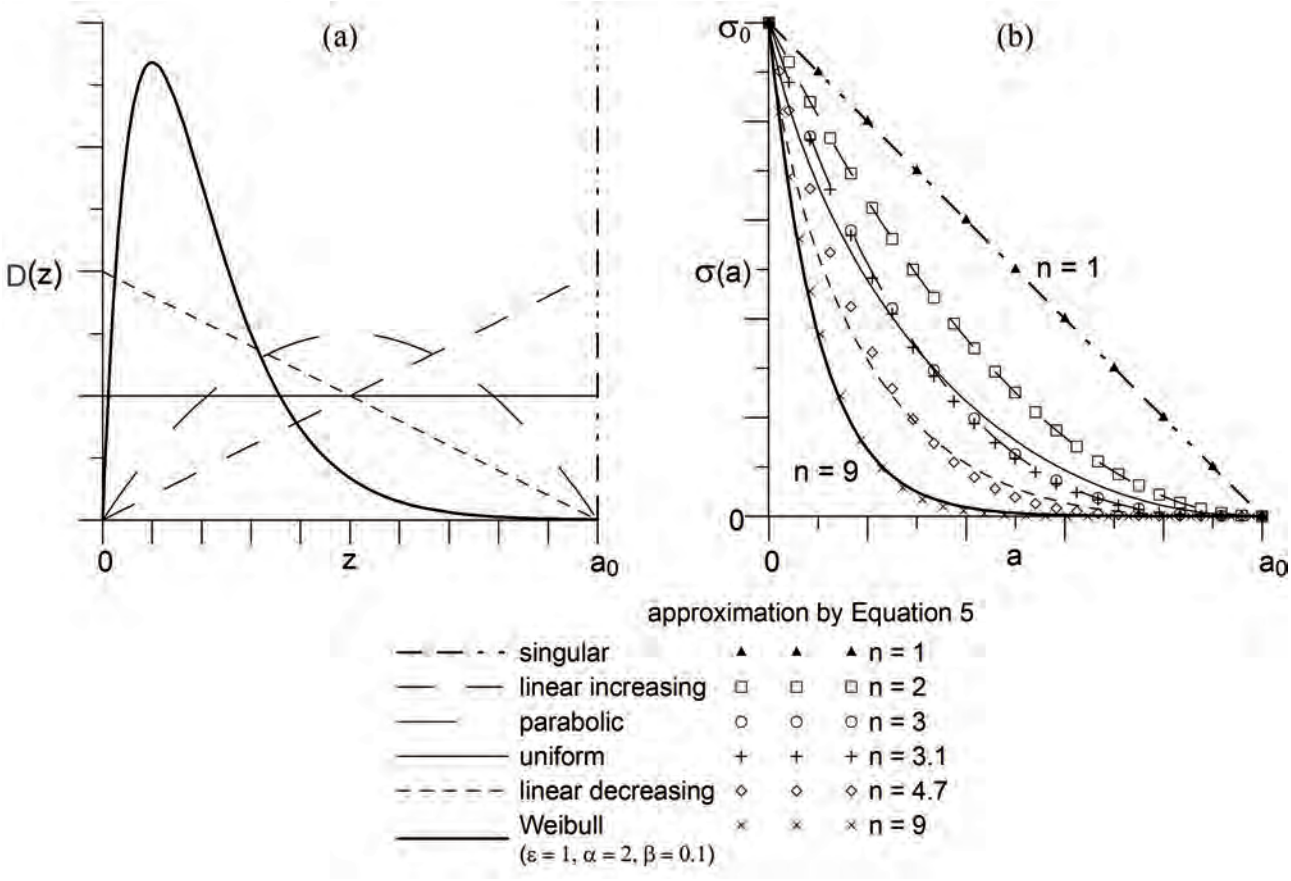

Figure 2.4: (a) Possible statistical continuous distributions of asperity length in a fracture, and (b) corresponding stress/aperture solutions, with their approximation by Eq. (2.5).

2.5 Relation with hydrodynamic parameters

Because of the saturated flow conditions considered in this work (i.e. fractures are completely filled by water exerting the pressure p), the normal effective stress σ' is taken into account instead of the normal total stress σ. In the case of lithostatic stress conditions $\sigma_z = \rho_r g Z$ and in the absence of shear stresses, the resulting effective stress σ' acting perpendicularly at a depth Z on a given fracture plane is obtained by:

$$\begin{aligned} \sigma' &= \boldsymbol{\sigma}\mathbf{n}\cdot\mathbf{n} - \alpha p\,, \quad \boldsymbol{\sigma} = \begin{bmatrix} \sigma_z\lambda & 0 & 0 \\ 0 & \sigma_z\lambda & 0 \\ 0 & 0 & \sigma_z \end{bmatrix} \\ &= \rho_r g Z(\lambda n_x^2 + \lambda n_y^2 + n_z^2) - \alpha\rho_w g h \end{aligned} \tag{2.9}$$

where ρ_r is the rock mass density, g is the gravitational acceleration, n_x,n_y,n_z are the components of the unit vector $\mathbf{n}$ normal to the fracture plane, ρ_w is the water density, h is the pressure head, and α is the Biot-Willis coefficient. The λ coefficient is the ratio of horizontal to vertical stress.

Expressing Eq. (2.5) for the aperture a:

$$a = a_0 \left[1 - \left(\frac{\sigma'}{\sigma'_0} \right)^{\frac{1}{n}} \right] \tag{2.10}$$

and assuming the validity of the cubic law in the fractured rock, the stress-dependent permeability is:

$$k = \frac{fa^3}{12} = \frac{fa_0^3 \left[1 - \left(\frac{\sigma'}{\sigma'_0} \right)^{\frac{1}{n}} \right]^3}{12} \tag{2.11}$$

yielding the hydraulic conductivity parallel to fracture plane:

$$K = K_0 \left[1 - \left(\frac{\sigma'}{\sigma'_0} \right)^{\frac{1}{n}} \right]^3 \tag{2.12}$$

where:

$$K_0 = \frac{\rho_w g}{\mu_w} \frac{fa_0^3}{12} \tag{2.13}$$

with a maximum K_0 for $\sigma' = 0$. The symbol $f = N_f/d$ is the frequency of the fracture family, namely the number of fractures N_f counted over a distance d, and μ_w is water dynamic viscosity. Note that Eq. (2.12) is very similar to the constitutive models proposed by [26, 23]. The same model function was found by [16] via a different approach. Eq. (2.12) can be used to compute the equivalent macroscopic hydraulic conductivity tensor of a rock mass intersected by m fracture families using the tensor summation:

$$\mathbf{K} = \sum_{i=1}^{m} K_{0_i} \left[1 - \left(\frac{\sigma'_i}{\sigma'_{0_i}} \right)^{\frac{1}{n_i}} \right]^3 (\mathbf{I} - \mathbf{n}_i \otimes \mathbf{n}_i) \tag{2.14}$$

For each fracture family i, K_{0_i} is the maximum parallel hydraulic conductivity, σ'_i is the normal effective stress, σ'_{0_i} is the fracture closure normal stress, n_i relates to the asperity distribution, $\mathbf{I}$ is the identity matrix, $\mathbf{n}_i$ is the unit vector normal to the fracture family i, and $\otimes$ denotes a tensor product.

If the contribution of the rock matrix is neglected, the porosity ϕ of the fractured rock mass is:

$$\phi = \sum_{i=1}^{m} f_i a_i \tag{2.15}$$

Introducing Eq. (2.10) into Eq. (2.15), a stress-dependent porosity is obtained:

$$\phi = \sum_{i=1}^{m} \phi_{0_i} \left[1 - \left(\frac{\sigma'_i}{\sigma'_{0_i}} \right)^{\frac{1}{n_i}} \right] \tag{2.16}$$

Neglecting the contribution of the rock matrix, Eq. (2.16) can be introduced in the definition

of the specific storage coefficient, S_s:

$$\begin{aligned} S_s &= \frac{\rho_w g \phi}{E_w} \\ S_s &= \sum_{i=1}^{m} S_{s_{0_i}} \left[1 - \left(\frac{\sigma'_i}{\sigma'_{0_i}} \right)^{\frac{1}{n_i}} \right]; \\ S_{s_{0_i}} &= \frac{\rho_w g \phi_{0_i}}{E_w} \end{aligned} \tag{2.17}$$

where ϕ_0 and S_{s_0} are the maximum fracture porosity and maximum specific storage coefficient, respectively. Eq. (2.16) can be used to determine, for each fracture family i, the vertical variation in fracture porosity, $\Delta\phi$, due to a change in effective stress, between an initial and a successive hydrogeological state at elevation z:

$$\begin{aligned} \Delta\phi(z) &= \sum_{i=1}^{m} \left(\phi_{h_i} - \phi_{h_{s_i}} \right) n_{z_i} \\ &= \sum_{i=1}^{m} \phi_{0_i} \left[\left(\frac{\sigma'_{h_{s_i}}}{\sigma'_{0_i}} \right)^{\frac{1}{n_i}} - \left(\frac{\sigma'_{h_i}}{\sigma'_{0_i}} \right)^{\frac{1}{n_i}} \right] n_{z_i} \end{aligned} \tag{2.18}$$

where the symbols ϕ_h and ϕ_{h_s} stand for fracture porosity at an initial and at a successive pressure head state. The multiplication with the component n_z of the unit normal vector $\mathbf{n}$ is used to obtain the vertical change in fracture porosity. Integrating all the porosity changes in the vertical direction, from the bottom of the aquifer z_b to the top z_t, results in the local settlement:

$$T(x, y) = \int_{z_b}^{z_t} \Delta\phi(z)\, dz \tag{2.19}$$

Eq. (2.19) provides aquifer vertical consolidation ($T > 0$) under increasing effective stress and aquifer vertical expansion ($T < 0$) under decreasing effective stress. Finally, considering both the hydraulic conductivity and the specific storage coefficient as functions of effective stress results in the non-linear groundwater flow equation:

$$S_s(\sigma') \frac{\partial H}{\partial t} = \nabla \cdot (\mathbf{K}(\sigma') \nabla H) \quad ; \quad H = h + z \tag{2.20}$$

where H is the hydraulic head, $\mathbf{K}(\sigma')$ is the hydraulic conductivity tensor as expressed in Eq. (2.14), $S_s(\sigma')$ is the specific storage coefficient as expressed in Eq. (2.17), and t is time. The symbols h and z stand for the relative pressure and elevation head, respectively.

2.6 Comparison between simulated, experimental and field measured permeabilities

Eq. (2.12) is verified by comparison with stress-dependent permeabilities from Durham [14] and Cappa [7]. Laboratory tests carried out by Durham [14] showed the behavior of the permeability of a fracture sample, taken at approximately 3.8 km depth, when subjected to an increasing confining pressure (stress). Simulated permeabilities correspond well to those measured by Durham [14], especially for high stresses (Figure 2.5a; Chapter 2.8 Appendix). With experiments at shallow conditions, Cappa [7] investigated the pressure-dependent increase and decrease of fracture aperture. Results showed that fracture aperture is subjected to hysteresis process. Eq. (2.12) is used to fit the field data of Cappa [7] (Figure 2.5b), which for that example were transformed from aperture and water pressure to permeability and normal effective stress. Fitted parameters are given in the Chapter 2.8 Appendix. Also for this example, the model provides a good comparison between simulated and measured data. However, only the rising branch of the hysteresis curve, which corresponds to an increasing water pressure and a decreasing effective normal stress, is correctly simulated. This because considering constant fracture parameters between hydraulic loading and unloading implies that Eq. (2.12) is purely elastic and can not reproduce a hysteresis. In this case, simulated permeabilities will be the same for rising or falling effective normal stresses. In Figure 2.5b the hysteresis occurs because the tested rock does not exactly follow Hooke's law. However the variation of permeability is so low, that this phenomenon may be neglected at regional scale. Note that, numerical values of the coefficient of asperities length statistical distribution, n, and the fracture closure effective stress, σ'_0, can be obtained by calibration of Eq. (2.12) on measured stress-dependent permeability data, and applied for large scale analysis.

2.7 Illustrative examples

2.7.1 Response of a deep fracture permeability to ice load/unload

An example showing the response of fracture permeability to a glaciation using Eq. (2.11) is illustrated below. Two cases are tested: (1) elastic, and (2) inelastic.

The fracture is horizontal and intersects a crystalline stiff rock mass at a depth of 500 m. The glaciation takes 100'000 years with the peak at 50'000 years, and symmetry between the rising (loading) and retreating (unloading) phases. The vertical stress acting on the fracture results from the addition of the overburden stress and the stress induced by ice cover. This vertical stress is computed using Eq. (1.6), without the Poisson's ratio effect. Table 2.2 details parameter values, and Figure 2.6a shows the problem geometry. Note that in this theoretical example, the effect of water pressure in fracture porosity is not taken into account.

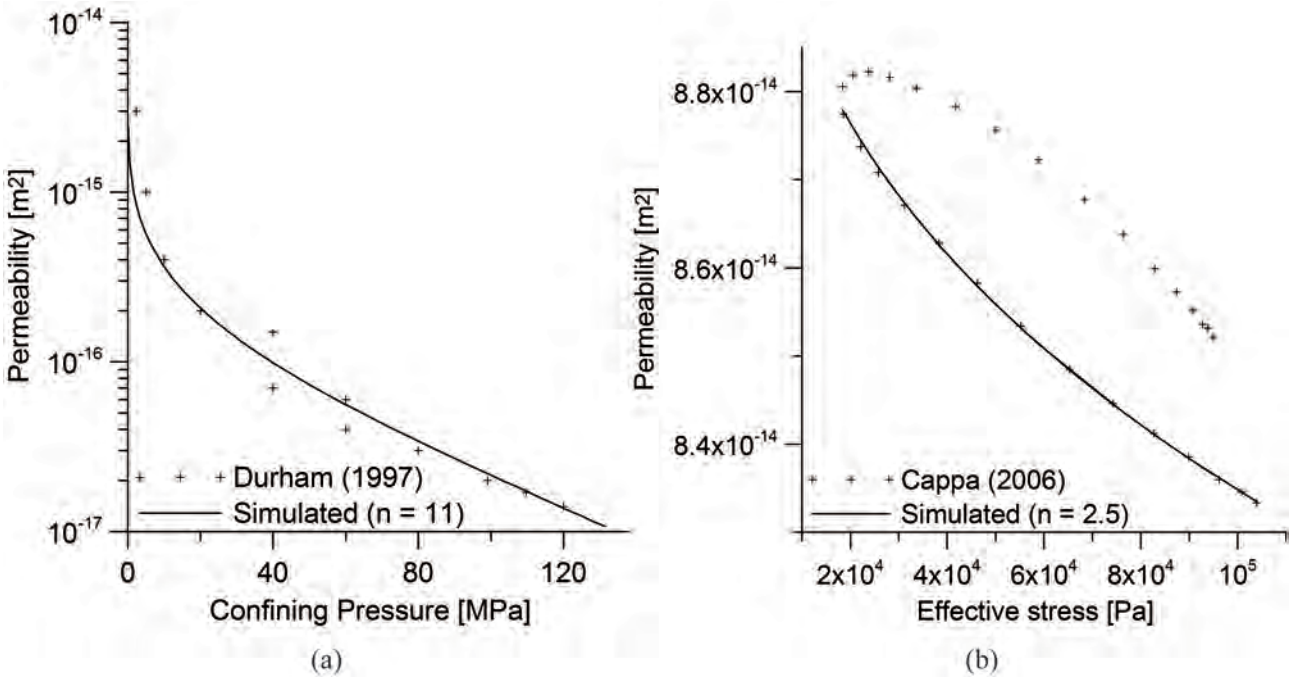

Figure 2.5: Verification of Eq. (2.12) model by comparison with stress-dependent fractured rock permeabilities of (a) Durham [14] and (b) Cappa [7].

Table 2.2: Parameter values used in the ice load/unload problem.

Parameter *Symbol*	**Unit**	**Value**
Fracture Depth Z	m	500
Rock Density ρ_r	kg m^{-3}	2700
Ice Density ρ_{ice}	kg m^{-3}	916.7
Gravitational Acceleration g	m s^{-2}	9.81
Vertical Stress due to the Overburden σ_v	MPa	13.2
No Stress Permeability k_0	m^2	$1.0 \cdot 10^{-11}$
Overburden Permeability $k(\sigma_v)$	m^2	$1.1 \cdot 10^{-12}$
Elastic Case		
Ice Loading and Unloading		
Fracture Closure Stress σ_0	MPa	100
Coefficient of asperities length statistical distribution n	-	3.1
Inelastic Case		
Ice Loading		
Fracture Closure Stress σ_0	MPa	100
Coefficient of asperities length statistical distribution n	-	3.1
Ice Unloading		
Fracture Closure Stress σ_0	MPa	144
Coefficient of asperities length statistical distribution n	-	4.7

Results and discussions

The permeability of the fracture decreases until the maximum ice cover (load), then increases during ice retreat (Figure 2.6b) . If the fracture behave elastically, the permeability returns to its initial value. If the fracture has been subject to inelastic deformations during the loading phase, the permeability can not return to its initial value. As indicated in section 1.4, this case

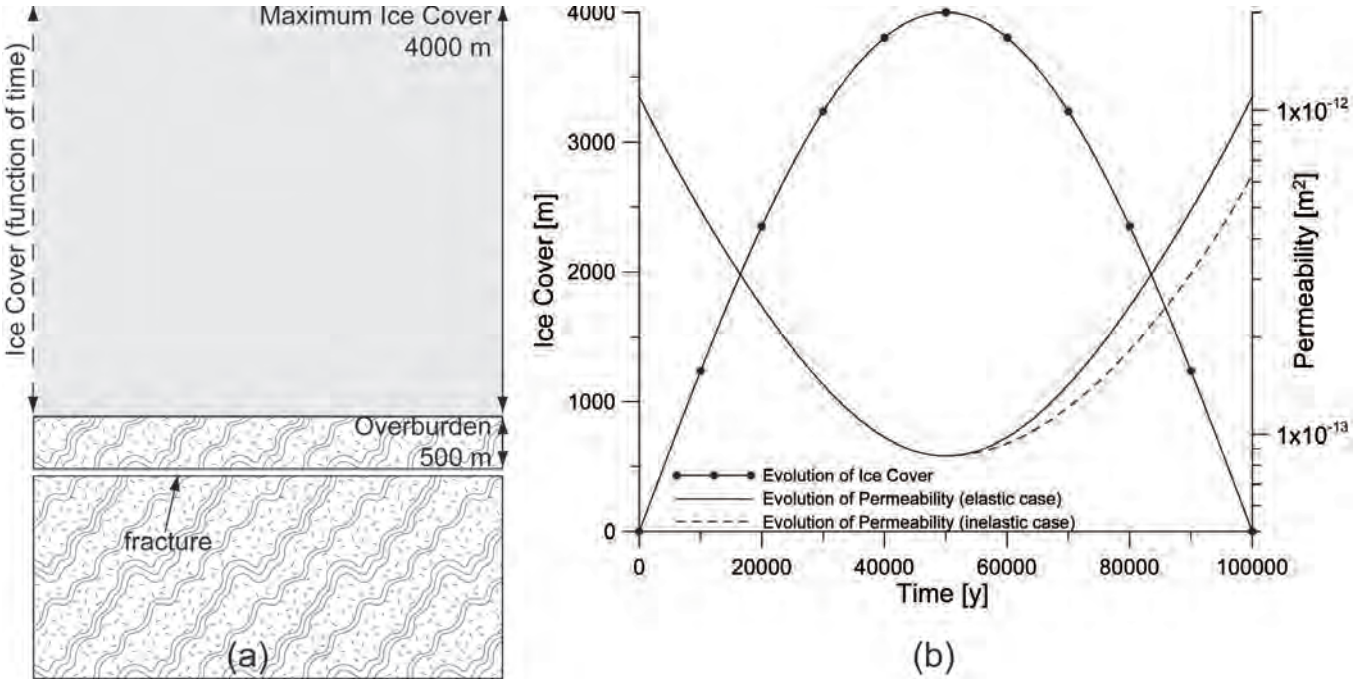

Figure 2.6: (a) Geometry for the ice loading/unloading problem, and (b) fracture permeability calculated with Eq. (2.11) as a function of time (ice cover), solid line: elastic case, dashed line: inelastic case.

needs a change in the numerical values of fracture parameters (σ_0 and n) involved in Eq. (2.11) (Table 2.2).

In such a case, the increase of n and σ_0 can be interpreted as a consequence of inelastic deformations: (1) if asperities length is decreased due to the loading phase, then n must change to a value characterizing a distribution with more short asperities, and therefore (2) the resistance of the fracture to high compression will increase.

The reversible rock-slope deformations investigated by [18] are due to seasonal variations of water table levels of about 100 m [24]. Glaciations can produce stresses from a column of ice of several thousands of meters. Within this context, it is highly probable that deep fractures are subject to inelastic non-recoverable deformations during ice load periods.

2.7.2 Fractured aquifer response to the excavation of a deep tunnel

Below follows a numerical example showing: (1) how simulation results vary, if the effect of effective stress on hydrodynamic parameters is taken into account; (2) the regional effects of the excavation of a deep tunnel on fractured aquifers. The before-developed stress-dependent equations are implemented in the multi-purpose Groundwater finite element software [9].

Steady state

At steady state and with stress-dependent hydraulic conductivity the flow equation is:

$$\nabla \cdot (\mathbf{K}(\sigma')\nabla H) = 0 \quad ; \quad H = h + z \tag{2.21}$$

The virtual model domain is a 2D vertical cross section representing an Alpine hydrogeological system composed of three geological formations, completely saturated with water, with different hydraulic properties (Figure 2.7; Chapter 2.8 Appendix). Numerical values used in the simulations are shown in the Chapter 2.8 Appendix, these are based on field investigations of the Emosson fractured rock mass (Switzerland), using the method described by Király [22]. In the Chapter 2.8 Appendix, K_{max} and K_{min} are the eigenvalues of the hydraulic conductivity tensor, and θ is the angle between the horizontal plane and the direction of K_{max}. The stress field is defined by vertical stresses $\sigma(z)$ set equal to the lithostatic pressure (the weight of overlying rocks above elevation z):

$$\sigma(z) = g \int_z^{z_t} \rho_r(u)\, du \tag{2.22}$$

In the present study horizontal stresses σ_x are 1.5 times stronger than vertical stresses. This

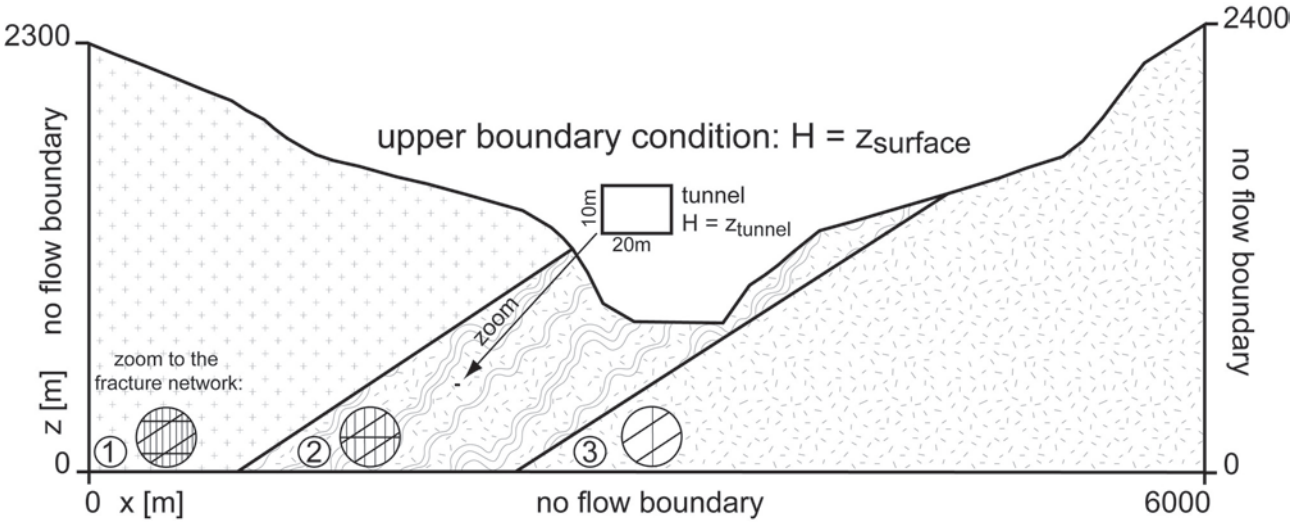

Figure 2.7: Model domain and boundary conditions; the hydrogeological system is composed of three rocks, each one exhibiting a different fracture network. Rock 2 is the most permeable, while rock 3 is the least. Three simulations are run for each statistical distribution of the asperities length: one without tunnel (natural system), one with tunnel, and finally one that simulates the aquifer consolidation.

applies well to orogenic belts or areas that have been glaciated, such as the Alps (see [29]). Before tunnel construction, a steady state flow is assumed from the highest points (crests) to the lowest points (valleys), by specifying boundary conditions at the domain surface as atmospheric pressure ($H = z$), and at other limits as no-flow conditions. Then, a tunnel is constructed. A constant atmospheric pressure is specified in the tunnel indicating that it behaves as a draining structure and consequently increases the effective stress which causes aquifer consolidation. Several simulations are computed to compare the present approach with the classical one neglecting the dependence of permeability on effective stress, and to study the influence of the coefficient n on discharge rates, pressure and consolidation distributions. Consolidation is computed between the initial state (without tunnel) and the disturbed state with perturbation caused by the tunnel (Figure 2.8). This illustrative model is directly inspired by real cases of fractured aquifer consolidation caused by tunnels excavation (see [25], and [45]).

Results and discussions for steady state

Results show that the introduction of stress-dependent permeabilities in Darcy's law leads to lower discharge rates, relative to the classical approach that only considers constant permeability, especially for high values of coefficient n (Figure 2.9a). This reduction in discharge rates is directly related to the variations of the hydraulic conductivity tensor in both strength and principal directions according to effective stresses. This spatial variation of hydraulic conductivity tensors also impacts the distribution and the magnitude of hydraulic heads, flow paths, flow velocities and transit times (Figures 2.8 and 2.9b). Overall permeabilities decrease in the deeper areas of the domain, while they tend toward the maximum near the surface. As previously mentioned, a high value of the coefficient n indicates a predominance of relatively small asperities. In such a case, the drop in permeability will be significant, because there are only a few large asperities to oppose the increase in normal effective stress. Compared to the classical approach, the impact of the tunnel on the system appears weaker when considering stress-dependent permeabilities. For the proposed method, the highest consolidation occurs in systems with an intermediate n value ($1 < n < 5$), because they are the most sensitive to pressure change with the largest porosity variation (Figure 2.9a). Fractured systems featuring large asperities are less affected by the process, because the asperities stop the closure. Overall, the magnitude of aquifer consolidation is low because the proposed method computes only elastic reversible deformations obeying Hooke's law, and acting on fracture network porosity. Moreover, boundary conditions specified at the domain surface provide unlimited water inflows that dampen aquifer depressurization.

Transient state

Eq. (2.20) is used to solve the transient groundwater flow problem having the same model domain, boundary conditions at the tunnel and hydrological parameters. The initial hydraulic heads are taken from the steady state model without tunnel. On the domain surface two different types of boundary conditions are tested: (1) constant atmospheric pressure ($H = z$); (2) no-flow condition. This no-flow condition could represent an aquifer filled with connate pore waters and isolated from recharge zones, or a confined aquifer suddenly cut-off from its recharge zone.

Results and discussions for transient state

For the first case where temporally constant atmospheric pressure hydraulic heads are specified at the domain surface, the initial and final discharge rates as well as the vertical settlements match those simulated by the steady state models. In transient state, the tunnel causes a hydraulic depressurization of the rock mass followed by gradual aquifer consolidation (Figure 2.10a). For the second case with sudden no-flow condition at the domain surface, the tunnel drainage empties the system, which gradually becomes hydrostatic. The recession curve of the water drained by the tunnel rapidly runs dry. In such a case, the magnitude of the aquifer

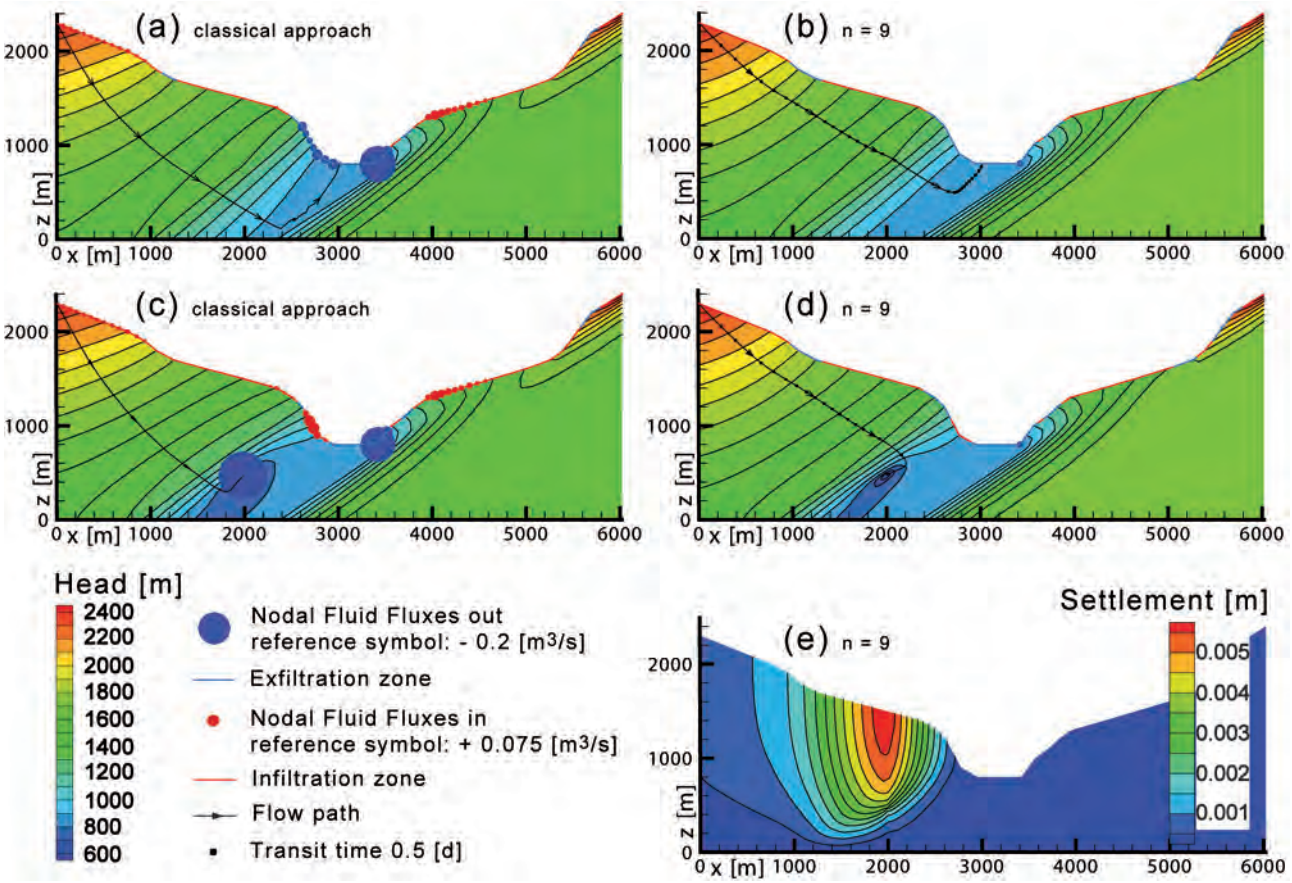

Figure 2.8: Hydraulic head, flow paths and infiltration/exfiltration fields for the classical approach, and for the Weibull distribution at initial conditions (a, b) and after the tunnel introduction (c, d). Note that, in (b) and (d) fluid fluxes are so much lower than in (a) and (c), that they are almost invisible. (e) Aquifer consolidation caused by the increase in effective stress following the tunnel construction (Weibull distribution).

consolidation increases because of the total depressurization of the system (Figure 2.10b). For the Weibull distribution ($n = 9$), which seems to be the more realistic for the description of real fractures, the fractured rock mass consolidation is (1) 5.8 mm in the case of constant recharge from surface (Figure 2.8e), and (2) 77.3 mm in the case of a total depressurization of the aquifer. In such a case, ground settlements can be problematic. Overall, the transient state is relatively fast because there is no release of water from the rock matrix, assumed impervious.

2.8 Conclusions

A model function relating fracture permeability to effective stress is derived from Hooke's law of elasticity and from the statistical distribution of asperity lengths. This model function is then implemented in the tensor form of Darcy's law, and its effects are assessed in simulations. Taking into account the sensitivity of permeabilities to depth and water pressure, this non-linear approach gains in phenomenology and is closer to physical reality, compared to classical approaches that neglect pressure-dependent permeability and porosity fields. From a general point of view, numerical simulations of deep tunnels considering the decrease in permeability

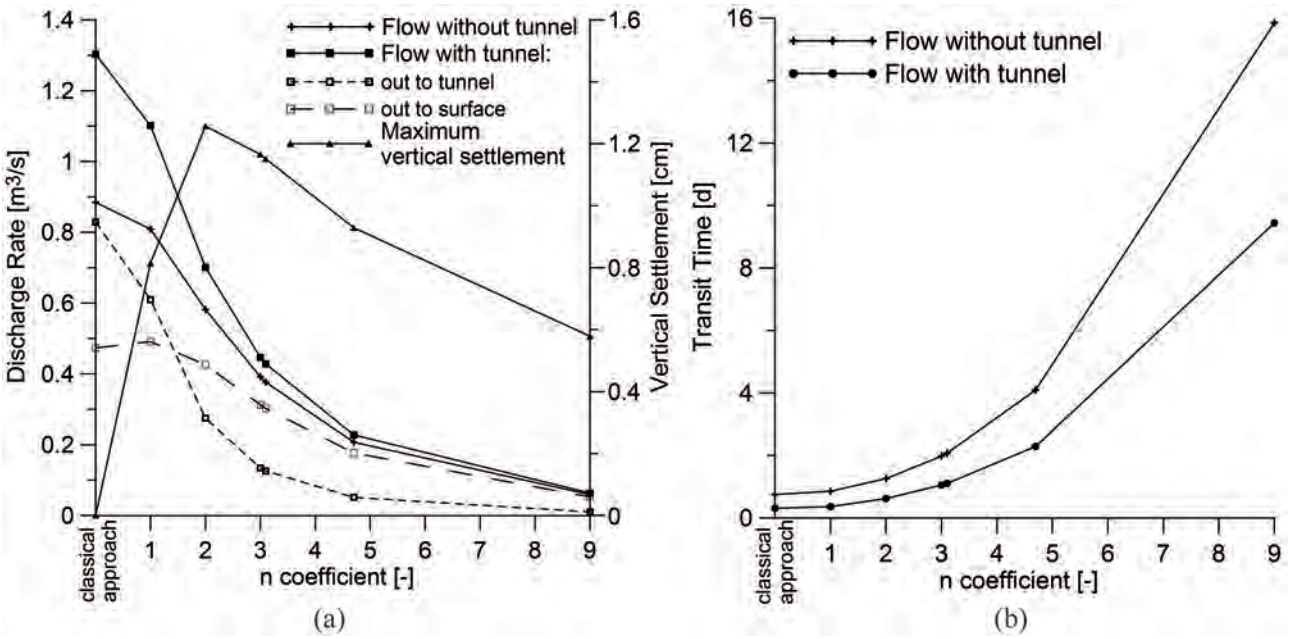

Figure 2.9: (a) Discharge rates, vertical settlement and (b) transit time as a function of coefficient n, and comparison with the classical approach for steady state flow before and after the tunnel construction. For transit time the particle is released at coordinates $x = 0$ and $z = 2300$, and exits: (1) at the bottom of the valley (without tunnel); (2) at the tunnel (particle tracks are shown in Figure 2.8 for the classical approach and for the Weibull distribution).

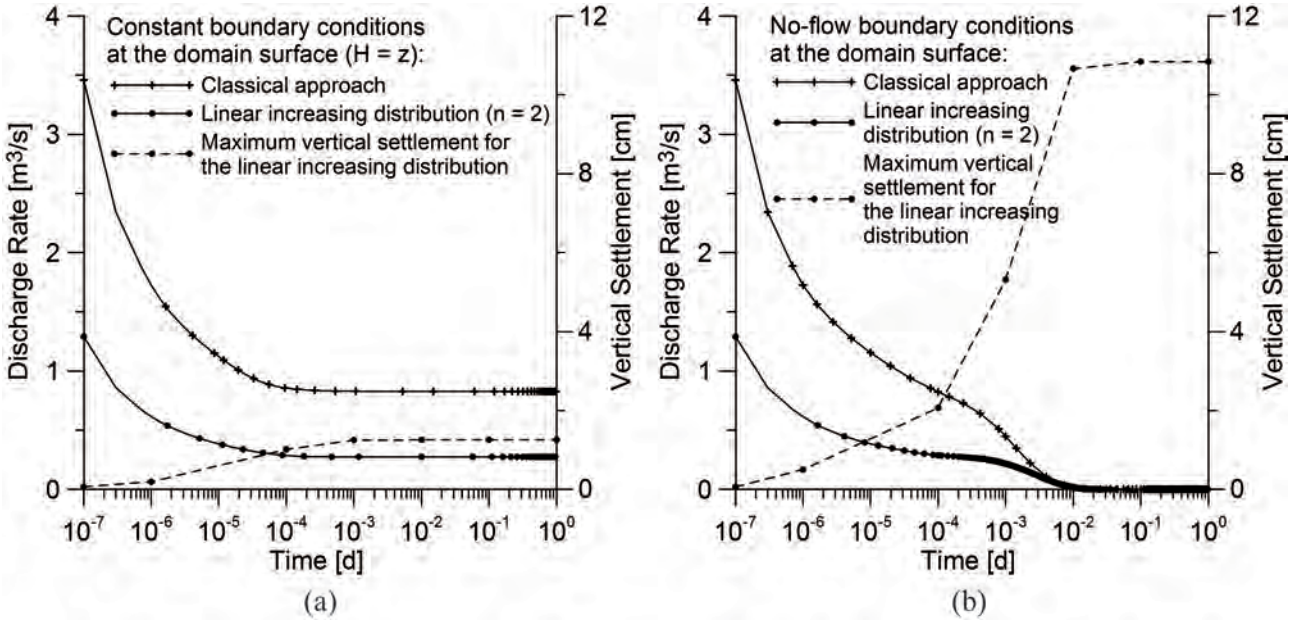

Figure 2.10: Evolution of the discharge rate drained by the tunnel (for the classical approach and the linear increasing distribution, solid lines), and of the maximum vertical settlement (for the linear increasing distribution, dashed line) as a function of time for (a) constant hydraulic head at the domain surface; (b) no-flow condition at the domain surface.

with increasing effective stress generate lower discharge rates. This theoretical observation goes in the line of safety in terms of problems related to groundwater inflow in underground excavations. In case of strong decrease in water pressures a non-negligible consolidation occurs,

even when flow is assumed in the fractures only. This can produce foundation instabilities of structures located at the surface, especially in the case of differential consolidation due to aquifer heterogeneity, and in the presence of heavy structures such as dams (see [25]). The changes in fracture permeability, porosity and specific storage in response to changes in effective stresses depend on, among other factors, the statistical distribution of asperity lengths, indicating the relative ratio of large to small asperities. For example, in the case of increasing effective stresses, a fracture characterized by a high ratio of large to small asperities (small n), will have a lower change in permeability than a fracture with a small ratio (high n). Overall, the limitation of the classical method is that it cannot compute aquifer consolidation, because no change in fracture porosity or permeability with pressure head variation is accounted for. On the contrary, with the proposed approach, a pressure head variation causing fracture porosity to change can be directly translated into aquifer consolidation (decreasing pressure) or expansion (increasing pressure).

Chapter 2 Appendix: Used values

	Fig. 2.5a	Fig. 2.5b	Illustration	Simulation	
			Rock 1	Rock 2	Rock 3
m [-]	1	1	3	3	2
a_{0_1} [mm]	-	0.1	0.5	0.5	0.5
a_{0_2} [mm]			1.2	1.92	1.2
a_{0_3} [mm]			1.0	1.63	
f_1 [m^{-1}]	-	1	5.44	3.27	0.1
f_2 [m^{-1}]			0.71	0.71	0.5
f_3 [m^{-1}]			1.00	0.01	
K_{max} [m s^{-1}]			$1.56 \cdot 10^{-3}$	$3.77 \cdot 10^{-3}$	$6.31 \cdot 10^{-4}$
K_{min} [m s^{-1}]			$5.47 \cdot 10^{-4}$	$2.1 \cdot 10^{-4}$	$6.1 \cdot 10^{-6}$
θ [°]			27	36	34
k_0 [m^2]	$1.72 \cdot 10^{-14}$	$9.24 \cdot 10^{-14}$	-	-	-
σ'_0 [MPa]	350	495	350	300	325
n [-]	11	2.5	variable	variable	variable
ρ_r [kg m^{-3}]	-	2400	2800	2200	2500
n_x, n_y, n_z [-]	-	[1,0,0]	[1,0,0]	[1,0,0]	[1,0,0]
			[-0.555,0,0.832]	[-0.555,0,0.832]	[-0.555,0,0.832]
			[0,0,1]	[0,0,1]	
λ [-]	-	0.41	1.5	1.5	1.5
Z [m]	-	15	-	-	-

Bibliography

[1] Abaqus: Abaqus theory manual, version 6.8. Systèmes Simulia Corp., Providence, RI, USA (2008)

[2] Berkowitz, B.: Characterizing flow and transport in fractured geological media: A review. Advances in Water Resources **25**(8–12), 861–884 (2002)

[3] Bordet, C.: L'eau dans les massifs rocheux fissurés. Observations dans les travaux souterrains. Tech. rep., Université de Liège, Liège, BEL (1971)

[4] Boutt, D., Diggins, P., Mabee, S.: A field study (Massachusetts, USA) of the factors controlling the depth of groundwater flow systems in crystalline fractured-rock terrain. Hydrogeology Journal **18**(8), 1839–1854 (2010)

[5] Brown, S.: Simple mathematical model of a rough fracture. J. Geophys. Res **100**(B4), 5941–5952 (1995)

[6] Bundschuh, J., Arriaga, M.: Introduction to the Numerical Modeling of Groundwater and Geothermal Systems, chap. Rock and fluid, pp. 13–100. Taylor & Francis Group, CRC Press (2010)

[7] Cappa, F.: Role of fluids in the hydromechanical behavior of heterogeneous fractured rocks: in situ characterization and numerical modelling. Bull. Eng. Geol. Env. **65**, 321–337 (2006)

[8] COMSOL-Multiphysics: Multiphysics user's guide. COMSOL AB, Sweden (2010)

[9] Cornaton, F.J.: Ground Water: a 3-D Ground Water and Surface Water Flow, Mass Transport and Heat Transfer Finite Element Simulator, Reference Manual, 398 pp. Centre for Hydrogeology and Geothermics, Neuchâtel, Switzerland (2007)

[10] Dershowitz, W., Busse, R., Geier, J.: A stochastic approach for fracture set definition. In: 2nd North American Rock Mechanics Symposium, June 19 - 21, 1996 , Montreal, Quebec, Canada. American Rock Mechanics Association (1996)

[11] Dershowitz, W., Lee, G., Geier, J., Foxford, T., LaPointe, P., Thomas, A.: FracMan - interactive discrete feature data analysis, geometric modeling, and exploration simulation: User Documentation. Golder Associates Inc., Seattle, USA (1998)

[12] Devenoges, Q.: Relations entre le lac de Salanfe et le Val d'Illiez: Fracturation et Tenseurs de Perméabilité appliqués à la modélisation 3D Géologique et Hydrogéologique. Master's thesis, Centre for Hydrogeology and Geothermics, University of Neuchâtel, Neuchâtel, Switzerland (2012)

[13] Dupont, E.: Etude de la Fracturation et des Ecoulements dans le socle cristallin du Massif des Aiguilles Rouges. Master's thesis, Centre for Hydrogeology and Geothermics, University of Neuchâtel, Neuchâtel, Switzerland (2012)

[14] Durham, W.B.: Laboratory observations of the hydraulic behavior of a permeable fracture from 3800 m depth in the KTB pilot hole. J. Geophys. Res. **102**, 18,405–18,416 (1997)

[15] Ferronato, M., Gambolati, G., Janna, C., Teatini, P.: Geomechanical issues of anthropogenic CO2 sequestration in exploited gas fields. Energy Conversion and Management **51**(10), 1918–1928 (2010)

[16] Gangi, A.F.: Variation of whole and fractured porous rock permeability with confining pressure. Int. J. Rock Mech. Min. Sci. Geomech. Abstr. **15**(5), 249–257 (1978)

[17] Glover, P., Matsuki, K., R., H., K., H.: Synthetic rough fractures in rocks. J. Geophys. Res. **103**(B5), 9609–9620 (1998)

[18] Hansmann, J., Loew, S., Evans, K.: Reversible rock-slope deformations caused by cyclic water-table fluctuations in mountain slopes of the Central Alps, Switzerland. Hydrogeology Journal **20**(1), 73–91 (2012)

[19] Hopkins, D.: The implications of joint deformation in analyzing the properties and behavior of fractured rock masses, underground excavations and faults. Int. J. Rock Mech. Min. Sci. Geomech. Abstr. **37**(1–2), 175–202 (2000)

[20] Itasca: UDEC Universal distinct element code. Itasca Consulting Group Inc., Minneapolis, USA (2006)

[21] Király, L.: Anisotropy and heterogeneity within jointed limestone. Eclogae Geologicae Helvetiae **62**(2), 613–619 (1969)

[22] Király, L.: Statistical analysis of fractures (orientation and density). International Journal of Earth Sciences **59**(1), 125–151 (1969)

[23] Li, S.Q., Xu, B.Y., Duan, Y.G.: Coupling seepage of liquid and solid in fractured reservoir. Chin. J. Comp. Mech. **18**(2), 133–137 (2001)

[24] Loew, S., Hansmann, J.: Annual opening and closure of alpine valleys. In: Conference. Centre for Hydrogeology and Geothermics, Neuchâtel (2010)

[25] Lombardi, G.: Les tassements exceptionnels au barrage de Zeuzier. Publ. Swiss Soc. Soil Rock Mech. **118**, 39–47 (1988)

[26] Lombardi, G.: The FES rock mass model - Part one. Dam Engineering **3**, 201–221 (1992)

[27] Londe, P.: The Malpasset dam failure. Eng. Geol. **24**(1–4), 295–329 (1987)

[28] Louis, C.: A study of groundwater flow in jointed rock and its influence on the stability of rock masses. Tech. Rep. 9, Rock Mechanics, Imperial College, London, UK (1969)

[29] Mayeur, B., Fabre, D.: Measurement and modeling of natural stresses. Application to the Maurienne-Ambin tunnel project. Bulletin of Engineering Geology and the Environment **58**(1), 45–59 (1999)

[30] Murdoch, L., Germanovich, L.: Analysis of a deformable fracture in permeable material. International Journal for Numerical and Analytical Methods in Geomechanics **30**(6), 529–561 (2006)

[31] National Research Council: Rock fractures and fluid flow, chap. Hydraulic and tracer testing of fractured rocks, pp. 243–286. National Academy Press, Washington D.C., U.S.A. (1996)

[32] Neuman, S.P.: Trends, prospects and challenges in quantifying flow and transport through fractured rocks. Hydrogeology Journal **13**(1), 124–147 (2005)

[33] Preisig, G., Cornaton, F., Perrochet, P.: Regional Flow Simulation in Fractured Aquifers Using Stress-Dependent Parameters. Ground Water **50**(3), 376–385 (2012)

[34] Priest, S.: Discontinuity Analysis for Rock Engineering. Chapman and Hall, London, U.K. (1994)

[35] Priest, S.: Determination of discontinuity size distributions from scanline data. Rock Mech. Rock Eng. **37**(5), 347–368 (2004)

[36] Priest, S., Hudson, J.: Estimation of discontinuity space and trace length using scanline survey. Rock Mech. Min. Sci. Geomech. Abs. **18**, 183–197 (1981)

[37] Rutqvist, J., Stephansson, O.: A cyclic hydraulic jacking test to determine the in situ stress normal to a fracture. Int. J. Rock Mech. Min. Sci. Geomech. Abstr **33**(7), 695–711 (1996)

[38] Rutqvist, J., Wu, Y.S., Tsang, C.F., Bodvarsson, G.: A modeling approach for analysis of coupled multiphase fluid flow, heat transfer, and deformation in fractured porous rock. Int. J. Rock Mech. Min. Sci. **39**(4), 429–442 (2002)

[39] Schweisinger, T., Svenson, E., Murdoch, L.: Introduction to hydromechanical well tests in fractured rock aquifers. Ground Water **47**(1), 69–79 (2009)

[40] Suárez, M.: Modelo Conceptual Integrado del Yacimiento Geotérmico de Los Humeros, Puebla. Rep. Tech. rep., GPG-CFE, Morelia, Mich., México (1995)

[41] Terzaghi, K.: Die berechnung der durchlässigkeitziffer des tones aus dem verlauf der hydrodynamischen spannungserscheinungen. Akad Wissensch Wien Sitzungsber Mathnaturwissensch Klasse IIa **142**(3–4), 125–138 (1923)

[42] Tsang, Y., Witherspoon, P.: Hydromechanical behavior of a deformable rock fracture subject to normal stress. J. Geophys. Res. **86**(B10), 9287–9298 (1981)

[43] Walsh, J.B.: Effect of pore pressure and confining pressure on fracture permeability. Int. J. Rock Mech. Min. Sci. Geomech. Abstr. **18**, 429–435 (1981)

[44] Zace-Service-Ltd.: Z-Soil.PC. Zace Service Consulting Group, Lausanne, Switzerland (2010)

[45] Zangerl, C., Eberhardt, E., Loew, S.: Ground settlements above tunnels in fractured crystalline rock: numerical analysis of coupled hydromechanical mechanisms. Hydrogeology Journal **11**, 162–173 (2003)

Chapter 3

Constitutive model functions relating effective stress to hydrodynamic parameters in granular porous aquifers *

Abstract

Changes in effective stress due to water pressure variations modify the intrinsic hydrodynamic properties of aquifers and aquitards. Overexploited groundwater systems, such as basins with heavy pumping, are subject to non-recoverable modifications. This results in a loss of permeability, porosity and specific storage due to system consolidation. This Chapter presents the analytical development of model functions relating effective stress to hydrodynamic parameters for aquifers and aquitards constituted of unconsolidated/consolidated granular sediments. The stress-dependent function were fit to laboratory data, and used in the modelling approach suggested in Chapter 4. Based on only few unknowns, this approach is computationally simple, efficiently captures the hydromechanical processes active in regional aquifer systems under stress, readily provides an estimate of their consolidation.

3.1 Introduction

Hydrodynamic parameters, such as hydraulic conductivity, porosity and specific storage, depend on effective stress [28, 18, 14, 38, 24, 12]. However, governing equations used for regional analysis of aquifer systems, in general consider hydrodynamic parameters as stress-independent constants [10, 29]. This assumption is acceptable for shallow aquifers and for incompressible lithologies. However, there can be significant change in hydrodynamic parameters in deep and confined units subject to consolidation.

As defined by Terzaghi [34, 35], effective stress describes the stress state of a saturated

*This Chapter is based on the paper:
Preisig, G., Cornaton, F.J., Perrochet, P.: Regional Flow and Deformation Analysis of Basin-Fill Aquifer Systems using Stress-Dependent Parameters. Accepted for publication in Ground Water.

porous rock, and results from the load of principal stress on contacting grains and from water pressure in voids, which bears a part of the load [4]. An increase of effective stress can result from (1) an increase of principal stress or (2) a decrease in water pressure. Both can lead to a reduction in porosity, and consequently in hydraulic conductivity and specific storage. These relationships are of an exponential type [10], and for coarse-grained aquifers are reversible only in the case of elastic small strains (voids closure/opening) [1, 15].

In earth sciences, many processes relate to changes in effective stress and hydrodynamic parameters. In hydrogeology, the decrease of hydraulic head due to groundwater pumping results in porosity reduction in aquifers and aquitards and causes land subsidence [20, 16, 19, 12], as well as a reduction in well productivity due to the decrease in reservoir permeability with the compaction. This last consequence is well known in petroleum engineering [30]. In geological engineering, the drilling of tunnels through porous units causes, among other responses, ground settlement [27, 39]. On the other hand, ground uplift is recorded in areas subjected to fluid injection for geothermal energy production or CO_2 sequestration [33, 11]. Finally, proposals regions for geologic radioactive waste repositories must be aware of such processes, which in the long term, can lead to brittle deformation. For granular porous media, model functions relating effective stress to hydrodynamic parameters can be developed from two main theoretical approaches: (1) functions based on the size changes of solid grains (Hertzian theory of deformation of spheres) [14], and (2) functions based on volumetric deformation of the bulk volume, i.e. grains and voids [24]. The deformation resulting from the change of the bulk volume is substantially greater than that derived from the compression of grains [24].

Two main methods are used for analysis of groundwater flow in a deformable aquifer system: (1) non-simultaneous analysis between groundwater flow (water pressures) and aquifer deformation, e.g., Jacob's approach [20, 21], and (2) simultaneous analysis, e.g., Biot's poroelastic theory [2]. Both approaches generally consider hydrodynamic parameters, in particular hydraulic conductivity and storage, as constants [10, 29]. In Jacob's approach [20, 21], groundwater flow and deformation equations are partially coupled via the specific storage coefficient. In Biot's poroelasticity theory [2] equations are fully coupled via the volumetric strain, which allows detailed simultaneous investigation of groundwater flow in a 3D deformable porous medium. However, the complexity of the governing equations and the large number of unknown parameters limits its use to local scales and simple geological geometries [23, 22, 12]. For a detailed review of the analysis and simulation of groundwater flow in deformable aquifer systems see Gambolati et al. [13], Verruijt [37] and Galloway and Burbey [12].

Regional simulation of coupled hydromechanical processes considering detailed geological structures typically requires simplification of governing algorithms. The aim of this Chapter is to develop practical model functions relating effective stress to hydrodynamic parameters specific to granular porous media, which can be used in the modelling approach presented in Chapter 4.

This Chapter is organized as follows. First, the main hydrodynamic parameters (hydraulic conductivity, porosity and specific storage) are linked to effective stress by means of analyt-

ical development. Then the modelling approach discussed in Chapter 4 using the equations developed in this Chapter, is verified by a comparison with the Biot's poroelasticity theory.

Chapter 6 will focus on regional simulation of the Mexico City basin using the approach discussed herein. Note that, in this work, the terms consolidation and compaction are treated as synonyms and express the reduction in porosity and vertical aquifer thickness due to an increase in effective stress.

3.2 Effective stress-dependent equations in granular porous media

Granular porous media are formed of fine (clays and silts) and coarse (sand and gravel) grained materials. Aquifers are composed mainly of coarse-grained materials, while aquitards are composed of silts and clays (Figure 3.1a). A Quaternary sedimentary basin is filled by spatial and temporal succession (sequential stratigraphy) and consists of several aquifers separated by areally extensive aquitards [17]. In both aquifers and aquitards, groundwater flow is Darcian. However, as described by Helm (1975) [17], in aquitards groundwater flow is primarily vertical and very slow compared to the flow in aquifers. In such a case, aquitards can be conceptualised as doubly draining units. In this work, the term "aquifer system" refers to the vertical and horizontal succession of aquifers, aquitards and confining units.

For elastic small strains, coarse-grained aquifers can be treated as Hookean materials [20, 21]. In Hookean materials, the change in porosity, hydraulic conductivity and specific storage caused by increasing or decreasing effective stresses is reversible (elastic). Conversely, fine-grained materials are subject to non-reversible deformations, and when consolidated only a portion of the loss in porosity is recoverable [17, 12]. Thus two or more different model functions have to be used to reproduce one or more cycles of compression / expansion due to changes in applied effective stresses.

At the regional scale, land subsidence results from the complex and differential consolidation (in terms of time and location) of aquifers and aquitards constituting the aquifer system [12] (Figure 3.1b).

In sedimentary basins and in the absence of tectonic stresses, the principal stress is the vertical component of the total stress tensor: $\sigma_v = \sigma_{zz}$. This corresponds to the weight of the overburden and increases with depth Z. The compression of sediments under the vertical stress induces horizontal stresses of equal magnitude $\sigma_h = \sigma_{xx} = \sigma_{yy}$ [31, 32]. Under these conditions, the effective stress tensor $\boldsymbol{\sigma'}$ is expressed as:

$$\begin{aligned} \boldsymbol{\sigma'} &= \boldsymbol{\sigma} - \boldsymbol{\alpha_b}\, p \\ \begin{bmatrix} \sigma'_{xx} & \sigma'_{xy} & \sigma'_{xz} \\ \sigma'_{yx} & \sigma'_{yy} & \sigma'_{yz} \\ \sigma'_{zx} & \sigma'_{zy} & \sigma'_{zz} \end{bmatrix} &= \begin{bmatrix} \lambda\sigma_{xx} & \sigma_{xy} & \sigma_{xz} \\ \sigma_{yx} & \lambda\sigma_{yy} & \sigma_{yz} \\ \sigma_{zx} & \sigma_{zy} & \sigma_{zz} \end{bmatrix} - \begin{bmatrix} \alpha_b & 0 & 0 \\ 0 & \alpha_b & 0 \\ 0 & 0 & \alpha_b \end{bmatrix} \rho_w g h \end{aligned} \tag{3.1}$$

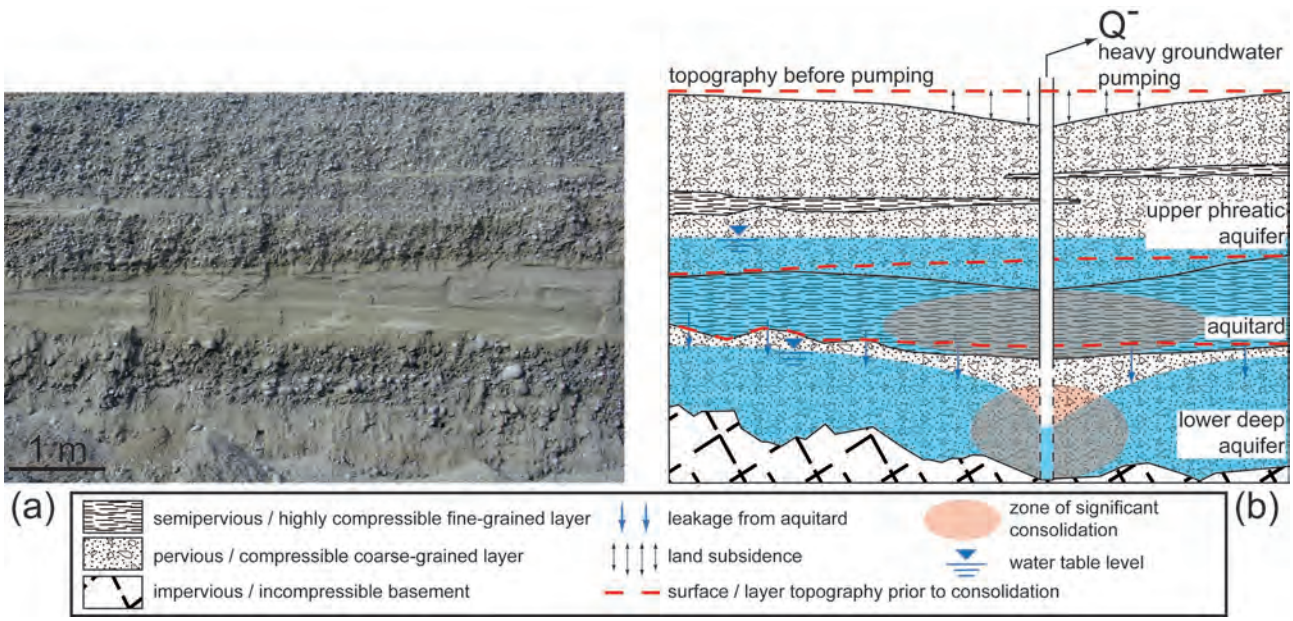

Figure 3.1: (a) Picture showing a sedimentary Quaternary sequence of two coarse-grained strata, separated and interbedded by fine-grained layers (Seeland aquifer system, Switzerland). (b) Illustrative section, based on the left-picture, showing a regional aquifer system affected by land subsidence because of the consolidation of both (1) a leaking aquitard and (2) a heavily pumped aquifer.

where $\boldsymbol{\sigma}$ and $\boldsymbol{\alpha_b}$ are the total stress and the Biot-Willis coefficient tensors, p is water pressure, ρ_w is water density, g is gravitational acceleration, h is pressure head, and λ expresses the ratio of horizontal to vertical stress: $\lambda = \sigma_h/\sigma_v$. The Biot-Willis coefficient expresses the ratio of pore volume change to total bulk volume change: if there are no pores then $\alpha_b \approx 0$, and if the total bulk volume change depends only on pore volume change then $\alpha_b \approx 1$ [4]. From Eq. (1.1), it follows that the effective shear stresses, non-diagonal terms of $\boldsymbol{\sigma'}$, correspond to those of the stress tensor $\boldsymbol{\sigma}$, because water can not support shear stresses [12].

At the afore-mentioned overburden stress conditions and assuming isotropy: (1) the weight of the overlying geological materials above elevation z corresponds to $\sigma_v = g \int_z^{z_t} \rho_r(u)\, du$, where ρ_r is the wet density of the granular material at a given elevation, and z_t is the top (surface) elevation; and (2) λ depends only on the Poisson's ratio: $\lambda = \nu/(1-\nu)$.

At the regional scale, the deformation of an aquifer system is essentially vertical. The value of horizontal strains is much lower, and may be difficult to detect. However, at the local scale, horizontal strains may be large, such as close to an abrupt inflection of the basement topography [12]. Despite this, in regional analysis, it is reasonable to neglect horizontal deformation. Moreover, assuming that the vertical deformation (vertical change of the bulk volume) is exclusively driven by the change in porosity due to the shifting of incompressible solid grains, i.e., no deformation of the solid volume V_s, yields:

$$\begin{aligned} dV_s &= d\left[(1-\phi)V\right] = 0 \\ -V\, d\phi + (1-\phi)\, dV &= 0 \\ \frac{dV}{V} &= \frac{d\phi}{(1-\phi)} \end{aligned} \tag{3.2}$$

and associating Eq. (3.2) with the law of elasticity for small strains induced by changes in effective stress, yields:

$$d\epsilon_v = \frac{dV}{V} = \frac{d\phi}{(1-\phi)} = -\frac{1}{E} d\sigma' \tag{3.3}$$

where ϵ_v is the vertical deformation, V is the bulk volume, ϕ is the porosity, and E is the formation vertical elasticity coefficient under fully saturated conditions (reciprocal of the vertical compressibility coefficient). Figure 3.2 illustrates the above concept. In this Figure, V_v is the void volume. The porosity at no stress is the fraction of the void volume over the bulk volume at no stress $\phi_0 = V_{v_1}/V_1$.

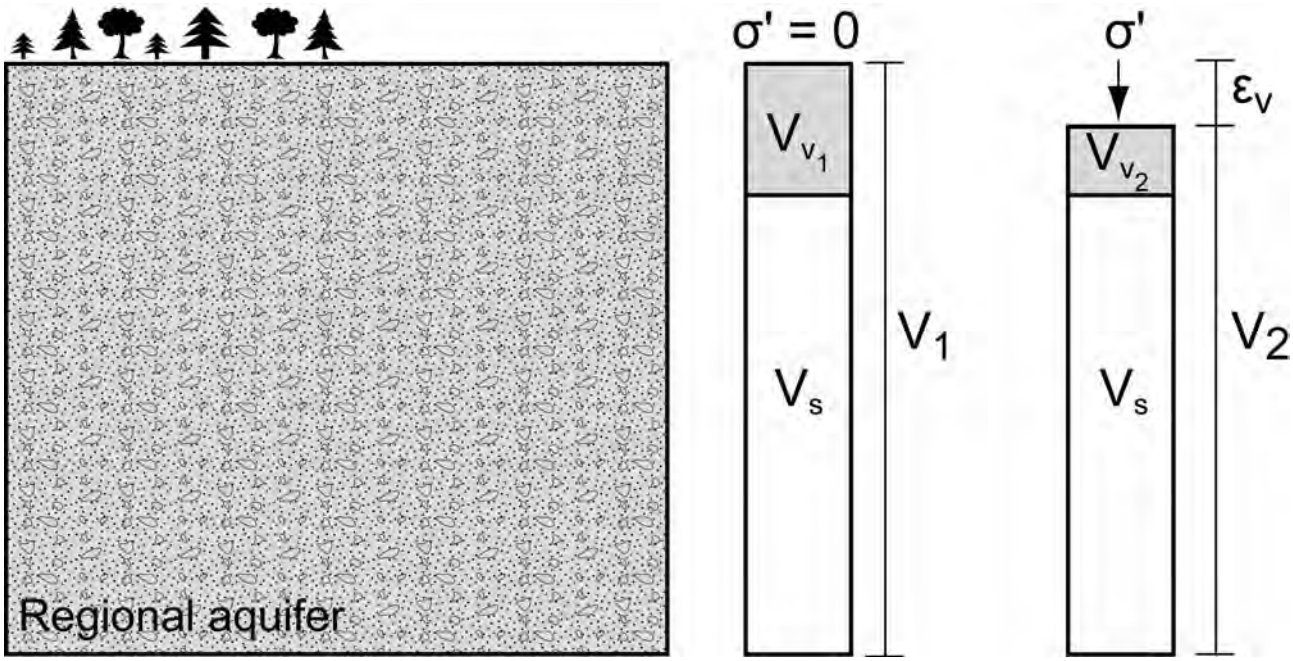

Figure 3.2: Vertical bulk volume change for a granular porous aquifer. This deformation is assumed to be exclusively driven by the change in porosity due to the shifting of incompressible solid grains.

From Eq. (3.3), it follows that at no effective stress (at ground level) the porosity is ϕ_0, and that under effective stress σ' the porosity is ϕ. Integrating Eq. (3.3) under these conditions yields:

$$\begin{aligned} \int_{\phi_0}^{\phi} \frac{d\phi}{1-\phi} &= \frac{-1}{E} \int_0^{\sigma'} d\sigma' \\ \sigma' &= E \ln\left(\frac{1-\phi}{1-\phi_0}\right) \end{aligned} \tag{3.4}$$

Following this method, a zero effective porosity ($\phi \approx 0$) occurs when the applied effective stress is:

$$\sigma'_0 = -E \ln(1-\phi_0) \tag{3.5}$$

where σ'_0 denotes the limit stress for pore closure. Expressing Eq. (3.5) for the elastic modulus

E, and introducing it into Eq. (3.4), yields:

$$\sigma' = \sigma'_0 \left(1 - \frac{\ln(1-\phi)}{\ln(1-\phi_0)}\right) \tag{3.6}$$

and an effective stress-dependent porosity is obtained by expressing Eq. (3.6) as:

$$\phi(\sigma') = 1 - (1-\phi_0)^{\left(1-\frac{\sigma'}{\sigma'_0}\right)} \tag{3.7}$$

A negative effective stress results in a porosity greater than the no-stress porosity: $\phi \geq \phi_0$. This can be interpreted as water pressure bearing all the applied load, so that grains are no longer in contact with each other, but suspended in the fluid (soil boiling phenomenon).

3.2.1 Hydraulic conductivity and specific storage coefficient

As expressed by the Kozeny-Carman equation [25, 5], the hydraulic conductivity of granular porous media depends on the dynamic properties of water and on the intrinsic properties of the granular material:

$$K = \frac{\rho_w g}{\mu_w} \frac{\phi^3}{b A_s^2} \tag{3.8}$$

where μ_w is the water viscosity, b is a factor taking into account the shape and spatial arrangement of grains (in general: $10 < b < 30$, usually $b \approx 20$), and A_s is the specific contact area, defined as [8]:

$$A_s = 3\,(1-\phi)\,C \tag{3.9}$$

where the coefficient C corresponds to the inverse of the harmonic mean radius of grains in the sample, R_h:

$$C = \int_0^\infty \frac{P(r)}{r}\,dr = \frac{1}{R_h} \tag{3.10}$$

In Eq. (3.10), the symbol r stands for the grain radius, and $P(r)$ is the frequency distribution: $P(r) = \frac{1}{P_0}\frac{\partial P_{cum}}{\partial r}$, where P_{cum} is the cumulative weight and P_0 is the total weight of the formation sample. For a soil with uniformly distributed grain size with minimum radius r_1 and maximum radius r_2, i.e., $P(r) = \frac{1}{r_2 - r_1}$, Eq. (3.10) yields:

$$C = \int_{r_1}^{r_2} \frac{1}{r_2 - r_1}\frac{dr}{r} = \frac{1}{r_2 - r_1} \ln\left(\frac{r_2}{r_1}\right) \tag{3.11}$$

Table 3.1 presents some values of C calculated from sample particle size distribution curves.

Assuming that at large scale the coefficient C is constant, i.e., it does not change despite the shifting of incompressible solid grains, and introducing Eq. (3.7) into Eq. (3.8) results in

Table 3.1: Typical ranges of coefficient C for different granular geological materials

Geological Material	C $[1/m]$
Pebble gravel stream channel	≈ 1000
Sandy gravel	≈ 3500
Fine sand	≈ 7000
Alluvial sandy gravel	≈ 13500
Sandy-silty gravel moraine	≈ 36000
Silty sand	≈ 36500
Lacustrine clayey silt	≈ 205500

an effective stress-dependent hydraulic conductivity:

$$K(\sigma') = \frac{\rho_w g}{\mu_w}\frac{1}{9}\frac{\left(1-(1-\phi_0)^{(1-\frac{\sigma'}{\sigma'_0})}\right)^3}{\left((1-\phi_0)^{(1-\frac{\sigma'}{\sigma'_0})}C\right)^2 b} \tag{3.12}$$

Similarly, Eq. (3.7) can be inserted in the definition of the specific storage coefficient, S_s:

$$S_s(\sigma') = \rho_w g(\frac{1}{E_s}+\frac{\phi}{E_w}) \tag{3.13}$$

$$S_s(\sigma') = \rho_w g(\frac{1}{E_s}+\frac{1-(1-\phi_0)^{(1-\frac{\sigma'}{\sigma'_0})}}{E_w}) \tag{3.14}$$

where the symbol E_w and E_s stand for the elasticity of water and the skeletal elasticity, respectively. If water is assumed incompressible, the skeletal elasticity E_s corresponds to the formation elasticity under fully saturated conditions E.

Using Eqs. (3.12), and (3.14) results in a nonlinear effective stress-dependent groundwater flow equation:

$$S_s(\sigma')\frac{\partial H}{\partial t} = \nabla\cdot(\mathbf{K}(\sigma')\nabla H) \quad ; \quad H = h + z \tag{3.15}$$

where H is hydraulic head and t is time. Knowledge of ϕ_0, E, C and b is sufficient to solve Eq. (3.15) under any given boundary conditions.

3.2.2 Deformation

From Eq. (3.7) it follows that a change in effective stress causes a change in porosity $\Delta\phi$:

$$\begin{aligned}\Delta\phi &= \phi(\sigma'_{\mathrm{i}}) - \phi(\sigma') \\ &= \left(1-(1-\phi_0)^{(1-\frac{\sigma'_{\mathrm{i}}}{\sigma'_0})}\right) - \left(1-(1-\phi_0)^{(1-\frac{\sigma'}{\sigma'_0})}\right) \\ &= (1-\phi_0)^{(1-\frac{\sigma'}{\sigma'_0})} - (1-\phi_0)^{(1-\frac{\sigma'_{\mathrm{i}}}{\sigma'_0})} \end{aligned} \tag{3.16}$$

where the subscript i denotes the effective stress state prior to the change. $\Delta\phi$ is positive in consolidation and negative in expansion. Integrating vertically over all the porosity changes from the bottom z_b to the top z_t leads to the system consolidation $T > 0$ or expansion $T < 0$:

$$T(x,y) = \int_{z_b}^{z_t} \Delta\phi(z)\, dz \tag{3.17}$$

3.3 Parameter estimation by fitting the measured data

Parameter values (ϕ_0, σ'_0 and C) can be obtained by fitting Eq. (3.7) or Eq. (3.12) to measured field or laboratory data.

Uygar and Doven [36] studied the porosity response of a uniformly graded fine sand at saturated, drained conditions under cyclic high effective stresses. Bolton [3] investigated the hydraulic conductivity of an artificial silty clay during a loading and unloading test. Fitting of Eq. (3.7) and of Eq. (3.12) on the measured data of [36] and [3] is presented in Figure 3.3 for a loading (compression) and unloading (swelling) cycle. The unique calibrated parameters are presented in Table 3.2.

Table 3.2: Numerical values used for the curve fitting of Figure 3.3.

	ϕ_0 $[-]$	σ'_0 $[Pa]$	E $[Pa]$	C $[1/m]$	b $[-]$
Uygar and Doven (2006)					
Loading	0.40	$50.0 \cdot 10^6$	$96.8 \cdot 10^6$	-	-
Unloading	0.35	$110.0 \cdot 10^6$	$255.3 \cdot 10^6$	-	-
Bolton (2000)					
Loading	0.40	$2.0 \cdot 10^6$	$3.9 \cdot 10^6$	10^6	20
Unloading	0.29	$3.5 \cdot 10^6$	$10.2 \cdot 10^6$	10^6	20

From the data of Figure 3.3, it follows that applied virgin compression results in a non-elastic irreversible deformation, changing the mechanical and hydraulic characteristics of the granular porous media.

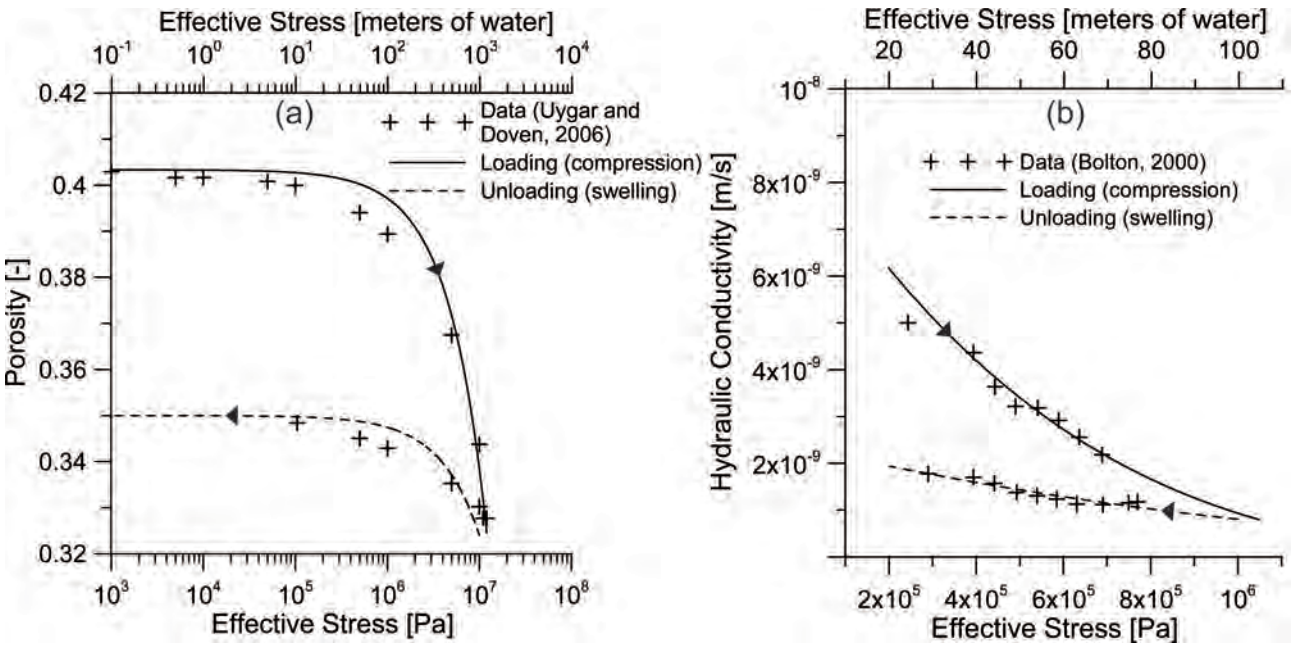

Figure 3.3: Fitting example of Eq. (3.7) and Eq. (3.12) on laboratory stress-dependent data for (a) an uniformly graded fine sand from Uygar and Doven (2006) [36], and (b) an artificial silty clay from Bolton (2000) [3]. Cross symbols are measured data and lines are simulated values for loading (solid line) and unloading (dashed line).

3.4 Illustrative simulation and verification

3.4.1 Pumping

An illustrative simulation represents vertical deformation of a regional aquifer system due to heavy groundwater pumping. Initial and boundary conditions are based on the compaction problem of Leake and Hsieh [26], and the illustrative modelling domain is inspired by the geometry of the Mexico City Basin.

An impervious and incompressible basement is faulted, creating a basin. This geometry is filled by four sedimentary layers: a strata of unconsolidated volcanic deposits overlaid by alluvial sediments constituting a thick and compressible lower aquifer, a layer of lacustrine sediments forming a semiconfining and highly compressible unit, and an upper alluvial aquifer. The 3D virtual basin geometry is obtained by full rotation of the cross section shown in Figure 3.4.

The upper aquifer is under a constant hydraulic head matching the topographic elevation of 2300 m.a.s.l. Heavy pumping in the center of the lower aquifer decreases the hydraulic head at a rate of 12 m/y until reaching a final hydraulic head of 1300 m.a.s.l. (Figure 3.4). The system is initially at hydrostatic conditions, 2300 m.a.s.l.

The simulation is run for a period of 100 years using (1) the approach presented in Chapter 4 based on Eqs. of section 3.2, and (2) the poroelasticity theory of Biot [2]. The boundary conditions for the poroelastic computation are those of the Leake and Hsieh problem [26, 7]. With poroelastic equations, the model is run only on the 2D basin cross section, because of

the afore-mentioned computational problems of this method in regional 3D analysis. With the proposed approach, the model is run on the 3D basin. Within the direction of rotation, this virtual basin is isotropic. Of course, this is geologically unlikely, but this allows to (1) test the proposed approach on a 3D model, and (2) compare its results with detailed poroelastic data. The approach discussed in Chapter 4 was implemented in the multipurpose Ground Water (GW) finite element software [9]. The multiphysics software COMSOL Multiphysics [6] was used to solve poroelastic equations. Parametric information is presented in Table 3.3.

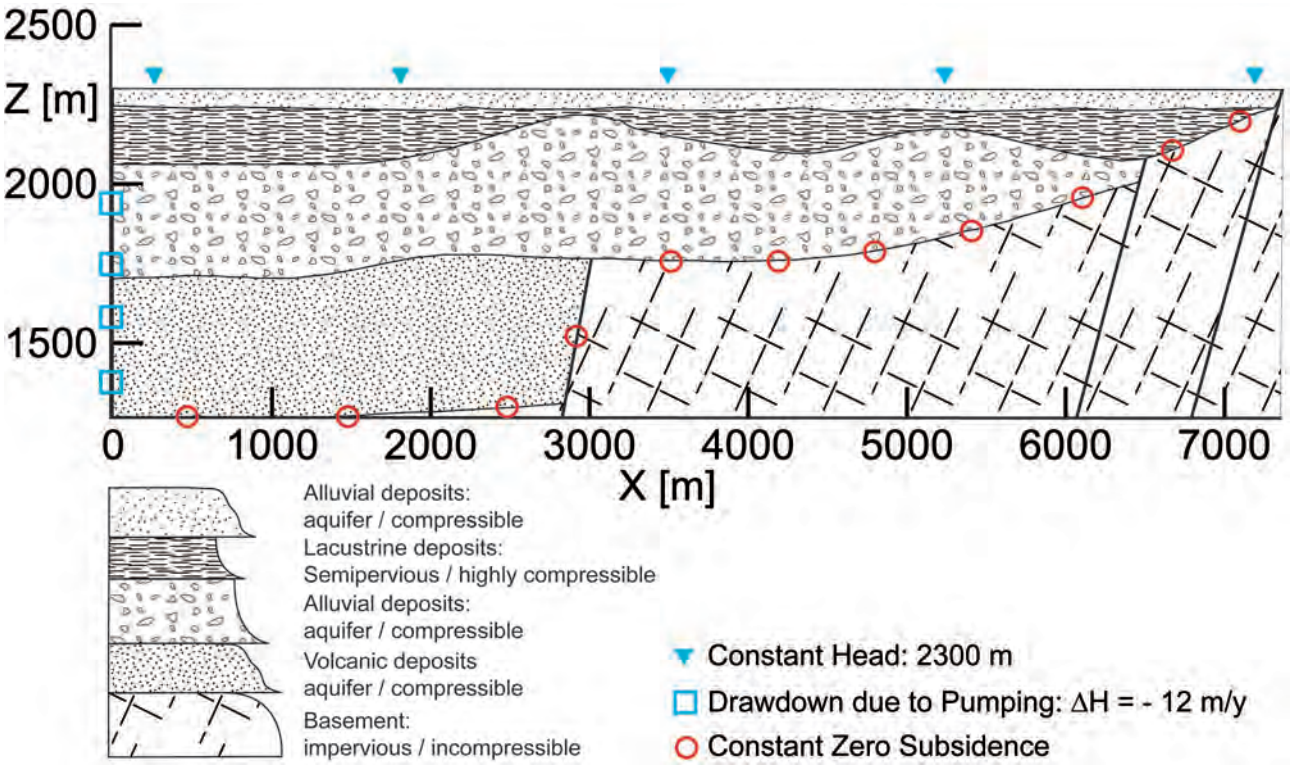

Figure 3.4: Cross section of the regional model geometry and boundary conditions. The left boundary corresponds to the basin center, the right boundary to the external limits (vertical exaggeration 2x).

3.4.2 Discussion and results

Using effective stress-dependent parameters in the groundwater flow equation (Eq. (3.15)) results in increased hydraulic gradients (Figure 3.5b) and in decreased simulated pumping rates (Figure 3.5c) compared to the linear form with constant parameters. This is because of the reduction in hydraulic conductivity and specific storage due to the decrease in water pressure and increase in effective stress. The overburden stress field used in the flow simulation and obtained using Eq. (4.3) is constant (Figure 3.5a).

The simplified approach presented in this work generally reproduces the vertical deformation obtained using the detailed poroelastic equations (Figure 3.5d). However, the consolidation is less pronounced. This is because the decline in water pressure is slowed by the parameter dependency. Note that: (1) in Table 3.3 E_Y denotes the Young's modulus of the porous

Table 3.3: Parameter values used in the pumping simulation. Note that: for the proposed approach σ'_0, K_0 and S_{s_0} are calculated via ϕ_0, E, C and b using Eqs. (3.5), (3.12) and (3.14).

Approach presented in Chapter 4								
Lithology	ρ_r $[kg/m^3]$	ϕ_0 $[-]$	σ'_0 $[MPa]$	E $[GPa]$	C $[1/m]$	b $[-]$	K_0 $[m/s]$	S_{s_0} $[1/m]$
Upper Alluvial	1800	0.23	286	1.1	1000	20	10^{-3}	10^{-5}
Lacustrine Deposits	1800	0.50	70	0.1	158100	20	10^{-6}	10^{-4}
Lower Alluvial	2000	0.37	464	1.0	2500	20	10^{-3}	$1.1 \cdot 10^{-5}$
Volcanic Deposit	2200	0.12	62	0.5	1000	20	10^{-4}	$2.0 \cdot 10^{-5}$

Poroelasticity theory						
Lithology	ρ_r $[kg/m^3]$	ϕ $[-]$	E_Y $[GPa]$	ν $[-]$	α_B	K $[m/s]$
Upper Alluvial	1800	0.23	11	0.25	1	10^{-3}
Lacustrine Deposits	1800	0.50	1	0.25	1	10^{-6}
Lower Alluvial	2000	0.37	10	0.25	1	10^{-3}
Volcanic Deposit	2200	0.12	5	0.25	1	10^{-4}

Fluid and other parameters			
ρ_w $[kg/m^3]$	μ_w $[Pa\ s]$	E_w $[GPa]$	g $[m/s^2]$
1000	10^{-3}	2.5	9.81

medium, and (2) poroelasticity theory does not use specific storage but rather uses Young's modulus and Poisson's ratio [26].

Differential ground settlement due to bedrock inflection is correctly highlighted by the proposed modelling approach. These areas can be subject to ground failure.

3.4.3 Recovery of porosity

After 100 years pumping stops and, due to the upper boundary condition, the aquifer system gradually returns to the initial hydrostatic situation. Here we compare porosity recovery using the proposed approach and the three cases illustrated in Figure 3.6a: (1) the aquifer system has an elastic behaviour, (2) only aquifer units are elastic and (3) the system has an inelastic behaviour.

3.4.4 Discussion and results

In the case of full elasticity, porosity recovery and media expansion are the same as the change in porosity and the compaction induced by the 100 y of pumping. If stress due to pumping causes non-recoverable deformations, the expansion curve is different than the compression curve (Figure 3.6a), and there is an important loss in porosity (and permeability), and only a fraction of the ground subsidence can be recovered, especially if all formations have inelastic behaviour (Figure 3.6b).

No change and recovery in porosity occurs in the upper aquifer, due to constant water pressure. Not surprisingly, in the inelastic case, considerable loss of porosity occurs in the lacustrine aquitard unit. However, the strongest decrease in porosity occurs in the deeper aquifer, where the increase in effective stresses during pumping caused significant non recoverable deformations.

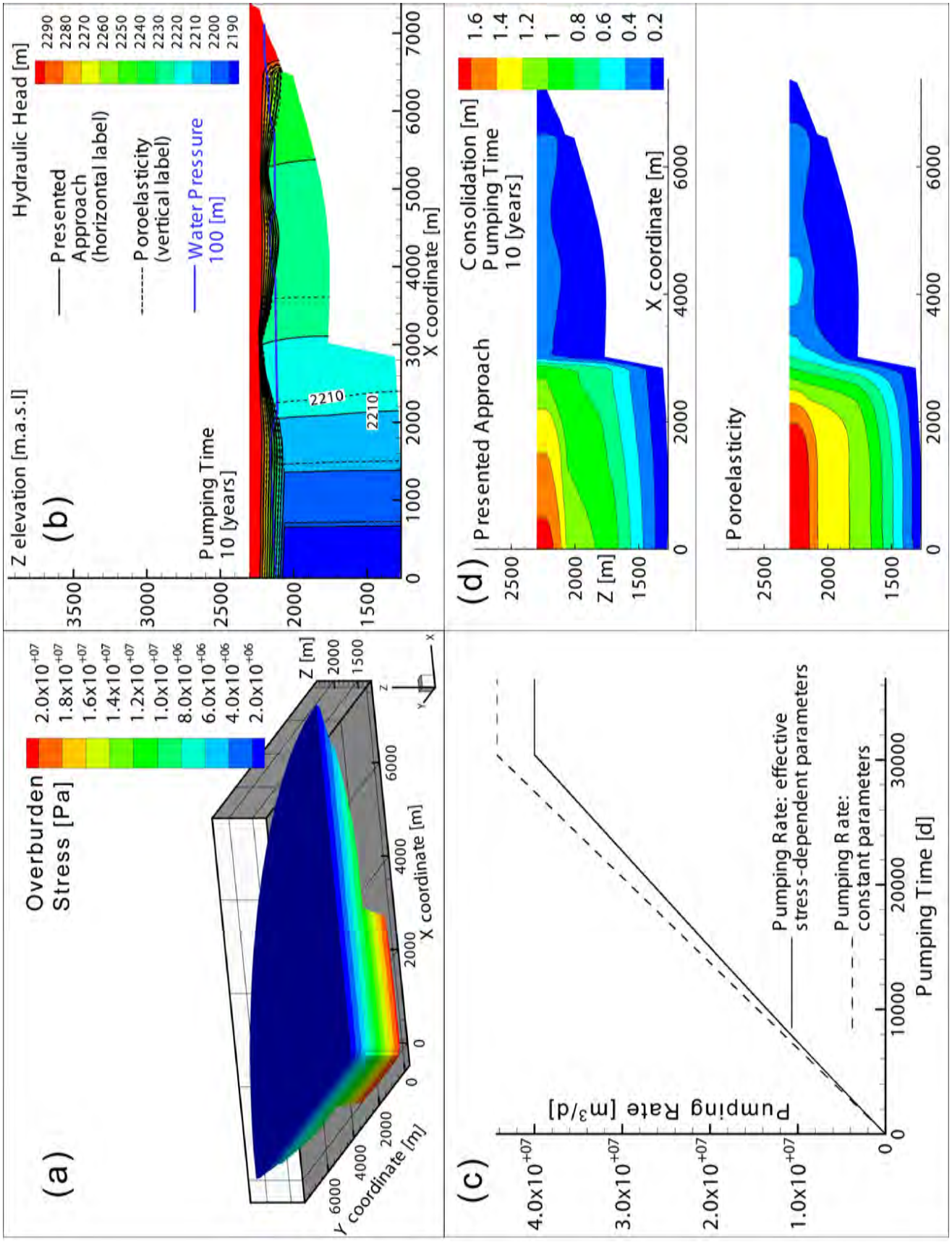

Figure 3.5: (a) 3D view of a quarter of the basin showing the simulated overburden stress. (b) Simulated hydraulic head field at 10 years of pumping with the presented approach (solid black lines) and with poroelasticity (dashed lines), the solid blue line is the isocontour of 100 [m] of water pressure calculated with the presented approach. (c) Pumping rate divergence considering constant (dashed line) or variable (solid line) hydrodynamic parameters. (d) Aquifer system consolidation at 10 years of pumping. Above: method illustrated in this work; below: Biot's poroelasticity.

Laboratory consolidation tests [3, 36, 12] and field observations [17] indicate that inelasticity must be considered when studying aquifer system deformation due to changing water pressure. Eqs. (3.7), (3.12), (3.14) can be used, after a fitting on laboratory consolidation tests, for first estimates of the recoverable porosity of regional aquifer systems affected by induced stresses such as heavy pumping.

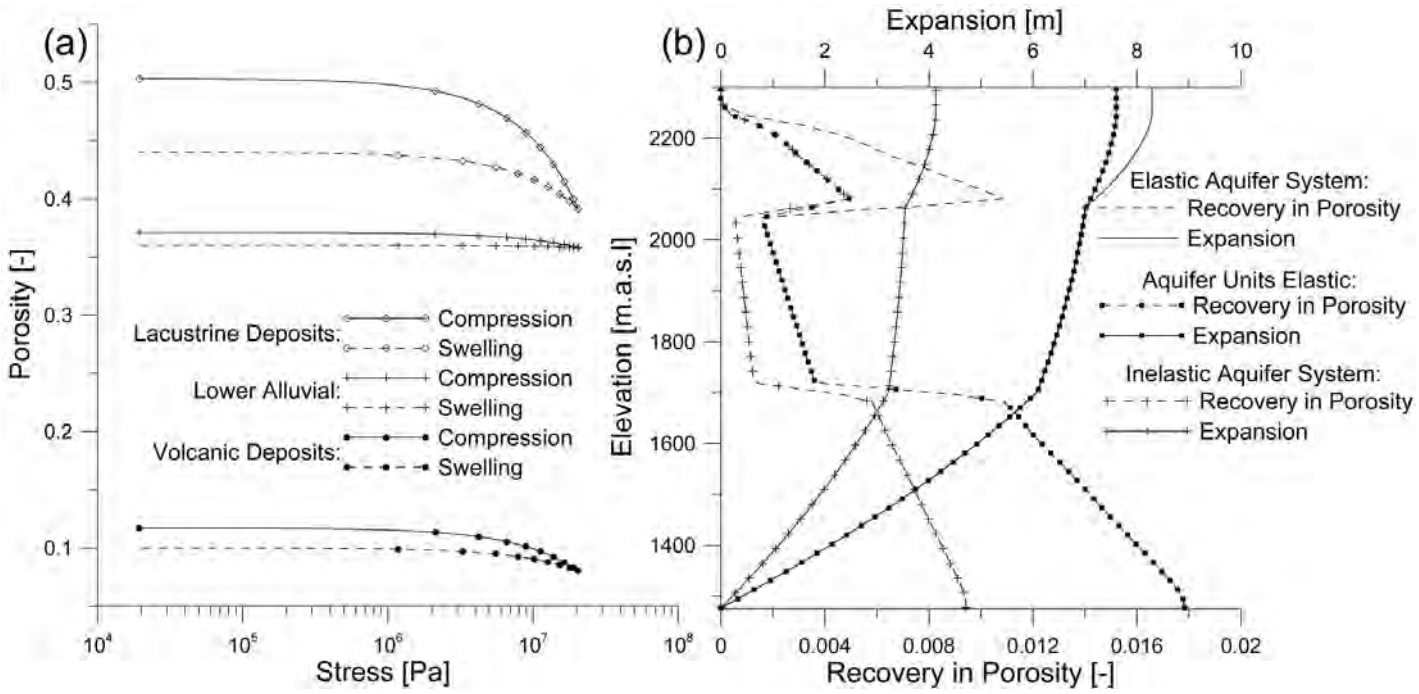

Figure 3.6: (a) Effective stress-dependent porosity functions used in the recovery analysis. Solid lines illustrates compression due to pumping, dashed lines swelling during recovery. (b) Simulated recovery in porosity (dashed lines) and expansion (solid lines) as a function of elevation. Note that curves of change in porosity and consolidation due to 100 y of groundwater pumping match curves of recovery in porosity and expansion for an elastic aquifer system.

3.5 Conclusions

Hydrodynamic parameters depend on effective stresses in regional basin-fill aquifer systems. Effective stress-dependent equations for porosity, hydraulic conductivity and specific storage have been developed based on the law of elasticity. These equations correctly reproduce the data obtained in stress-porosity/hydraulic conductivity laboratory tests.

The Chapter has also presented a theoretical numerical simulation, based on the approach detailed in Chapter 4, illustrating the dynamics of regional aquifer systems affected by significant changes in water pressures. With this approach, the groundwater flow equation becomes physically more accurate because it considers the afore-mentioned relationships. The simple deformation equations based on the change in porosity due to the variation in water pressures require only five unknown parameters to reproduce vertical deformation similar to that obtained by detailed poroelastic equations.

The presented approach is limited by the following assumptions: (1) the stress field is constant with water pressure variations, and (2) horizontal displacements and (3) deformation within solid grains are negligible. However, each of these assumptions are reasonable for most regional hydrogeological problems, so that the proposed approach can be a simple and rapid tool for estimating the dynamics of aquifer systems affected by change in water pressures.

Chapter 6 handles the application of the method for simulating land subsidence in Mexico City due to groundwater overpumping.

Bibliography

[1] Bell, J., Amelung, F., Ferretti, A., Bianchi, M., Novali, F.: Permanent scatterer InSAR reveals seasonal and long-term aquifer system response to groundwater pumping and artificial recharge. Water Resources Research **44**, 18pp (2008)

[2] Biot, M.: General theory of three-dimensional consolidation. J App Phys **12**(2), 155–164 (1941)

[3] Bolton, A.: Some measurements of permeability and effective stress on a heterogeneous soil mixture: implications for recovery of inelastic strains. Engineering Geology **57**(1–2), 95–104 (2000)

[4] Bundschuh, J., Arriaga, M.: Introduction to the Numerical Modeling of Groundwater and Geothermal Systems, chap. Rock and fluid, pp. 13–100. Taylor & Francis Group, CRC Press (2010)

[5] Carman, P.: Fluid flow through granular bed. Trans. Inst. Chem. Engrs. (London) **15**, 150–156 (1937)

[6] COMSOL-Multiphysics: Multiphysics user's guide. COMSOL AB, Sweden (2010)

[7] COMSOL-Multiphysics: Biot Poroelasticity (2011)

[8] Cornaton, F., Perrochet, P.: Groundwater age, life expectancy and transit time distributions in advective-dispersive systems: 2. Reservoir theory for sub-drainage basins. Advances in Water Resources **29**(9), 1292–1305 (2006)

[9] Cornaton, F.J.: Ground Water: a 3-D Ground Water and Surface Water Flow, Mass Transport and Heat Transfer Finite Element Simulator, Reference Manual, 398 pp. Centre for Hydrogeology and Geothermics, Neuchâtel, Switzerland (2007)

[10] Detournay, E., Cheng, A.D.: Comprehensive Rock Engineering: Principles, Practice and Projects, Vol. II, chap. Fundamentals of poroelasticity, pp. 113–171. C. Fairhurst, Pergamon Press (1993)

[11] Ferronato, M., Gambolati, G., Janna, C., Teatini, P.: Geomechanical issues of anthropogenic CO2 sequestration in exploited gas fields. Energy Conversion and Management **51**(10), 1918–1928 (2010)

[12] Galloway, D., Burbey, T.: Review: Regional land subsidence accompanying groundwater extraction. Hydrogeology Journal **19**, 1459–1486 (2011)

[13] Gambolati, G., Teatini, P., Ferronato, M.: Encyclopedia of Hydrological Sciences, chap. Anthropogenic Land Subsidence, p. 17pp. Anderson M.G., John Wiley & Sons (2005)

[14] Gangi, A.F.: Variation of whole and fractured porous rock permeability with confining pressure. Int. J. Rock Mech. Min. Sci. Geomech. Abstr. **15**(5), 249–257 (1978)

[15] Hansmann, J., Loew, S., Evans, K.: Reversible rock-slope deformations caused by cyclic water-table fluctuations in mountain slopes of the Central Alps, Switzerland. Hydrogeology Journal **20**(1), 73–91 (2012)

[16] Helm, D.: Simulation of aquitard compaction due to changes in stress. Trans Am Geophys Union **53**(11), 979 (1972)

[17] Helm, D.: One-Dimensional Simulation of Aquifer System Compaction Near Pixley, California. 1. Constant Parameters. Water Resources Research **11**(3), 465–478 (1975)

[18] Helm, D.: One-Dimensional Simulation of Aquifer System Compaction Near Pixley, California. 2. Stress-Dependent Parameters. Water Resources Research **12**(3), 375–391 (1976)

[19] Holzer, T.: Man induced land subsidence. Geol. Soc. of America, Washington, DC (1984)

[20] Jacob, C.: On the flow of water in an elastic artesian aquifer. American Geophysical Union **21** (1940)

[21] Jacob, C.: Engineering hydraulics: Proceedings of the Fourth Hydraulics Conference, Iowa Institute of Hydraulic Research, Iowa City, IW, chap. Flow of ground water. Rouse H (ed) (1950)

[22] Kihm, J., Kim, J., Song, S., Lee, G.: Three-dimensional numerical simulation of fully coupled groundwater flow and land deformation due to groundwater pumping in an unsaturated fluvial aquifer system. Journal of Hydrology **335**(1-2), 1–14 (2007)

[23] Kim, J.: Three-dimensional numerical simulation of fully coupled groundwater flow and land deformation in unsaturated true anisotropic aquifers due to groundwater pumping. Water Resour Res **41**, 1–16 (2005)

[24] Kim, J.M., Parizek, R.: A Mathematical Model for the Hydraulic Properties of Deforming Porous Media. Ground Water **37**(4), 546–554 (1999)

[25] Kozeny, J.: Ueber kapillare leitung des wassers im boden. Tech. Rep. 2a, Akad. Wiss., Wien, AUT (1927)

[26] Leake, S., Hsieh, P.: Simulation of Deformation of Sediments from Decline of Ground-Water Levels in an Aquifer Underlain by a Bedrock Step. Tech. Rep. 97, USGS (1997)

[27] Lombardi, G.: Les tassements exceptionnels au barrage de Zeuzier. Publ. Swiss Soc. Soil Rock Mech. **118**, 39–47 (1988)

[28] Louis, C.: A study of groundwater flow in jointed rock and its influence on the stability of rock masses. Tech. Rep. 9, Rock Mechanics, Imperial College, London, UK (1969)

[29] Murdoch, L., Germanovich, L.: Analysis of a deformable fracture in permeable material. International Journal for Numerical and Analytical Methods in Geomechanics **30**(6), 529–561 (2006)

[30] National Research Council: Rock Fractures and fluid flow. National Academy Press, Washington, DC (1996)

[31] Parriaux, A.: Géologie: Bases pour l'Ingénieur. Presses Polytechniques et Universitaires Romandes (2006)

[32] Price, D., de Freitas, M.: Engineering Geology. Springer-Verlag Berlin Heidelberg (2009)

[33] Rutqvist, J., Wu, Y.S., Tsang, C.F., Bodvarsson, G.: A modeling approach for analysis of coupled multiphase fluid flow, heat transfer, and deformation in fractured porous rock. Int. J. Rock Mech. Min. Sci. **39**(4), 429–442 (2002)

[34] Terzaghi, K.: Die berechnung der durchlässigkeitziffer des tones aus dem verlauf der hydrodynamischen spannungserscheinungen. Akad Wissensch Wien Sitzungsber Mathnaturwissensch Klasse IIa **142**(3–4), 125–138 (1923)

[35] Terzaghi, K., Peck, R.: Soil Mechanics in Engineering Practice. John Wiley and Sons, Inc. (1967)

[36] Uygar, E., Doven, A.: Monotonic and cyclic oedometer tests on sand at high stress levels. Granular Matter **8**(1), 19–26 (2006)

[37] Verruijt, A.: Encyclopedia of Hydrological Sciences, chap. Consolidation of Soils, p. 15pp. Anderson M.G., John Wiley & Sons (2008)

[38] Walsh, J.B.: Effect of pore pressure and confining pressure on fracture permeability. Int. J. Rock Mech. Min. Sci. Geomech. Abstr. **18**, 429–435 (1981)

[39] Zangerl, C., Eberhardt, E., Loew, S.: Ground settlements above tunnels in fractured crystalline rock: numerical analysis of coupled hydromechanical mechanisms. Hydrogeology Journal **11**, 162–173 (2003)

Chapter 4

Modelling strategy, verification and illustrative examples *

Abstract

Effective stress plays an important role in aquifer dynamics, especially in those affected by high variations of water pressures. Increasing/decreasing effective stresses affect hydrodynamic parameters and aquifer properties, even in media of high stiffness, such as fractured rocks. This Chapter focuses on a regional scale modelling approach for Fluid-to-Solid hydromechanical coupled processes taking into account the dependency of hydrodynamic parameters on effective stress. This approach has been verified on theoretical 1D, 2D and 3D examples and illustrated by modelling a fractured aquifer dynamic, the Zeuzier arch dam settlement. The calibrated model showed agreement with measured data. This simulation method could be used to analyze the sensitivity of aquifers on significant variations of water pressure.

4.1 Introduction

This Chapter proposes an approach to simulate Fluid-to-Solid hydromechanical coupled processes, i.e. a change in fluid pressure leads to a change in the volume of the porous media, at regional scales. The method consists of three successive phases: a first one computing the distribution of overburden stresses in the aquifer; a second non-linear simulation of water flow in which the equivalent hydraulic conductivity tensor of the rock mass and the specific storage coefficient depend on effective stresses; and a third simulation computing the aquifer deformation.

The main advantage of this approach is that it is based on simple, elliptic governing equations taking into account the dependency of hydrodynamic parameters on effective stress. This results in a relatively economic numerical schemes able to model large scale problems involv-

*This Chapter is based on the paper:
Preisig, G., Cornaton, F.J., Perrochet, P.: Simulation of flow in fractured rocks using effective stress-dependent parameters and aquifer consolidation. In: Models - Repositories of Knowledge, Modelcare 2011. 18-22.09.2011, UFZ, Leipzig, Germany.

ing detailed geological geometries and hydrogeological processes. The modelling approach is based on the following assumptions: (1) the stress fields remain constant during the water depletion/recovery, (2) aquifer compaction/expansion only results from the opening/closing of porosity (no rock matrix/grains deformation), (3) the validity of Hooke's law within the context of small strains, and (4) horizontal deformations are neglected and assumed much smaller than vertical deformations. These assumptions are believed to be appropriate at regional hydrogeological scales [3, 14].

4.2 Modelling approach

The resolution of stress-dependent equations as well as porosity change and settlement equations, e.g., Eqs. (2.12), (2.16), (2.17), (2.18), (2.19), (2.20), (3.7), (3.12), (3.14), (3.16), (3.17) developed in Chapters 2 and 3 needs to know the overburden stress acting at a given depth of a geological volume. In a regional finite element model considering detailed topography and geology, this is problematic because the depth of each nodes must be known for solving Eq. (1.3), as highlighted in Figure 4.1. Within this context, a mathematical strategy must be found in order to address the afore-mentioned issue.

Computation of the overburden stress field

The overburden stress defined in Eq. (1.3) results from the vertical integration of a variable rock density ρ_r multiplied by the gravity g, assumed vertical and constant. Therefore, stress variation with depth (or elevation z) is expressed by:

$$\frac{d\sigma}{dz} = -\rho_r(z)g \tag{4.1}$$

Dividing Eq. (4.1) by $\rho_r(z)$ and differentiating a second time with respect to z yields:

$$\frac{d}{dz}\left(\frac{1}{\rho_r(z)}\frac{d\sigma}{dz}\right) = 0 \tag{4.2}$$

Eq. (4.2) can be expressed in a 3D or 2D vertical domain Ω using the gradient (∇) and the divergence ($\nabla\cdot$) operators:

$$\nabla \cdot \frac{1}{\rho_r(z)}\mathbf{N}\nabla\sigma = 0 \text{ in } \Omega \tag{4.3}$$

provided $\mathbf{N}$ is a singular tensor of the type:

$$\mathbf{N} = \nabla z \otimes \nabla z = \begin{bmatrix} 0 & 0 & 0 \\ 0 & 0 & 0 \\ 0 & 0 & 1 \end{bmatrix} \tag{4.4}$$

Eq. (4.3) is a steady state diffusion equation analogous to a flow equation in a heterogeneous and vertically anisotropic domain, and can be solved straightforwardly with appropriate boundary

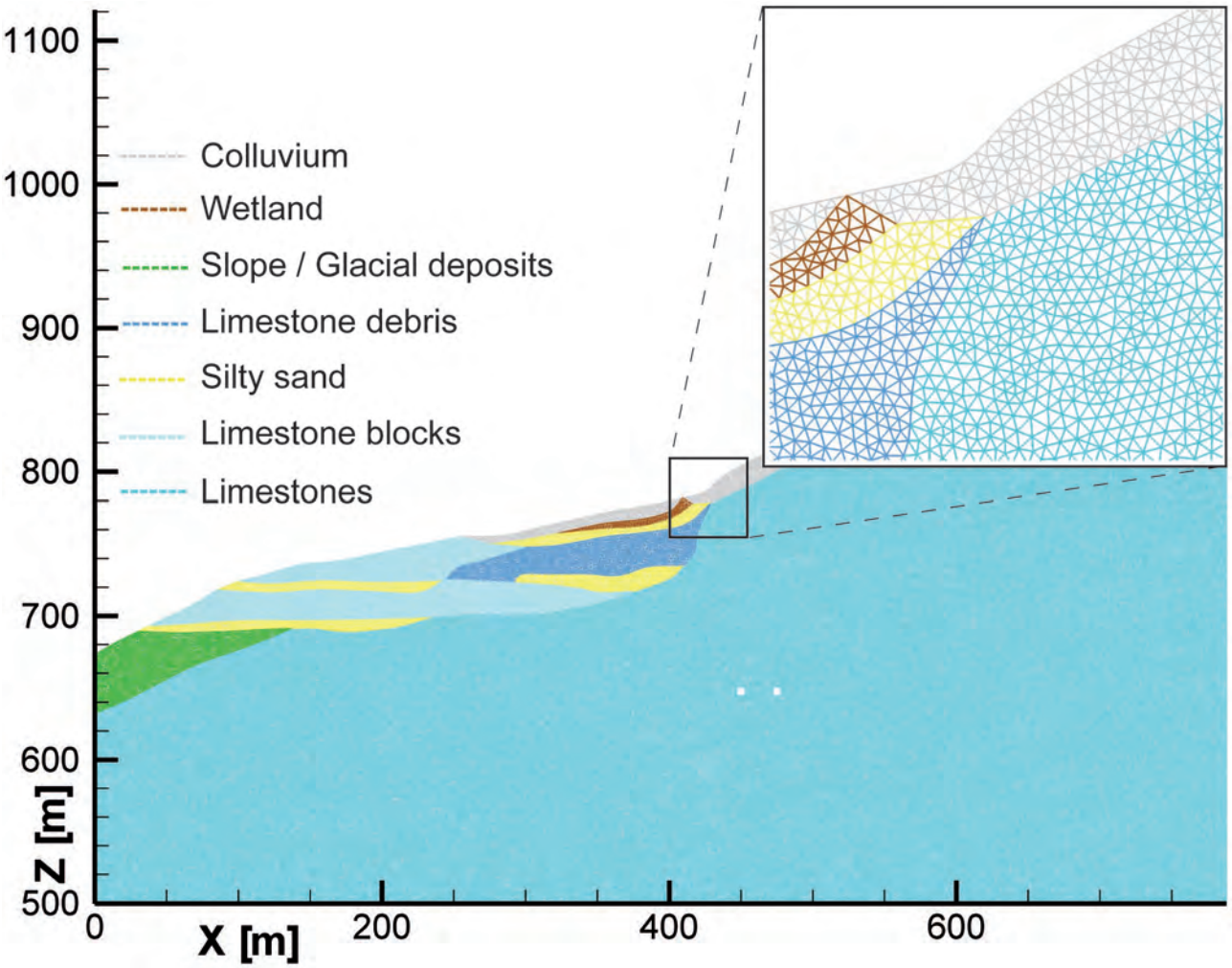

Figure 4.1: 2D vertical mesh of triangular elements illustrating the problematic of nodes depth computation. This finite element mesh is based on a cross section orthogonal to the Loetschberg double track rail tunnel (circular holes in the mesh) [15, 8] and was constructed using the finite element mesh generator `GMSH` [4].

conditions.

From Eq. (1.3) it follows that on the upper boundary Γ_+ of domain Ω (topographic surface) the value of the overburden stress is known and can be specified by a Dirichlet boundary condition:

$$\sigma = f_1(x, y, z_{surface}, t) \text{ on } \Gamma_+ \tag{4.5}$$

where $f_1(x, y, z_{surface}, t)$ is a known function detailing the stress state at the surface nodes. Neglecting the atmospheric pressure, Eq. (4.5) is in general assumed to be zero $\sigma(z_{surface}) = 0$ and constant over time, but could take any other specific values in presence of significant superficial loads, such as a dam lake or heavy buildings.

The gradient of the scalar field, i.e., a Neumann boundary condition, can be applied on the bottom boundary Γ_- of domain Ω:

$$\mathbf{N}\nabla\sigma \cdot \mathbf{n} = \frac{d\sigma}{dz} = -g\rho_{r_{bottom}} \text{ on } \Gamma_- \tag{4.6}$$

where **n** is the unit vector normal to the boundary, $\rho_{r_{bottom}}$ indicates the density of the rock at the domain bottom.

The resolution of Eq. (4.3) with the conditions Eqs. (4.5) and (4.6) leads to the overburden stress computation:

$$\sigma(z) = g \int_{z}^{z_{surface}} \rho_r(u)\, du \tag{4.7}$$

This approach allows the computation of the overburden stress field in a geologically oriented mesh with detailed topography without worrying on the depth of each nodes. Geological heterogeneity is taken into account by the different density of rocks constituting the model (Figure 4.2). Horizontal stresses are then obtained using Eq. (1.4). This stress field is then used in groundwater flow and aquifer consolidation simulations.

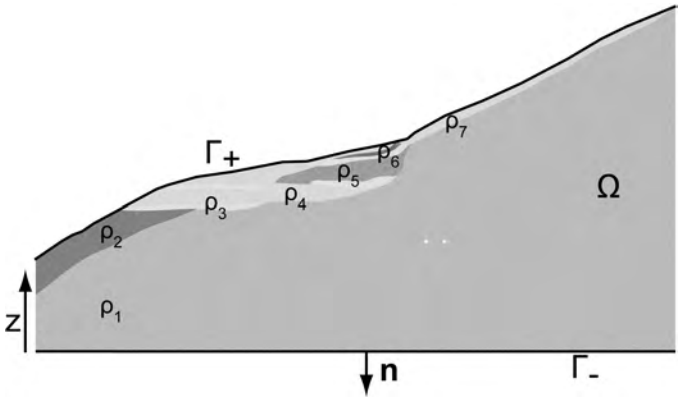

Figure 4.2: Schematic illustration showing the modelling strategy for solving Eq. (4.7) in a heterogeneous domain Ω.

Simulation of flow

Introducing in the transient groundwater flow equation the stress-dependent equations for porosity, specific storage coefficient and hydraulic conductivity (tensorial form) developed in Chapters 2 and 3, yields:

$$S_s(\sigma')\frac{\partial H}{\partial t} = \nabla \cdot (\mathbf{K}(\sigma')\nabla H) \quad ; \quad H = h + z \tag{4.8}$$

This non-linear equation can be solved for the distribution of hydraulic heads and recharge / discharge rates under hydromechanical coupling.

As presented in subsection 1.6.1, fluid-to-solid processes are essentially due to man-induced perturbations. For example, tunnel excavation or groundwater pumping are perturbations disturbing the natural equilibrium of an aquifer system. In a numerical model, those perturbations are mainly handled by boundary conditions of the first or fourth type.

A first type or a Dirichlet boundary condition specifies the value of the variable along a boundary:

$$H = f_2(t) \text{ on } \Gamma \tag{4.9}$$

where f_2 is a known function of time, detailing the evolution of hydraulic head on a boundary Γ, e.g., nodes forming the trajectory of a tunnel or a well. Nodes having a Dirichlet boundary condition must be constrained† by an imposed minimum or maximum flowrate. This prevents boundary nodes to have an unexpected behaviour. For example, the simulation of a draining

†limitation of the boundary condition

tunnel implies that boundary nodes forming the tunnel must be constrained by a maximum flowrate of zero, i.e., at this boundary water can only exit the model (seepage face). This avoids these nodes to recharge the model if the water table is lower than their elevation. Introducing the perturbation as a boundary condition of the first kind implies that the matching between observed and simulated data (calibration) is done by comparing flow rates.

A fourth type or a Well boundary condition is a condition specifying the extraction of a known volumetric discharge rate at a well / tunnel location:

$$Q = f_3(t) \text{ on } \Gamma \tag{4.10}$$

where f_3 is a known function of time. Boundary nodes with a condition of the fourth type must be constrained by imposed hydraulic heads. For example, this allows to stop pumping if the water table in the well becomes lower than the pump or the aquifer bottom elevation [1]. With wells boundary conditions, the matching between measured and simulated data is done by comparing hydraulic heads.

Within this context, the procedure to simulate an external aquifer perturbation, such as tunnel excavation or groundwater excessive pumping, is to: (1) calibrate the model in undisturbed conditions, and (2) simulate impacts of the perturbations on the aquifer system.

Simulation of the aquifer deformation and consolidation

The aquifer deformation and consolidation/expansion, due to the change in the effective stress field caused by external perturbations, is subsequently calculated with the settlement equation presented in Chapters 2 and 3:

$$T(x,y) = \int_{z_b}^{z_t} \Delta\phi(x,y,z)\, dz \tag{4.11}$$

where T is the vertical settlement ($T > 0$) or expansion ($T < 0$) at spatial coordinates x and y, $\Delta\phi$ is the change in porosity (deformation) due to the variation in effective stress, and z_b and z_t are the bottom and the top elevation of the system, respectively.

Eq. (4.11) is in line with the overburden stress Eq. (4.7), and the mathematical strategy formerly presented can also be used to solve it as a boundary value problem. Replacing z_t by z in Eq. (4.11) and differentiating twice with respect to elevation z yields:

$$\begin{aligned} \frac{dT(x,y,z)}{dz} &= \Delta\phi(x,y,z) \\ \frac{d}{dz}\left(\frac{dT(x,y,z)}{dz}\right) &= \frac{d\Delta\phi(x,y,z)}{dz} \end{aligned} \tag{4.12}$$

Eq. (4.12) can also be expressed by the more convenient 3D formulation:

$$\nabla \cdot \mathbf{N}\nabla T = \frac{d\Delta\phi}{dz} \text{ in } \Omega \tag{4.13}$$

where the tensor **N** again implies vertical anisotropy only.

Assuming that the basement is incompressible, a constant Dirichlet boundary condition of zero subsidence / settlement can be applied there:

$$T(x, y, z_b) = 0 \text{ on } \Gamma_- \tag{4.14}$$

As the change in porosity (deformation) tends to zero close to the domain surface, a Neumann boundary condition can be applied to it:

$$\mathbf{N}\nabla T \cdot \mathbf{n} = 0 \text{ on } \Gamma_+ \tag{4.15}$$

where **n** is the unit vector normal to the boundary.

These boundary conditions are consistent with the consolidation process and allow the resolution of Eq. (4.11) in a regional computational domain of arbitrary complexity. At this point, it is also important to note that another problem related to the computation of horizontal strains at a regional scale is the definition of realistic boundaries conditions.

In the case of an incompressible layer overlying the units under consolidation, with the equations presented above, there is a total settlement migration to ground surface. This compaction conservation seems to be specific of groundwater systems which are shallow compared to deep oil/gas reservoirs. In such systems, the compaction migration through incompressible strata may be contrasted by mechanical stresses reducing the subsidence magnitude at the surface [3].

4.3 Verification

The verification of this modelling strategy implemented in the multipurpose finite element software `Ground Water` [1] is based on the comparison with the results obtained via analytical solutions. A set of 1D, 2D and 3D verification examples for fractured and granular porous media is presented below.

4.3.1 Steady flow in a fracture under stress[‡]

A stiff rock mass is intersected by a fracture under hydrostatic and overburden stress conditions. The hydrostatic condition is constant due to the connection of the fracture to a superficial reservoir lake, and the overburden stress, i.e., rock mass weight, don't change with time. A tunnel is projected through the rock mass and, inevitably, will intersect the fracture plane causing a steady groundwater flow from the reservoir to the tunnel (Figure 4.3a).

If the stress-dependent hydraulic conductivity of Eq. (2.12) is considered, the steady flow rate through the fracture under stress and the hydraulic head field can be derived analytically from:

[‡]This verification example is based on the exercise Permeability-Stresses of the MSc course: Hydrodynamic and Transport Processes in underground media, Pierre Perrochet, CHYN.

$$Q = -DK_0(\sigma')\frac{dH}{ds} \quad ; \quad H = h + z \quad ; \quad K_0 = f\frac{a_0^3}{12}\frac{\rho_w g}{\mu_w} \tag{4.16}$$

where s is the local position along the fracture of length L. f is the fracture frequency: $f = \frac{N}{D}$, where N is the number of fractures over the outflow distance D. In this example $f = 1/D$. The detailed effective stress acting orthogonal to the fracture plane is:

$$\sigma' = \sigma(z) - p = \rho_r g z(\lambda n_x^2 + \lambda n_y^2 + n_z^2) - \rho_w g h \tag{4.17}$$

Integrating Eq. (4.16) over H applying two Dirichlet conditions of (1) $H = H_0$ at the upstream end, (2) $H = 0$ at the downstream end of the fracture, and considering the detailed effective stress in Eq. (4.17) yields the following solution:

$$Q = -\frac{DK_0}{L}\int_{H_0}^{0}\left(1 - \left(\frac{\sigma'(H)}{\sigma_0'}\right)^{\frac{1}{n}}\right)^3 dH \tag{4.18}$$

To verify the simulation approach numerical results are compared with those obtained using Eq. (4.18). The three cases of fracture geometry illustrated in Figure 4.3a are considered. The properties within the fracture are: $K_0 = 1$ m s^{-1}, $\sigma_0 = 100$ MPa and $n = 1.0$. The properties of the stiff rock mass are: $\rho_r = 2700$ kg m^{-3} and $\lambda = \nu/(1-\nu) = 0.33$. At the connection with the water reservoir, i.e., the upstream boundary condition, the hydraulic head is constant and matches $H_0 = h + z = 1000$ m, and at the tunnel, i.e., the downstream boundary condition, corresponds to the atmospheric pressure $H = h + z = 0$ m.

Results and discussion

Figure 4.3b compares the distribution of hydraulic head along the fracture obtained with the standard Darcy solution, and by analytical and numerical simulations considering the fracture dependency on effective stress. Figure 4.3c illustrates the difference in hydraulic conductivity along the fracture if considering or not the dependency. Table 4.1 compares the calculated inflow rates.

Table 4.1: Calculated flow rates in tunnel and ratio relative to Darcy standard flow.

Geometry	Q_{Darcy} [m^3/s/m]	$Q_{Analytical}$ [m^3/s/m]	$Q_{Numerical}$ [m^3/s/m]	$\alpha = Q/Q_{Darcy}$
Horizontal	0.500	0.242	0.242	0.484
Vertical	1.000	0.877	0.877	0.877
Oblique	0.447	0.307	0.307	0.687

Note (1) the agreement between numerical and analytical results, (2) the fact that with $n = 1.0$ the fracture closure and decrease in permeability under effective stress is essentially governed by the depth z. Indeed, with $n = 1.0$ the geometry and the λ coefficient have no influence due to the mathematical formulation of the fracture porosity change model: Eq.

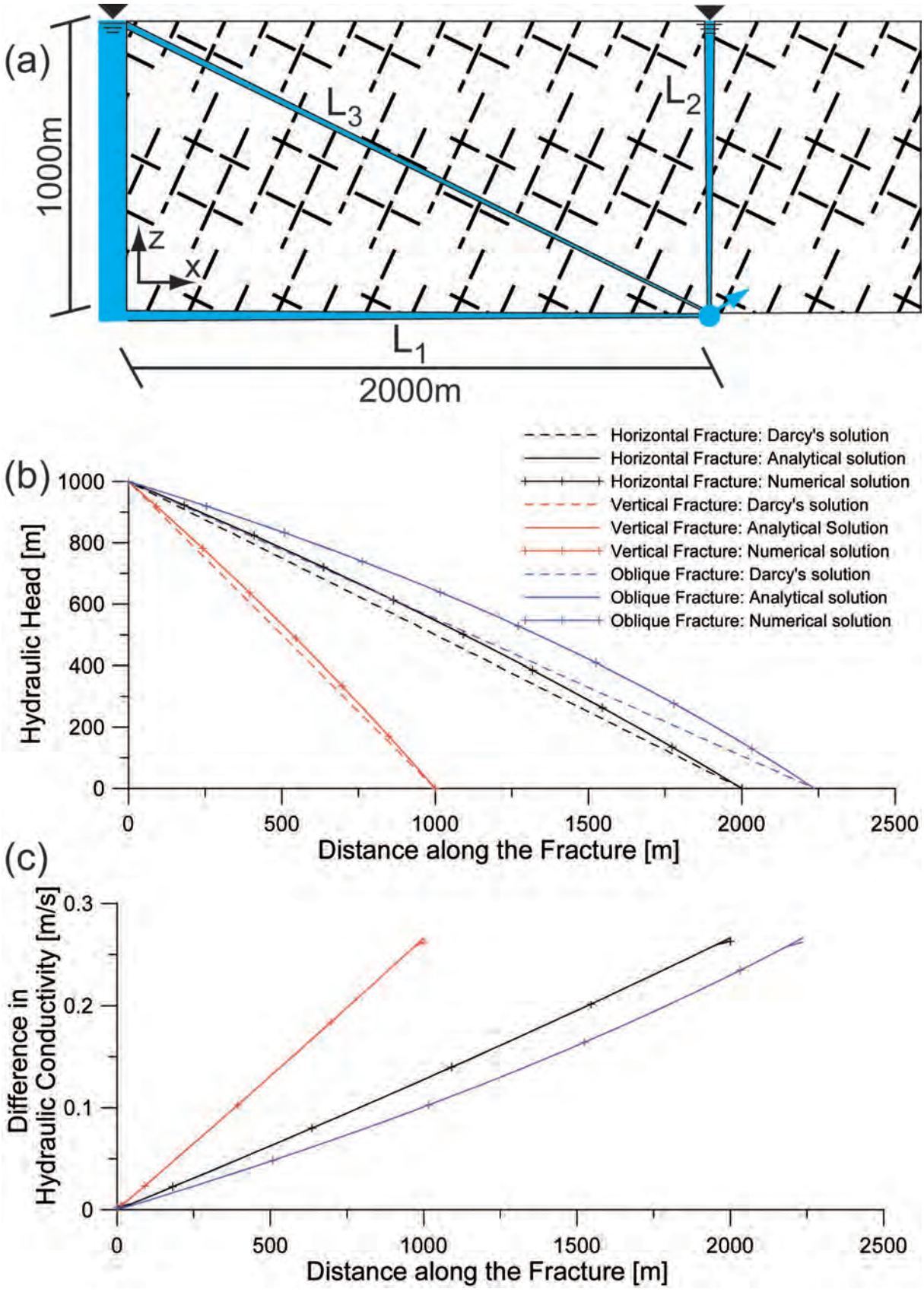

Figure 4.3: (a) Schematic cross section illustrating the three types of fracture geometry tested in the verification example. (b) Hydraulic head and (c) difference in fracture hydraulic conductivity as a function of distance along the fracture: the line color specifies the fracture geometry (black for horizontal, red for vertical and blue for oblique), the line style details the method of calculation (dashed lines for Darcy solutions, solid lines for analytical solutions and solid lines with crosses for numerical solutions).

(2.18). For this example, the reduction in fracture hydraulic conductivity is about a quarter of magnitude between the recharge and the discharge zones (Figure 4.3c).

4.3.2 Transient flow in a horizontal fracture

It is hard to derive an analytical solution for the transient groundwater flow through a fracture under effective stress, because of the non-linearity of the problem. However, to verify the numerical code [1], one approach consists in running the problem with stresses set as zero. In such a case, Eq. (4.8) results in the classical transient diffusion solution, and the numerical results must match those of the following analytical formulas [10, 5]:

$$Q(t)_{Hconstant} = \frac{DKH_0}{L}\left(1 + 2\sum_{m=1}^{\infty} \mathrm{e}^{\left(\frac{-K\pi^2 m^2 t}{S_s L^2}\right)}\right) \tag{4.19}$$

$$Q(t)_{No\ Flow} = \frac{2DKH_0}{L}\sum_{m=1}^{\infty} \mathrm{e}^{\left(\frac{-K\pi^2 (2m+1)^2 t}{4S_s L^2}\right)} \tag{4.20}$$

where H_0 is the hydraulic head at the initial hydrostatic condition. Note that, Eqs. (4.19) and (4.20) are obtained by the method of images [10].

Eq. (4.19) expresses the transient flow rate through a horizontal fracture of hydraulic conductivity K. At the system entry, the fracture is subject to a constant Dirichlet boundary condition matching the initial hydraulic head (in this verification $H = 1000$ m). At the system exit, the hydraulic head corresponds to the atmospheric pressure. Under such conditions, the final flow rate converges to the steady flow rate obtained with Darcy's law.

In Eq. (4.20) a no flow boundary is considered at the system entry. This results in the emptying of the fracture and in a final flow rate of zero.

The same parameters used in the previous verification are considered. The specific storage coefficient is: $S_s = 0.01$.

Results and discussion

Figure 4.4 shows the perfect agreement between analytical and numerical results (stress = 0), and details values obtained if considering the influence of overburden stress and water pressure on hydrodynamic parameters. In such a case, there is a reduction of the flow rate, and the fracture depressurization is slowed due to decreasing fracture hydraulic conductivity and storage with increasing effective stresses.

Note that: (1) with the constant head boundary condition at the fracture entry, final simulated flow rates correspond to those obtained by steady solutions (see Table 4.1). (2) For the no flow boundary condition at the fracture entry and considering no stress, the total volume extracted is:

$$V_{tot} = \int_0^{\infty} Q(t)\, dt = SL\Delta H = \ 20000\ \mathrm{m}^3/\mathrm{m} \tag{4.21}$$

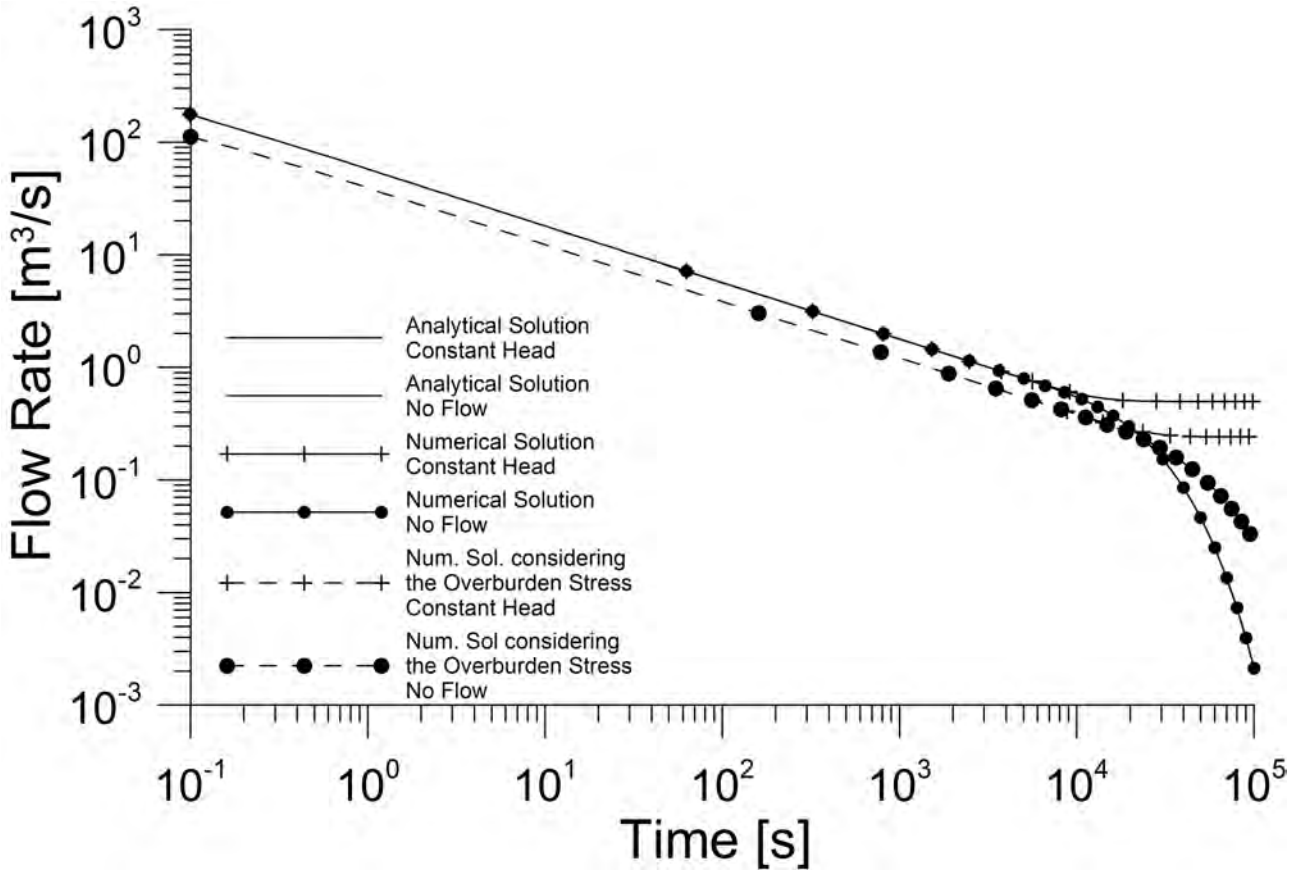

Figure 4.4: Flow rate at the fracture discharge extremity as a function of time. Solid lines detail analytical results, solid lines with symbols numerical results without considering stresses, and dashed lines with symbols numerical results considering stresses. Cross and circle symbols stand for constant head and no flow boundary at the system entry, respectively.

where S is the storage coefficient: $S = S_s\, D$. In this example $S = S_s$.

4.3.3 Consolidation of a column of sediments under flow

A 100 m column of sediments is saturated with water and is at hydrostatic conditions. Then, the bottom boundary of the column is open and a transient groundwater flow occurs until (1) a steady state, if a constant Dirichlet boundary condition is specified at the column top, or (2) the emptying of the column, if there is a no flow boundary condition at the column top. The decrease in water pressure because of flow leads to the column consolidation.

Eq. (4.18) but considering the stress-dependent hydraulic conductivity for granular media, i.e., Eq. (3.12), is used to verify the steady flow rate obtained with `Ground Water` [1]. The deformation and vertical consolidation reproduced with the numerical code are verified by the 1-dimensional application of Eqs. (3.16) and (3.17).

The verification is run for a homogeneous and heterogeneous column, parameter values are specified in Table 4.2. Note that suction and others non-saturated phenomena are neglected, because they do not affect hydromechanical processes.

Table 4.2: Parameter values used in the verification example: consolidation of a column of sediments under flow. Strata thickness is from the bottom of the column.

Lithology	Strata Thickness [m]	ρ_r [kg/m^3]	ϕ_0	σ'_0 [MPa]	E [MPa]	C [1/m]	b	K_0 [m/s]	S_{s_0} [1/m]
Homogeneous Case									
Fine Sand	100	1800	0.23	26	100	10000	20	10^{-5}	$9.9 \cdot 10^{-5}$
Heterogeneous Case									
Fine Sand	36.36	1800	0.23	26	100	10000	20	10^{-5}	$9.9 \cdot 10^{-5}$
Clayey Silt	24.24	1400	0.40	5.1	10	150000	20	$3.8 \cdot 10^{-7}$	$9.8 \cdot 10^{-4}$
Fine Sand	39.40	1800	0.23	26	100	10000	20	10^{-5}	$9.9 \cdot 10^{-5}$

Results and discussion

Table 4.3 shows numerical and analytical steady flow rates for the first scenario with a constant Dirichlet boundary condition specified at the column top, and consolidations of the column due to (scenario 1) the change from hydrostatic to hydrodynamic steady flow, and (scenario 2) the system emptying, i.e. from hydrostatic to empty. Notice the agreement between results. The little difference between analytical and numerical results for the heterogeneous consolidation case becomes from a different treatment of the change in porosity, in particular at the contact between strata. In the analytical computation, the change in porosity is computed at a given point/node. This implies a sudden variation at interfaces. On the contrary with the finite element method, the change in porosity is calculated at nodes, interpolated at Gauss points, and distributed on the element. This results in a negligible difference.

Table 4.3: Numerical and analytical steady flow rates through the column of sediments, and column consolidations because of flow.

	Homogeneous	Heterogeneous
Scenario 1		
Analytical Steady Flow Rate [m^3/s/m]	$0.892 \cdot 10^{-5}$	no solution
Numerical Steady Flow Rate [m^3/s/m]	$0.892 \cdot 10^{-5}$	$0.859 \cdot 10^{-6}$
Darcy's Steady Flow Rate [m^3/s/m]	$0.994 \cdot 10^{-5}$	$0.141 \cdot 10^{-5}$
Analytical Consolidation [m]	0.367	0.861
Numerical Consolidation [m]	0.367	0.831
Scenario 2		
Analytical Consolidation [m]	0.381	1.068
Numerical Consolidation [m]	0.381	1.067

For both scenario, an important conclusion is that hydraulic gradients increasing considering the dependency. This implies that the depressurisation of the system, and consequently the consolidation, is significantly slowed compared to the solutions obtained with the linear form of Darcy's law, especially in case of system emptying (Figure 4.5 a-b).

Another important conclusion in terms of deformation due to groundwater pressure is that an unconfined aquifer system is at its maximum expansion at fully saturated hydrostatic con-

ditions, and at its maximum consolidation if it is empty. The hydrodynamic case represents an intermediate state. Figure 4.5 c-d illustrates changes in porosity and consolidations calculated via analytical and numerical analysis for scenario 2, and for a homogeneous and heterogeneous column of sediments, respectively.

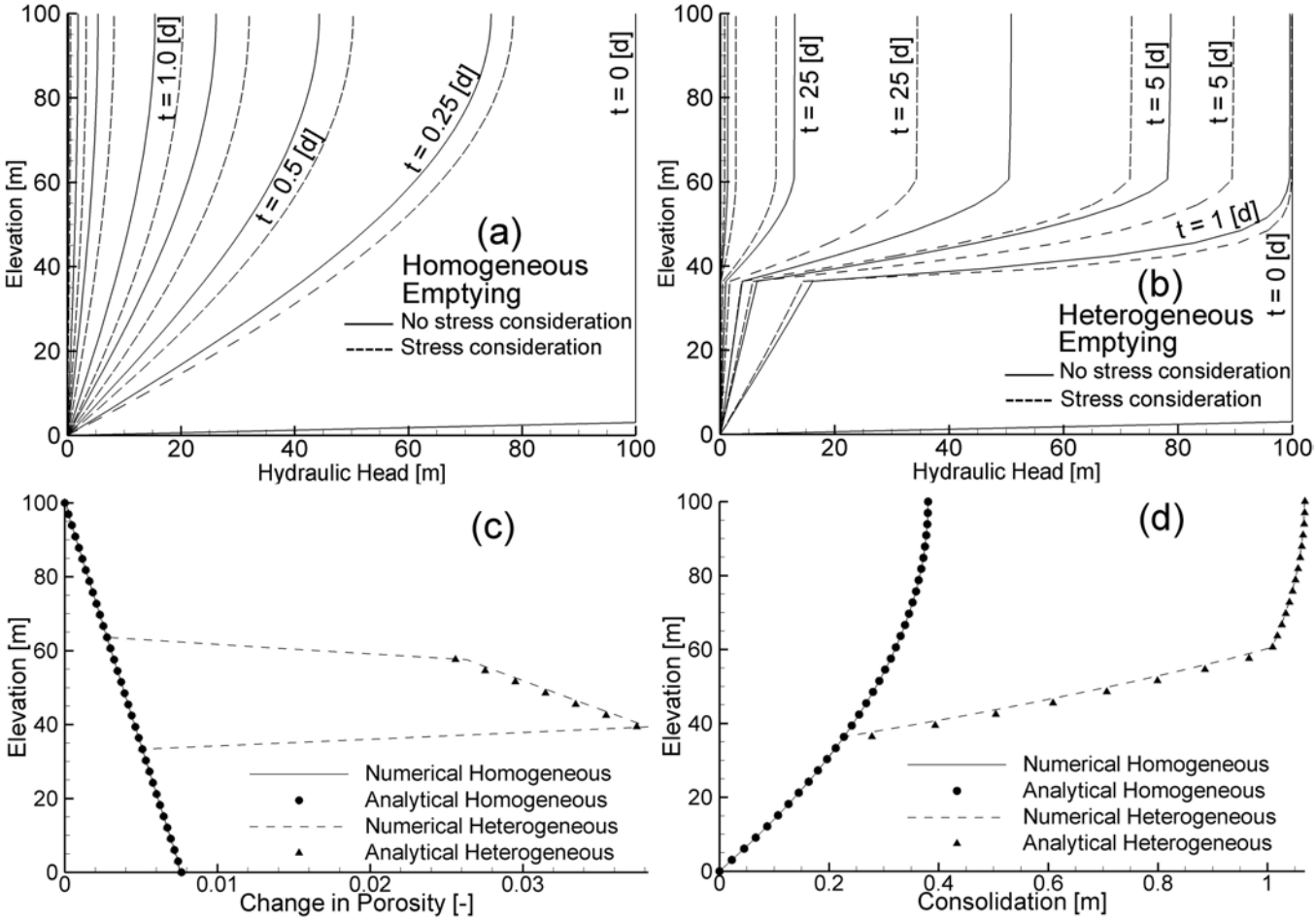

Figure 4.5: Hydraulic head as a function of elevation at different times of scenario 2 taking into account the stress dependency (dashed lines) or not (solid lines) for (a) a homogeneous and (b) a heterogeneous column of sediments. (c) Change in porosity and (d) consolidation due to the emptying of the column of sediments (homogeneous and heterogeneous): lines stand for numerical calculations, symbols for analytical.

4.3.4 2D/3D verification: flow in a horizontal fractured rock mass under stress

A rock mass 2000 m long, 1000 m large, and 1000 m height is horizontally fractured (Figure 4.7a). The horizontal joints have an aperture of $a = 0.1$ mm and a frequency of $f = 100$/m. Using the cubic law, Eq. (2.11), this leads to a no stress hydraulic conductivity for the fractured rock of $K_0 = 7.27 \cdot 10^{-5}$ m s^{-1}. The properties within the rock mass are: $\rho_r = 2500$ kg m^{-3}, $\sigma'_0 = 350$ MPa and $\lambda = 1.00$. Note that, despite a λ ratio of unity, there is no effect of horizontal stresses on fractures because they are horizontal (only vertical closure).

At the coordinate $x = 0$ m and over the full width, the fractured rock mass is under a constant hydraulic head of $H_0 = 1000$ m. On the contrary, the hydraulic head on the other extremity ($x = 2000$ m) is at a constant atmospheric pressure (Figure 4.7a). Originally the fractured rock mass was subject to hydrostatic conditions matching the rock height (1000 m). The afore-mentioned boundary conditions lead to a steady groundwater flow and to the consolidation of the rock mass due to the change from hydrostatic to hydrodynamic conditions.

In such a system, analytical solutions for the steady flow rate and for the pressure head field can be derived only in the case of a n coefficient of 1. In such a case, the steady groundwater flow rate Q through the fractured rock mass is:

$$q(x,z) = K_0 \int_0^L \left(1 - \left(\frac{\alpha P - h(x,z)}{s_0}\right)^1\right)^3 \, dH \tag{4.22}$$

where q is the unitary discharge rate, P is depth, L is the length of fractures in the x-direction (2000 m), and α and s_0 correspond to: $\alpha = \rho_r/\rho_w$, $s_0 = \sigma_0'/\rho_w/g$, respectively. The fractured rock mass is isotropic in the y-direction implying the volumetric discharge rate:

$$Q = \Delta y \int_{z=0}^{z=H_0} q(x,z)dz \tag{4.23}$$

where Δy matches 1000 m.

The pressure head field within the flow system is:

$$\begin{aligned} h(x,y,z) \;=\; & \left[(\alpha P - h_0 - s_0)^4 - \frac{x{h_0}^2}{l}(2\alpha P - h_0 - 2s_0)^2 + \frac{x^2 h_0}{l}(2\alpha P - h_0 - 2s_0)(\alpha P - s_0)^2\right]^{1/4} \\ & -s_0 + \alpha P \end{aligned} \tag{4.24}$$

where h_0 is the pressure head at the initial hydrostatic condition: $h_0 = 1000$ - z, and l is the length along the x-axis. The analytical rock mass deformation and consolidation are then computed using the pressure head field and Eqs. (2.18), (2.19).

Results and discussion

Results are presented in Table 4.4 and in Figures 4.6 and 4.7. Note the perfect agreement between numerical and analytical solutions. Not surprisingly, the maximum consolidation is located at the discharge boundary, where the greatest change in water pressure from the hydrostatic to the hydrodynamic state occurred (Figure 4.7d).

4.3.5 Reproduce the excavation of tunnels in groundwater flow models

In regional 3D groundwater flow models, one approach to simulate the excavation of tunnels through saturated lithologies consists in considering the structure as a time-varying inner

Table 4.4: Calculated analytical and numerical steady flow rates and maximum consolidations.

	Flow Rate [m^3/s] no stress consideration	Flow Rate [m^3/s] stress consideration	Maximum consolidation [m]
Analytical	18.173	16.222	0.140
Numerical	18.173	16.222	0.140

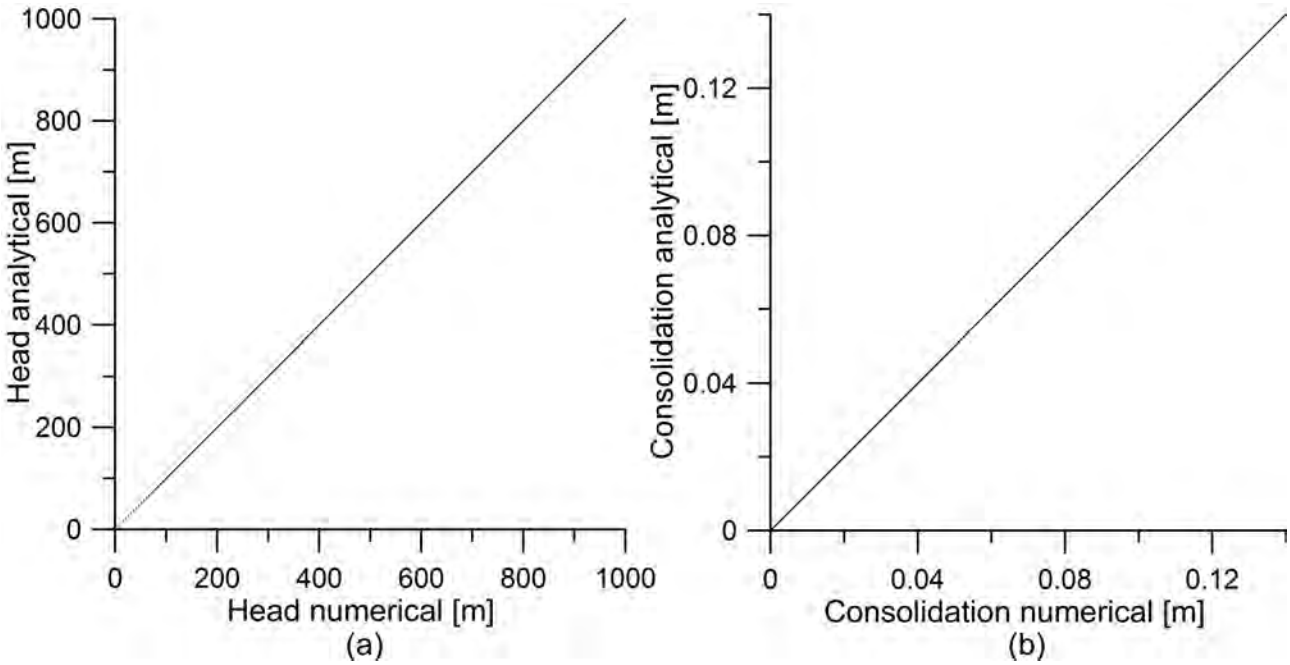

Figure 4.6: Perfect equality between analytical and numerical (a) hydraulic heads and (b) consolidations.

boundary [7]. Tunnel nodes become active as Dirichlet boundary condition at constant atmospheric pressure (elevation head) with reference to the excavation recorded data. In the special case, where the tunnel drainage empties the saturated lithologies, e.g., in case of no recharge zones, a constraint of no recharge flow rate must be prescribed on upper nodes of the tunnel. This prevents these nodes to supply the model when the water table is lower their elevation. A disadvantage of this discretization method is the presence of the tunnel as an inactive hole in the mesh since the start of the calculation. However, this approach is not computationally demanding compared to moving grid methods reproducing the advance of tunnel front, and is practical at regional geological scales. An important note is that the finite element mesh must be refined as much as possible around the tunnel. This because in the model the active hydraulic radius of the tunnel also includes half of the size of neighboring elements. This radius is of major importance in the computation of the flow rate in tunnel.

The analytical formula of Perrochet and Dematteis [11] solving for the transient discharge rate produced by the excavation of a tunnel in a heterogeneous formation can be used to control `Ground Water` [1] when dealing with time-varying inner boundary, constraints and

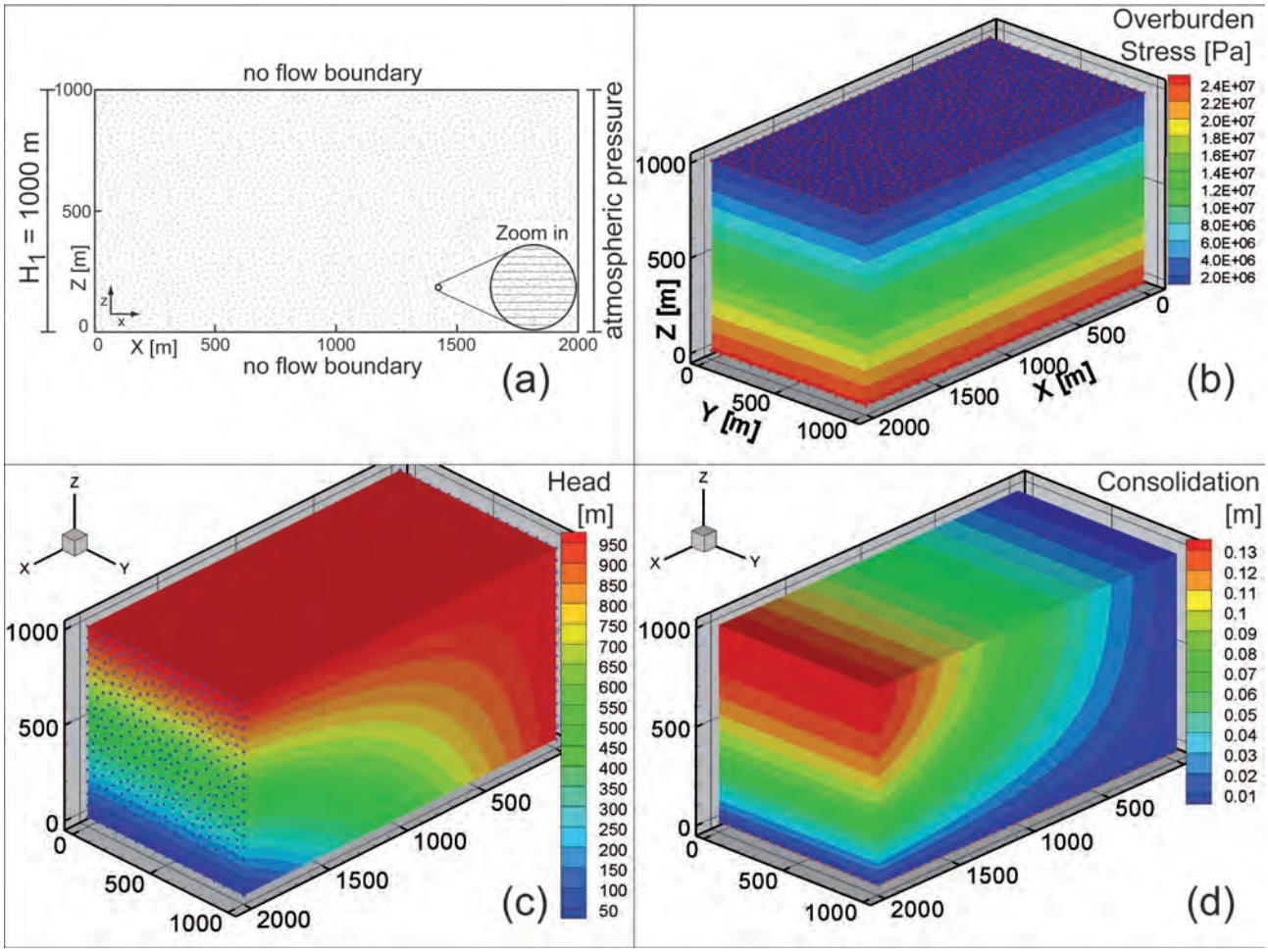

Figure 4.7: (a) Model geometry and boundary conditions for the verification 4.3.4, and simulated (b) overburden stress, (c) hydraulic head, and (d) consolidation fields. Points correspond to nodes with a boundary condition.

stress-dependency:

$$Q(t) = 2\pi \sum_{i=1}^{N} \mathrm{H}(t - t_i) \int_0^{v_i(t-t_i)} \frac{K_i s_i \mathrm{H}(L_i - x)}{\ln\left[1 + \sqrt{\frac{\pi K_i}{S_i {r_i}^2}\left(t - t_i - \frac{x}{v_i}\right)}\right]} dx \tag{4.25}$$

where for each tunnel sector i, t is the time, t_i is the sector entry excavation time, H(u) is the Heaviside step-function, v_i is the excavation speed, s_i is the drawdown at the tunnel, L_i is the length over which the tunnel intersects the ith sector, x is the spatial coordinate along the tunnel axis with an origin at the entry of the permeable zone, and S_i is the specific storage coefficient.

The flow rate curve generated by the excavation of the Modane/Villarodin - Bourget exploratory adit for the basis tunnel of the Lyon-Turin railway project [11, 13, 9, 2] is used for the verification model. This tunnel was excavated by drill & blast in metamorphic impervious quartzites crossed by subvertical fault zones characterized by cargnieules and mylonitic marbles having a permeable character [11]. Groundwater inflows into the tunnel were recorded in the

first 1000 m, then the excavation was dry. The permeable sectors are subject to low recharge rates, and the tunnel drainage caused heavy water table drawdown. The tunnel radius is 5 m.

Figure 4.8a shows the geological cross section along the Modane/Villarodin - Bourget exploratory adit. On the basis of this cross section, the analytical solution of [11] was used to reproduce the transient flow rate in tunnel during the excavation phase. For the verification, the numerical model was constructed respecting the assumptions and geological sectors of the analytical model (Figure 4.8b). As done before, the stress field is set to zero, in order to maintain constant hydraulic conductivities.

Results and discussion

Figure 4.8c illustrates analytical and numerical simulated flow rates in tunnel, and the time function describing the excavation history. The little difference between analytical and numerical results is probably due to (1) the tunnel discretization: in the analytical model the tunnel is a circle, in the numerical model the tunnel is a square of equivalent area; (2) the numerical model can not be infinite. Parametric information are based on [11] and are presented in Table 4.5. Note that (1) in this verification there are two additional sectors compared to [11], (2) the assumption of radiality allows the numerical model to be reduced to a quarter of the total domain (Figure 4.8b).

Table 4.5: Geologic, hydrogeologic and parametric information used for the verification (modified from [11]). s_i and L_i stand for drawdown at the tunnel and sector length, respectively.

	Geology	L_i [m]	s_i [m]	K_i [m s^{-1}]	S_i [m^{-1}]
1	Quartzites	191	5	10^{-8}	10^{-3}
2	Quartzites with cargnieules	160	25	10^{-6}	10^{-1}
3	Cargnieules and faults	14	75	10^{-5}	10^{-1}
4	Mylonitic marbles and faults	6	75	$5 \cdot 10^{-5}$	10^{-1}
5	Quartzites	35	75	10^{-8}	10^{-3}
6	Quartzites and faults	52	75	10^{-6}	10^{-1}
7	Quartzites	153	75	10^{-8}	10^{-3}
8	Quartzites with cargnieules	36	105	10^{-6}	10^{-1}
9	Cargnieules and faults	9	105	10^{-5}	10^{-1}
10	Quartzites	168	105	10^{-8}	10^{-3}
11	Cargnieules and faults	6	105	10^{-5}	10^{-1}
12	Quartzites and schists	256	105	10^{-8}	10^{-3}

4.4 3D example: the Rawyl tunnel and the Zeuzier arch dam

The Rawyl tunnel and the Zeuzier arch dam are located in the Canton Valais, Switzerland, close to the city of Sion (Fig. 4.9a). From a geological point of view, the dam and the tunnel

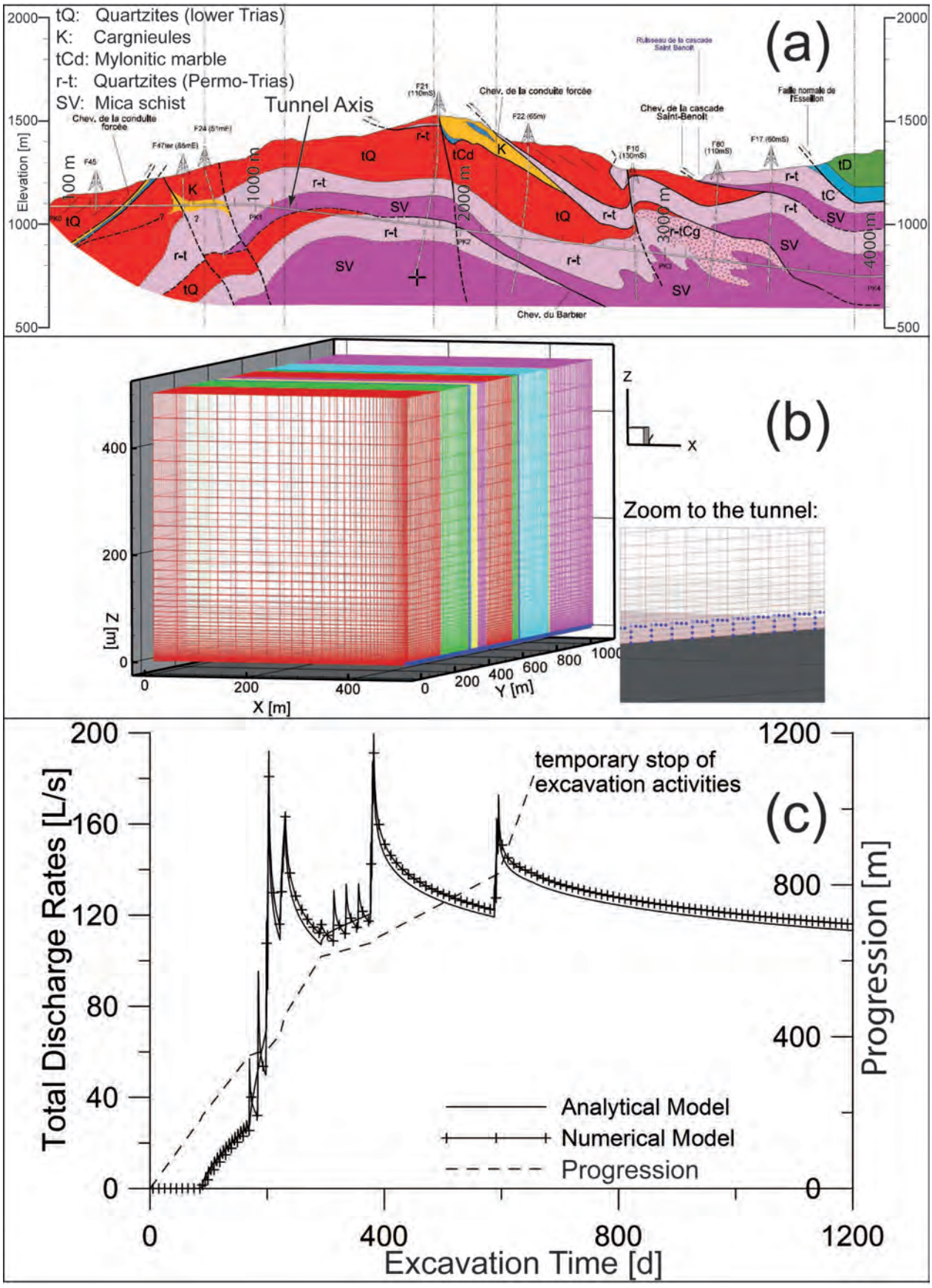

Figure 4.8: (a) Cross section along the Modane/Villarodin - Bourget exploratory adit (modified from [13]). (b) 3D view of a quarter of the numerical model for the verification simulation with zoom to the tunnel discretization, tunnel nodes are highlighted by blue points. (c) Simulated discharge rates and tunnel progression as a function of excavation time: analytical (solid line) and numerical (solid line with symbols) results. Dashed line illustrates excavation progression.

are situated in the Helvetic nappe system of the Swiss Alps, more precisely in the Wildhorn nappe. At the end of 1978, the Zeuzier arch dam showed an abnormal deformation. The board of experts proposed the following conceptual model to explain the dam deformation:

1) An exploratory adit under construction, the Rawyl tunnel, drained, through vertical and subvertical faults (Figure 4.10a), an underlying confined aquifer in the fractured Dogger sedimentary rocks. Extremely high flow rates (maximum of 1000 L/s) were drained by the tunnel at the crossing of subvertical fault zones. The discharge rate dropped rapidly to a steady state (40 L/s), corresponding to the aquifer recharge (Fig. 4.11b).

2) The release of the water pressures in the fractures leads to an increasing effective stress distribution in the rock mass, resulting in the closure of fracture porosity, and in the consolidation of the confined aquifer. This consolidation resulted in the regional settlement, which affected also the overlying massive Malm limestones that constitute the foundation of the Zeuzier arch dam. The settlement at the valley bottom reached finally about 13 cm.

More details on this case study can be found in: [12, 6]. Figure 1.9 in the subsection 1.6.1 of the Introduction 1 shows a cross section along the Rawyl exploratory tunnel, a cross section between the Zeuzier arch dam and the Rawyl adit, and the data measured about flow rate in tunnel and deviation of the dam medium pendulum as a function of time.

The multi-purpose `Ground Water` finite element software [1] is used to model the present case study. The detailed regional finite element mesh considering the topography and the geology of the Zeuzier area (Figure 4.9b) was constructed using the mesh generator `GMSH` [4].

The first step consists in the calculation of the lithostatic stress field. The simulation domain is composed of two material classes: the non aquifer sedimentary rocks (mainly composed of Malm limestones) and the aquifer, both having a density of 2200 kg/m^3 (Fig. 4.9b). At the top of the domain a Dirichlet boundary condition is specified, that matches a zero stress state (except for the nodes forming the bottom of the dam lakes, whose stress corresponds to the weight of the above water column). At the bottom of the aquifer the implicit Neumann condition $-g\rho_{r_{bottom}}$ is indicated.

The resulting stresses are then used in the groundwater transient flow model. The domain presented in Fig. 4.9b is reduced to the aquifer and to six vertical faults, introduced in the 3D domain as 2D discrete structures. Note that, rock masses form a local fold near the dam, which extends to the aquifer (Figure 4.10b). The geometry of this fold has been simplified to allow the finite element discretization (Fig. 4.11a). The tunnel is discretized as a square of 4 m edge, representing a hole in the mesh, which crosses the faults. Constant atmospheric pressures are specified at the tunnel nodes, this Dirichlet boundary condition is activated according to a time function of excavation progression. The initial heads present in the model matches 1400 m a.s.l. The aquifer recharge has been neglected, because of its low value as compared to the discharge rate drained by the tunnel. The model is calibrated using the measured discharge rate drained by the Rawyl exploratory adit, by varying the hydraulic conductivity and the specific storage coefficient of faults and aquifer (Fig. 4.11b). The hydrodynamic parameters of the aquifer in the Dogger formation are considered as stress-dependent. On the contrary, the vertical faults

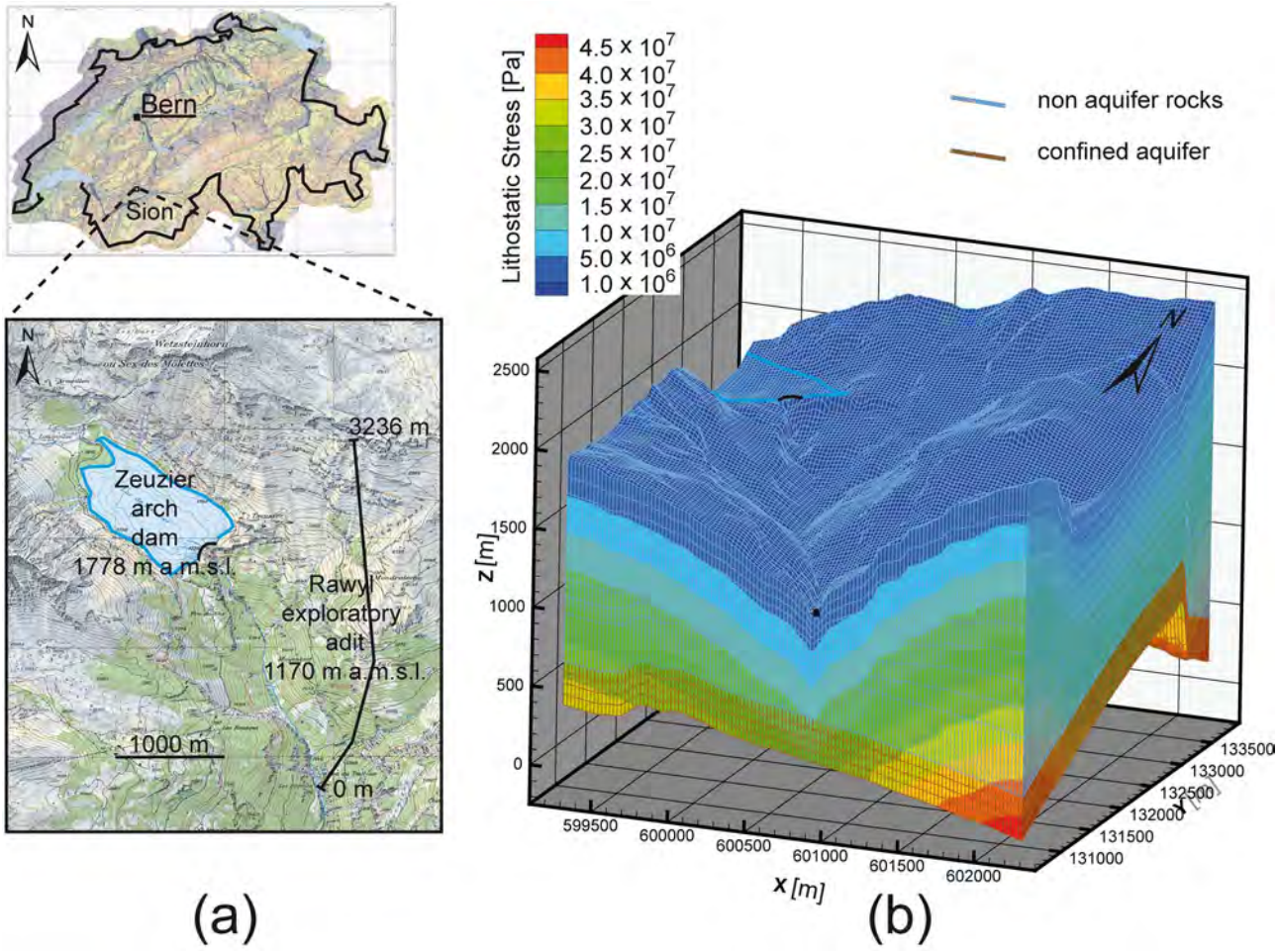

Figure 4.9: (a) Location and information about the Zeuzier arch dam and the Rawyl tunnel site. (b) Simulated lithostatic stress field, and material classes forming the domain.

are set as stress-independent because of their vertical geometry (no Poisson's ratio or horizontal stresses effects). The calibrated parametric information are shown in Table 4.6.

Using Eqs. (2.18) and (2.19) and the final pressure head distribution as input, consolidation and settlement are computed. The change in porosity only takes place in the aquifer, where the pressure head varied; no deformation occurs in the overlying non aquifer sedimentary rocks. The model assumes a total migration of the consolidation to the surface, as indicated by [3] for groundwater systems. The computed settlement near the dam at the valley bottom is 8 cm. Maximum simulated subsidence reaches about 20 cm, and is located at the valley bottom between coordinates 131'500-132'300 °N and 600'100-600'250 °E. Here, the change in porosity and the consolidation are important because: (1) the confined aquifer is nearly cropping out (low lithostatic stress), and consequently the fracture porosity was high; (2) after the excavation of the Rawyl tunnel there is a wide drop in water pressure leading to significant closure of fracture porosity (Fig. 4.12).

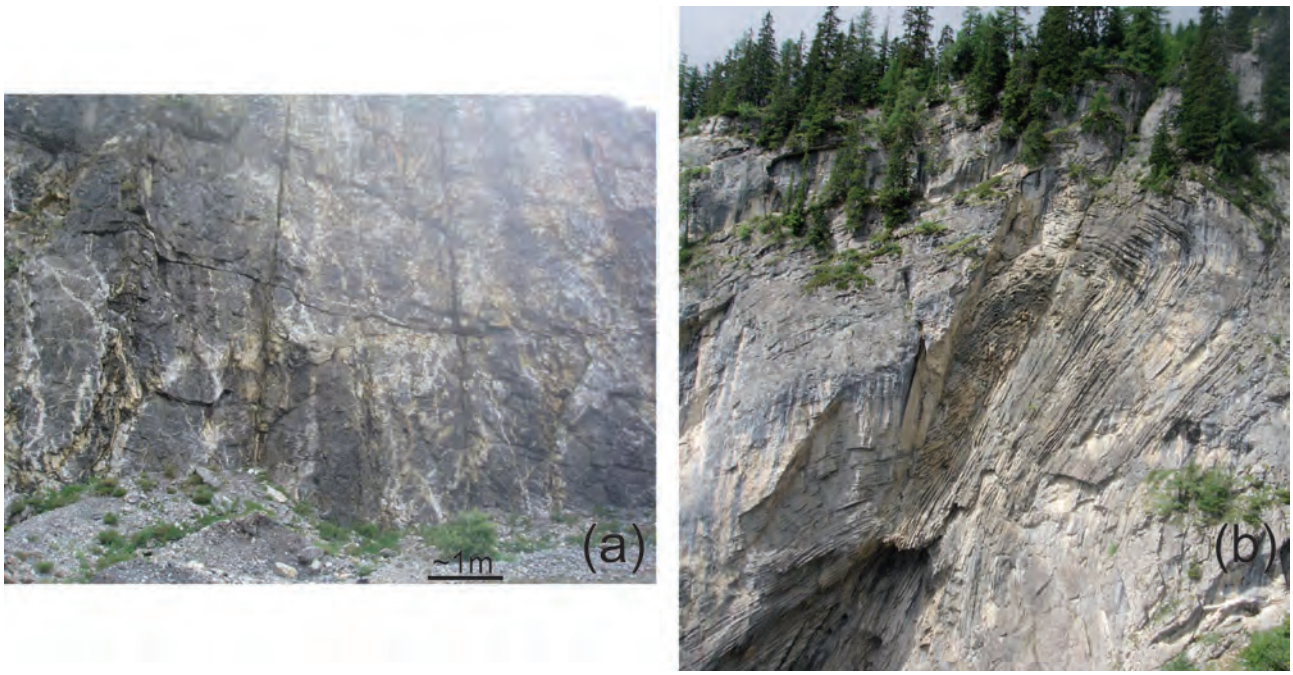

Figure 4.10: (a) Subvertical faults near the Zeuzier arch dam, such structures allowed the flow of groundwater from the unexpected aquifer in the Dogger formations to the Rawyl exploratory adit (photograph by G. Preisig, August 2011). (b) Local fold near the Zeuzier arch dam, named: Pli de Zeuzier in Figure 1.9a (photograph by G. Preisig, August 2011).

Table 4.6: Parametric information used in "the Rawyl tunnel and the Zeuzier arch dam" model.

Overburden Stress Model					
Geology	ρ_r [kg m^{-3}]				
Non aquifer rocks	2200				
Confined aquifer	2200				
Groundwater Flow Model					
Geology	K [m s^{-1}]	S_s [m^{-1}]	σ_0' [MPa]	n	
Confined aquifer	$7.3 \cdot 10^{-5}$	$4.3 \cdot 10^{-8}$	100	3.1	
Fault 1	$5.0 \cdot 10^{-4}$	$1.0 \cdot 10^{-4}$			
Fault 2	$5.0 \cdot 10^{-6}$	$1.0 \cdot 10^{-3}$			
Fault 3	$5.0 \cdot 10^{-5}$	$1.0 \cdot 10^{-3}$			
Fault 4	$1.0 \cdot 10^{-3}$	$1.0 \cdot 10^{-3}$			
Fault 5	$1.0 \cdot 10^{-5}$	$1.0 \cdot 10^{-3}$			
Fault 6	$5.0 \cdot 10^{-3}$	$1.0 \cdot 10^{-4}$			
Consolidation Model					
Geology	f [m^{-1}]	a [m]	$\mathbf{n} = [n_x, n_y, n_z]$	σ_0' [MPa]	n
Confined aquifer	100	10^{-4}	[0,0,1]	100	3.1

4.5 Conclusions

Effective stress plays an important part in groundwater flow, especially for deep confined aquifer. These effects must be considered also in fractured rocks.

A modelling method for fluid-to-solid coupled hydromechanical processes in fractured and

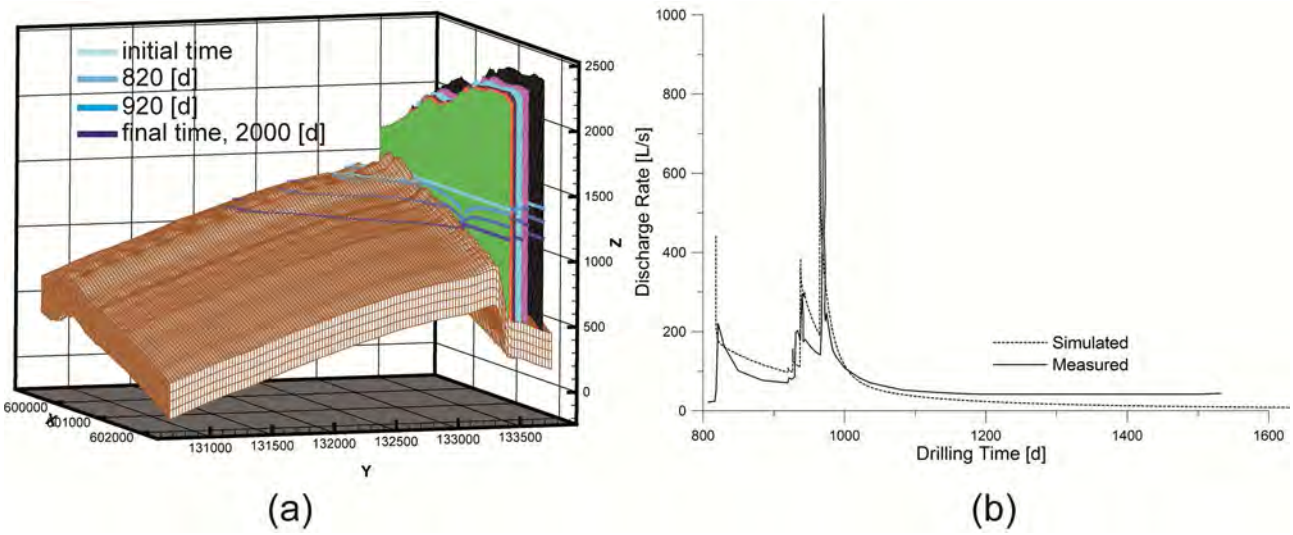

Figure 4.11: (a) Evolution of the water table level with excavation progression, and groundwater flow domain. (b) Discharge rate drained by the exploratory tunnel as a function of excavation progression time (measured data, solid line; modelled data, dashed line).

granular porous aquifers has been described, verified and illustrated. Stress-dependent parameters are used to solve the governing equations of groundwater flow and aquifer deformation. First the overburden stress field is computed, solving an original and very practical boundary value problem. A non-linear form of the groundwater flow equation is then solved, followed by the solution of a second original boundary value problem providing aquifer consolidation/expansion.

The present approach is limited to fluid-to-solid hydromechanical phenomena at hydrogeological scales because of the following assumptions: (1) the stress field remains constant during water depletion/recovery, (2) deformation results only from the closure/opening of porosity, (3) the validity of Hooke's law for small strains, and (4) horizontal deformations are neglected. All these assumptions are reasonable for groundwater problems [3, 14].

In this context, this approach can be used to study the sensitivity of aquifers on decreasing/increasing water pressures. Especially in the presence of civil engineering works, such as dams or tunnels; and in projects of geologic radioactive waste repositories or CO_2 sequestration fields.

Bibliography

[1] Cornaton, F.J.: Ground Water: a 3-D Ground Water and Surface Water Flow, Mass Transport and Heat Transfer Finite Element Simulator, Reference Manual, 398 pp. Centre for Hydrogeology and Geothermics, Neuchâtel, Switzerland (2007)

[2] Dematteis, A., Perrochet, P., Thiery, M.: Nouvelle liaison ferroviaire transalpine Lyon-Turin, Etudes hydrogéologiques 2002-2004. Tech. rep., Lyon Turin Ferroviaire, Chambéry, France (2005)

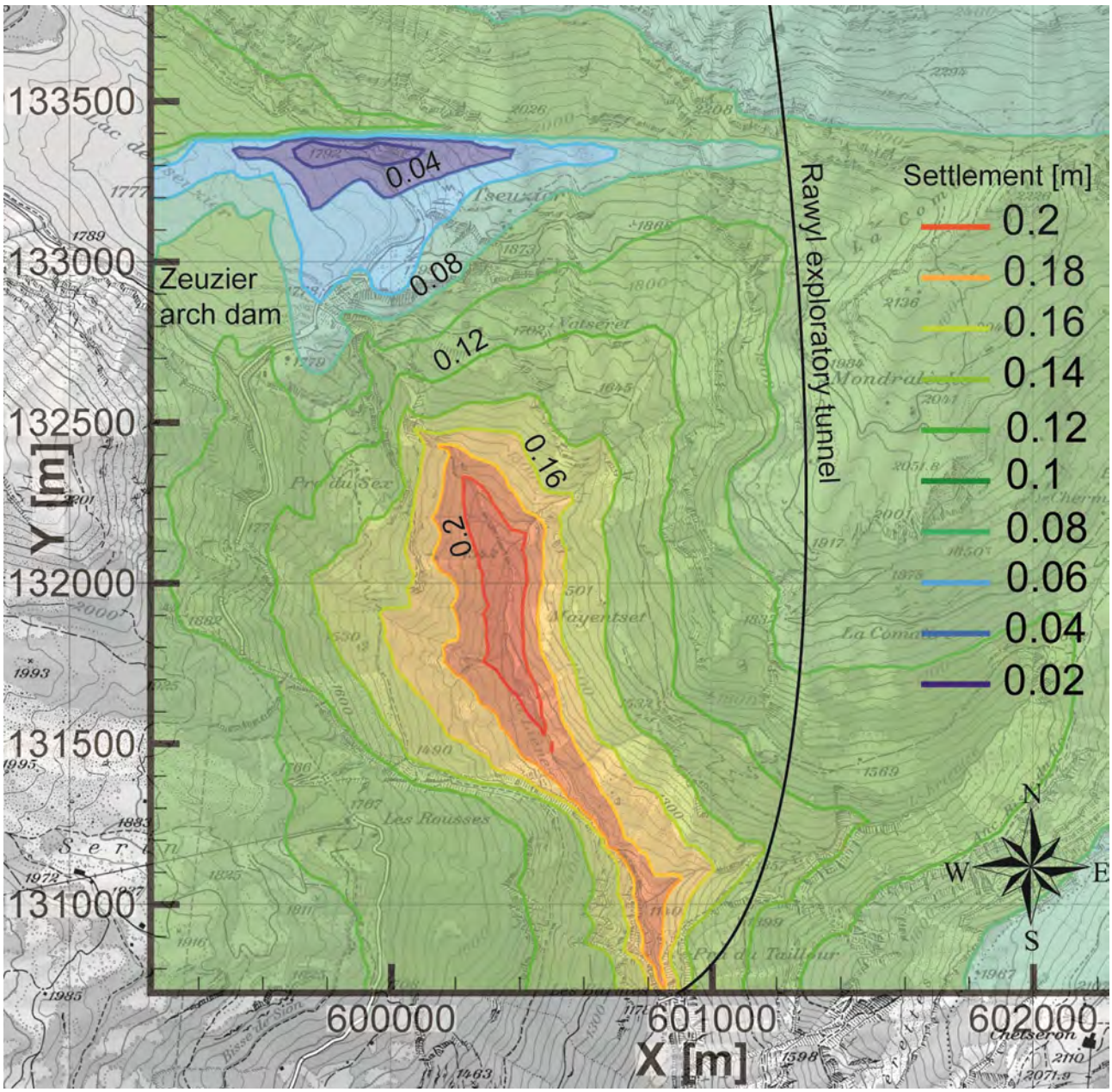

Figure 4.12: Simulated settlement map resulting from the final distribution of water pressures. The tunnel drains the system; this depressurization causes aquifer consolidation.

[3] Gambolati, G., Teatini, P., Ferronato, M.: Encyclopedia of Hydrological Sciences, chap. Anthropogenic Land Subsidence, p. 17pp. Anderson M.G., John Wiley & Sons (2005)

[4] Geuzaine, C., Remacle, J.F.: Gmsh: a three-dimensional finite element mesh generator with built-in pre- and post-processing facilities. International Journal for Numerical Methods in Engineering **79**(11), 1309–1331 (2009)

[5] Kovács, A., Perrochet, P.: A quantitative approach to spring hydrograph decomposition. Journal of Hydrology **352**, 16–29 (2008)

[6] Lombardi, G.: Les tassements exceptionnels au barrage de Zeuzier. Publ. Swiss Soc. Soil Rock Mech. **118**, 39–47 (1988)

[7] Molinero, J., Samper, J., Juanes, R.: Numerical modeling of the transient hydrogeological response produced by tunnel construction in fractured bedrocks. Engineering Geology **64**(4), 369–386 (2002)

[8] Parriaux, A.: Géologie: Bases pour l'Ingénieur. Presses Polytechniques et Universitaires Romandes (2006)

[9] Perrochet, P.: Facteur de réduction des débits en tunnels profonds. Tech. rep., Centre d'Hydrogéologie Neuchâtel, Neuchâtel, Suisse

[10] Perrochet, P.: Personal communication

[11] Perrochet, P., Dematteis, A.: Modeling Transient Discharge into a Tunnel Drilled in a Heterogeneus Formation. Ground Water **45**(6), 786–790 (2007)

[12] Schneider, T.: Geological Aspects of the Extraordinary Behaviour of Zeuzier Arch Dam. Wasser, energie, luft - eau, énergie, air **74**(3), 81–94 (1982)

[13] SOGREAH Consultants: Descenderie de Modane/Villarodin-Bourget: étude de faisabilité de reutilisation des eaux d'exhaure de la partie montante. Tech. rep., Lyon Turin Ferroviaire (LTF), Chambery, France (2007)

[14] Verruijt, A.: Encyclopedia of Hydrological Sciences, chap. Consolidation of Soils, p. 15pp. Anderson M.G., John Wiley & Sons (2008)

[15] Vulliet, L., Koelbl, O., Parriaux, A., Védy, J.C.: Gutachtenbericht über die Setzungen von St. German, in Auftrag der BLS Alptransit AG. Tech. rep. (2003)

Chapter 5

Application to real cases, part I: modelling discharge rates and ground settlement induced by tunnel excavation*

Abstract

Interception of aquifers by tunnel excavation results in water inflow and leads to drawdown of the water table which may induce ground settlement. In this Chapter, analytical and numerical models are presented which specifically address these groundwater related processes in tunnel excavation. These developed models are compared and their performance as predictive tools is evaluated. Firstly, the water inflow in deep tunnels is treated. It is shown that introducing a reduction factor accounting for the effect of effective stress on hydrodynamic parameters avoids overestimation. This effect can be considered in numerical models using effective stress-dependent parameters. Then, quantification of ground settlement is addressed by a transient analytical solution. These solutions are then successfully applied to the data obtained during the excavation of the La Praz exploratory tunnel in the Western Alps (France), validating their usefulness as predictive tools.

5.1 Introduction

Tunnel excavation modifies the natural hydrodynamic behaviour of groundwater systems. Under saturated conditions, tunnels behave as drainage structures causing drawdown of the water table. Depending on rock hydraulic conductivity, this may result in high flow rates into the underground excavation coupled with decreasing water pressures. Water inflow is a major cause which negatively affects tunnel progression, particularly when underestimated by the design phase. An example for this is shown in Figure 5.1, where the total tunnel discharge rate and

*This Chapter is based on the paper:
Preisig, G., Dematteis, A., Torri, R., Monin, N., Milnes, E., and Perrochet, P.: Modelling Discharge Rates and Ground Settlement induced by Tunnel Excavation. Rock Mechanics and Rock Engineering, DOI 10.1007/s00603-012-0357-4 (2013).

excavation progression are presented as a function of time as well as the encountered geology. From 340 m to 380 m the geology indicates a permeable sector of cargneules, mylonitic marbles and faults correlating with the first water inflow and the slowing down of excavation progression [34]. The highest water inflow occurred at the end of the permeable sector before the excavation speed increased again. From this point onward the total tunnel discharge rate can no longer be directly correlated with the excavation speed since the major part of water inflow occurs along an already excavated tunnel section. Another issue of concern related to

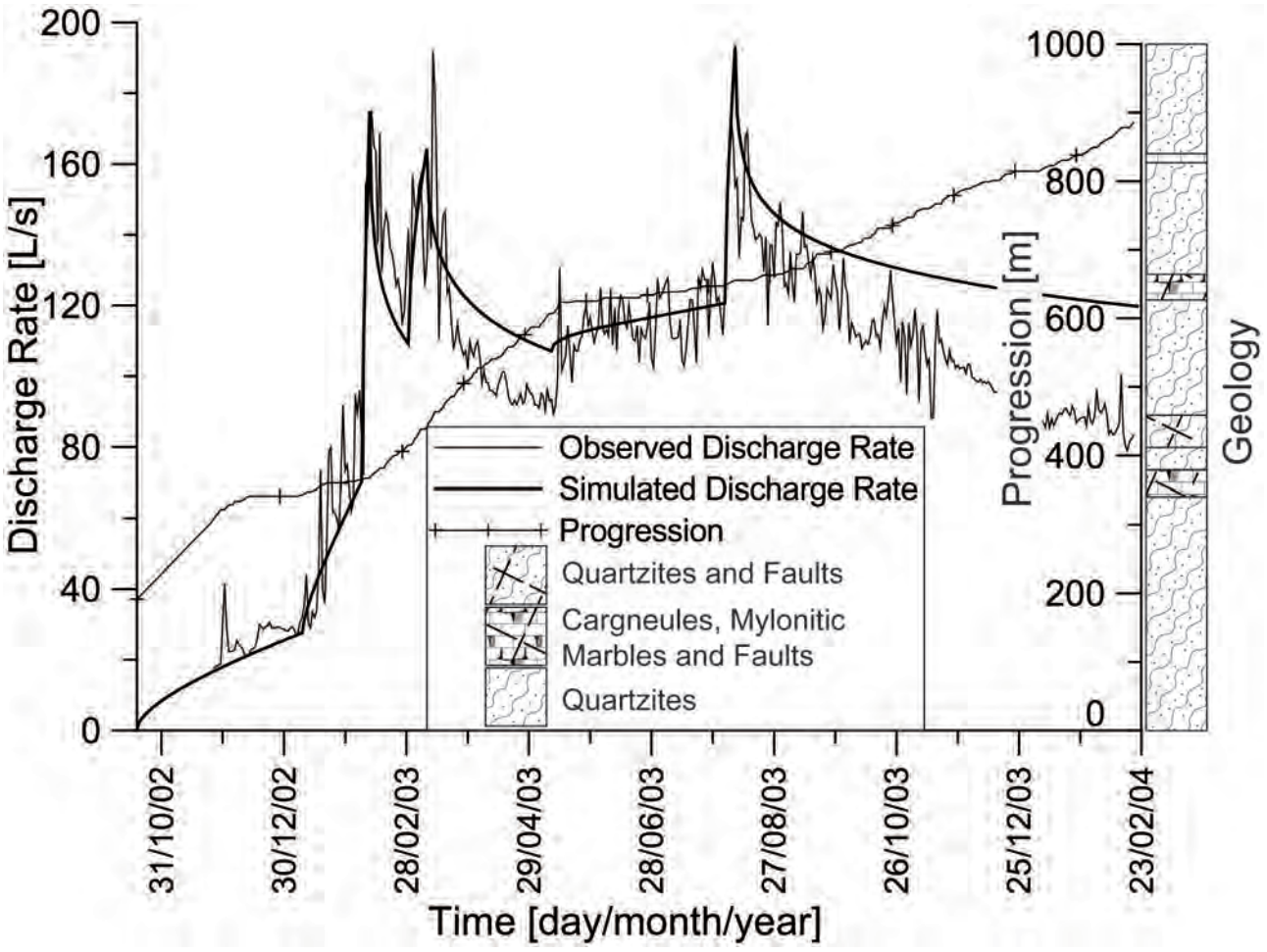

Figure 5.1: Total observed (solid line) and simulated (solid bold line) discharge rates and tunnel progression (solid line with symbols) as a function of time as well as the encountered geology, for the Modane/Villarodin - Bourget tunnel (exploratory adit for the basis tunnel of the Lyon-Turin railway project). From 340 m to 380 m water inflow due to a permeable sector causes a significant slowing down of excavation progression between November 2002 and January-February 2003. For a detailed description of this case see [34].

tunnel drainage are decreasing water pressures (water table decline) which may result in (1) the drying up of springs, and (2) ground settlement (aquifer consolidation) due to increased effective stress [26, 45, 32, 33, 34, 15].

As opposed to existing empirical approaches [19], two principal quantitative methods are used for the prediction of both discharge rates drained by the tunnel and drawdown. One method is based on numerical simulation [1, 30, 45], while the other one is an analytical analysis

[17, 8, 13, 32, 34].

Numerical simulations allow a detailed evaluation of the 3D evolution of the groundwater table with tunnel progression, but are computationally demanding and time consuming. Hence, in practice, hydrogeologists prefer analytical solutions for preliminary predictions and parametric sensitivity studies [34]. However, this latter approach is limited to specific flow configurations and boundary conditions, and requires significant hydrogeological simplifications. Moreover, the effect of effective stresses on parameters is neglected, which implies an overestimation of the flow rate drained by the underground excavation, especially for deep tunnels.

In non karstic alpine systems, as described by Bordet [5], a tunnel excavated in fractured rock masses will first pass through a shallow and post-glacial decompression fractured slope with significant steady water inflow. Then, it will reach a deeper zone where steady water inflow is reduced by the increase of effective stress (closure of fractures) [27], and by the decrease of fracture occurrence [6]. In both zones, but especially in the deeper zone, a tunnel intersecting a permeable saturated formation, will lead to a water inflow peak caused by a high initial hydraulic head, followed by a decreasing transient state.

The discharge rate and drawdown in the shallow zone after excavation will eventually become a function of the recharge regime [15], as shown in Figure 5.2 (sector 1). However, in the deep zone water inflow will either drop and reach steady state, if connected to a recharge body at the surface (such as a lake or a superficial quaternary aquifer), or will rapidly run dry, if not connected to a recharge zone. In the latter case significant ground settlement may be observed on the surface due to the total water table decline [26, 45, 28, 35]. Due to the tunnel depth it is very unlikely that a fluctuation of recharge on the surface will affect the inflow rate.

Figure 5.2 represents a conceptual model of a tunnel excavated in an alpine environment, illustrating the different situations described above.

The main aim of this Chapter is to introduce a coupling of analytical solutions, pre-existing and newly developed ones, based on the conceptual model in Figure 5.2, able to solve the drawdown, the drained discharge rate and the ground settlement caused by tunnel excavation, and to compare them with numerical methods. The impact of effective stress on discharge rates has been analysed by analytical and numerical analysis, leading to a reduction factor for equations solving the water inflow, in order to avoid overestimation.

This Chapter is divided in two sections: the first section presents analytical solutions and numerical methods specific to the modelling of the discharge rate, drawdown and ground settlement produced by tunnel excavation and proposes a reduction factor accounting for effective stress. The second section provides a field example.

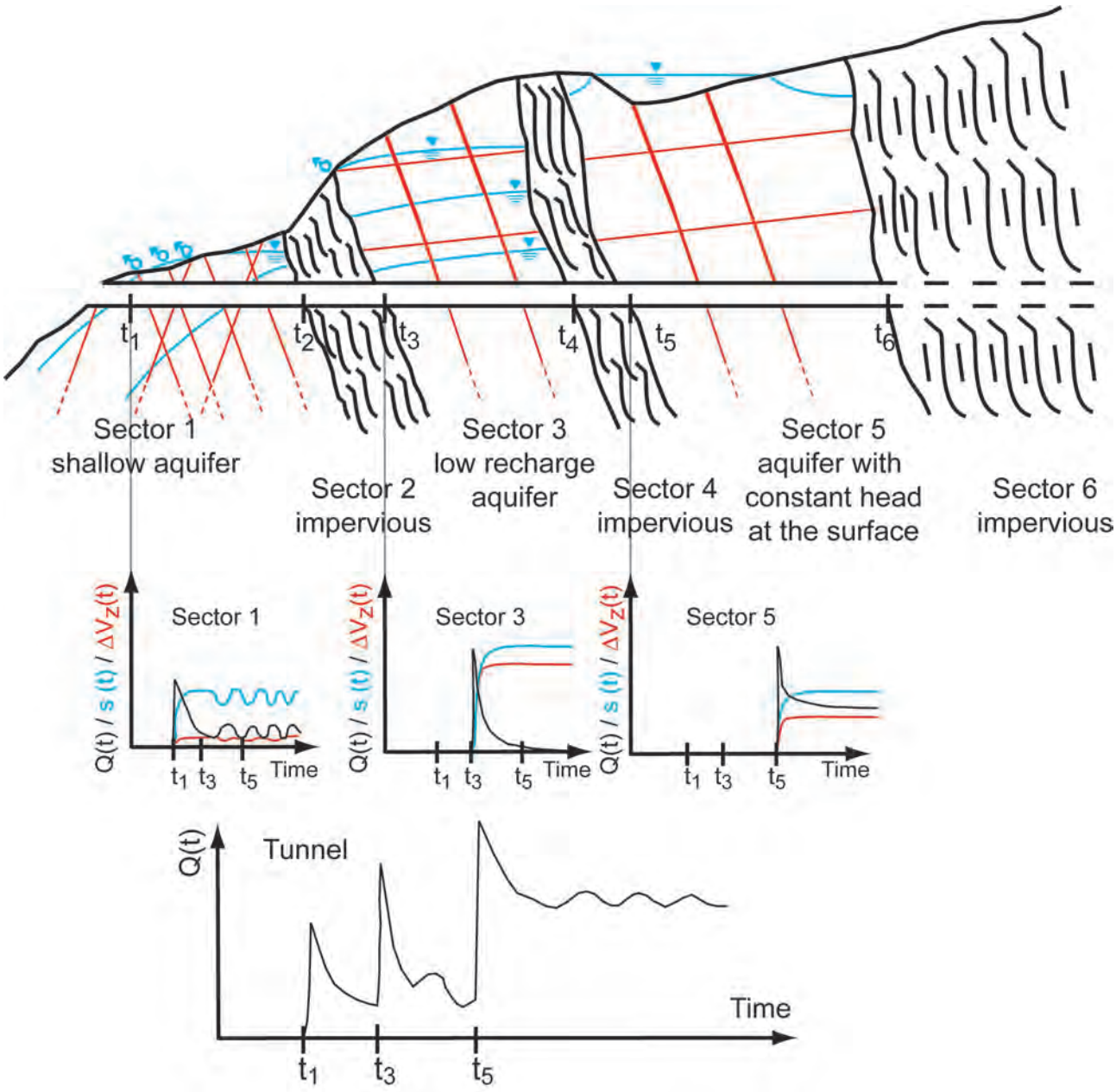

Figure 5.2: Schematic cross section showing the main hydrogeological situations encountered during tunnel excavation into a typical alpine environment. Sector 1 is a shallow aquifer, after the initial transient depressurisation caused by tunnel excavation the discharge rate $Q(t)$ and the water table drawdown $s(t)$ become a function of recharge (rain and snow melt). Sector 3 is situated in the deep zone and is isolated from superficial recharge. The tunnel construction empties the system after strong initial water inflow, leading to complete water table decline and significant ground settlement $\Delta V_z(t)$. In sector 5, the presence of a lake at the surface provides substantial recharge rates that reduce aquifer depressurisation. Steady state water inflow will depend on the rock mass permeability and depth. Sectors 2, 4 and 6 are impervious.

5.2 Analytical and numerical methods

5.2.1 Analytical solutions

There is a wide range of analytical formulas for solving the discharge rate drained by a tunnel. Goodman et al. in 1965 [17] presented a seminal steady state solution:

$$Q = \frac{2\pi K H_0 L}{\ln(\frac{2d}{r_0})} \tag{5.1}$$

where the symbols stand for hydraulic conductivity K, initial hydraulic head in tunnel H_0 (drawdown at the tunnel), tunnel depth d, tunnel length L, tunnel radius r_0 and discharge rate Q. If the tunnel is excavated through different geological zones, the total flow rate in the tunnel is obtained by the sum of each sector's discharge rate. Since then, other specific and practical formulas for the steady state case have been developed [8, 13, 10]. For example, in Eq. (5.1) the assumption of an infinite aquifer can be removed by limiting the flow rate in the tunnel to a maximum corresponding to the local recharge, or by multiplying the flow rate in the tunnel with a factor considering the lateral extension of the permeable sector [10]. Another possible improvement of Eq. (5.1) is to take into account the detailed geometry of the aquifer system, as shown in Figure 5.3 [10]:

$$Q = \frac{4\pi K H_0 L}{\ln\left(\dfrac{e^{\frac{4\pi d}{a}} + e^{\frac{-4\pi d}{a}} - 2}{e^{\frac{2\pi r_0}{a}} + e^{\frac{-2\pi r_0}{a}} - 2}\right)} = \frac{4\pi K H_0 L}{\ln\left(\dfrac{1-\cosh\left(\frac{4\pi d}{a}\right)}{1-\cosh\left(\frac{2\pi r_0}{a}\right)}\right)} \tag{5.2}$$

where a is the lateral spacing of the aquifer system perpendicular to the distance d between the

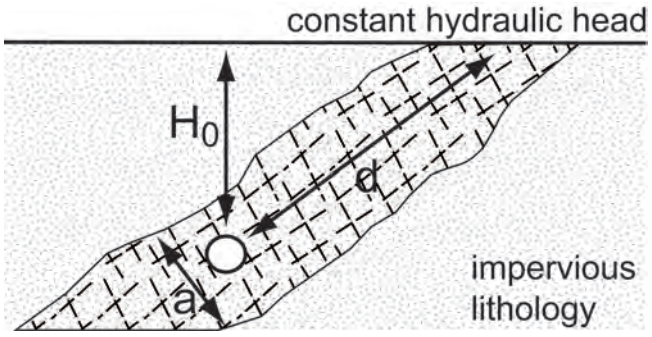

Figure 5.3: Schematic cross section perpendicular to the tunnel axis showing the intersection between the tunnel and an inclined aquifer structure.

tunnel and the surface via the aquifer (Figure 5.3). When d is vertical and a tends to infinity, Eq. (5.2) equals Eq. (5.1).

Concerning the transient state, Perrochet [32] proposed an analytical solution for the discharge rate produced during the excavation of a tunnel in a homogeneous formation, and

subsequently expanded it to the heterogeneous case [34]:

$$Q(t) = 2\pi \sum_{i=1}^{N} \mathrm{H}(t-t_i) \times \int_0^{v_i(t-t_i)} \frac{K_i s_i \mathrm{H}(L_i - x)}{\ln\left[1 + \sqrt{\frac{\pi K_i}{S_i {r_i}^2}\left(t - t_i - \frac{x}{v_i}\right)}\right]} dx \tag{5.3}$$

where for each tunnel sector i, t is the time, t_i is the sector entry excavation time, H(u) is the Heaviside step-function, v_i is the excavation speed, s_i is the drawdown at the tunnel, L_i is the length over which the tunnel intersects the ith sector, x is the spatial coordinate along the tunnel axis with an origin at the entry of the permeable zone, and S_i is the specific storage coefficient. Using a geological oriented strategy of modelling, this transient solution reproduced satisfactorily the flow rate curve produced by the driving of the Modane/Villarodin - Bourget exploratory adit (Figure 5.1), which was excavated by drill & blast.

In general, analytical formulas solving for the flow rate in a tunnel [17, 8, 13, 32, 34] are accurate and rapidly provide first estimations and sensitivity analysis. However, these formulas neglect the dependency of permeability on effective stress and tend to overestimation when depths/effective stress become significant. To avoid overestimation, one approach consists in multiplying the calculated flow rates in a tunnel with a reduction factor, considering the dependency of hydraulic conductivity on effective stress.

Effective stress consideration for deep tunnels

Karl Terzaghi in 1923 [41] revealed that at a given depth, the effective stress state of a geological saturated material results from the total stress state lowered by the fluid pressure (one-dimensional form):

$$\sigma'_{zz} = \sigma_{zz} - \alpha_B p \tag{5.4}$$

where σ'_{zz} is the vertical effective stress, σ_{zz} is the vertical stress, α_B is the Biot-Willis coefficient and p is the fluid pressure. If the fluid is water, then $p = \rho_w g h$, where ρ_w is the water density, g is the gravitational acceleration and h is the pressure head.

Hydrodynamic parameters, e.g. hydraulic conductivity, porosity and specific storage coefficient, depend on the effective stress. This has been clearly identified by laboratory tests [27, 44, 42, 11, 20], field tests [7, 39], field measurements [26, 37, 45] and analytical developments [24, 35]. The increase in effective stress results in decreasing hydrodynamic parameters. In fractured stiff rock masses, these relationships have a dominant elastic reversible behaviour [18], and are well approximated by mathematical functions of the exponential type [27, 35]. In unconsolidated materials, especially in clays and silts, at high effective stresses these relationships become plastic and irreversible [14].

From Eq. (5.4) it follows that a change in effective stress can result from (1) a variation in total stress and/or (2) a change in fluid pressure. Concerning underground excavations, an

increase in total stress can occur with increasing depth, and a drop in water pressure occurs because of tunnel drainage. However, it is important to note that the increase in total stress with depth does not always occur, because, depending on the principal stress orientation, the water pressure conditions, the Poisson's ratio effect and the geometry of aquifer structures (fractures/faults orientation), significant hydraulic conductivities can be found even at great depths [28].

This permeability dependency on effective stress can not be directly introduced in formulas for tunnel drainage, because the permeability varies differently at each point of the aquifer. However, a reduction factor can be estimated by means of analytical or numerical analysis, and used to correct the calculated water flow rate in a tunnel, thereby avoiding overestimation.

Analytical reduction factor

Perrochet [31] developed an analytical reduction factor, based on the water pressure-dependent fracture hydraulic aperture of Louis [27]. By combining this latter model function with the classical cubic law he obtained a pressure-dependent hydraulic conductivity $K(h)$:

$$K(h) = K_0 e^{-3\ b\ (h_0 - h)} \tag{5.5}$$

where K_0 is the hydraulic conductivity prior to a change in pressure head h, h_0 is the initial pressure head state, and b is a coefficient characterising the elastic resistance of fractures to compression. This parameter is linked to the elastic rock modulus E_s by: $b = \rho_w g/\phi/E_s$, where ϕ is rock porosity.

Considering Eq. (5.5) results in the non-linear steady groundwater flow equation:

$$\nabla \cdot (K(h) \nabla H) = 0 \quad ; \quad H = h + z \tag{5.6}$$

where H is the hydraulic head and z is the elevation potential. The flow rate in a tunnel Q_{red} obtained with Eq. (5.6) can be compared to that obtained with the linear form of the groundwater flow equation Q_0:

$$Q_{red} = Q_0\ \alpha \tag{5.7}$$

where α is the reduction factor. For any geometry and boundary conditions, it was shown [31] that the reduction factor can be derived directly from a Kirchhoff transform of Eq. (5.5) as:

$$\alpha = \frac{Q_{red}}{Q_0} = \frac{1 - e^{-3\ b\ (h_0 - h)}}{3\ b\ (h_0 - h)} \tag{5.8}$$

For a tunnel with an initial pressure head of $h_0 = 1000$ m and with $b = 0.001$ m^{-1}, Eq. (5.8) yields a reduction factor of 0.32.

The major advantage of Eq. (5.8) is the development from sound analytical principles. The main limitation is the neglection of the role of total stress on hydraulic conductivity reduction.

Numerical reduction factor

By considering the model function relating effective stress to fracture permeability proposed by Preisig et al. [35] and introducing it in a numerical simulator, it is possible to simulate groundwater flow rates in a tunnel taking into account or not effective stress-dependent permeabilities. The reduction factor is then calculated by the relation: $\alpha = Q_{red}/Q_0$.

The elastic model proposed by Preisig et al. [35] is:

$$K = K_0 \left[1 - \left(\frac{\sigma'}{\sigma'_0} \right)^{\frac{1}{n}} \right]^3 \tag{5.9}$$

where K is the hydraulic conductivity, K_0 is the no stress hydraulic conductivity, σ'_0 is the fracture closure effective stress, and n is a coefficient. This coefficient can be related to the statistical distribution of the fracture asperities, described in detail in [35]. For a fracture characterised by many large asperities: $1 < n < 3.1$, and for a fracture characterised by small asperities: $3.1 < n < 9$. Eq. (5.9) allows considering the principal stress acting on the compressed asperities, and the water pressure in the fracture porosity:

$$\begin{aligned} \sigma' &= \boldsymbol{\sigma}\, \mathbf{n} \cdot \mathbf{n} - \alpha_B\, p\,, \quad \boldsymbol{\sigma} = \begin{bmatrix} \sigma_{zz}\lambda & 0 & 0 \\ 0 & \sigma_{zz}\lambda & 0 \\ 0 & 0 & \sigma_{zz} \end{bmatrix} \\ &= \rho_r g Z(\lambda n_x^2 + \lambda n_y^2 + n_z^2) - \alpha_B \rho_w g h \end{aligned} \tag{5.10}$$

where ρ_r is the rock mass density, n_x,n_y,n_z are the components of the unit vector $\mathbf{n}$ normal to the fracture plane, and Z is the depth. The λ coefficient is the ratio of horizontal to vertical stress: $\lambda = \sigma_h/\sigma_v$. For an isotropic elastic compressible rock and in absence of tectonic, erosional or post-glacial stress, horizontal stresses are driven by vertical stress. In such a case, λ depends on the Poisson's ratio ν: $\lambda = \nu/(1-\nu)$.

Here follows a quantification example of the reduction factor for a tunnel excavated into a vertical fault zone.

Theoretically, a vertical fault filled with water can be able to support a horizontal stress having a closing behaviour. As stated above, in absence of tectonic, erosional or post-glacial stresses, the horizontal stress $\sigma_h = \sigma_{xx} = \sigma_{yy}$ acting perpendicularly onto the fracture plane, results from the vertical stress (overburden) $\sigma_v = \sigma_{zz}$ multiplied by the λ coefficient:

$$\sigma_h = \sigma_{zz}\lambda = \sigma_{zz}\frac{\nu}{(1-\nu)} \tag{5.11}$$

In crystalline fractured rocks, ν is of the order 0.25, which implies a λ of 0.33. If the pressure head h in the fracture equals the depth Z, it follows that water pressure equals the horizontal stress, because $\rho_w \approx \rho_r\lambda$, and effective stress is close to zero. This equilibrium state results in a vertical fault being open even at great depths (Figure 5.4). A tunnel excavation through

the fracture causes a sudden water pressure decrease, and consequently a rapid decrease of the fracture hydraulic conductivity and of the discharge rate into the underground structure.

To highlight the reduction of the flow rate in a tunnel, several finite element numerical simulations have been realised for a tunnel excavated into a vertical fault at different depths. The numerical simulations are performed with no effective stress-dependent hydraulic conductivities and with effective stress-dependent ones. The fault is discretised by a vertical section of 3000 $\times$ 3000 m^2, with a tunnel of 10 $\times$ 10 m^2. For the different simulations, the initial pressure head h in the tunnel (tunnel depth) varies from 300 to 2700 m, at intervals of 300 m. A constant hydraulic head of H = 3000 m is specified at the domain top, while lateral and bottom boundaries are impervious. Finally, a constant atmospheric pressure is assigned in the tunnel, with a hydraulic head H that matches the tunnel elevation z: $H = z = 3000 - Z$. The initial head in the fault is at hydrostatic conditions. The right part of Figure 5.4 summarises the boundary conditions and geometrical configurations used in the analysis. The fracture presents a no stress

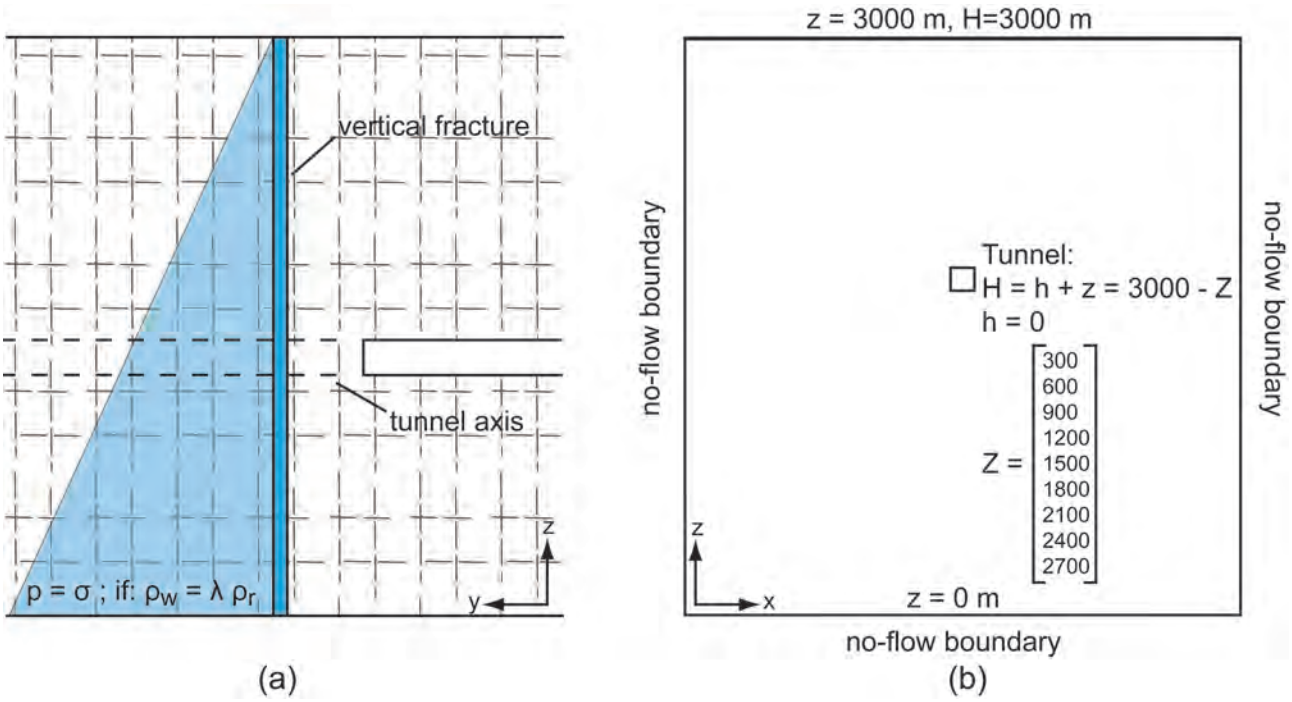

Figure 5.4: Schematic cross sections (a) along the tunnel axis showing the water pressure state in the fracture, (b) perpendicular to the tunnel axis illustrating the geometrical configuration and the boundary conditions used in the numerical tests.

hydraulic conductivity K_0 of 10^{-4} m/s, and the host rock is considered as an unaltered granite with standard values of: $\rho_r = 3000$ kg/m^3, $\sigma_0 = 3.5 \cdot 10^{10}$ Pa, and $n = 9$. In granitic rocks the λ coefficient generally matches 0.33, which implies the above explained initial equilibrium. For this analysis three λ values are tested: $\lambda = 0.33$, $\lambda = 1.00$ (horizontal stresses correspond to the vertical ones), and $\lambda = 3.00$ (horizontal stresses are three times stronger than the vertical stress). The latter is possible in presence of tectonic stresses or in areas that have been glaciated, such as in orogenic belts as measured in Mayeur and Fabre [29]. Note that, in the absence of horizontal stresses $\lambda = 0.00$, there is no effective stress reduction and the vertical

fracture preserves a constant permeability, despite the water pressure decrease.

Simulations are carried out in steady and transient states. For the transient analysis the fracture effective stress-dependent specific storage coefficient proposed by Preisig et al. [35] is used:

$$\begin{aligned} S_s &= S_{sm} + S_{sf}; \\ S_{sf} &= S_{sf_0}\left[1 - \left(\frac{\sigma'}{\sigma'_0}\right)^{\frac{1}{n}}\right]; \end{aligned} \tag{5.12}$$

where the symbols stand for specific storage coefficient S_s, rock matrix specific storage coefficient S_{sm}, fracture specific storage coefficient S_{sf} and fracture specific storage coefficient S_{sf_0} under no stress conditions. In the analysis, S_s corresponds to 10^{-8} m^{-1} at no stress. Transient simulations are achieved with two types of boundary conditions on the domain surface: (1) constant atmospheric pressure ($H = z$), such as in the steady state case, and (2) no-flow condition. This latter condition implies the emptying of the fracture under tunnel drainage, as it happens when an underground excavation intersects an aquifer without a recharge zone or very weakly recharged.

Results and discussion

As expected, flow rates in tunnels simulated with constant fault permeability is greater than those modelled with effective stress-dependent hydraulic conductivity, and increases with increasing initial pressure head at the tunnel location. On the contrary, with effective stress-dependent fracture hydraulic conductivity, the computed flow rate in tunnel tends to stabilise despite increasing tunnel initial head (depth). This is due to the decrease of fracture permeability with the increase of effective stress caused by the tunnel drainage, and the subsequent fracture depressurisation and closure, especially for the case with horizontal stresses three times greater than vertical stress ($\lambda = 3$).

Figure 5.5 compares the simulated steady discharge rates into the tunnel, and shows the reduction coefficient $\alpha = Q_{red}/Q_0$ as a function of initial pressure head in tunnel. With λ equal to 0.33, the α coefficient varies from 0.32 for 300 m of initial head in tunnel to 0.21 for 2700 m of initial head in tunnel, and the mean is 0.25. This slight decrease is due to the increase of horizontal stress with depth. These values correlate fairly well with the analytical reduction factor proposed by Perrochet [31]. With λ increasing from 1 to 3, the reduction factor decreases, due to the magnitude of horizontal stresses.

In transient state, the reduction already starts when the excavation intersects the fracture. The value of the reduction is comparable to that obtained in steady state and remains relatively constant during transient drainage. For the case with constant atmospheric pressure at the surface, simulated discharge rates and reduction factors stabilise to values calculated at steady state conditions. For the case with no flow conditions at the surface, the fracture is emptied. This total drainage is much slower with effective stress-dependent hydraulic conductivity.

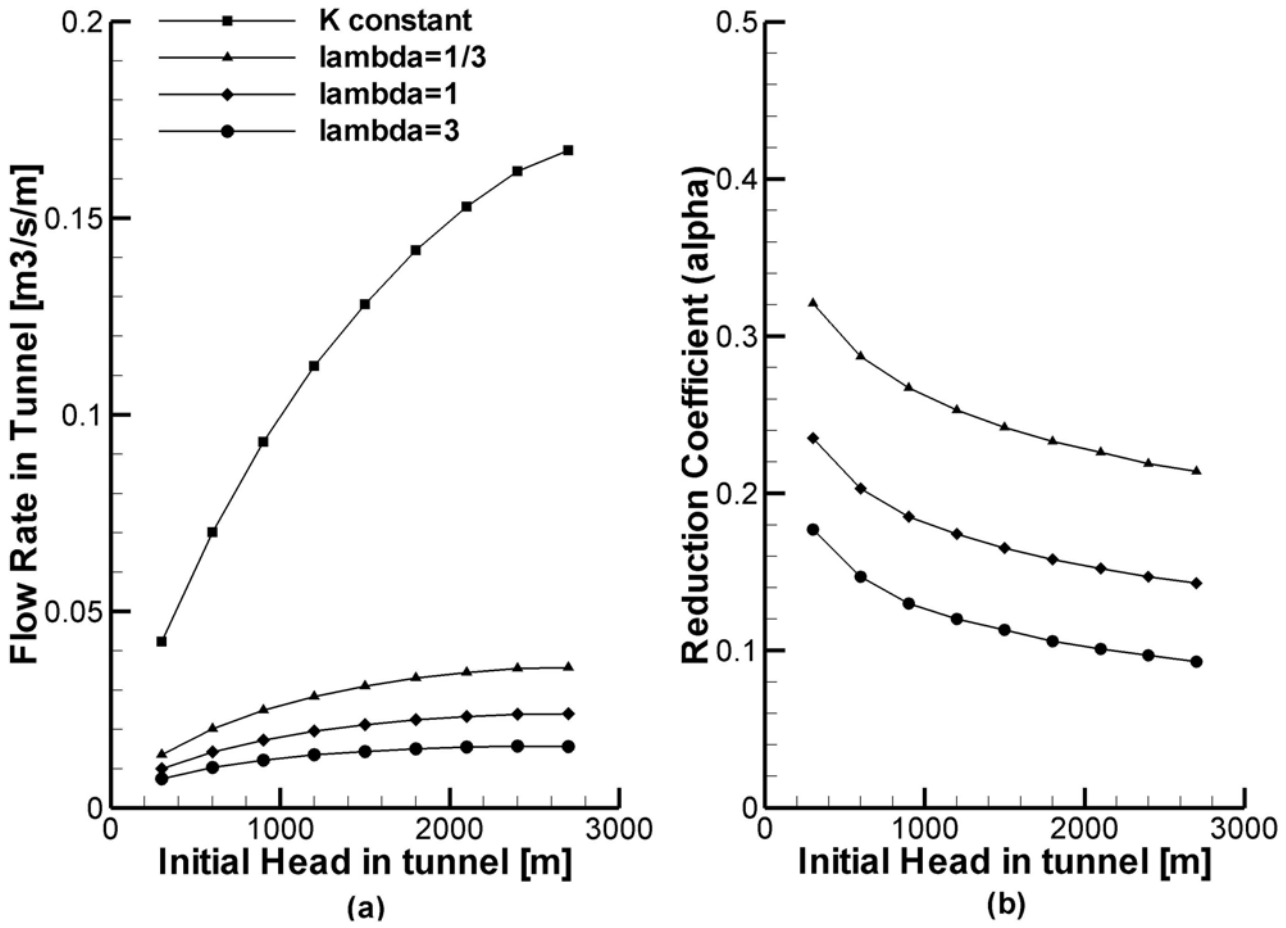

Figure 5.5: (a) Simulated steady water flow rates in tunnel and (b) reduction coefficient as a function of initial pressure head in tunnel.

The numerical analysis highlights the influence of principal stresses on the reduction factor. If stresses are negligible, the decrease in hydraulic conductivity depends only on the decrease in water pressures. In such a case, the value of the reduction factor is similar to those obtained with Eq. (5.8). When principal stresses become significant, the reduction coefficient decreases, especially in case of horizontal stresses greater than vertical stresses. The reduction coefficient also applies in transient conditions. Given its magnitude, this reduction should be considered in deep tunnels, beyond the post-glacial decompression shallow zone.

Coupling discharge rate in a tunnel to aquifer consolidation

The consolidation of an aquifer intersected by a tunnel is a subtle process, especially in stiff rock masses. However, it can be detected by detailed geodetic measurements such as differential leveling, GPS or InSAR methods [14]. Despite the low magnitude of the phenomenon, a few tens of centimeters, differential consolidations can lead to very dangerous ground settlements. The abnormal behaviour of the Zeuzier arch dam (Switzerland) during the excavation of the Rawyl exploratory tunnel in 1978/1979 is a well known case study [26, 38].

The amount of ground settlement is directly linked to two principal parameters: (1) the compressibility of the aquifer and (2) the magnitude of the drawdown. Indirectly, it is also

related to the flow rate in tunnel (Table 5.1).

Table 5.1: Maximum inflow, drawdown and ground settlement for different alpine tunnels

Tunnel	**Flow Rate** L/s	**Drawdown** m	**Settlement** cm	**Geology**	**References**
Gotthard Road Tunnel Switzerland	300	no data	12	fractured crystalline rocks	Zangerl et al., 2003 [45]
Rawyl Exploratory Adit Switzerland	> 1000	230	12	fractured meta-sedimentary calcareous schist	Schneider, 1982 [38] Lombardi, 1988 [26]
La Praz Exploratory Adit France	40	90	5	fractured meta-sedimentary sandy schist	Dzikowski and Villemin, 2009 [12]
Modane/Villarodin-Bourget Exploratory Adit France	180	90	> 3	cargnieules, mylonitic marbles and faults	SOGREAH Consultants, 2007 [40] Lassiaz and Previtali, 2007 [25]
Loetschberg Railway Tunnel Switzerland	no data	60	19	limestones and unconsolidated sediments	Vulliet et al., 2003 [43]
Campo Valle Maggia Landslide drain Switzerland	no data	300	50	fractured crystalline rocks and unconsolidated sediments	Bonzanigo, 1999 [4]

Using an alternative approach, Perrochet [33] suggests that the effect of drawdown $s(r,t)$ vanishes beyond a no-flow moving boundary located at the time-dependent radial distance $r = R(t)$:

$$s(r,t) = s_0 \left(1 - \frac{2R(t)^2 \ln(r/r_0) - r^2 + r_0^2}{2R(t)^2 \ln(R(t)/r_0) - R(t)^2 + r_0^2}\right) \tag{5.13}$$

where the symbols stand for drawdown at the tunnel s_0, radial coordinate r and tunnel radius r_0. The no-flow moving boundary $R(t)$ is found to be [2]:

$$R(t) = r_0 \ \exp\left(\frac{\tan^{-1}(2\sqrt{\pi\alpha_t})}{\pi}\right) \ (1 + \sqrt{\pi\alpha_t}) \tag{5.14}$$

where the dimensionless time α_t is:

$$\alpha_t = \frac{Tt}{Sr_0^2} \tag{5.15}$$

and where T is the transmissivity, t is the time, and S is the storage coefficient. A constant or a no-flow boundary can be added on equation 5.13 using the image method.

Considering Eq. (5.13) and integrating over the tunnel circumference, yields the tunnel

discharge rate Q:

$$\begin{aligned} Q &= 2\pi r_0 T \frac{\partial s(r,t)}{\partial r} \mid_{r=r_0} \\ &= \frac{2\pi T s_0}{\ln(1+\sqrt{\pi\alpha_t})} \end{aligned} \tag{5.16}$$

This latter equation constitutes the basis formula for the development of Eq. (5.3) [34].

Using Eq. (5.13) and considering the classical aquifer-system consolidation theory proposed by Jacob [22, 23], a transient ground settlement $\Delta V_z(x,t)$ is obtained by expressing the drawdown in Cartesian coordinates (origin at the surface above the tunnel) and by a vertical integration of the drawdown cone (Figure 5.6):

$$\begin{aligned} \Delta V_z(x,t) &= C_v \int_{z_b(x,t)=-s_0-\sqrt{R(t)^2-x^2}}^{z_t(x,t)=-s_0+\sqrt{R(t)^2-x^2}} s(x,z,t)\ dz \\ &= \frac{2}{3} C_v s_0 \sqrt{R(t)^2-x^2}\cdot \\ &\quad \frac{\left(4R(t)^2+2x^2-6R(t)^2\, x \tan^{-1}\left(\frac{\sqrt{R(t)^2-x^2}}{x}\right)\frac{1}{\sqrt{R(t)^2-x^2}}\right)}{2R(t)^2\left(\ln\frac{R(t)}{r_0}-1\right)+r_0^2} \end{aligned} \tag{5.17}$$

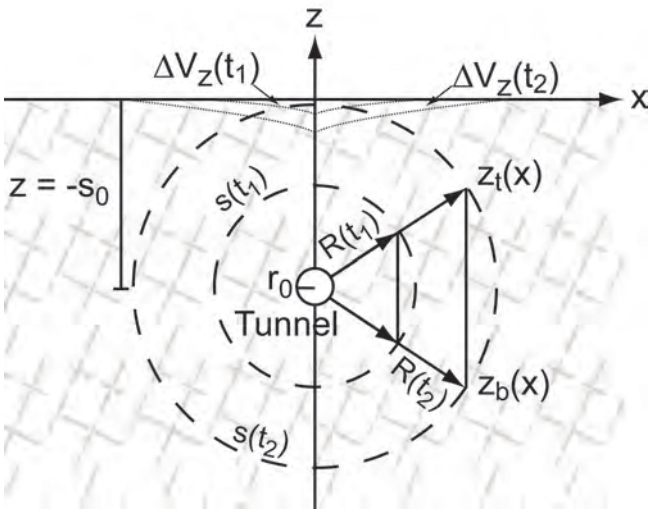

Figure 5.6: Illustrative cross section perpendicular to the tunnel axis showing the temporal evolution of the drawdown cone (dashed lines). This aquifer depressurisation causes local deformations resulting in ground settlements (dotted lines).

where C_v is the aquifer compressibility expressed as: $C_v = \rho_w\, g\, /E_s$, E_s is the aquifer elasticity, and $z_t(x,t)$ and $z_b(x,t)$ are the top and the bottom elevation coordinates of the drawdown cone for the coordinate x and time t, respectively. Note that, for fractured rock masses the elasticity of water acting in fractures can be neglected because of the very low values of the rock mass porosity: in general < 0.02. In such a case, the aquifer elasticity can be assumed equivalent to the rock elasticity. Eq. (5.17) computes the transient settlement in an infinite

domain due to the tunnel drainage. In reality, aquifers are finite and the consolidation stops when the drawdown reaches the system boundaries. In such a case, the transient settlement of Eq. (5.17) must end when it reaches the maximum possible value $\Delta V_{z_{max}}$:

$$\Delta V_{z_{max}} = C_v s_0 e \tag{5.18}$$

where e is aquifer thickness. Because of tunnel drainage the horizontal strain can be obtained by a horizontal integration of Eq. (5.17) from the tunnel axis to the drawdown cone boundary, and taking into account the Poisson's ratio effect.

5.2.2 Numerical methods

A numerical groundwater flow model is a simplified version of: (1) a real aquifer, (2) the physical processes that take place within it, and (3) the aquifer's external solicitations [3]. The tunnel excavation is the external solicitation. Below some generalities are discussed on the treatment of tunnels in 3D numerical simulations of groundwater flow and aquifer deformation.

As mentioned in Molinero et al. [30], a tunnel can be introduced in a boundary value problem as a time-varying inner boundary. According to a time function describing the excavation progression, tunnel nodes become active as Dirichlet boundary conditions at constant atmospheric pressure (elevation head). This approach does not need the use of moving grids to simulate the advancing of the tunnel front, and consequently, it is not computationally demanding or time consuming, which is important in regional models. However, this method implies the presence of the tunnel as an inactive hole in the mesh since the start of the calculation.

For deep tunnels, effective stresses can be considered by combining stress-dependent functionals with the groundwater flow equation, as proposed by [35]:

$$S_s(\sigma')\frac{\partial H}{\partial t} = \nabla \cdot (\mathbf{K}(\sigma')\nabla H) \quad ; \quad H = h + z \tag{5.19}$$

where $\mathbf{K}(\sigma')$ is the effective stress-dependent hydraulic conductivity tensor, and $S_s(\sigma')$ is the "storage" defined in Eq. (2.17).

The pressure head distributions resulting from the groundwater flow model can then be used to compute aquifer consolidation and ground subsidence. In this work, aquifer consolidation is computed following the modelling strategy proposed in [36].

5.3 Field example: the La Praz exploratory tunnel

The La Praz exploratory tunnel is located in the French Western Alps (Maurienne Valley), and is part of the geological investigations undertaken by the Lyon-Turin railway project for the 57 km basis tunnel. From a tectonic point of view, this exploratory adit is situated in the "Zone Houillère Brian- çonnaise", which in this area is composed of fractured meta-sedimentary sandy schist. The tunnel was entirely excavated in this formation by drill & blast (Figure 5.7).

The first 900 m of the tunnel were excavated in the zone affected by post-glacial decompression, resulting in a permeable shallow fracture network (fractured sandy schists) [10]. Then, the tunnel entered in the deeper zone of the mountain (unaltered sandy schists). The saturated zone was reached approximatively at a distance of 100 m from the tunnel portal. From this point, hydraulic heads before excavation increase because the tunnel gets deeper relative to both the topographic surface and the water table. The maximum tunnel depth and hydraulic head above the tunnel were 790-800 m and 500 m, respectively. The average overburden (tunnel depth) is about 600 m (Figure 5.7c).

During the excavation phase, the monitored data were the water inflow at the tunnel front, the total water inflow in the tunnel and the excavation progression. These data approximately cover the excavation period (1100 days) corresponding to a progression of 2500 m. Note that, the measure of total water inflow began only after the first water inflow. The monitoring network also includes several observation wells, geodetic points and springs (Figure 5.7a and 5.7b).

The discharge rates in the tunnel indicate that the La Praz exploratory adit was excavated through an unconfined permeable shallow sector (decompression zone), before entering a deeper semipervious sector, where the rock mass permeability decreases because of (1) the diminution of fracture occurrence, and (2) the decrease of fracture permeability due to the increase of effective stress. Tunnel drainage caused an important water table drawdown, observed in wells. However, tunnel drainage did not completely empty the slope system, indicating active recharge from the nearby mountains. The water table decline resulted in a ground settlement of about 5 cm along the tunnel axis [12].

5.3.1 Analytical simulations

On the basis of the conceptual model presented above, and following the modelling strategy proposed in [34], the transient discharge rate drained during the excavation of the La Praz exploratory tunnel is simulated using Eq. (5.3). In a first model, the tunnel is separated into 3 sectors: an unsaturated sector, a saturated permeable sector representing the fractured sandy schists and a saturated semipervious sector representing the unaltered sandy schists. Sector lengths are estimated from the cross section of Figure 5.7c, the excavation times are provided (green line of Figure 5.7b), allowing to calculate the excavation speed for each sector.

In a second model, the tunnel is also separated into three principal zones according to the geology, but each zone is refined in order to correctly simulate the observed peaks (total of 16 sectors). The drawdown at the tunnel is estimated from the tunnel depth and the piezometric level measured at the observation wells. The analytical formula (Eq. (5.3)) is calibrated using the measured water flow rates in the La Praz tunnel, by varying the hydraulic conductivity and the specific storage coefficient (Table 5.2, Figure 5.8a).

The calibrated hydraulic conductivities are then introduced into Eq. (5.2) in order to compute the steady water flow rate in tunnel (with $H_0 = d$, $a \to \infty$). From an initial head in the tunnel greater than 100 m, the calculated steady discharge rates are multiplied with the

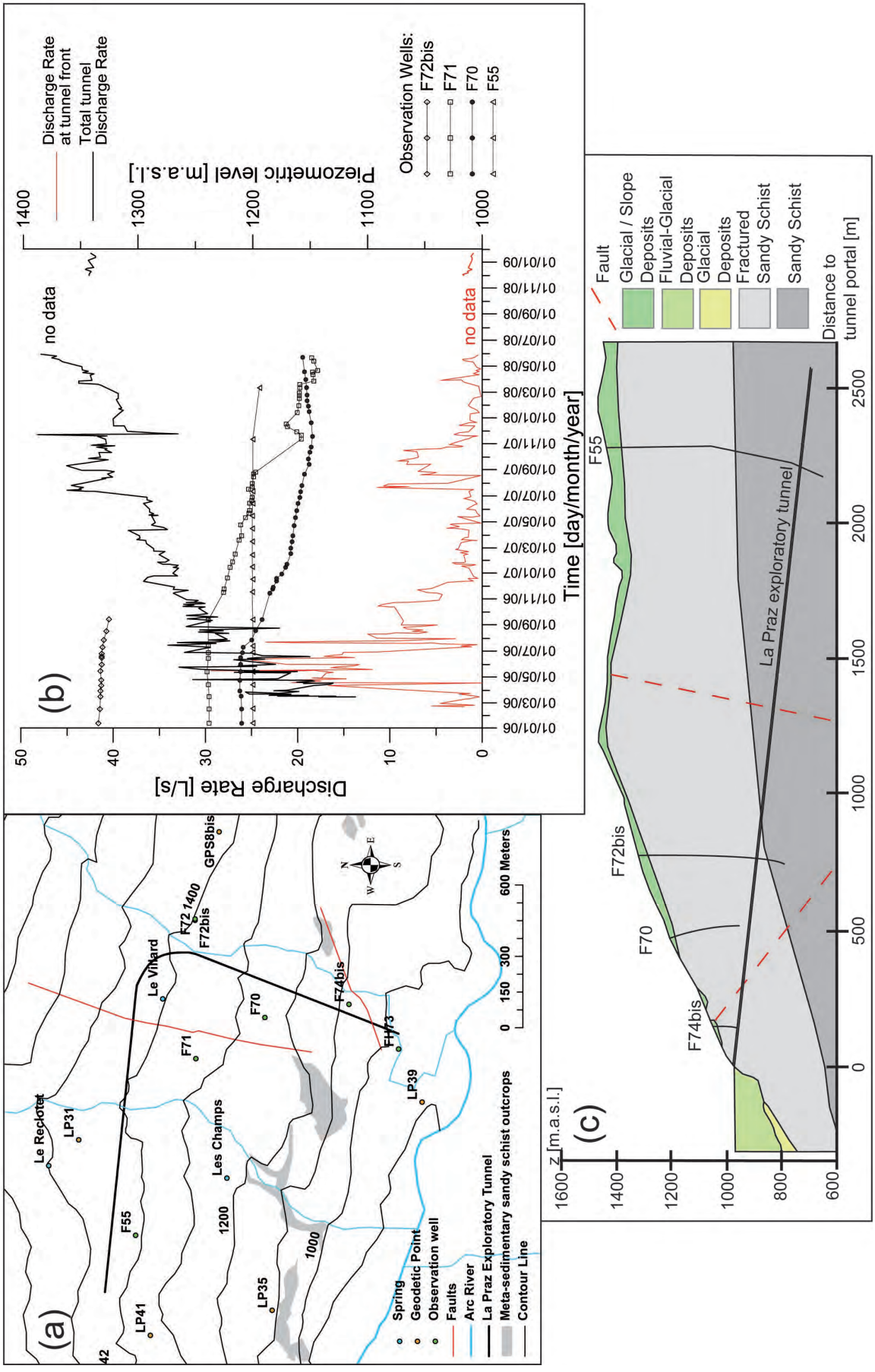

Figure 5.7: (a) Map of the La Praz exploratory tunnel with observation wells, geodetic points and springs location (modified after [12]). (b) Flow rate in tunnel, piezometric level as a function of time. (c) Cross section along the La Praz exploratory tunnel (modified after [21]).

reduction factors calculated with Eq. (5.8) ($b = 0.001$), or with those estimated from Figure 5.5b for $\lambda = 0.33$ (Table 5.2). The tunnel radius is 4.5 m.

Table 5.2: Parametric values used in transient and steady calculations of the groundwater inflows, and results.

Sectors	Geology	L_i [m]	t_i [d]	t_{i+1} [d]	v_i [m/d]	$s_i = H_{0_i}$ [m]	K_i [m/s]	S_i [1/m]	$Q_{Eq.5.2}$ [L/s]	$\alpha_{Eq.5.8}$	Q_{red1}	$\alpha_{Fig.5.5b}$	Q_{red2}
Model 1: hydrogeological units													
1	Unsaturated Zone	104	0	35	3.0	0	10^{-7}	$5 \cdot 10^{-4}$	0.0	1.00	0.0	1.00	0.0
2	Fractured sandy schist	875	35	537	2.0	220	10^{-7}	$5 \cdot 10^{-4}$	26.4	0.73	19.3	0.39	10.3
3	Unaltered sandy schist	1521	168	1100	2.7	550	$5 \cdot 10^{-8}$	$1 \cdot 10^{-5}$	4.8	0.49	2.3	0.29	1.4
								$\sum$	**31.2**		**21.6**		**11.7**
Model 2: refined hydrogeological units													
1	Unsaturated Zone	104	0	36	2.9	0	$1 \cdot 10^{-5}$	$5 \cdot 10^{-3}$	0.0	1.00	0.0	1.00	0.0
2	Fractured	16	36	67	0.5	60	$1 \cdot 10^{-5}$	$5 \cdot 10^{-3}$	18.4	1.00	18.4	1.00	18.4
3	sandy schist	16	67	96	0.6	60	$1 \cdot 10^{-8}$	$1 \cdot 10^{-3}$	0.0	1.00	0.0	1.00	0.0
4	"	7	96	98	3.5	80	$5 \cdot 10^{-6}$	$1 \cdot 10^{-3}$	4.9	1.00	4.9	1.00	4.9
5	"	12	98	119	0.6	80	$1 \cdot 10^{-8}$	$1 \cdot 10^{-3}$	0.0	1.00	0.0	1.00	0.0
6	"	8	119	127	1.0	85	$5 \cdot 10^{-6}$	$1 \cdot 10^{-3}$	5.9	1.00	5.9	1.00	5.9
7	"	113	127	152	4.5	85	$1 \cdot 10^{-8}$	$1 \cdot 10^{-3}$	0.2	1.00	0.2	1.00	0.2
8	"	32	152	166	2.3	150	$1 \cdot 10^{-6}$	$1 \cdot 10^{-3}$	7.2	0.81	5.8	0.45	3.2
9	"	43	166	196	1.4	150	$1 \cdot 10^{-8}$	$1 \cdot 10^{-3}$	0.1	0.81	0.1	0.45	0.0
10	"	622	196	532	1.9	300	$1 \cdot 10^{-8}$	$1 \cdot 10^{-3}$	2.4	0.66	1.6	0.32	0.8
11	"	6	532	537	1.2	400	$1 \cdot 10^{-6}$	$1 \cdot 10^{-3}$	2.9	0.58	1.7	0.31	0.9
12	Unaltered	111	537	591	2.1	400	$1 \cdot 10^{-9}$	$1 \cdot 10^{-3}$	0.1	0.58	0.0	0.31	0.0
13	sandy schist	20	591	598	2.9	500	$1 \cdot 10^{-7}$	$1 \cdot 10^{-4}$	1.2	0.52	0.6	0.30	0.3
14	"	416	598	776	2.3	500	$1 \cdot 10^{-9}$	$1 \cdot 10^{-3}$	0.2	0.52	0.1	0.30	0.1
15	"	288	776	862	3.3	600	$5 \cdot 10^{-9}$	$1 \cdot 10^{-3}$	1.0	0.46	0.5	0.29	0.3
16	"	686	862	1100	2.9	600	$1 \cdot 10^{-10}$	$1 \cdot 10^{-4}$	0.0	0.46	0.0	0.29	0.0
								$\sum$	**44.5**		**39.8**		**35.0**

The water table drawdown and the ground settlement are simulated using Eqs. (5.13), and (5.17) for a cross section perpendicular to the tunnel axis at the penetration distance of 900 m. This distance corresponds to the contact between the weathered and the unaltered sandy schist. The available data of two observation points can be used for the calibration: the observation well **F71** and the geodetic point **GPS8bis** (Figure 5.7a). For the settlement problem, only the consolidation of the fractured zone is considered. In such a case, the aquifer thickness in Eq. (5.18) corresponds to the thickness of the weathered sandy schist. The results of the analytical drawdown and ground settlement are presented in Figure 5.8b, and the parametric values are shown in Table 5.3.

Table 5.3: Parametric values used in transient simulations of the drawdown and the ground settlement generated by the tunnel opening at the distance of 900 m.

K $[m/s]$	S $[1/m]$	s $[m]$	E_s $[Pa]$	e $[m]$
$1 \cdot 10^{-5}$	$2 \cdot 10^{-3}$	400	$1 \cdot 10^{10}$	400

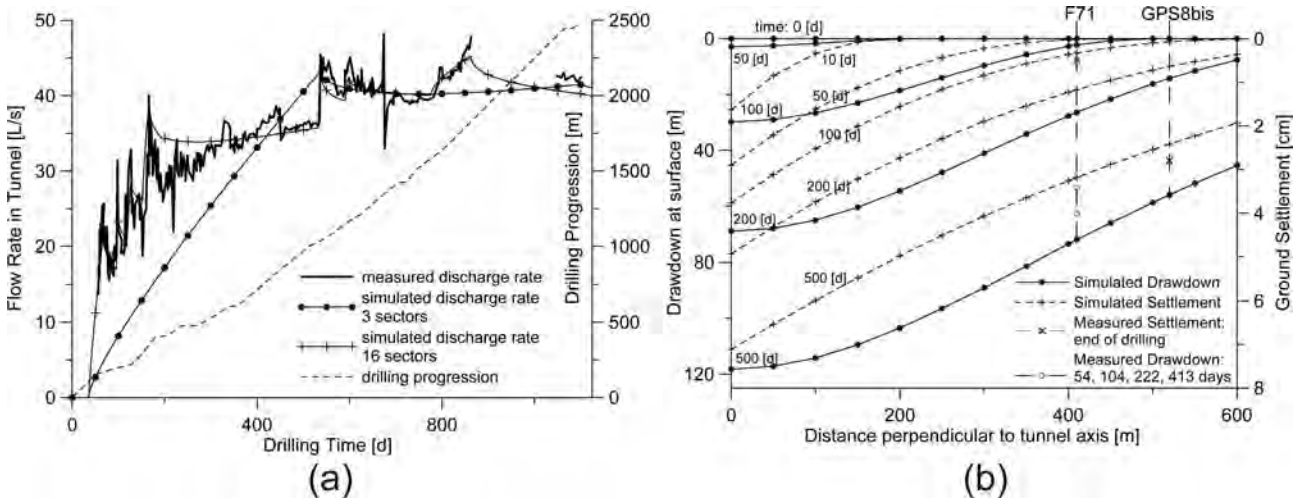

Figure 5.8: (a) Comparison of measured water flow rates in tunnel (bold line) with analytical transient simulations: (1) hydrogeology oriented model of 3 sectors (solid line with circles) and (2) refined model of 16 sectors (solid line with crosses). (b) Simulated drawdown at the surface and ground settlement for a cross section perpendicular to the tunnel axis, at the tunnel distance of about 900 m. Note that: (1) the system is symmetric, and (2) the time is relative to the tunnel opening at 900 m.

Discussion

The formulas used in the analysis rapidly and correctly reproduce the discharge rate, drawdown and ground settlement generated by the excavation of the La Praz exploratory tunnel.

As expected, the model 1 with 3 sectors is not able to accurately capture each flow rate pattern. However, this simple strategy allows good approximation of the general shape of the curve, and reproduces the essential features of the process. The detailed model can reproduce the observed flow spikes, but it is less coherent relative to its hydrodynamical parametrisation. In steady state calculations, the use of the reduction coefficient decreases the water inflow by a factor of 2 or 3, especially in deep sectors. The decrease is greater using the reduction coefficient in Figure 5.5b, because, both the increase of total stress and the decrease of water pressure are taken into account. The use of this coefficient allows analytical formulas to be more realistic, in particular for deep tunnels. Unfortunately, due to the absence of long term field measurements, calculated steady flow rates cannot be compared with real observed values.

The analytical simulations of the drawdown and the ground settlement successfully reproduce the theoretical water table and ground surface depression cone induced by the opening of the tunnel (Figure 5.8b). Moreover, the simulated values are in the same range of those observed in the field. A major disadvantage regarding the presented formulas is that they are constructed for an infinite domain. Also, in field applications, it is hard to define the aquifer boundaries, especially for the settlement problem. One approach consists in considering the base of the tunnel as the system bottom, neglecting the drawdown and the deformations below the tunnel.

5.3.2 Numerical simulations

From the conceptual model presented above, a groundwater and a consolidation finite element model is constructed in order to reproduce the discharge rate, the water table decline and the ground settlement produced by the excavation of the La Praz exploratory tunnel. The 3D model discretisation respects the local topography and geology presented in Figure 5.7 (Figure 5.9). The before-mentioned conceptualisation of the rock mass, i.e. a permeable shallow sector, and a deeper semipervious sector, is reproduced using a contrast of hydraulic conductivities. As measured in [29] for the North slope of the Arc Valley, vertical stresses correspond to the weight of the overburden. Both principal horizontal stresses are set 1.5 times higher than the vertical stresses; this condition applies well to orogenic and formerly glaciated areas, such as the Alps.

As reported earlier, groundwater flow occurs from the upstream area of the mountain slope towards the valley bottom. To reproduce the initial shape of the water table (before tunnel excavation), a steady state groundwater flow model is realised by specifying constant hydraulic heads along the upstream and downstream boundaries of the model, approximately matching the topographic elevation (Figure 5.9a). The model is calibrated using the pre-tunnel measured hydraulic heads, by varying the components of the hydraulic conductivity tensor (Table 5.4).

Tunnel excavation is then modelled. The tunnel is discretised as a cylinder of radius 4.5 m, following the trace shown in Figure 5.7, and representing an inactivated hole in the mesh at the initial state. The excavation progression is simulated according to the recorded excavation data of Figure 5.7b, by successively activating tunnel nodes as atmospheric Dirichlet boundaries (Figure 5.9b). The calibrated hydraulic conductivity, and the hydraulic heads calculated with the steady state model before tunnel excavation, are introduced as input. In this transient analysis, hydrodynamic parameters are considered as stress-dependent. The temporal evolution of the simulated inflows and water table drawdown can be seen in Figure 5.10.

Finally, the rock mass consolidation, ground settlement, caused by the tunnel drainage is computed using the simulated pressure head distributions before and after tunnel perturbation (Figure 5.9c). The problem is solved using the deformation equations proposed by [35, 36], based on the assumptions that aquifers deform elastically, the principal stresses do not change with water depletion and the consolidation only results from fractures porosity closure. The calibrated parameters are shown in Table 5.4, where ϕ_0 is the no stress porosity of the rock mass.

The detailed 3D finite element model of Figure 5.9 respecting the topography and geology of the La Praz area, and the 3D tunnel trajectory was constructed and generated using the mesh generator software `GMSH` [16]. The groundwater flow and rock consolidation models were computed using the multipurpose `Ground Water (GW)` finite element software [9].

Discussion

Groundwater inflow in tunnel and the ground settlement are well reproduced by the numerical analysis (Figure 5.10a and 5.10c). On the contrary, at observation wells, simulated hydraulic

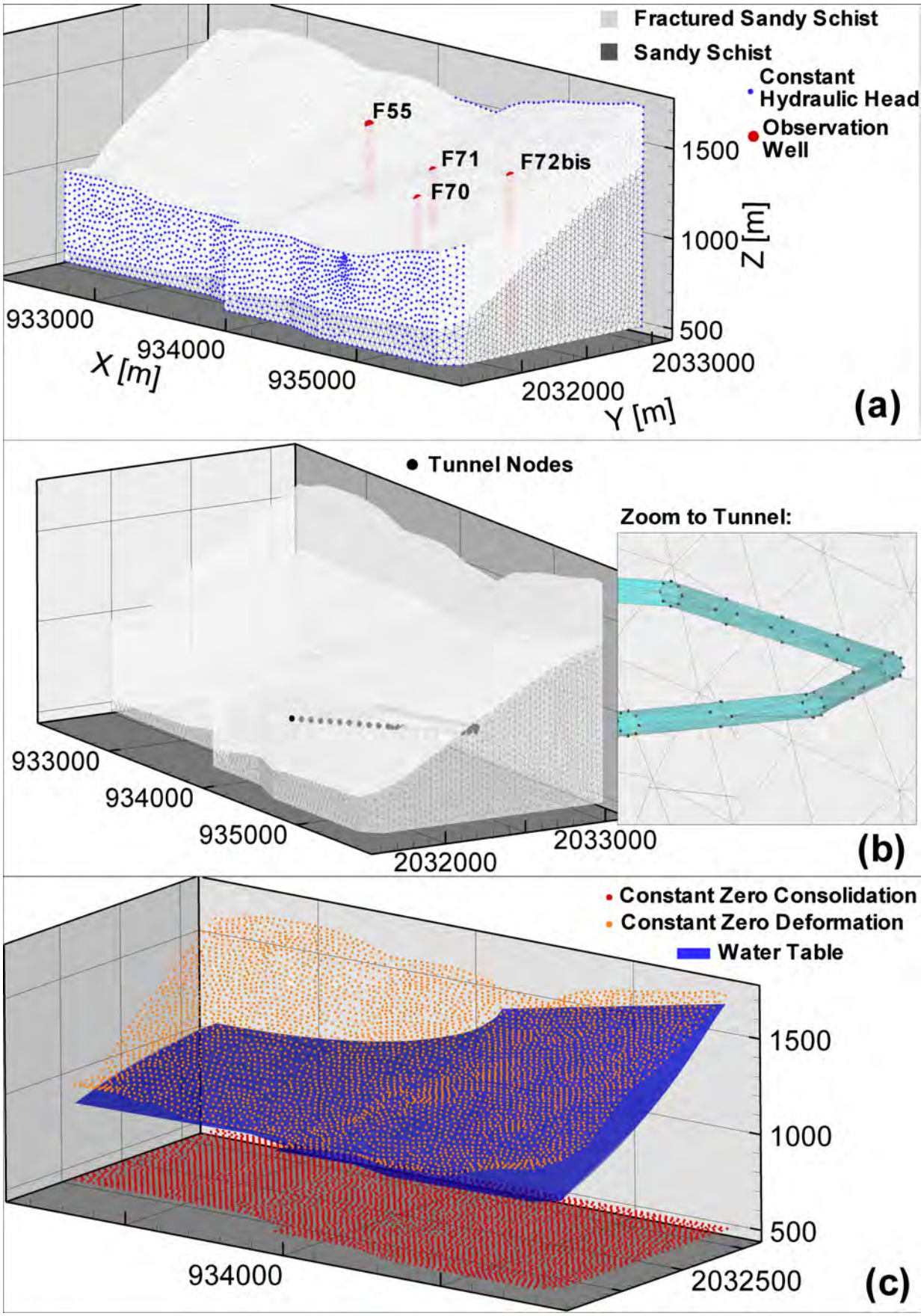

Figure 5.9: 3D model geometry showing (a) local geology, boundary conditions and observation wells for the steady state groundwater flow model, (b) the discretisation of the La Praz exploratory adit used in the transient model with a zoom to a part of the tunnel, and (c) boundary conditions and piezometric water levels for the consolidation simulation.

heads and drawdowns do not satisfactorily reproduce the observed values (Figure 5.10b). This is due to the upstream hydraulic boundary condition used in the model, which is considered to be constant. In reality the upstream hydraulic heads have also to be modified with time and excavation progression.

As anticipated, the numerical analysis has been time consuming, especially during (1) the discretisation of the tunnel in the 3D finite element mesh, and (2) the calibration phase.

Table 5.4: Parametric and geologic information used in the numerical models

Geology	$K_{0_{xx}}$ [m/s]	$K_{0_{yy}}$ [m/s]	$K_{0_{zz}}$ [m/s]	S_{s_0} [1/m]	ϕ_0	σ_0 [Pa]	λ	n
weathered sandy schist	$2 \cdot 10^{-5}$	$1 \cdot 10^{-5}$	$1 \cdot 10^{-5}$	$1 \cdot 10^{-4}$	0.05	$5 \cdot 10^{8}$	1.5	9
unaltered sandy schist	$2 \cdot 10^{-7}$	$1 \cdot 10^{-7}$	$1 \cdot 10^{-7}$	$1 \cdot 10^{-4}$	0.005	$5 \cdot 10^{8}$	1.5	9

5.4 Conclusions

This work has focused on quantitative tools specific to the problem of groundwater inflow and related mechanisms during and after tunnel excavation. Three major hydrogeological issues are related to tunneling: (1) transient and steady inflow rates in tunnels due to the drainage of surrounding aquifers, (2) water table decline leading to the drying up of springs, and (3) consolidation of the aquifer (related to the water table decline) leading to ground settlement. All of these processes can be correctly reproduced by analytical solutions or by numerical simulation.

It has been shown that both approaches capture the main hydrogeological processes, and can be used as predictive tools. However, in practice, the use of numerical models is limited because (1) the method is time consuming and (2) of the difficulty to introduce tunnels in large scale, geologically oriented 3D meshes. Moreover, at a regional scale 3D geological models usually have a low reliability.

Analytical formulas require simplifications of aquifer structures and of the groundwater flow system, but are able to reproduce the governing mechanisms. Based on the geological and hydrogeological information along and perpendicular to the tunnel axis, the presented analytical solutions lead to rapid first estimations of the transient and steady discharge rates produced by a tunnel, as well as of water table decline and associated ground settlement, as demonstrated in the La Praz field example. The reduction factor allows overall consideration of the impact of effective stress on hydrodynamic parameters, in particular on hydraulic conductivity, and improves the accuracy of standard equations. This factor should be used in the analysis of groundwater inflow in deep tunnels.

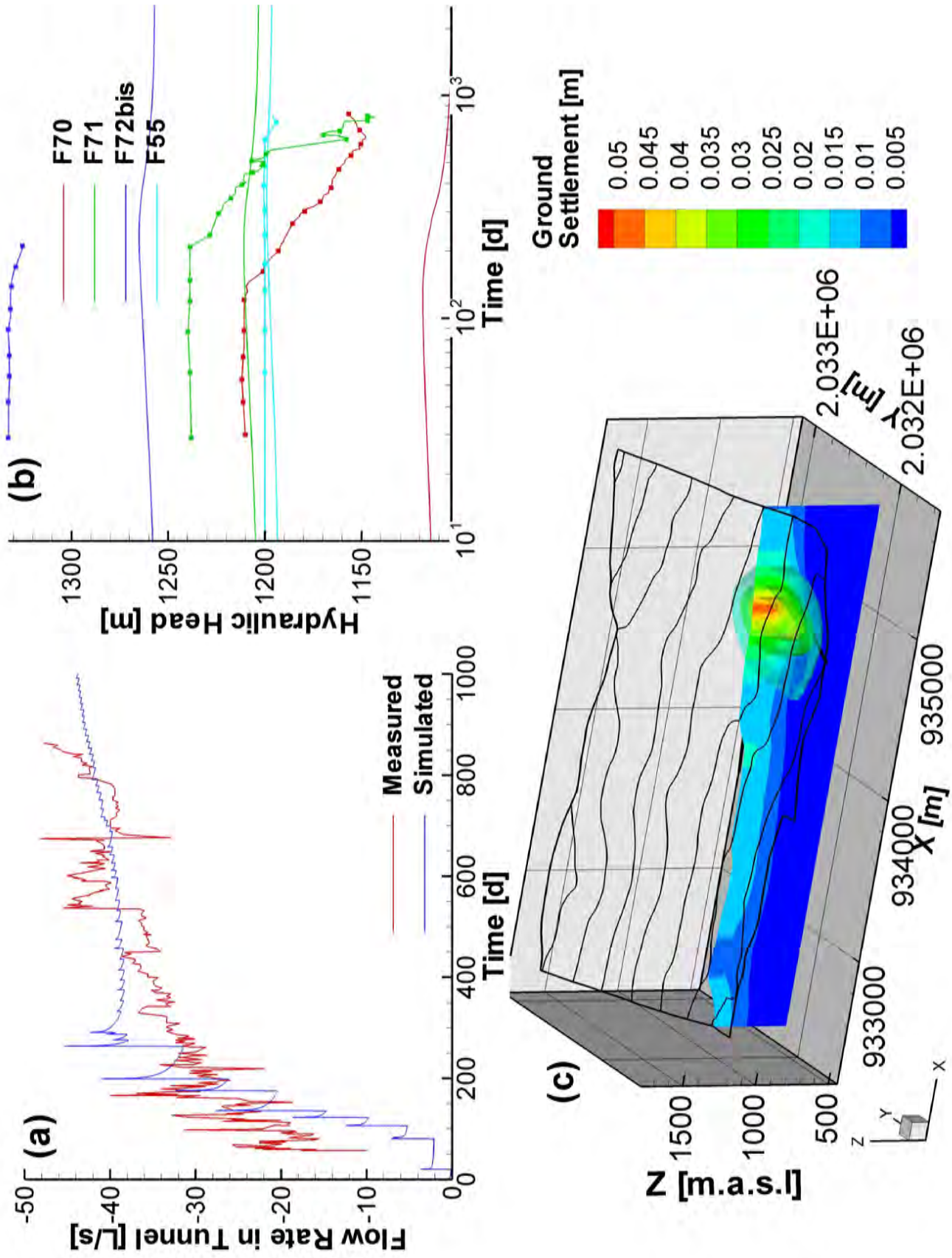

Figure 5.10: Comparison of (a) measured water flow rates in tunnel (red line) with simulated values (blue line), and (b) measured drawdown in observation wells (solid lines with dots) with simulated ones (solid lines). (c) Simulated bulbs and cross section of ground settlement with the La Praz tunnel trajectory and the local topography.

Bibliography

[1] Anagnostou, G.: The influence of tunnel excavation on the hydraulic head. International Journal for Numerical and Analytical Methods in Geomechanics **19**(10), 725–746 (1995)

[2] Barbosa, R.: Personal communication (2009)

[3] Bear, J., Cheng, A.H.D.: Modeling Groundwater Flow and Contaminant Transport. Springer Science (2010)

[4] Bonzanigo, L.: Lo slittamento di Campo Vallemaggia. Ph.D. thesis, Swiss Federal Institute of Technology Zürich (1999)

[5] Bordet, C.: L'eau dans les massifs rocheux fissurés. Observations dans les travaux souterrains. Tech. rep., Université de Liège, Liège, BEL (1971)

[6] Boutt, D., Diggins, P., Mabee, S.: A field study (Massachusetts, USA) of the factors controlling the depth of groundwater flow systems in crystalline fractured-rock terrain. Hydrogeology Journal **18**(8), 1839–1854 (2010)

[7] Cappa, F.: Role of fluids in the hydromechanical behavior of heterogeneous fractured rocks: in situ characterization and numerical modelling. Bull. Eng. Geol. Env. **65**, 321–337 (2006)

[8] Chisyaki, T.: A study of confined flow of ground water through a tunnel. Ground Water **22**(2), 162–167 (1984)

[9] Cornaton, F.J.: Ground Water: a 3-D Ground Water and Surface Water Flow, Mass Transport and Heat Transfer Finite Element Simulator, Reference Manual, 398 pp. Centre for Hydrogeology and Geothermics, Neuchâtel, Switzerland (2007)

[10] Dematteis, A., Perrochet, P., Thiery, M.: Nouvelle liaison ferroviaire transalpine Lyon-Turin, Etudes hydrogéologiques 2002-2004. Tech. rep., Lyon Turin Ferroviaire, Chambéry, France (2005)

[11] Durham, W.B.: Laboratory observations of the hydraulic behavior of a permeable fracture from 3800 m depth in the KTB pilot hole. J. Geophys. Res. **102**, 18,405–18,416 (1997)

[12] Dzikowski, M., Villemin, T.: Rapport d'expertise: hydrogéologie et géodésie de la descenderie de La Praz. Tech. rep., Belonging to Lyon Turin Ferroviaire (LTF), Chambery, France (2009)

[13] El Tani, M.: Circular tunnel in a semi-infinite aquifer. Tunnelling and Underground Space Technology **18**(1), 49–55 (2003)

[14] Galloway, D., Burbey, T.: Review: Regional land subsidence accompanying groundwater extraction. Hydrogeology Journal **19**, 1459–1486 (2011)

[15] Gargini, A., Vincenzi, V., Piccinini, L., Zuppi, G., Canuti, P.: Groundwater flow systems in turbidites of the Northern Apennines (Italy): natural discharge and high speed railway tunnel drainage. Hydrogeology Journal **16**(8), 1577–1599 (2008)

[16] Geuzaine, C., Remacle, J.F.: Gmsh: a three-dimensional finite element mesh generator with built-in pre- and post-processing facilities. International Journal for Numerical Methods in Engineering **79**(11), 1309–1331 (2009)

[17] Goodman, R., Moye, D., Van Schaikwyk, A., I., J.: Ground water inflows during tunnel driving. Bulletin of the International Association of Engineering Geologists **2**(1), 39–56 (1965)

[18] Hansmann, J., Loew, S., Evans, K.: Reversible rock-slope deformations caused by cyclic water-table fluctuations in mountain slopes of the Central Alps, Switzerland. Hydrogeology Journal **20**(1), 73–91 (2012)

[19] Heuer, R.: Estimating Rock Tunnel Water Inflow. In: Rapid Excavation and Tunneling Conference. San Francisco, U.S.A., June 18-21 (1995)

[20] Hopkins, D.: The implications of joint deformation in analyzing the properties and behavior of fractured rock masses, underground excavations and faults. Int. J. Rock Mech. Min. Sci. Geomech. Abstr. **37**(1–2), 175–202 (2000)

[21] Ingénierie-ITM: Descenderie de La Praz: synthèse géologique, hydrogéologique et géotechnique. Tech. rep., Lyon Turin Ferroviaire (LTF), Chambery, France (2005)

[22] Jacob, C.: On the flow of water in an elastic artesian aquifer. American Geophysical Union **21** (1940)

[23] Jacob, C.: Engineering hydraulics: Proceedings of the Fourth Hydraulics Conference, Iowa Institute of Hydraulic Research, Iowa City, IW, chap. Flow of ground water. Rouse H (ed) (1950)

[24] Kim, J.M., Parizek, R.: A Mathematical Model for the Hydraulic Properties of Deforming Porous Media. Ground Water **37**(4), 546–554 (1999)

[25] Lassiaz, P., Previtali, I.: Descenderie et Galerie de reconnaissance de Modane / Villarodin-Bourget: Suivi et Auscultation Géodésique. Tech. rep., Lyon Turin Ferroviaire, Chambéry Cedex, France (2007)

[26] Lombardi, G.: Les tassements exceptionnels au barrage de Zeuzier. Publ. Swiss Soc. Soil Rock Mech. **118**, 39–47 (1988)

[27] Louis, C.: A study of groundwater flow in jointed rock and its influence on the stability of rock masses. Tech. Rep. 9, Rock Mechanics, Imperial College, London, UK (1969)

[28] Masset, O., Loew, S.: Hydraulic conductivity distribution in crystalline rocks, derived from inflows to tunnels and galleries in the Central Alps, Switzerland. Hydrogeology Journal **18**(4), 863–891 (2010)

[29] Mayeur, B., Fabre, D.: Measurement and modeling of natural stresses. Application to the Maurienne-Ambin tunnel project. Bulletin of Engineering Geology and the Environment **58**(1), 45–59 (1999)

[30] Molinero, J., Samper, J., Juanes, R.: Numerical modeling of the transient hydrogeological response produced by tunnel construction in fractured bedrocks. Engineering Geology **64**(4), 369–386 (2002)

[31] Perrochet, P.: Facteur de réduction des débits en tunnels profonds. Tech. rep., Centre for Hydrogeology and Geothermics, University of Neuchâtel, Neuchâtel, Switzerland (2004)

[32] Perrochet, P.: Confined Flow into a Tunnel during Progressive Drilling: An Analytical Solution. Ground Water **43**(6), 943–946 (2005)

[33] Perrochet, P.: A simple solution to tunnel or well discharge under constant drawdown. Hydrogeology Journal **13**, 886–888 (2005)

[34] Perrochet, P., Dematteis, A.: Modeling Transient Discharge into a Tunnel Drilled in a Heterogeneus Formation. Ground Water **45**(6), 786–790 (2007)

[35] Preisig, G., Cornaton, F., Perrochet, P.: Regional Flow Simulation in Fractured Aquifers Using Stress-Dependent Parameters. Ground Water **50**(3), 376–385 (2012)

[36] Preisig, G., Cornaton, F., Perrochet, P.: Simulation of flow in fractured rocks using effective stress-dependent parameters and aquifer consolidation. In: Models - Repositories of Knowledge, MODELCARE 2011, IAHS Red Books (in press)

[37] Rutqvist, J., Stephansson, O.: A cyclic hydraulic jacking test to determine the in situ stress normal to a fracture. Int. J. Rock Mech. Min. Sci. Geomech. Abstr **33**(7), 695–711 (1996)

[38] Schneider, T.: Geological Aspects of the Extraordinary Behaviour of Zeuzier Arch Dam. Wasser, energie, luft - eau, énergie, air **74**(3), 81–94 (1982)

[39] Schweisinger, T., Svenson, E., Murdoch, L.: Introduction to hydromechanical well tests in fractured rock aquifers. Ground Water **47**(1), 69–79 (2009)

[40] SOGREAH Consultants: Descenderie de Modane/Villarodin-Bourget: étude de faisabilité de reutilisation des eaux d'exhaure de la partie montante. Tech. rep., Lyon Turin Ferroviaire (LTF), Chambery, France (2007)

[41] Terzaghi, K.: Die berechnung der durchlässigkeitziffer des tones aus dem verlauf der hydrodynamischen spannungserscheinungen. Akad Wissensch Wien Sitzungsber Mathnaturwissensch Klasse IIa **142**(3–4), 125–138 (1923)

[42] Tsang, Y., Witherspoon, P.: Hydromechanical behavior of a deformable rock fracture subject to normal stress. J. Geophys. Res. **86**(B10), 9287–9298 (1981)

[43] Vulliet, L., Koelbl, O., Parriaux, A., Védy, J.C.: Gutachtenbericht über die Setzungen von St. German, in Auftrag der BLS Alptransit AG. Tech. rep. (2003)

[44] Walsh, J.B.: Effect of pore pressure and confining pressure on fracture permeability. Int. J. Rock Mech. Min. Sci. Geomech. Abstr. **18**, 429–435 (1981)

[45] Zangerl, C., Eberhardt, E., Loew, S.: Ground settlements above tunnels in fractured crystalline rock: numerical analysis of coupled hydromechanical mechanisms. Hydrogeology Journal **11**, 162–173 (2003)

Chapter 6

Application to real cases, part II: anthropogenic land subsidence in Mexico City

Abstract

The regional simulation of coupled hydromechanical processes requires a simplification of existing solutions (see section 1.7). A modelling approach specific for fluid-to-solid coupled hydromechanical processes was presented in Chapter 4. The present work aims at verifying the proposed approach by simulating the regional land subsidence affecting the Mexico City Basin. First, based on past-to-present literature a regional hydrogeological conceptual model is elaborated. Second, a 3D numerical model is constructed and used in conjunction with the proposed approach to simulate the regional water table drawdown and land subsidence. The modelling approach satisfactorily reproduces both phenomena. Some significant differences with findings of other authors are most probably related to errors within the 3D geological model, as well as to specified boundary conditions. Despite this, the model can be considered as a solid tool to evaluate the impacts of intensive groundwater pumping on a basin-fill aquifer system.

6.1 Introduction

In deep aquifer systems, groundwater overpumping results in regional water table drawdown and in land subsidence [16, 15]. This is principally due to the increase of effective stress leading to the consolidation of aquitards, but also of aquifers [31, 21, 22, 5, 32, 18, 19, 29]. Moreover, the change in effective stress modifies hydrodynamic parameters, i.e., porosity, hydraulic conductivity and storage, which can no longer be considered as constants in groundwater and deformation analyses [20, 17, 23].

Two principal approaches can be used to analyse groundwater flow and compaction in an aquifer system subject to excessive groundwater pumping [4]: (1) the non-simultaneous analysis of water pressure changes and aquifer deformation [21, 22], and (2) the simultaneous analysis,

e.g., the aquitard drainage model [29] or Biot's poroelasticity theory [5]. These approaches correctly reproduce the deformation of a porous mass that follows a change in fluid pressure. However, despite the before-mentioned dependency on effective stress, hydrodynamic parameters are in general considered as constants [14]. Moreover, in such models only the compaction of aquitards is often taken into account, neglecting the possible compressibility of aquifer units. Biot's poroelastic theory allows a detailed 3D groundwater flow in a deformable porous mass, but this approach is not well suited for regional groundwater systems due to the complexity of governing equations and the large spatial scales involved. The modelling approach presented in Chapter 4 has been developed in order to analyse fluid-to-solid hydromechanical processes at a regional scale and considering detailed geological structures. In this Chapter, the ability of this approach is tested on a benchmark case study: the land subsidence in the Mexico City basin.

Mexico City is built on a deep regional aquifer, which is overexploited, i.e., groundwater pumping is greater than the system recharge. This has lead to a regional water table drawdown, resulting in a compaction, especially of the confined upper unit of lacustrine deposits, and land subsidence [30, 27, 2, 3]. Using differential interferometry, Osmanoglu et al. [28] recently detected a subsidence rate of 300 mm/y. This seems to be the world's largest reported subsidence rate [15].

The great paradox within the context of groundwater overexploitation and land subsidence in Mexico City is that surface waters are drained and evacuated outside the basin [6, 27, 2].

The present work aims at testing the modelling approach presented in Chapter 4 on a real regional case in order to identify its advantages but also its limitations. The model is also designed to perform a sensitivity analysis able to illustrate the long term behaviour of the aquifer system in the case of an unsustainable use of groundwater.

6.2 Geological and anthropological setting of the Mexico City basin

The Mexico City Basin has been shaped by the emplacement of tertiary and quaternary basalts. Those extrusive rocks are interbedded and can be divided into two principal formations: (1) fractured Tertiary / Quaternary basalts (Tb / Qb), and (2) pyroclastic rocks such as tuff, pumice and lahar (the Tarango formation: T) [26, 12]. After these volcanic activities, the basin was first an open alluvial system with a regional surface waters flow from N to S leading to the deposition of Quaternary alluvial sediments (Qal) over the Tarango formation. Then, the basin became a closed system due to a new extrusion of Quaternary basalts forming today the Sierra Chichinautzin, South to Chalco basin. These volcanoes have formed a natural barrier leading to the Lake Texcoco formation as well as the sedimentation of lacustrine deposits (Qla). From a hydrological point of view the basin became endorheic*. Figure 6.1 shows a regional geological map of the Mexico City Basin with two cross sections, longitudinal and perpendicular to the

*basin without a discharge zone, the recharge is balanced by the evapotransiration [8]

basin, as well as the regional stratigraphy.

The geological dynamic of the basin has then been governed by anthropogenic activities. In the 14th century, the Aztecs opted for piles construction to deal with lacustrine characteristics of the plain. In the 16th century, Spanish settlers started important drainage works that were completed in the 19th century with the catchment and the evacuation of surface water in the basin upstream zones [7]. The lands acquired from Lake Texcoco allowed the rapid urbanization of the plain and an impressive demographic growth. Springs located in the western part of the basin could no longer allow the water supply, leading to the construction of first wells. Nowadays, the aquifer system under Mexico City is overexploited [30, 27, 6, 12]. The water discharge rate leaving the aquifer system due to intense pumping is very much greater than the recharge from the surroundings volcanoes. Over the years, this has result in a regional water table drawdown leading to the system consolidation and to land subsidence [30, 27, 6, 12, 28]. In addition, ground fracturing is related to differential consolidation due to the presence of an abrupt slope in the basement topography or aquifer heterogeneity [2, 3, 10].

6.2.1 Aquifer system description

The term "aquifer system" was first used by Helm [19, 20] to refer to the regional set resulting from the vertical and horizontal succession of aquifers, aquitards and semi-confining units. Within this context the Tarango formation (T) and the alluvial deposits (Qal) form a heterogeneous sandy aquifer of variable thickness, with a maximum of $\approx$ 800-900 m in the southern part of the Basin. Tertiary basaltic rocks (Tb) constitutes the aquifer system basement. This surface is discontinuous and faulted. The upper system boundary is formed by the lacustrine deposits (Qla), which confine the aquifer in the basin center. This aquitard is not present on basin slopes, resulting here in a phreatic system. Qla formation is heterogeneous and of variable thickness: (1) silty clayey lacustrine deposits are interbedded with some strata of fine sand 1 to 3 m thick ("Capas Duras"), and (2) the total thickness varies between 50 to a maximum of $\approx$ 300 m in the Chalco sub-basin. At this point, it is important to note that locally the aquifer system geometry is discontinued by the extrusion of Quaternary basalts (Qb). From a geomechanical point of view, Qla represents a highly compressible unit, the aquifer (Qal and T) is compressible, and basaltic rocks can be considered as incompressible [30, 27, 6].

6.2.2 Hydrogeological conceptual model and compaction

The hydrogeological conceptual model must be divided into two states: before and after groundwater exploitation by pumping.

As afore-mentioned the basin is endorheic, implying that before the demographic growth and groundwater pumping the recharge from surroundings volcanoes was balanced by the evapotranspiration, especially in the ancient Lake Texcoco. The aquifer system was completely confined leading to (1) springs on basin slopes due to the water table cropping out, and (2) a vertical upward flux through lacustrine deposits recharging the ancient Lake Texcoco (Figure

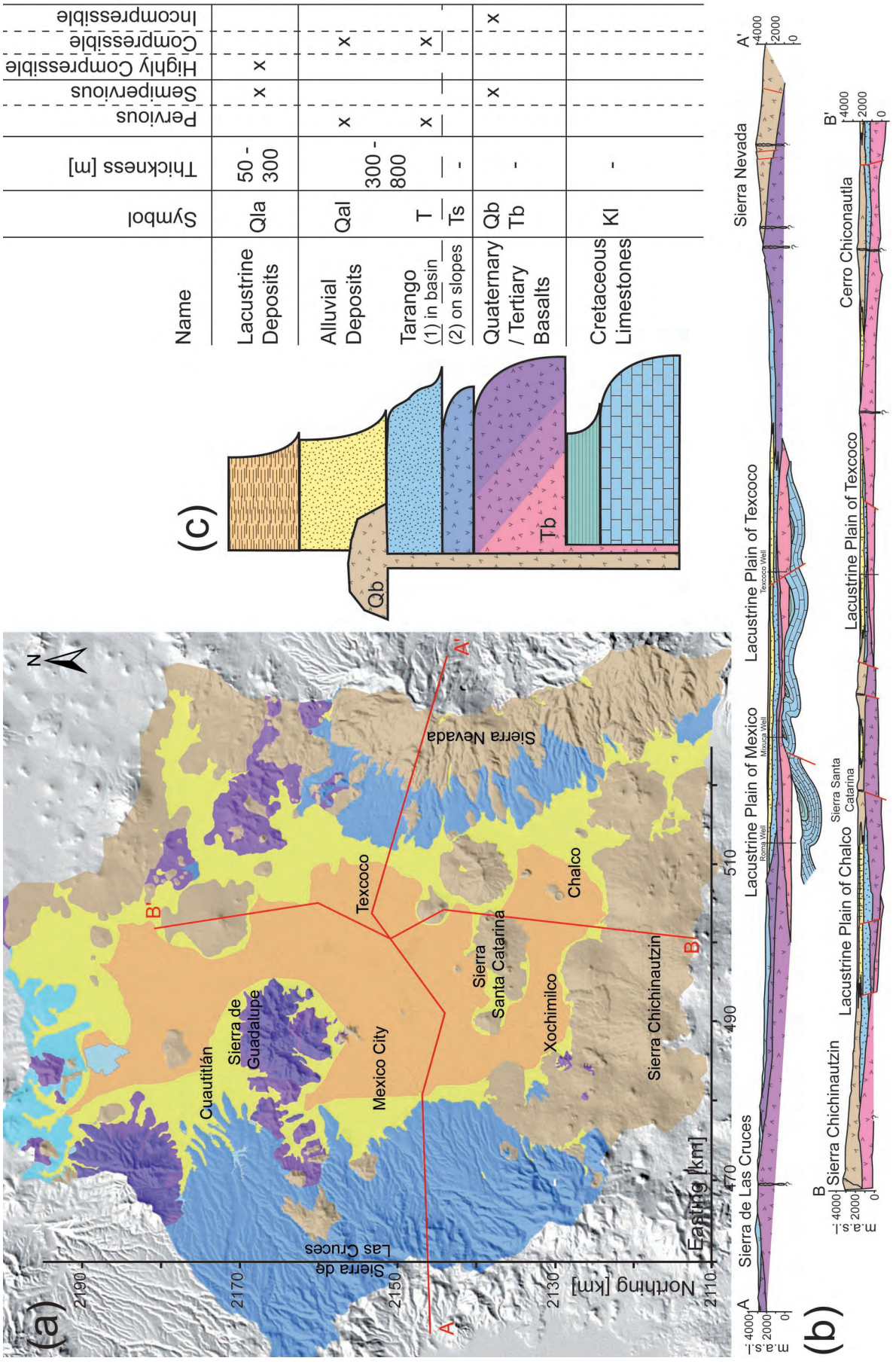

Figure 6.1: (a) Geological map of the Mexico City basin [12] with (b) a cross section longitudinal and one transversal to the basin [33]. (c) Regional aquifer system stratigraphy with a qualitative description of hydraulic and geomechanical properties for formations considered in the model.

6.2a) [27].

Groundwater exploitation by wells pumping increasingly deeper has resulted in a regional water table drawdown leading to the drying up of springs mainly located on the basin western slopes, and the loss of artesian mechanisms. Locally, the aquifer system is now unconfined also in the central zone with a possible inversion of the vertical flux through the lacustrine formation [27, 12]. On one hand, Carrera-Hernández and Gaskin [12] mentions that the basin total recharge is approximately 16 m^3 s^{-1}. On the other hand, groundwater extraction due to pumping is estimated 2.7 to 4 times greater than the recharge [30, 6, 12]. Intense groundwater extraction has resulted in a diminution in storage and in a regional water table drawdown causing principally the consolidation of lacustrine deposits but also of the aquifer, and leading to land subsidence [27] (Figure 6.2b). Furthermore, soil cracking as a result of differential settlement deteriorates groundwater quality, because fractures can behave as preferential infiltration flow paths of surface waste waters [7].

6.3 Modelling strategy

The numerical approach detailed in the previous Chapter 4 is used to model and analyse the process. This approach is an innovative method to simulate regional hydromechanical processes considering detailed geology and the dependency of hydrodynamic parameters on effective stress. As was discussed in Chapter 3, the integration of stress-dependent parameters in the groundwater flow equation, theoretically, leads to an aquifer depressurisation and compaction slower than that obtained with the approaches considering constant parameters, such as in linear poroelasticity theory [5].

Available data for model construction are provided by the Basin of Mexico Hydrogeological Database (BMHDB) of Carrera-Hernández and Gaskin [13].

6.3.1 3D regional geological model

The first step consists in the elaboration of a 3D regional geological model. This was carried out by Mercier [25] in her Master's thesis using `GeoModeller` [9]. This software interpolates vector fields of geological contacts and dips orientation in order to construct potential fields of scalar functions constituting the 2D surfaces forming the 3D model [24, 11]. The geological cross sections of Vázquez Sánchez and Jaimes-Palomera [33], and the geological data of Carrera and Gaskin [13] were used to reproduce the basin. Contacts between formations are based on the regional stratigraphy presented in Figure 6.1c. The model topography has been constructed using a digital elevation model (dem) of 1990.

Resulting surfaces and volumes are then used to build a regional geologically oriented 3D mesh respecting strata geometries (Figure 6.3a). The main assumptions related to the basin discretisation are:

- the basin constitutes an unique hydrogeological entity

- the domain area is limited to the extension of alluvial deposits (Figure 6.1a). This implies that (1) recharge must be considered as a flux entering the lateral aquifer system boundaries, as shown in the conceptual model (Figure 6.2), and (2) rocks beyond this limit are not taken into account: Tertiary / Quaternary basalts and Tarango on slopes.

- there are no displacements of aquifer strata in areas where deep faults may extend into the aquifer (Figure 6.1b).

- within the domain boundaries, rocks considered are Quaternary basalts, such as the Sierra Santa Catarina massif having a non-negligible role on recharge, Tarango formation, alluvial and lacustrine deposits. Tertiary basalts are not taken into account due to their impervious character and constitute the system basement as illustrated on cross sections of Figure 6.1b. The distinction between rocks is done in terms of hydrodynamic and geomechanical parameters (Figure 6.3a).

The overburden stress field affecting the basin is then computed with the method detailed in subsection 4.2 by specifying saturated rock densities (Table 6.1). Boundary conditions for this simulation corresponds to (1) a Dirichlet constant condition at the domain upper surface of zero overburden stress, and (2) a Neumann constant condition on the bottom boundary corresponding to $-g\,\rho_{r_{bottom}}$, where g is gravitational acceleration and $\rho_{r_{bottom}}$ is the saturated density of the rock on domain bottom. In the present model, horizontal stresses $\sigma_{xx} = \sigma_{yy}$ are set equivalent to the corresponding vertical overburden stress σ_{zz} ($\nu = 0.5$, $\lambda = 1$).

6.3.2 Transient groundwater flow model

Based on the literature survey presented in section 6.2 a conceptual model is proposed and used for the construction of a transient groundwater flow numerical model (Figure 6.2). The aim of this simulation is to correctly reproduce the regional water table drawdown due to massive pumping.

Characteristics of the initial hydraulic head field, i.e., before that the excessive groundwater pumping started, are not known in detail. However, the conceptual model in Figure 6.2a can be used as a basis schematising the aquifer system initial state. In this context, an average hydraulic head matching the Lake Texcoco elevation can be used to reproduce the initial state:

$$H(x, y, t_0) = f_1(x, y, z_{top}) \tag{6.1}$$

where H is hydraulic head, t_0 is initial simulation time, and f_1 is a known function detailing Lake Texcoco average elevation z_{top} at spatial coordinates x, y. The spatial extension of the Lake Texcoco matches lacustrine deposits (Figure 6.1a).

Recharge from surrounding basaltic mountains is based on the BMHDB [13] and is introduced as a regionalised constant water flux, i.e., a Neumann boundary condition, entering the lateral aquifer system boundaries. The total groundwater flux recharging the basin corresponds to a volumetric discharge rate of approximately 10 m^3/s.

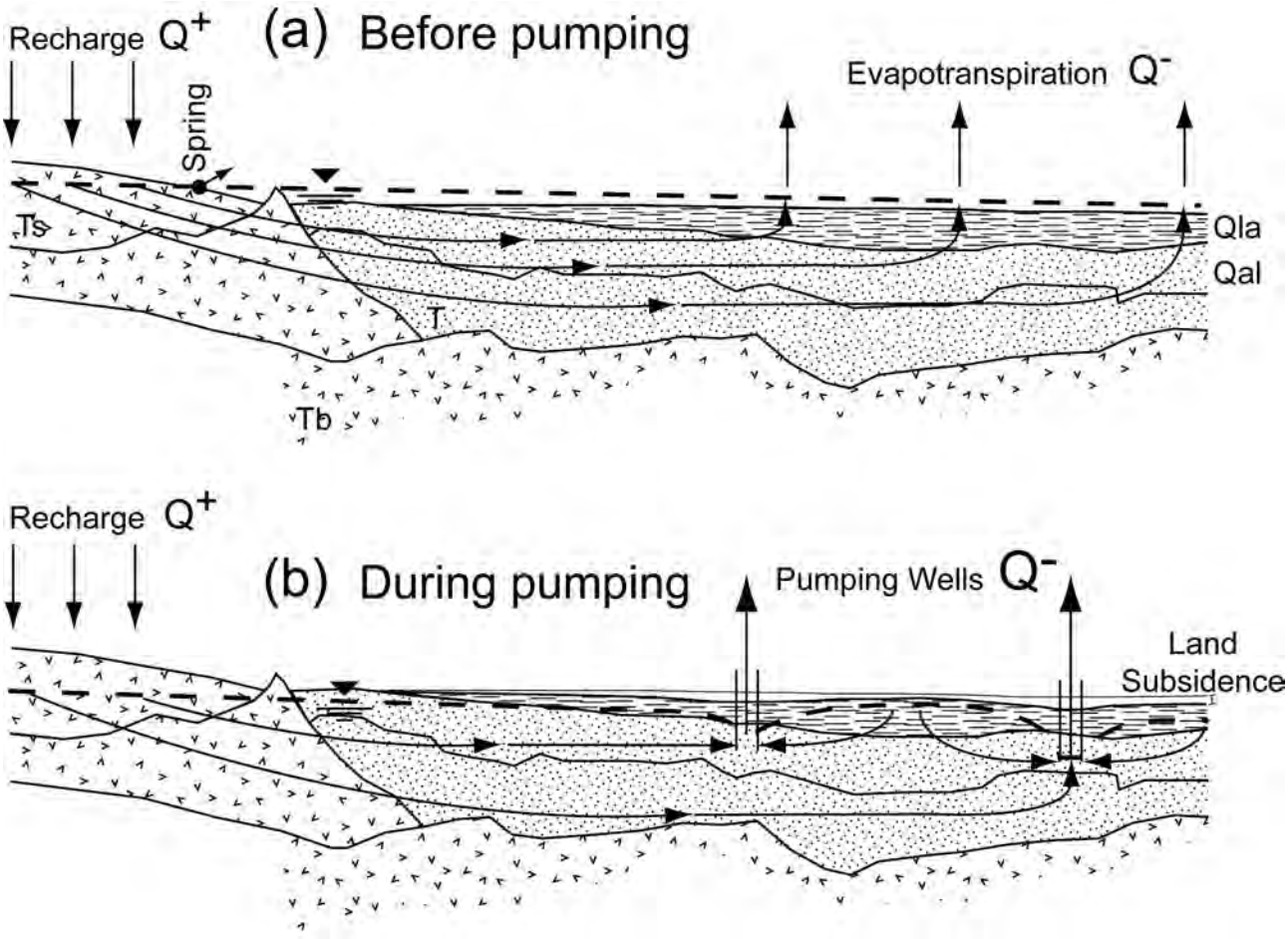

Figure 6.2: Conceptual model showing the aquifer system behaviour (a) before and (b) after groundwater overexploitation by pumping wells (vertical exaggeration 5x).

Two types of boundary conditions are used to consider groundwater pumping in the aquifer, and both conditions are expressed as time varying functions acting in the Qal formation. Available data in the form of pumping rates are introduced as boundary conditions of the fourth type (Well boundary condition):

$$Q_{well} = f_2(x, y, z, t) \tag{6.2}$$

where f_2 is a known time varying function describing the pumping rate Q_{well} evolution with time t for a well extracting groundwater at coordinates x, y, z. The above boundary condition is constrained by a minimum hydraulic head H^{min} corresponding to the bottom elevation of Qal strata at the well location added by a pressure head of 10 m. With this constraint, the calculated hydraulic head H^{sim} cannot be lower than the imposed minimum hydraulic head H^{min}: if $H^{calc} < H^{min}$ then $H^{calc} = H^{min}$, and the resulting extraction rate is reduced accordingly.

Groundwater pumping is also introduced using boundary conditions of the first-kind (Dirichlet type):

$$H_{well} = f_3(x, y, z, t) \tag{6.3}$$

where f_3 is a known time varying function describing the hydraulic head H_{well} evolution with time t in a well located at coordinates x, y and z. The calculated extracted pumping rates are constrained to a maximum value of zero: $Q_{max}^{calc} = 0$. This prevents wells to behave as recharging boundaries ($Q > 0$) in the case where simulated hydraulic heads in the model become lower than the imposed ones in the wells. The location of boundary nodes in the model is shown in Figure 6.3.

At this point, it is important to note that the model remains rather uncertain because of three main issues having impacts on its reliability:

1. time functions describing the evolution of pumping rates or hydraulic heads in wells do not cover the entire simulation time. This implied an extrapolation of data, especially at the early stage of the simulation, having significant impact on the results. Also the initial simulation time cannot be exactly superimposed to a real time, which approximately corresponds to a period prior to the impressive urban growth, such as 1930 / 1940.

2. only the $\approx$ 3500 officially registered wells [12, 13] are present in the model. No data are available for the non-registered wells.

3. the reference system used for measuring hydraulic heads has probably been affected by the regional land subsidence. The digital elevation model used to construct the 3D regional geological model is also not representative for years prior to 1990, because of the regional land subsidence.

The matching between simulated and observed data is done by adjusting hydrodynamic parameters, i.e., porosity, hydraulic conductivity and specific storage coefficient. The data used for the calibration are the total pumping rates extracted from the aquifer system [30, 27, 6, 12], as well as the regional piezometric maps of Carrera-Hernández and Gaskin [12] obtained by means of geostatistical analysis.

6.3.3 Consolidation model

Simulated hydraulic head fields can subsequently be used for computing the regional anthropogenic subsidence affecting the basin. This is done following the approach presented in subsection 4.2 using Eqs. (3.16) and (3.17) of Chapter 3. Quaternary basalts are considered as incompressible.

6.4 Results and discussions

The numerical model is able to reproduce the regional water table drawdown affecting the Mexico City basin (Figure 6.4a-b), as well as the aquifer system overexploitation as shown in Figure 6.4c. The overexploitation begins after 20 years of simulation time, which correlates well with the explosion of demography and water consumption from the 1950's on.

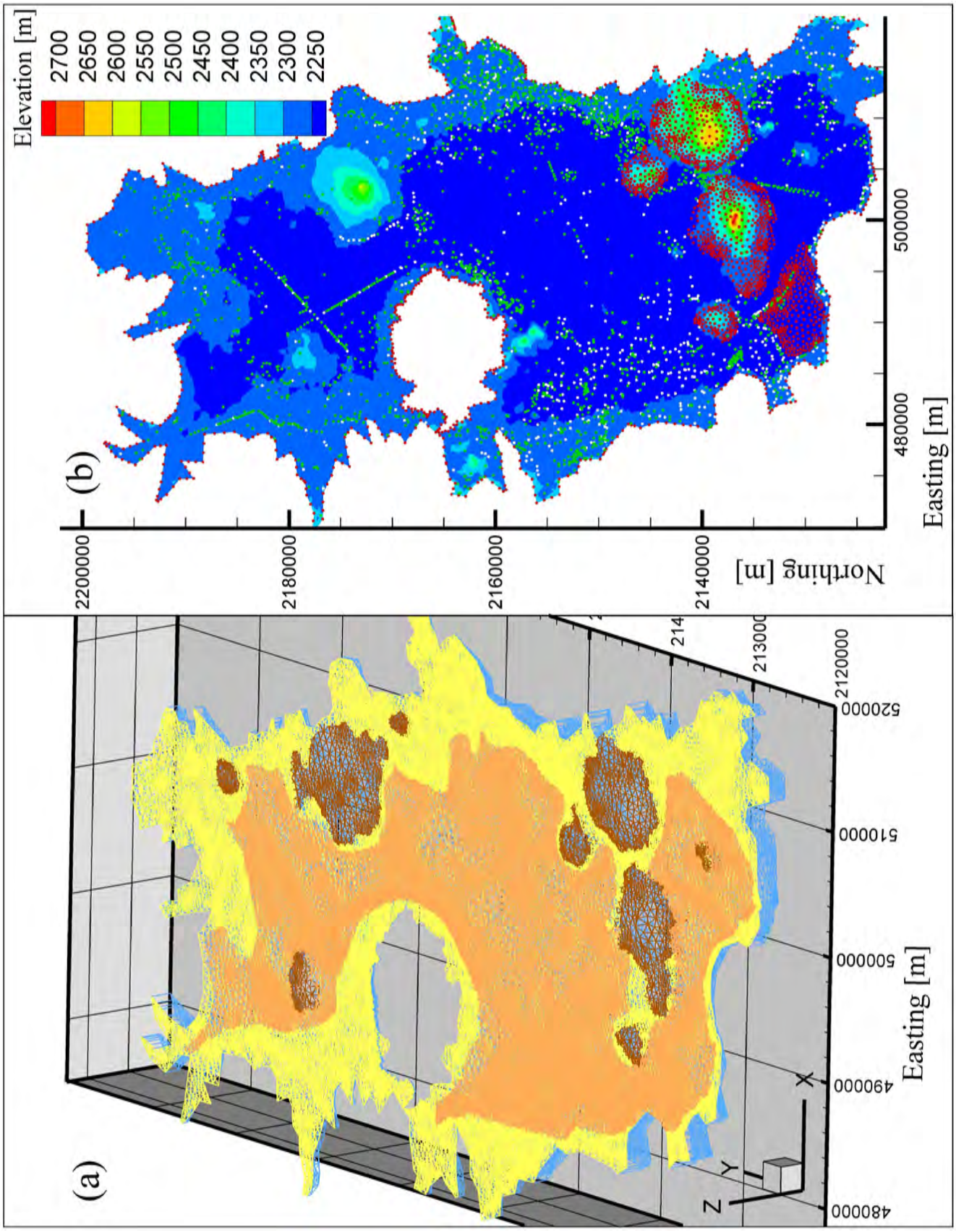

Figure 6.3: (a) 3D view of the regional geologically oriented mesh respecting strata geometries (vertical exaggeration 2x). The color of elements is based on Figure 6.1 and denotes hydrodynamic properties. (b) Topographic map of the basin with model boundaries conditions. Red, white and green points denote a Neumann, Dirichlet and Well type boundary condition, respectively.

As was pointed out by Carrera [12], the groundwater flow model shows that the North of the Basin is also subject to significant water table drawdown, especially after 40 years of simulation time. Concerning the flux direction through lacustrine deposits, the model reproduces the modification from an upward to a downward oriented gradient. This was outlined in Ortega [27]. With the increase of simulation time, the regional water table drawdown results in a semi-confined aquifer system, i.e., in some areas the aquifer is still confined, whereas, it has changed to phreatic conditions in other areas. This also results in a division of the regional aquifer into several sub-basins (Figure 6.6a).

Overall, the regional simulated aquifer system depressurisation is faster compared to the geostatistical data of Carrera-Hernández and Gaskin [12] (Figure 6.4a-b). This difference is mainly related to the extrapolation of specified transient pumping rates.

As mentioned before the excess of simulated groundwater pumping over recharge starts after 20 years of simulation, and is in line with the divergence obtained taking into account the estimated pumping rate curve, based on data of Rivera [30] (Figure 6.4c). The estimated and the simulated pumping rate curves have not the same behaviour, as the modelled curve obviously depends principally on the imposed boundary conditions. Indeed, (1) the abrupt increase of curve slope after 40 years is due to a substantial activation of pumping wells; and (2) the reduction towards the end of the calculation is related to the activation of constraints on imposed pumping rates, especially in the North area of the basin.

Parametric data used in the groundwater flow and consolidation models are presented in Table 6.1.

Table 6.1: Parameter values used in the groundwater flow and consolidation models. Note that: (1) hydraulic conductivity K_0 and specific storage coefficient S_{s_0} are calculated via ϕ_0, E, C and b using Eqs. (3.12) and (3.14); (2) Quaternary basalts are considered to be incompressible.

Lithology	ρ_r	ϕ_0	E	C	b	K_0	S_{s_0}
Lacustrine deposits Qla	1500	0.50	$5.0 \cdot 10^7$	492245	20	$1.0 \cdot 10^{-6}$	$2.0 \cdot 10^{-4}$
Alluvial deposits Qal	1800	0.23	$1.0 \cdot 10^8$	3007	20	$1.1 \cdot 10^{-4}$	$1.0 \cdot 10^{-4}$
Tarango T	2000	0.12	$5.0 \cdot 10^8$	1868	20	$3.1 \cdot 10^{-5}$	$2.0 \cdot 10^{-5}$
Quaternary basalts Qb	2800	-	-	-	-	$1.4 \cdot 10^{-4}$	10^{-4}

Figure 6.5 presents the simulated regional land subsidence obtained using the modelled hydraulic head field after 60 years of massive groundwater pumping ($\approx$ 1990-2000), as well as a zoom to differential consolidation in the Chalco sub-basin. The model correctly reproduces the regional shape of the subsidence affecting the Mexico City Basin and respects the magnitude of the process.

Locally, the simulated subsidence presents some errors compared to a regional map provided by Auvinet [1], which is based on repeated ground leveling. These errors are principally due to the 3D geological model, in particular to the thickness of the highly compressible upper formation (lacustrine deposits) and to the presence of quaternary volcanoes within the basin.

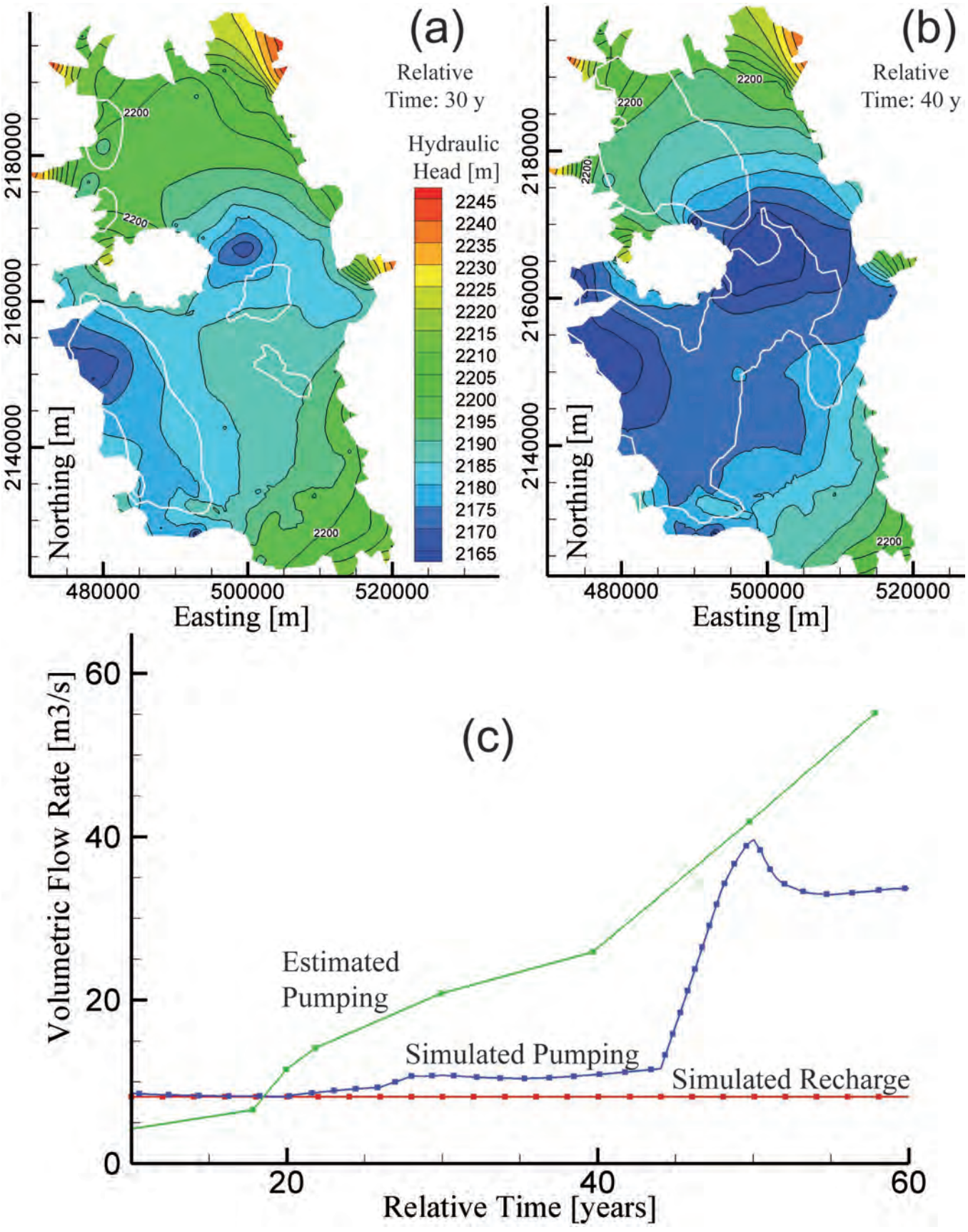

Figure 6.4: Simulated hydraulic head fields at (a) 30 and (b) 40 years of massive groundwater pumping. For comparison; the white contour line is the 2200 m hydraulic head for (a) 1980 and (b) 1990 of Carrera-Hernández and Gaskin [12]. (c) Pumping and recharge rates as a function of simulation time. Estimated volumetric pumping rate is based on [30].

On one hand, in the Chalco sub-basin, the thickness of Qla seems to be overestimated, leading also to an overestimation of the consolidation (Figure 6.6). On the other hand, the geological model overestimates the lateral extension of a volcanic zone in the urban area of Mexico City, leading to an underestimation of land subsidence north of this zone (Figure 6.5).

Interestingly, Figure 6.5 shows that the North of the basin should be also affected by the regional land subsidence. This is due to the significant water table drawdown in this sector, already highlighted in the groundwater flow model. The simulated consolidation is weaker compared to the South of the Basin because of the thinning of lacustrine deposits (Figure 6.6a).

Differential consolidations are correctly highlighted by the proposed model (Figures 6.5 - 6.6). These are mainly located around the incompressible basaltic volcanoes within the basin, such as Sierra Santa Catarina, and are due to an abrupt inflection in the basement topography leading to a strong thinning of the aquifer system. Such areas should be concerned with high horizontal strains, with the possible formation of ground fractures. One substantial differential settlement concerns the airport, which is situated SSE of the afore-mentioned volcanic zone in the urban area of Mexico City (Figure 6.5).

6.5 Simulation of the basin future evolution

The simulated hydraulic head fields allow the construction of regional water table drawdown trends. These trends combined with the hydrodynamic and geomechanical parameters presented in Table 6.1 can be used as a basis for a simulation showing the future evolution of the aquifer system if the regional water table drawdown will continue.

The water table drawdown trends are imposed as Dirichlet boundary conditions on wells nodes, in order to analyse groundwater depletion, and the associated land subsidence. The average and the maximum specified drawdown rates match 1.56 and 2.28 m/y, respectively. The initial state corresponds to the situation after 60 years of pumping obtained in the preceding section.

Results and Discussion

With the specified water table drawdown trend, the aquifer system is obviously overexploited, but it will be able to provide groundwater still for long, via extraction increasingly deeper (Figure 6.7a). In such a case, land subsidence and related processes, such as ground cracking, will continue, having a substantial impact on the region. As shown in Figure 6.7b consolidation depends mainly on water table drawdown, as well as local geology. Thus, where the aquifer system becomes unconfined, i.e., water table level is lower than the bottom of confining lacustrine deposits, land subsidence will continue but at a lower rate. This because consolidation is still active only in the deep aquifer, whereas the compaction of highly compressible lacustrine deposits is over.

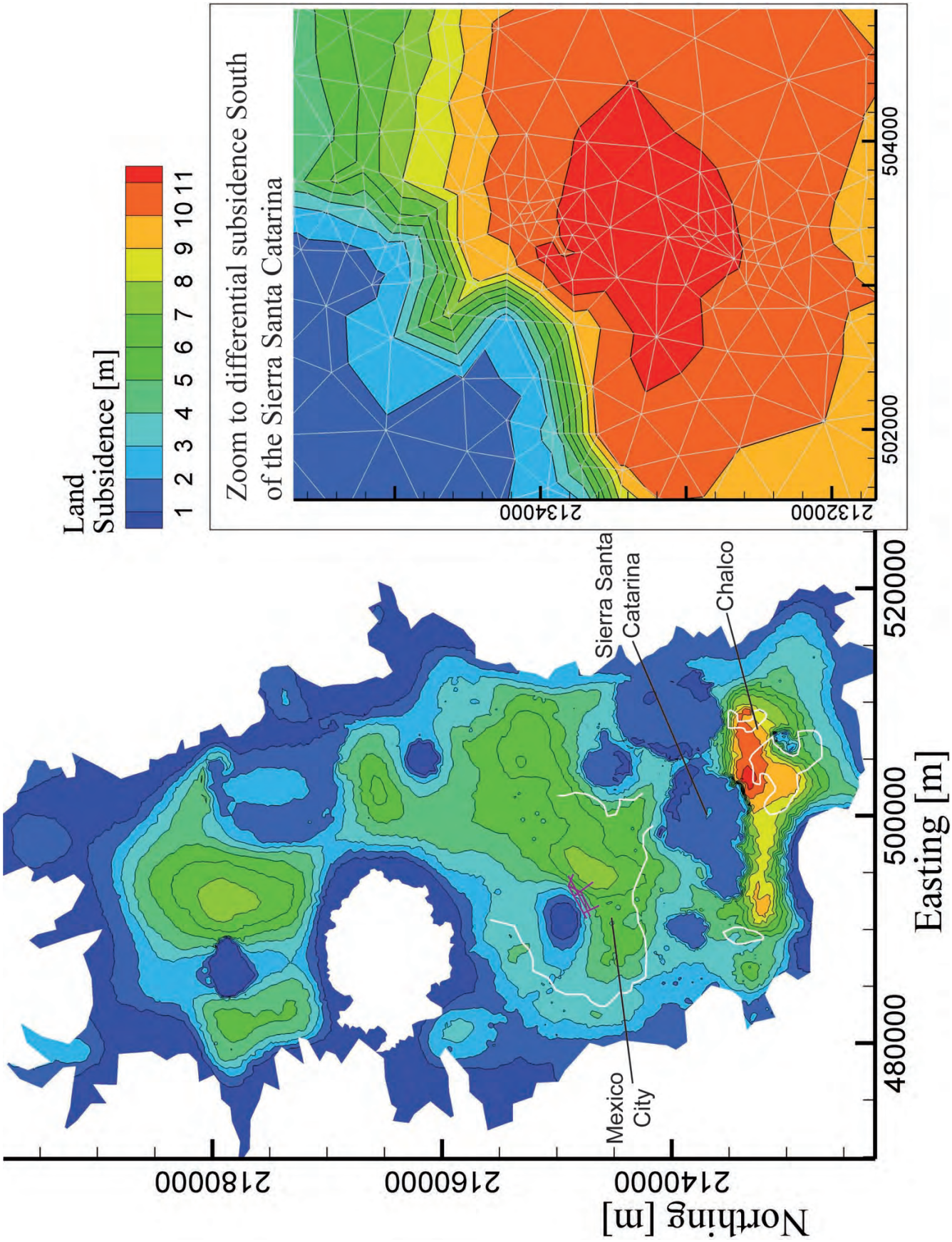

Figure 6.5: Simulated regional land subsidence map at 60 years of intense groundwater pumping, with a zoom to an area of differential consolidation. The white contour line expresses the land subsidence isocontour of 8 m for the period 1862-2005. This is based on Auvinet [1] for a comparative purpose. The purple lines situate the airport.

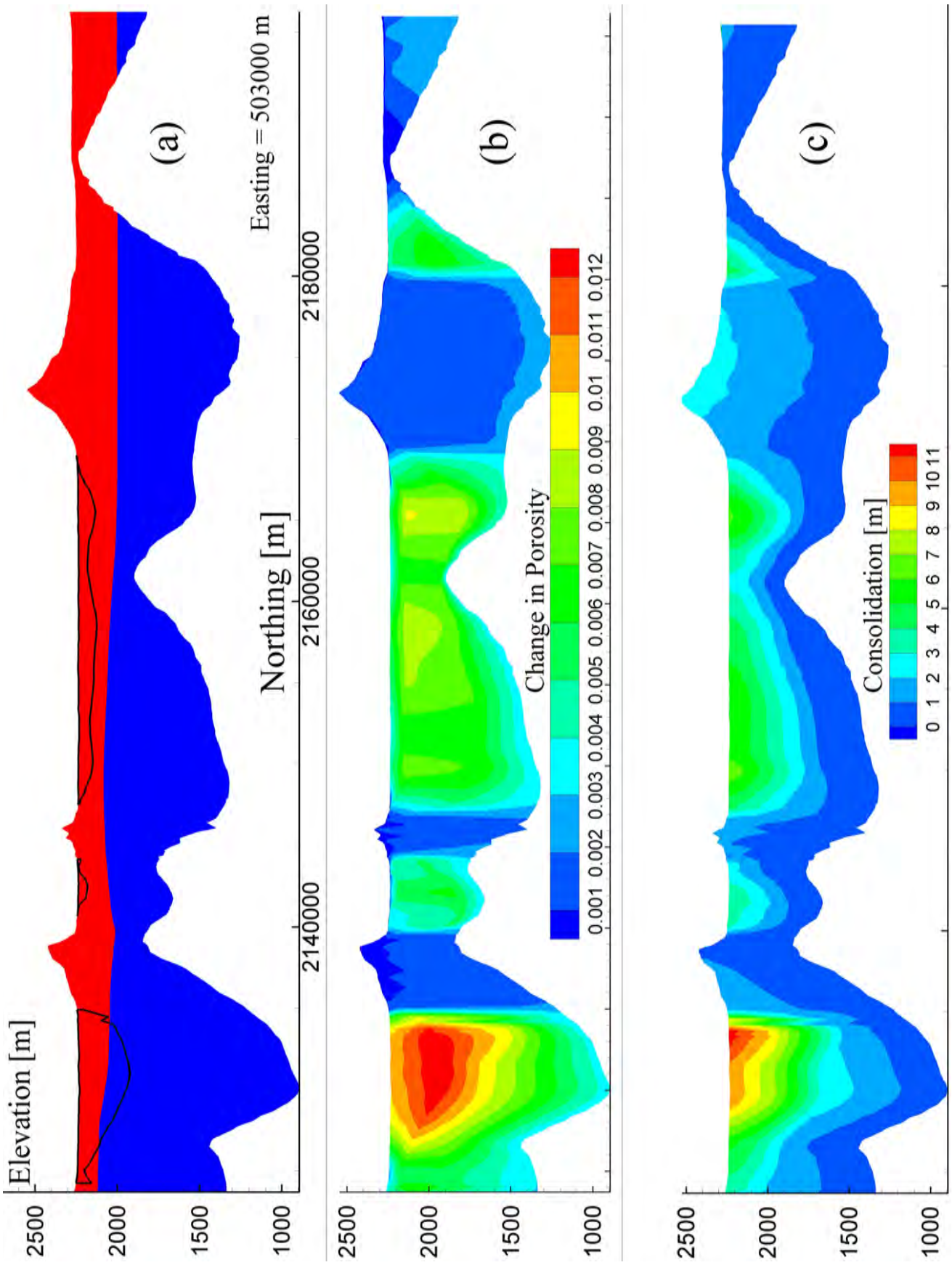

Figure 6.6: Cross sections extracted from the 3D model (Easting = 503'000 m) at 60 years of simulation time illustrating (a) the regional water table drawdown, leading to (b) a diminution of porosity resulting in (c) the consolidation of the aquifer system and land subsidence. The black line in (a) denotes the vertical extension of lacustrine confining deposits, showing that the deep aquifer system is now semi-confined.

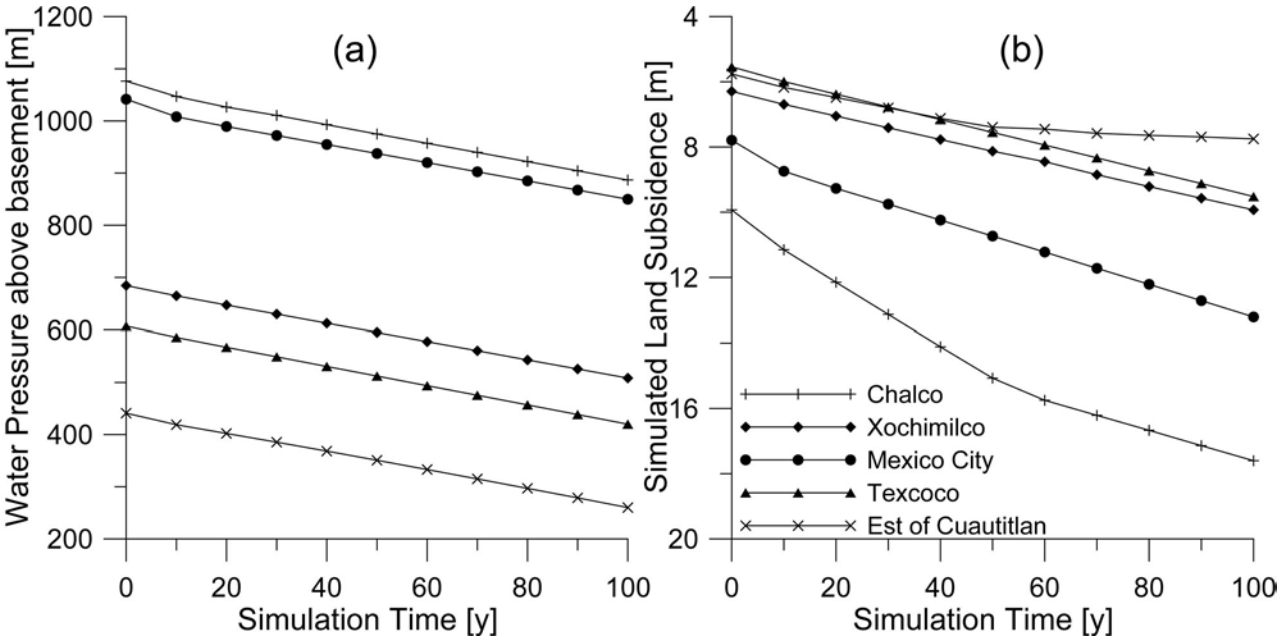

Figure 6.7: Simulation of the basin future evolution: simulated (a) water pressure in meters of water above local basement and (b) land subsidence as a function of simulation time for the principal sub-basins of the region.

6.6 Conclusions

The numerical approach proposed in Chapter 4 with the equations developed in Chapter 3 has been used to simulate regional groundwater flow and land subsidence in Mexico City. The model correctly reproduces the regional consolidation of lacustrine and alluvial deposits due to groundwater withdrawal. The aquifer system under Mexico City is heavily overexploited. However, this reservoir is very deep and may be able to provide water for a long time, even in the case of an unsustainable groundwater extraction. In such a case, land subsidence will continue but at a lower rate. This because lacustrine deposits will stop to compact when totally depressurised, and land subsidence will depend mostly on the consolidation of aquifer units, i.e., alluvial deposits and Tarango. The development of ground fractures will also continue with substantial damages for superficial civil engineering works, such as the airport or the metro. Therefore, wells injecting treated surface waters or other techniques able to recharge the aquifer system are well suited for slowing down land subsidence and aquifer system overexploitation. The proposed approach was able to locate areas of differential consolidation, which may be subject to high strains resulting in the formation of fractures (Figure 6.8). These zones are situated around incompressible Quaternary basaltic rocks, where there is an abrupt inflection of the basement topography leading to a strong thinning of the aquifer and differential land subsidence. Such areas of differential consolidation deserve detailed stress-strain analysis, in order to investigate the long term evolution of fractures in relation to groundwater exploitation.

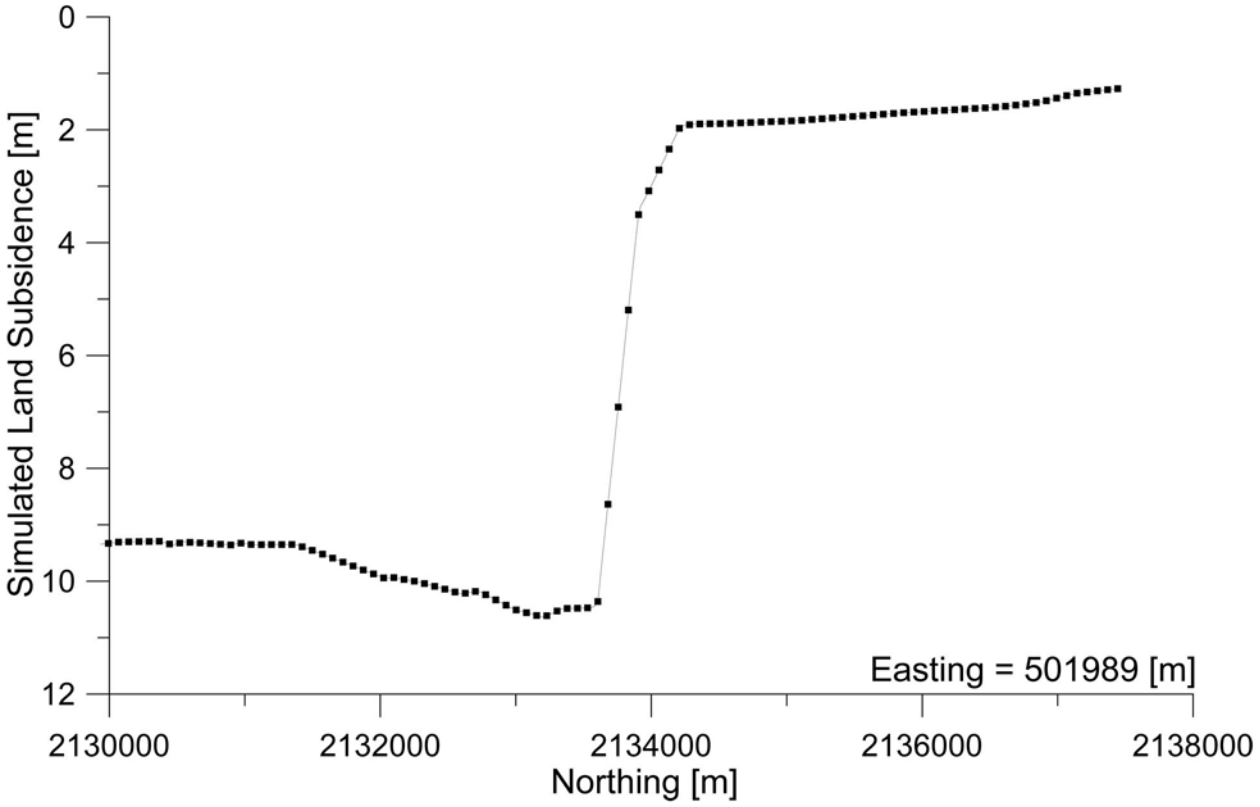

Figure 6.8: Simulated land subsidence between Sierra Santa Catarina and Chalco sub-basin, showing a sector with differential consolidation, which should be treated by specific stress-strain models.

Bibliography

[1] Auvinet, G.: Land subsidence in Mexico City. In: Geotechnical Engineering in Urban Areas affected by Land Subsidence, pp. 3–11 (2009)

[2] Auvinet, G.: Soil fracturing induced by land subsidence. In: Land Subsidence, Associated Hazards and the Role of Natural Resources Development, pp. 20–26 (2010)

[3] Auvinet, G., Méndez, E., Lermo, J.: Advances in geotechnical characterization of soil fracturing in Mexico City basin. In: Land Subsidence, Associated Hazards and the Role of Natural Resources Development, pp. 3–8 (2010)

[4] Bear, J., Cheng, A.H.D.: Modeling Groundwater Flow and Contaminant Transport. Springer Science (2010)

[5] Biot, M.: General theory of three-dimensional consolidation. J App Phys **12**, 155–164 (1941)

[6] Birkle, P., Torres Rodríguez, V., González Partida, E.: The water balance for the Basin of the Valley of Mexico and implications for future water consumption. Hydrogeology Journal **6**, 500–517 (1998)

[7] Blunier, P.: Méthodologie de gestion durable des ressources du sous-sol urbain. Ph.D. thesis, Ecole Polytechnique Fédérale de Lausanne (2009)

[8] Bradbury, J.: Paleolimnology of Lake Texcoco, Mexico. Evidence from diatoms. Limnology and Oceanography **16**(2), 180–200 (1971)

[9] BRGM, Fitzgerald, D., Associates, Ltd: GeoModeller User Manual, 352 pp. Intrepid Geophysics, Brighton, Australia (2012)

[10] Burbey, T.: Mechanisms for earth fissure formation in heavily pumped basins. In: Land Subsidence, Associated Hazards and the Role of Natural Resources Development, pp. 3–8 (2010)

[11] Calcagno, P., Chilès, J., Courrioux, G., Guillen, A.: Geological modelling from field data and geological knowledge Part I. Modelling method coupling 3D potential-field interpolation and geological rules. Physics of the Earth and Planetary Interiors **171**(1-4), 147–157 (2008)

[12] Carrera-Hernández, J., Gaskin, S.: The Basin of Mexico aquifer system: regional groundwater level dynamics and database development. Hydrogeology Journal **15**, 1577–1590 (2007)

[13] Carrera-Hernández, J., Gaskin, S.: The Basin of Mexico Hydrogeological Database (BMHDB): implementation, queries and interaction with open source software. Environmental Modelling & Software **23**, 1271–1279 (2008)

[14] Detournay, E., Cheng, A.D.: Comprehensive Rock Engineering: Principles, Practice and Projects, Vol. II, chap. Fundamentals of poroelasticity, pp. 113–171. C. Fairhurst, Pergamon Press (1993)

[15] Galloway, D., Burbey, T.: Review: Regional land subsidence accompanying groundwater extraction. Hydrogeology Journal **19**, 1459–1486 (2011)

[16] Gambolati, G., Teatini, P., Ferronato, M.: Encyclopedia of Hydrological Sciences, chap. Anthropogenic Land Subsidence, p. 17pp. Anderson M.G., John Wiley & Sons (2005)

[17] Gangi, A.F.: Variation of whole and fractured porous rock permeability with confining pressure. Int. J. Rock Mech. Min. Sci. Geomech. Abstr. **3**, 249–257 (1978)

[18] Helm, D.: Simulation of aquitard compaction due to changes in stress. Trans Am Geophys Union **53**(11), 979 (1972)

[19] Helm, D.: One-Dimensional Simulation of Aquifer System Compaction Near Pixley, California. 1. Constant Parameters. Water Resources Research **11**(3), 465–478 (1975)

[20] Helm, D.: One-Dimensional Simulation of Aquifer System Compaction Near Pixley, California. 2. Stress-Dependent Parameters. Water Resources Research **12**(3), 375–391 (1976)

[21] Jacob, C.: On the flow of water in an elastic artesian aquifer. American Geophysical Union **21** (1940)

[22] Jacob, C.: Engineering hydraulics: Proceedings of the Fourth Hydraulics Conference, Iowa Institute of Hydraulic Research, Iowa City, IW, chap. Flow of ground water. Rouse H (ed) (1950)

[23] Kim, J.M., Parizek, R.: A Mathematical Model for the Hydraulic Properties of Deforming Porous Media. Ground Water **37**(4), 546–554 (1999)

[24] Lajaunie, C., Courrioux, G., Manuel, L.: Foliation Fields and 3D Cartography in Geology: Principles of a Method Based on Potential Interpolation. Mathematical Geology **29**(4), 571–584 (1997)

[25] Mercier, J.: Modélisation hydrogéologique du bassin de Mexico City. Master's thesis, Centre for Hydrogeology and Geothermics, University of Neuchâtel, Neuchâtel, Switzerland (2012)

[26] Mooser, F., Molina, C.: New hydrogeological model for the Basin of Mexico. Bol centro invest sismic Fundacion Barros Sierra **3**(1), 48–68 (1993)

[27] Ortega-Guerrero, A., Cherry, J., Rudolph, D.: Large-scale aquitard consolidation near Mexico City. GroundWater **31**(5), 708–718 (1993)

[28] Osmanoglu, B., Dixon, T., Wdowinski, S., Cabral-Cano, E., Jiang, Y.: Mexico City subsidence observed with persistent scatterer InSAR. Int Journal Applied Earth Observation **13**(1), 1–12 (2011)

[29] Riley, F.: Analysis of borehole extensometer data from central California. In: Land Subsidence, IAHS RedBooks Pub. 88, pp. 423–431 (1969)

[30] Rivera, A., Ledoux, E., De Marsily, G.: Nonlinear Modeling of Groundwater Flow and Total Subsidence of the Mexico City Aquifer-Aquitard System. Land Subsidence. IAHS Publ **200**, 45–58 (1991)

[31] Terzaghi, K.: Die berechnung der durchlässigkeitziffer des tones aus dem verlauf der hydrodynamischen spannungserscheinungen. Akad Wissensch Wien Sitzungsber Mathnaturwissensch Klasse IIa **142**(3–4), 125–138 (1923)

[32] Terzaghi, K., Peck, R.: Soil Mechanics in Engineering Practice. John Wiley and Sons, Inc. (1967)

[33] Vázquez Sánchez, E., Jaimes-Palomera, R.: Geología de la Cuenca de México (Geology of the Mexico Basin). Geofisica Internacional **28**, 133–190 (1989)

Chapter 7

Conclusions

7.1 Effective stress-dependent parameters

7.1.1 Summary

The variations of effective stresses modify hydrodynamic parameters because of the elastic deformations they generate. This process can be neglected in shallow aquifers, such as in a post-glacial fractured decompression mountain slope, or in a phreatic system in superficial quaternary deposits. On the contrary, in deep aquifers as well as in confined units, porosity, hydraulic conductivity and storage coefficient must be considered as highly dependent on mechanical stresses.

The effects of this dependency have been detailed in the Introduction (Chapter 1). Effective stress-dependent equations were developed from sound hydrodynamic and physical concepts by means of mathematical analysis (Chapter 2 and 3). For **fractured rocks**, this approach takes into account (1) the compressive normal stress acting on fracture asperities and having a closing behaviour, and (2) the water pressure in the fracture porosity alleviating stress on asperities and having an opening behaviour. The resisting stress produced by a single asperity follows Hooke's law, and the integration of all the stresses is done at the fracture scale by assuming known statistical distribution of asperity lengths. This allows to relate effective stress to fracture hydraulic aperture, and successively to hydrodynamic parameters. For **granular porous rocks**, the microscopic processes are not taken into account because solid grains seem to be relatively incompressible compared to the total change of the bulk porous volume. Such a change is mainly driven by the closure of voids due to the rearrangement of grains. In this case, stress-dependent equations were developed by considering only the macroscopic change of porosity.

The next important step consisted in the implementation of these constitutive laws in a format suitable for large scale numerical investigations of volumetric discharge rates and hydraulic head fields in systems where hydrodynamic parameters cannot be considered as stress-independent.

7.1.2 Limitations

The presented models allow investigating the change of hydrodynamic parameters in relation to the changes in effective stresses. From a geomechanical point of view, the developed approach is limited to reversible deformations. Shear stresses and brittle deformations were not included in the analysis as water pressure variations in hydrogeological systems are too weak to induce such phenomena.

In the case of elastic reversible deformations, i.e., the decrease of hydraulic properties under loading follows the same curve as the increase under unloading, one single model parameterisation is necessary. Such a situation seems to be specific for fractured rocks [5, 1, 2]. On the contrary, in case of inelastic or irreversible deformations, i.e., only a fraction of the variation may be recovered, a parameterisation must be used for each branch taken during the successive loading / unloading cycles. This may be for instance the case in the analysis of fine granular sediments, such as silts or clays [3, 4].

Under high geodynamic (tectonic) stresses a fractured and/or granular porous rock undergoes elasto-plastic deformations (Figure 1.4). In such a case the proposed stress-dependent equations are not reliable.

7.2 Regional simulation of coupled hydromechanical processes

7.2.1 Summary

A modelling approach aiming at simulating the consolidation / expansion of an aquifer system affected by important water pressure perturbations has been presented in Chapter 4. The approach consists of three phases. First, the stress field acting on the aquifer system is computed, and is in general assumed to be lithostatic. Second, the groundwater flow equation with stress-dependent hydrodynamic parameters is solved in order to simulate (1) the aquifer recharge and discharge rates, and (2) the modification of the hydraulic head field due to an external perturbation, such as tunnel drainage or groundwater overpumping. Third, the perturbed hydraulic head field is used to calculate the changes in porosity and the associated ground settlement / uplift due to the total variations of water pressures between an undisturbed states, such as before the excavation of a tunnel or groundwater overpumping, and the final perturbed state.

This method was especially developed to solve these coupled hydromechanical processes at large regional hydrogeological scales, and considering the relevant geological structures as well as the essential processes and parametric information.

The approach is based on few parameters and on conventional boundary conditions, and was able to reproduce (1) the complex shape of ground settlements in the context of tunnel drainage in fractured rocks, such as in the Rawyl exploratory adit (Chapter 4) or in the La Praz tunnel (Chapter 5), as well as (2) land subsidence in the context of groundwater overpumping in basin-fill aquifer systems, such as in Mexico City (Chapter 6).

7.2.2 Limitations

Areas subject to differential aquifer consolidations are correctly identified by this approach. These areas may be concerned by brittle deformations, such as ground fracturing, due to significant horizontal strains. However, the proposed method is only applicable to vertical volume changes and does not account for strain analysis, i.e., the study of the relative displacement between two points originally adjacent which may result in brittle deformations. One possible approach could be to use the presented method at a regional scale in order to identify areas of differential consolidations. Then, a detailed strain analysis could be performed in such local areas in order to investigate the possibility of brittle deformations. Additionally, calculated regional consolidation could be used as boundary conditions for the local strain analysis.

Another important finding is that volumetric discharge rates calculated considering the relation between stress and hydrodynamic parameters are much lower compared to an approach neglecting this dependency, which tends to overestimation. The computed depressurisation and emptying of an overexploited deep aquifer, or a permeable sector intersected by a tunnel, is also slower. This is due to the decrease of hydraulic conductivity and storage with decreasing water pressure and system compression. This implies that with the presented approach the consolidation will be slower compared to an approach considering hydrodynamic parameters as constants. However, it is important to note that this depends also on (1) the stress regime and (2) the geomechanical properties of the porous medium. Indeed, in the absence of compressive stresses there is no reduction of hydrodynamic parameters despite a decrease of water pressure, e.g., a vertical fracture in an extensive geodynamic environment or in the case of an incompressible porous medium (no asperities compression and/or porosity reduction despite the increase in effective stress).

7.3 Outlook

This work has given rise to many implications and questions that need further investigation. Below is a list of suggestions for future applications and research.

Research

- **Coupling the proposed equations with fracture genesis or activation**. One approach would be to work on the limits of the proposed models. For example, on one hand, if the applied compressive effective stress becomes greater than the fracture/porosity closure stress, this could be coupled to the genesis of new fractures due to brittle ruptures. This relation between compaction and fracture genesis is of particular interest for petroleum engineering, because reservoir permeability and connectivity increases with fracturing. On the other hand, if the effective stress becomes negative (fluid pressure is greater than total stress), this could be related to shear / sliding movement or to a soil boiling phenomenon.

- **Combine hydrogeological and geomechanical field measurements**. For example, perform long term pumping tests at constant and significant pumping rate in thick and deep fractured or granular porous aquifer system by monitoring the hydromechanical response of the aquifer. Measurements will consist in hydraulic heads in observation wells and three-dimensional surface deformations by detailed geodetic monitoring: repeated ground leveling, GPS surveys or InSAR/LiDAR measurements. Processing of data will serve as a basis for the elaboration of a method for interpreting pumping tests taking into account the response of hydrodynamic parameters to geomechanical deformations.

- **Reduction factor for deep wells**. In Chapter 5, it is shown that the implementation of a reduction factor in analytical solutions solving for the inflow rate in deep excavations, allows to consider the effects of effective stress on hydrodynamic parameters. The same concept could be applied to analytical solution solving for the discharge rate produced by deep wells.

- **Parameter uncertainty and method reliability**. Modelling natural systems always requires investigations on parameter sensibility and uncertainty, as well as verification of the theoretical approach by back analysis of real cases in order to validate the reliability of the method. In this thesis, this verification is performed for the cases of Rawyl, Modane, La Praz and Mexico City. However, the work has not focused on a detailed investigation on parameter estimation and uncertainty. Moreover, at this point it is also important to note that modelling natural systems often implies non-unique solutions. In this context, emerging calibration algorithms could be combined to the proposed approach in order to analyse parameter estimation, uncertainty and method reliability. In such a case, satellite/airborne radar data, e.g., InSAR/LiDAR measurements will provide the field data required to assess the reliability of the model.

- **Combine quantitative and field-oriented approaches for the estimation of the inflow rate in a tunnel**. The reliability of quantitative methods for the inflow rate in a tunnel can be verified and constrained by field methods. For example, one approach consists in comparing analytical/numerical results with infiltration rates obtained by field-oriented hydrological study. In such a case, the analytical/numerical flow rate in a deep excavation may be constrained by the recharge rate obtained by field investigations.

Applications

- **Sensitivity of hydrodynamic parameters on effective stresses**. The proposed equations are simple and seem sufficiently accurate to enable the analysis of the evolution of hydrodynamic parameters in the case of substantial changes of water pressures and/or external stresses, e.g., the evolution of fracture hydraulic conductivity during a glaciation. This latter case is particularly interesting for projects related to geologic radioactive waste repositories.

- **Application of the proposed approach to overexploited groundwater systems**. For thick and deep groundwater systems, the proposed approach can be used to investigate the deterioration of hydrodynamic parameters and future deformations in cases where groundwater overexploitation is suspected, as well as the identification of areas subject to differential subsidence leading to fractures formation. These areas deserve detailed stress-strain analysis, in order to investigate the ground fissure genesis and propose a mitigation technique. For the basin-fill aquifer system under Mexico City, as proposed by many authors, treated surface waste waters must imperatively be used to recharge the deep aquifer in order to restore higher water pressures at depth, and possibly reduce the regional land subsidence and associated ground fracturing which have affected the region for several decades. This implies the optimisation of techniques for the injection / infiltration of water in saturated media or in semipervious geological formations. For such an issue numerical modelling is critical.

- **Application of the proposed approach to large scale projects**. The proposed modelling approach for regional coupled fluid-to-solid hydromechanical processes was successfully applied to systems affected by increasing effective stresses (Chapters 5, and 6). This method could be used to investigate the dynamic of deep aquifers / reservoirs subject also to decreasing effective stresses due to fluid injections for maintaining fractures aperture or hydraulic fracturing, such as in projects related to CO_2 sequestration, shale gas or geothermal energy production. These systems are concerned by regional ground uplifts close to injection wells, as well as land subsidence related to pumping wells.

- **Hydromechanical processes in Switzerland**. To date, Switzerland is not concerned by land subsidence due to groundwater pumping, principally because the thick basin-fill aquifer systems are not subject to overexploitation and substantial water table drawdowns. However, regional hydromechanical processes are present in Switzerland, particularly in the framework of tunnel excavations through the Alps. Projects related to geothermal energy production should also be investigated because of the hydromechanical processes they involve. Future studies should aim at detecting, monitoring and modelling coupled hydromechanical processes. This also implies the development of measurement and simulation tools.

Bibliography

[1] Cappa, F.: Role of fluids in the hydromechanical behavior of heterogeneous fractured rocks: in situ characterization and numerical modelling. Bull. Eng. Geol. Env. **65**, 321–337 (2006)

[2] Hansmann, J., Loew, S., Evans, K.: Reversible rock-slope deformations caused by cyclic water-table fluctuations in mountain slopes of the Central Alps, Switzerland. Hydrogeology Journal **20**(1), 73–91 (2012)

[3] Helm, D.: One-Dimensional Simulation of Aquifer System Compaction Near Pixley, California. 1. Constant Parameters. Water Resources Research **11**(3), 465–478 (1975)

[4] Helm, D.: One-Dimensional Simulation of Aquifer System Compaction Near Pixley, California. 2. Stress-Dependent Parameters. Water Resources Research **12**(3), 375–391 (1976)

[5] Louis, C.: A study of groundwater flow in jointed rock and its influence on the stability of rock masses. Tech. Rep. 9, Rock Mechanics, Imperial College, London, UK (1969)

Appendix A

Numerical comparison of analytical models

Effective stress and fracture permeability in regional groundwater flow: numerical comparison of analytical models

Preisig Giona & Perrochet Pierre
Centre of Hydrogeology and Geothermics, Emile-Argand 11, CH-2009 Neuchâtel
giona.preisig@unine.ch

7 SWISS GEOSCIENCE MEETING 2009

1. Introduction and Problematic

The dependency of fracture permeability on effective stress is a well known research topic. Effective stress increases with depth in saturated aquifers, leading to a decreasing permeability. Moreover underground draining structures as tunnels, cause a decrease of pore pressure accelerating the process. In this work, regional simulations considering the effects of effective stress are compared to each other and to the classical approach, based on a constant permeability field.

2. Methodology and Modelling Approach

Three different model functions relating effective stress to permeability are implemented in the tensor form of Darcy's law (Table 1). Numerical simulations are based on an hypothetic initial fractured hydrostatic system where a deep draining structure is activated, causing a steady-state saturated flow from the upper boundary condition (surface) to the lower boundary condition (underground structure). The governing non linear equations are solved using the finite element method (Fig. 1).

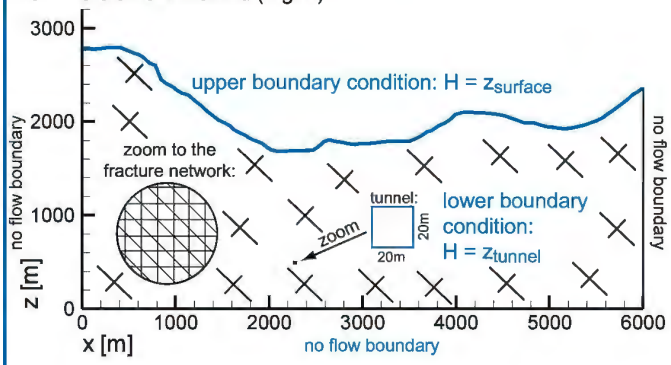

Fig. 1: Geometry of the finite element model and boundary conditions; the mesh consists of 30'651 nodes and 7'500 nine-node quadrangular elements.

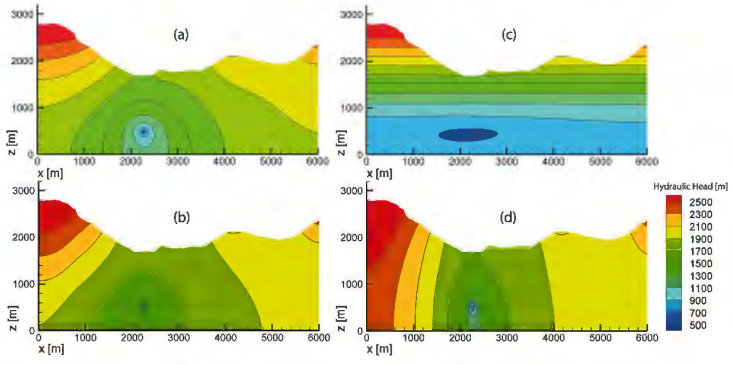

Fig. 2: Steady-state flow to a tunnel, equipotentials: classical approach with a constant permeability field (a); permeability tensors corrected by Louis' modified model (b); by Walsh's modified model (c); and by the elasto-statistical model analytically derived from Hooke's law (d).

4. Conclusion and Perspectives

This numerical study has shown the importance of considering the effects of effective stress variations in deep regional simulations of discharge rates, pressure distributions and flow paths. Variations of effective stresses also generate variations of aquifer porosities, which are then translated into ground settlements (consolidation). The method is now being tested on real cases.

Table 1: Model functions relating effective stress to permeability implemented in the tensor form of Darcy's law, and respectively model parameters.

Derived Model Function	Initial Author	Origin
$K_h = K_0 e^{-3\beta(\sigma' - \sigma'_0)}$	Louis C. (1969)	Experimental
$K_h = K_0 (1 - \alpha \ln(\frac{\sigma'}{\sigma'_0}))^3$	Walsh J.B. (1981)	Experimental
$K_h = K_{max} (1 - (\frac{\sigma'}{\sigma'_{max}})^{\frac{1}{m}})^3$	Hooke's law	Theoretical
Symbol	*Parameter*	*Units*
K_h	hydraulic conductivity depending on effective stress	$m\ s^{-1}$
K_0	hydraulic conductivity at initial hydrostatic condition	$m\ s^{-1}$
β	parameter characterizing the elastic resistance of fractures to crushing: $\beta = (\Phi E_s)^{-1}$	Pa^{-1}
Φ	porosity of the fracture family	-
E_s	elastic modulus	Pa
σ'	effective stress: $\sigma_L - p$	Pa
σ_L	lithostatic stress considering fracture's geometry: $\sigma_L = \rho_r g Z (\lambda n_x^2 + \lambda n_y^2 + n_z^2)$	Pa^{-1}
ρ_r	rock's density	$kg\ m^{-3}$
g	gravitational acceleration	$m\ s^{-2}$
Z	depth	m
λ	ratio of horizontal stress to vertical stress	-
$n_{x,y,z}$	normals to the plane of fracture	-
p	pore pressure: $p = \rho_w g h$	Pa
ρ_w	water's density	$kg\ m^{-3}$
h	water pressure	m
σ'_0	effective stress at initial hydrostatic condition ($h_0 = 0$)	Pa
α, m	parameters characterizing fracture morphology	-
K_{max}	maximum hydraulic conductivity: $\sigma' = 0 \rightarrow K_h = K_{max}$	$m\ s^{-1}$
σ'_{max}	maximum effective stress: $\sigma' = \sigma'_{max} \rightarrow K_h = 0$	Pa

Table 2: Values used for the numerical simulation, calculated flow rates to the tunnel and ratio of flow rates with differential permeability tensors to flow rates with classical approach.

Fracture Family	K_{max} / K_0	n_x	n_y	n_z	ρ_r	λ	σ_{max}	m	Φ	E_s	σ
1	10^{-4}	0	0	1	2500	0.5	$1.5 \cdot 10^8$	11	$5 \cdot 10^{-4}$	$2 \cdot 10^{10}$	0.5
2	10^{-5}	1	0	1	2500	0.5	$3.5 \cdot 10^8$	11	$2 \cdot 10^{-4}$	$5 \cdot 10^{10}$	1.0
3	10^{-4}	1	0	0	2500	0.5	$1.5 \cdot 10^8$	11	$5 \cdot 10^{-4}$	$2 \cdot 10^{10}$	0.5

Model	Flow rates to the tunnel [L min^{-1}]	Ratio
Classical Approach	**9840**	**-**
Louis C. (1969)	**2877**	**0.29**
Walsh J.B. (1981)	**296**	**0.03**
Elasto-statistical	**87**	**0.01**

3. Numerical Results

In the three cases, results show that the introduction of stress-dependent permeabilities in Darcy's law leads to discharge rates significantly lower than those calculated with the classical approach, this is explained by a decreasing permeability due to an increasing effective stress (Table 2).

Louis' experimental model yields the smaller differences to the classical approach because only the effect of pore pressure diminution is considered; in effect the lithostatic stress term in this model does not affect the solution. Therefore the equipotentials distribution are similar to the classical approach, the principal differences are noted in the vicinity of the deep draining structure, because the pore pressure variation is maximal (Fig. 2).

Walsh's model is difficult to solve numerically due to higher order non linearities, and the modification of permeability tensors is so great (especially for the horizontal fracture family) that the hydraulic system returns quasi hydrostatic conditions.

The elasto-statistical model analytically derived from Hooke's law seems to be better adapted for solving such problems, because in this case permeability values depend on the pore pressure, and on the depth in the model (lithostatic stress), therefore at every nodes there is a different value of permeability. Moreover the calculated flow rates appear more realistic than those calculated by other models.

References
Louis C. 1969: A study of groundwater flow in jointed rock and its influence on the stability of rock masses. Technical Report No 10, 9/69, Rock Mechanics, Imperial College, UK.
Walsh J.B. 1981: Effect of pore pressure and confining pressure on fracture permeability. Int. J. Rock Mech. Min. Sci. Geomech. Abstr., 18: 429 - 435.

Appendix B

Mountains - up and down: the role of groundwater pressure

Mountains - Up and Down: the Role of Groundwater Pressure

Giona Preisig* & Pierre Perrochet*
*Centre for Hydrogeology and Geothermics (CHYN), University of Neuchâtel, Emile-Argand 11, CH-2000 Neuchâtel
giona.preisig@unine.ch

10th SWISS GEOSCIENCE MEETING 2012 BERN

Introduction

In aquifers, an important variation in groundwater pressure results in a modification of the effective stress state, leading to a change of the porous volume. This coupled hydromechanical fluid-solid process is mainly related to anthropogenic activities, such as groundwater overpumping or deep excavation drainage, resulting in land subsidence. However, Hansmann et al. (2012) by means of high precision leveling surveys in the framework of the Gotthard Alp transit Base Tunnel Project, also detected this process in fractured granitic rocks subject only to natural variations of water pressures. Here, increasing / decreasing water pressures during groundwater recharge / discharge periods lead to cyclical expansions / compressions of the fractured rock mass resulting in a subtle reversible mountain "up and down" (Figure 1).

A recent modelling approach specific for fluid-solid coupled hydromechanical processes has been proposed by Preisig et al. (2012). This method allows the simulation of groundwater flow in the deformable fractures of the aquifer. Within this context, this work aims to illustrate the ability of the afore-mentioned modelling approach to simulate the natural process observed by Hansmann et al. (2012).

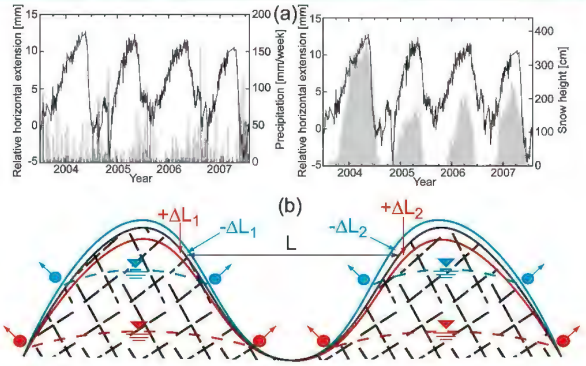

Fig. 1: (a) Relative horizontal extension between two reflectors located on slopes of the Val Termine, Canton Ticino (solid black line), precipitation and snow height (in gray) as a function of time (Hansmann et al., 2012). (b) Conceptual model illustrating the fractured rock mass expansion (blue line) / compression (red line) under seasonal variations in water table levels, leading to a shortening/extension of the distance L orthogonal to the valley (modified from Hansmann et al., 2012).

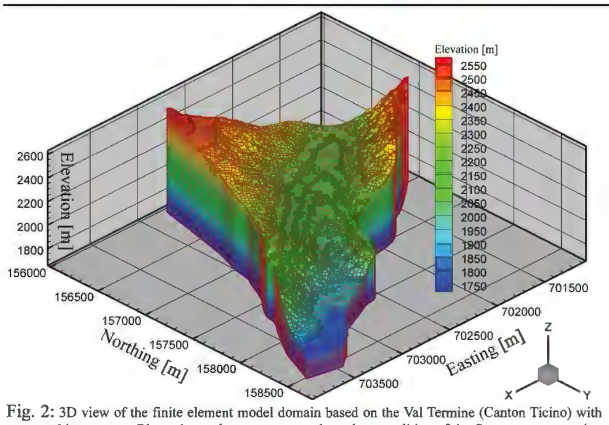

Fig. 2: 3D view of the finite element model domain based on the Val Termine (Canton Ticino) with topographic contours. Blue spheres denote a constant boundary condition of the first-type representing the water level in the St. Maria Dam Lake. The recharge function presented in Figure 4 is applied on superficial nodes of the 3D model.

Modelling Approach

The modelling approach is based on a governing equation relating fracture aperture to effective stress. Thus, a change of the effective stress state due to a variation of water pressure leads to the opening or closure of fracture porosity. The integration of all fractures porosity changes results in an expansion or compression of the fractured rock mass. Within this context, a 3D finite element model of the Val Termine was constructed (Figure 2). Three simulations must be computed to perform the analysis. First, the overburden stress acting on the aquifer is calculated. Then, a transient groundwater flow simulation with stress-dependent parameters is solved in order to reproduce the variation of water table levels due to recharge / discharge periods. Obtained water pressure fields are then introduced in a final calculation solving for changes in fractures porosity and associated cyclical aquifer expansions / compressions.

Boundaries conditions for the transient groundwater flow are: (1) a cyclical recharge function applied on upper nodes of the 3D model based on rain and snow melt data, and (2) a constant water table level at the valley bottom representing the St. Maria Dam Lake in which Val Termine culminates.

Results & Discussion

Considering an isotropic fractured rock having a hydraulic conductivity parallel to fracture planes of 10^{-6} m/s and porosity lower than 1%, the proposed model correctly reproduces the mechanical response of the fractured rock to a change in water pressure (Figs. 3 & 4). As shown in Fig. 4, the increase of recharge due to significant rain or snow melt events, leads to increasing hydraulic head (H) resulting in the fractured rock mass expansion and in a shortening of the distance (L) between two points located on valley slopes. The response of deformation to an important recharge or discharge event is quasi instantaneous. This is a consequence of the low porosity and storage of fractured rocks, implying that these aquifers can be filled / emptied very rapidly. In mountain systems, this results in substantial variation of water pressure leading to a natural fluid-rock hydromechanical coupled process.

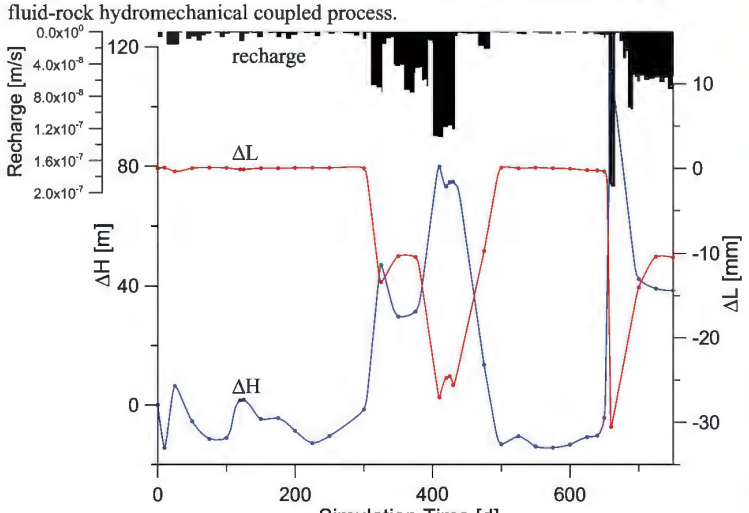

Fig. 4: Recharge, relative change in hydraulic head (ΔH) for an observation point within the aquifer, and relative change in the distance between two points located on model slopes (ΔL) as a function of simulation time.

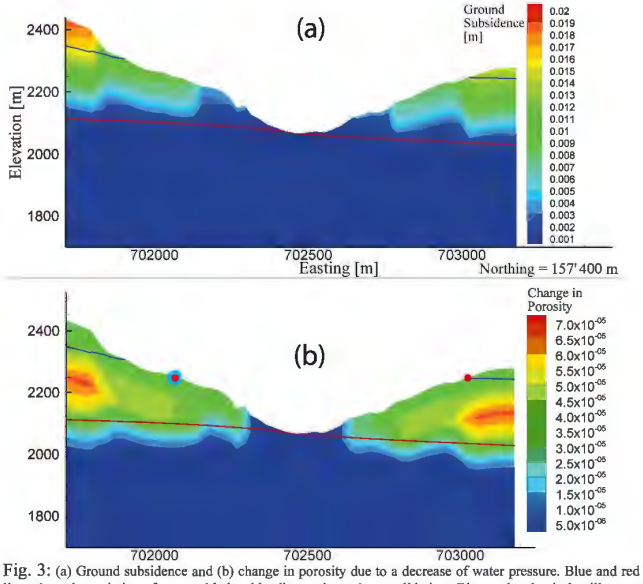

Fig. 3: (a) Ground subsidence and (b) change in porosity due to a decrease of water pressure. Blue and red lines show the variation of water table level leading to the rock consolidation. Blue and reds circles illustrate the location of observation and geodetic points used for the elaboration of Fig. 4.

Conclusion

A modelling approach specific for the mechanical response of fractures aperture to a change in water pressure was used to reproduce the seasonal deformations observed in fractured granitic rocks of the Gotthard massif. Results clearly show coherence between the conceptual and the numerical model, which is also used in hydromechanical analysis related to tunnels drainage or intensive groundwater pumping.

References

[1] Hansmann J., Loew S., & Evans K.F. (2012): Reversible rock-slope deformations caused by cyclic water-table fluctuations in mountain slopes of the Central Alps, Switzerland. *Hydrogeol J*, 20(1), 73-91.
[2] Preisig, G., Cornaton, F. & Perrochet P. 2012: Regional Flow Simulation in Fractured Aquifers Using Stress-dependent Parameters. *Ground Water*, 50(3), 376-385.